2014

Advanced semiconductor silicon detector for dosimetry and microdosimetry in radiation protection and hadron therapy

Linh T. Tran
University of Wollongong, tlt822@uowmail.edu.au

ADVANCED SEMICONDUCTOR SILICON DETECTOR FOR DOSIMETRY AND MICRODOSIMETRY IN RADIATION PROTECTION AND HADRON THERAPY

A Thesis Submitted in Fulfillment of

the Requirements for the Award of the Degree of

Doctor of Philosophy

from

UNIVERSITY OF WOLLONGONG

by

Thuy Linh Tran

Dip. Sp. (Phys. Eng., Dubna University)

Centre for Medical Radiation Physics, Engineering Physics
Faculty of Engineering

2014

ADVANCED SEMICONDUCTOR SILICON DETECTOR FOR DOSIMETRY AND MICRODOSIMETRY IN RADIATION PROTECTION AND HADRON THERAPY

Thuy Linh Tran

A Thesis for Doctor of Philosophy

Centre for Medical Radiation Physics, Engineering Physics

Faculty of Engineering

Abstract

This thesis presents research for the application of silicon dosimetry and microdosimetry for radiation protection and Quality Assurance (QA) in radiation therapy.

The first part of this thesis describes the development and characterisation of a charged particle silicon detector to assess the radioactivity of contaminated soil from nuclear power plant accidents.

The second part of the thesis is continuing research into the development of novel silicon on insulator (SOI) microdosimeter aimed at deriving relative

biological effectiveness (RBE) in mixed radiation fields using microdosimetry which does not require any prior knowledge of the components of this field.

Different generations of CMRP SOI microdosimeters were investigated and tested in ^{12}C heavy ion therapy, and the derived RBE_{10} values obtained by the SOI microdosimeters agreed with a Tissue Equivalent Proportional Counter (TEPC).

A novel 3D SOI microdosimeter was proposed in this thesis and the fabrication processes are described in detail. Using the GEANT4 Monte Carlo toolkit, simulations were developed to study the response of the new 3D microdosimeters in various radiation fields and optimize the design. A heavy ion microprobe was used to comprehensively study the charge collection properties of the silicon detectors using the Ion Beam Induced Charge Collection (IBICC) technique.

A monolithic ΔE-E telescope was evaluated in response to a ^{12}C heavy ion therapy beam. Information about the radiation field was obtained by measuring the energy deposition coincidently in the ΔE and E stage in coincidence. The detector provides two-dimensional (2D) information of the LET of the particles as well as identifying the types of particles produced from the primary radiation field. An experimental and theoretical study was carried out and is presented in this thesis.

KEY WORDS: Alpha charged particle detector, nuclear power plant accident, Microdosimetry, 3D detector, heavy ion therapy, RBE.

Acknowledgements

Firstly, I would like to express my sincere appreciation to my supervisor, Professor Anatoly Rosenfeld for his guidance, encouragement and continuous support throughout my PhD study. Professor Rosenfeld is a wonderful mentor and supervisor, and without his guidance and persistent help this thesis would not have been possible. I also thank Professor Rosenfeld for giving me opportunities to undertake research at the international medical facilities and present this work at a number of prestigious international conferences.

I would also like to thank Dr. Dale Prokopovich for his time and effort in supervising and assisting me with the measurements at ANSTO and overseas. His kind help and discussions about the experiments and theories are very much appreciated.

I wish to thank my co-supervisor, Dr. Susanna Guatelli for teaching me Geant4 and helping me with the debug code. Her careful guidance and advices for my PhD study and future professional career are really helpful.

I would like to express my appreciation to Dr. Mark Reinhard for hosting me at the ANSTO Detector Lab and providing me with extremely helpful feedback on preparing my paper.

My appreciation is also extended to the following people for their help and support during my PhD study:

- *Associate Professor Michael Lerch for his help and advice with my paper preparation and Dr. Marco Petasecca for his informative discussion and assistance with the electronic readout system.*
- *Dr. Angela Kok of SINTEF Company in Oslo, Norway for sharing her deep knowledge about 3D detector technology and providing me with really helpful advice on my thesis chapter.*
- *Prof. Naruhiro Matsufuji of National Institute for Radiological Science (NIRS) in Chiba, Japan for his kind help and support during our experiments in HIMAC, Japan.*
- *Mr. Adam Sarbutt of ANSTO for his help with producing electronic devices for my experiments overseas. His advice and careful preparation helped us succeed in the experiments.*
- *Dr. Dean Cutajar for his great help with preparing MOSkin dosimeters for experimenting in HIMAC, Japan and in general for any technical issue at the University.*
- *Dr. Rainer Siegele of ANSTO for his help in running the ANTARES Heavy Ion Microprobe.*
- *Mrs. Karen Ford for the administrative assistance and all her kind help during my 3 years of PhD.*

To CMRP PhD students: Thank you Jayde for helping me with the experiments at ANSTO in the first year of my PhD and the useful discussions about microdosimetry concepts, and to Jeremy for giving me a basic understanding of the Geant4 simulation toolkit. Thank you Sianne, Saber for helping me with Endnote, Matlab and LaTeX. Special thanks to David, Lachlan and Vanja for proof reading part of my thesis.

I would especially like to thank my husband Sinh Manh for his love and encouragement as well as both our parents and my sister Jennifer Tran for their wonderful support throughout my studies.

Last but not the least I thank my son Jacob Manh Tran for his unconditional love and being the primary motivation for my life.

Preamble

All of the experiments, work, simulations and analytical results presented within this thesis were performed by myself, Thuy Linh Tran, with assistance from the following:

The experimental data using a 1st and 2nd generation microdosimeter, ultra-thin 3D detector and bridge microdosimeter in HIMAC, Japan for chapter 9 was collected with help from Dr. Dale Prokopovich, but I carried out all the data processing and analysis.

The original Geant4 code for ΔE-E telescope simulation presented in chapter 8 was written in collaboration with Dr. Susanna Gualelli, but I carried out the simulation and data processing with help from David Bolst, a PhD student.

The experiment with the bridge microdosimeter collected for chapter 7 was obtained with help from Lachlan Chartier, an honors student, but I carried out all the data processing and analysis.

Publications

1. Linh T. Tran, Susanna Guatelli, Michael L. F. Lerch, Dale A. Prokopovich, Mark I. Reinhard, James F. Ziegler, Marco Zaider and Anatoly B. Rosenfeld (2014). *A Novel Silicon Microdosimeter using 3D Sensitive Volume: Modeling the Response in Neutron Field Typical of Aviation*. IEEE Transactions on Nuclear Science, 61(4), 1552-1557.

2. Linh T. Tran, Dale A. Prokopovich, Marco Petasecca, Michael L. F. Lerch, Angela Kok, Anand Summanwar, Cinzia Da Via, Mark I. Reinhard, Kari Schjølberg-Henriksenand (2014). *3D Radiation Detectors: Charge Collection Characterisation and Applicability of Technology for Microdosimetry*. IEEE Transactions on Nuclear Science, 61(4), 1537-1543.

3. Linh T. Tran, Michael L. F. Lerch, Marco Petasecca, Dale A. Prokopovich, Mark I. Reinhard, V. Perevertaylo and Anatoly B. Rosenfeld (2012), *Development of large area silicon alpha particle detector*. Journal Applied Radiation and Isotopes. DOI: 10.1016/j.apradiso.2014.06.009 (accepted 14th May 2014).

4. Jayde Livingstone, Dale A. Prokopovich, Linh T. Tran, Susanna Guatelli, Marco Petasecca, Michael L. F. Lerch, Mark I. Reinhard, Vladimir L. Perevertaylo, James F. Ziegler, Marco Zaider, and Anatoly B. Rosenfeld

(2013), *Charge Collection in n-SOI Planar Microdosimeters,* IEEE Trans. Nuclear Science, 60(6), 4289-4296.

5. Linh T. Tran, David Bolst, Susanna Guatelli, Dale A. Prokopovich, Ying C. Keat, Marco Petasecca, Michael L. F. Lerch, Mark I. Reinhard, Alberto Fazzi, Elena Sagia, Stefano Agosteo, Naruhiro Matsufuji and Anatoly B. Rosenfeld (2014). *High spatial resolution microdosimetry with ΔE-E detector on ^{12}C beam: Monte Carlo simulations*, submitted to Physics Medicine and Biology (under review).

6. Linh T. Tran, Dale A. Prokopovich, Marco Petasecca, Michael L. F. Lerch, Celeste Fleta, Giulio Pellegrini, Consuelo Guardiola, Mark I. Reinhard, and Anatoly B. Rosenfeld (2014). *Ultra-thin 3D Detectors: Charge Collection Characterisation and Application for Microdosimetry*, submitted to IEEE Trans. Nuclear Science (accepted).

7. Linh T. Tran, Lachlan Chartier, Dale A.Prokopovich, Marco Petasecca, Michael L. F. Lerch, Mark I. Reinhard, Vladimir Perevetaylor, Naruhiro Matsufuji and Anatoly B. Rosenfeld (2014). Development of Large Area 3D-Mesa "Bridge" Microdosimeter for RBE Studies in ^{12}C Radiation Therapy. Submitted to IEEE Trans. Nuclear Science (Under review).

Conferences

1. Linh T. Tran, Michael L. F. Lerch, Marco Petasecca, Dale A. Prokopovich, Mark I. Reinhard, V. Perevertaylo and Anatoly B. Rosenfeld (2012). *Development of large area silicon alpha particle detector*. Presented at RADIATION 2012 Radioprotection: Past, Present and Future, 15th - 17th February, Lucas Heights, AINSE, NSW, Australia.

2. Linh T. Tran, Michael L. F. Lerch, Marco Petasecca, Dale A. Prokopovich, Mark I. Reinhard, V. Perevertaylo and Anatoly B. Rosenfeld (2012). *Development of large area silicon alpha particle detector*. Presented at Heavy Ion Accelerator Symposium for Fundamental and Applied Research 11th - 13th April 2012, Canberra, ACT, Australia.

3. Linh T. Tran, Susanna Guatelli, Michael L. F. Lerch, Dale A. Prokopovich, Mark I. Reinhard and Anatoly B. Rosenfeld (2012). *Improvement of Silicon Microdosimeter using 3D Sensitive Volume*. Presented at Micro- Mini- Nano- Dosimetry and International Prostate Cancer Treatment Workshop, 6th - 9th December 2012, Wollongong, Australia.

4. Linh T. Tran, Susanna Guatelli, Michael L. F. Lerch, Dale A. Prokopovich, Mark I. Reinhard and Anatoly B. Rosenfeld (2012). *Improvement of Silicon Microdosimeter using 3D Sensitive Volume.* Presented at MedPhys12, The 7th Student Research Symposium of the ACT/NSW Branch of the ACPSEM, 13th December 2012, University of Sydney, Australia.

5. Linh T. Tran, Susanna Guatelli, Michael L. F. Lerch, Dale A. Prokopovich, Mark I. Reinhard, James F. Ziegler, Marco Zaider and Anatoly B. Rosenfeld (2013). *A Novel Silicon Microdosimeter using 3D Sensitive Volume: Modeling the Response in Neutron Field Typical of Aviation.* Presented at Monte Carlo Workshop, 19th-23rd April 2013, Wollongong, Australia.

6. Linh T. Tran, Dale A. Prokopovich, Marco Petasecca, Michael L. F. Lerch, Angela Kok, Anand Summanwar, Cinzia Da Via, Mark I. Reinhard, Kari Schjølberg-Henriksen and (2013). *3D Radiation Detectors: Charge Collection Characterisation and Applicability of Technology for Microdosimetry*. Presented oral presentation at Radiation Effects and Components and Systems RADECS 23rd -27th September 2013, Oxford, UK.

7. Linh T. Tran, Susanna Guatelli, Michael L. F. Lerch, Dale A. Prokopovich, Mark I. Reinhard, James F. Ziegler, Marco Zaider and Anatoly B. Rosenfeld (2013). *A Novel Silicon Microdosimeter using 3D Sensitive Volume: Modeling the Response in Neutron Field Typical of Aviation.* Presented poster presentation at Radiation Effects and Components and Systems RADECS 23rd -27th September 2013, Oxford, UK.

8. Linh T. Tran, David Bolst, Susanna Guatelli, Dale A. Prokopovich, Michael L. F. Lerch, Marco Petasecca, Mark I. Reinhard, Eleni Sagia, Alberto Fazzi, Stefano Agosteo, Naruhiro Matsufuji and Anatoly B. Rosenfeld (2013). *High spatial resolution microdosimetry with ΔE-E detector on ^{12}C beam: Monte Carlo simulations and experiment.* Presented oral presentation at MICROS conference 20th – 25th October 2013, Treviso, Italy.

9. Linh T. Tran, Susanna Guatelli, Dale A. Prokopovich, Marco Petasecca, Michael L. F. Lerch, Angela Kok, Cinzia Da Via, Mark I. Reinhard, James. F. Ziegler, Marco Zaider and Anatoly B. Rosenfeld (2013). *3D Microdosimeter for Dosimetry in Avionic and Space Applications.* Presented oral presentation at Nuclear Science Symposium IEEE conference 27th October – 2ndNovember, 2013 Coex, Seoul, Korea.

10. Linh T. Tran, Susanna Guatelli, Michael L. F. Lerch, Dale A. Prokopovich, Mark I. Reinhard, James F. Ziegler, Marco Zaider and Anatoly B. Rosenfeld (2013). *A Novel Silicon Microdosimeter using 3D Sensitive Volume: Modeling the Response in Neutron Field Typical of Aviation.* Presented at Radiation Dosimetry and its Applications Workshop – IEEE conference 27th October – 2nd November, 2013Coex, Seoul, Korea.

11. Linh T. Tran, David Bolst, Susanna Guatelli, Dale A. Prokopovich, Michael L. F. Lerch, Marco Petasecca, Mark I. Reinhard, Eleni Sagia, Alberto Fazzi, Stefano Agosteo, Naruhiro Matsufuji and Anatoly B. Rosenfeld (2013). *High spatial resolution microdosimetry with ΔE-E detector on ^{12}C beam: Monte Carlo simulations and experiment.* Presented oral presentation at Hadron Therapy Workshop - IEEE conference 27th October – 2nd November, 2013 Coex, Seoul, Korea.

12. Linh T. Tran, Susanna Guatelli, Michael L. F. Lerch, Dale A. Prokopovich, Mark I. Reinhard, James F. Ziegler, Marco Zaider and Anatoly B. Rosenfeld (2013). *A Novel Silicon Microdosimeter using 3D Sensitive Volume: Modeling the Response in Neutron Field Typical of Aviation.* Presented poster at AIP Physics in Industry day 2013.

13. Linh T. Tran, Dale A. Prokopovich, Jayde Livingstone, Marco Petasecca, Mark Reinhard, Michael L. F. Lerch, Naruhiro Matsufuji, and Anatoly B. Rosenfeld (2013). *High spatial resolution microdosimetry with SOI Microdosimeter on ^{12}C beam at HIMAC, Japan.* Presented oral presentation at MedPhys13 conference 5th December, 2013 at University of Sydney, Australia

14. Linh T. Tran, Dale A. Prokopovich, Jayde Livingstone, Marco Petasecca, Mark Reinhard, Michael L. F. Lerch, Naruhiro Matsufuji, and Anatoly B. Rosenfeld (2014). *High spatial resolution microdosimetry with SOI Microdosimeter on ^{12}C beam at HIMAC, Japan.* Presented oral presentation at Asian Forum for Accelerators and Detectors (AFAD) conference 14th-16th Jan, 2014 at Australian Synchrotron, Melbourne, Australia.

15. Linh T. Tran, David Bolst, Susanna Guatelli, Dale A. Prokopovich, Michael L. F. Lerch, Marco Petasecca, Mark I. Reinhard, Eleni Sagia, Alberto Fazzi, Stefano Agosteo, Naruhiro Matsufuji and Anatoly B. Rosenfeld (2014). *High spatial resolution microdosimetry with ΔE-E detector on ^{12}C beam: Monte Carlo simulations and experiment.* Presented oral presentation at Heavy Ion Accelerators Symposium

(HIAS) conference 30th June - 1st July 2014 at Australian National University, Canberra, Australia

16. Linh T. Tran, Dale A. Prokopovich, Jayde Livingstone, Marco Petasecca, Mark Reinhard, Michael L. F. Lerch, Naruhiro Matsufuji, and Anatoly B. Rosenfeld (2014). *High spatial resolution microdosimetry with SOI Microdosimeter on ^{12}C beam at HIMAC, Japan.* Presented oral presentation at Heavy Ion Accelerators Symposium (HIAS) conference 30th June - 1st July 2014 at Australian National University, Canberra, Australia

17. Linh T. Tran, Dale A.Prokopovich, Marco Petasecca, Michael L. F. Lerch, Celeste Fleta, Giulio Pellegrini, Consuelo Guardiola, Mark I. Reinhard and Anatoly B. Rosenfeld (2014). *Ultra-thin 3D Detectors: Charge Collection Characterisation and Application for Microdosimetry*. Accepted for poster presentation at Nuclear and Space Radiation Effects Conference (NSREC), Paris, 14-18th July, 2014.

Awards

1. ***Trainee grant*** and ***Paul-Phelps scholarship*** at IEEE Nuclear Science Symposium and Medical Imaging (NSS/MIC) Conference in Seoul, Korea.

2. Third award for 2013 ***Ken Doolan Prize*** at Physics in Industry Day 2013 - The Future of Aerospace, CSIRO, Australia for Presentation: "Si microdosimetry for radiation protection in avionics".

3. ***Paul-Phelps Continuing Education Grant***, Nuclear and Space Radiation Effects (NSREC) Conference in Paris, France.

4. The **Jak Kelly award** for Postgraduate Excellence in Physics Royal Society of New South Wales 2014.

Table of Contents

Abstract 2

Acknowledgements 4

Preamble 7

Publications 8

Conferences 10

Awards 16

Table of Contents 17

List of Figures 24

List of Tables 37

Glossary of Abbreviations 38

Thesis Outline 40

Chapter 1 43

Introduction 43

Literature Review 44

1.1 Introduction to Semiconductor Charged Particle Detectors 44

1.1.1 P-N Junction 44

1.1.2 Classification of Semiconductor Detector 52

1.1.3 Operational Characteristics 55

1.1.4 Applications of Charged Particle Detector 59

1.2 Microdosimetry 60

1.2.1 Microdosimetry Approach 60

1.2.2 Radiobiological Models based on Microdosimetry 64

1.2.3 Experimental Microdosimetry 73

1.3 3D Detector Architectures 81

1.3.1 Conventional planar detector fabrication 84

1.3.2 3D detector Fabrication 89

1.4 Monte Carlo and Geant4 Simulation Toolkit 97

1.4.1 Geant4 geometry component 98

1.4.2 Geant4 General Particle Source 99

1.4.3 Physics Processes 99

Chapter 2 103

The ANSTO Heavy Ion Microprobe 103

2.1 Introduction 103

2.2 Australian National Tandem Research (ANTARES) Accelerator Facility 104

2.2.1 Ion Sources 104

2.2.2 Accelerator 105

2.2.3 Microprobe 106

2.2.4 Target chamber 106

2.2.5 Data Acquisition System 107

Chapter 3 110

Large Area Silicon Alpha Particle Detector 110

3.1 Introduction 110

3.2 Design and Technology of the Detector 112

3.3 Electrical Characterisation of the Detector 114

3.3.1 Methods 114

3.3.2 Results and Discussion 114

3.4 Spectral Characterisation 117

3.4.1 Methods 117

3.4.2 Results and Discussion 118

3.5 Radial Energy Resolution of Detectors 120

3.5.1 Methods 120

3.5.2 Results and Discussion 120

3.6 Geant4 Simulations 122

3.6.1 Methods 122

3.6.2 Results and Discussion 122

3.7 Charge collection studies - IBICC 124

3.7.1 Methods 124

3.7.2 Results and Discussion 124

3.8 Determining the Dead layer 127

3.8.1 Methods 127

3.8.2 Results and Discussion 128

3.9 Sediment Sample Measurement 131

3.9.1 Methods 131

3.9.2 Results and Discussion 131

3.10 Conclusions 132

Chapter 4 134

3D Radiation Detectors: Charge Collection Characterisation 134

4.1 Introduction 134

4.2 Material and Methods 136

4.2.1 Test structure of SINTEF 3D detectors 136

4.2.2 Electrical Characterisation 137

4.2.3 Charge Collection Study 137

4.2.4 Radiation Damage Study 138

4.3 Results and Discussion 138

4.3.1 Electrical Characterisation 139

4.3.2 Charge Collection Study 140

4.3.3 Radiation Damage Study 149

4.4 Conclusions 156

Chapter 5 157

Ultra-thin 3D Detectors: Charge Collection Characterisation 157

5.1 Introduction 157

5.2 Material and Methods 159

5.2.1 Test structure of ultra-thin 3D detectors 159

5.2.2 Ion Beam Induced Charge (IBICC) Technique 162

5.3. Results and Discussions 162

5.3.1 Electrical Characterisation 162

5.3.2 Response of the ultra-thin 3D detector to the 5.5 MeV He^{2+} ion microbeam 164

5.3.3 Response of the ultra-thin 3D detector to 20 MeV ^{12}C ion microbeam. 168

5.3.4 Effect of charge collection after scanning with heavy charged particles. 172

5.4 Conclusions 176

Chapter 6 178

New 3D Silicon Microdosimeter: Designs, Fabrication Method and Simulations of the Response in Neutron Radiation Fields. 178

6.1 Introduction 178

6.2 Materials and Methods 179

6.2.1 3D Microdosimeter fabrication 179

6.2.2 Geant4 Model of 3D “mushroom” microdosimeter 185

6.2.3 Geant4 Simulation Application 187

6.3 Results and Discussions 188

6.3.1 Response of 3D SV microdosimeter to ^{252}Cf and Pu-Be neutron fields. 188

6.3.2 Comparison of 3D mushroom microdosimeter with 3D embedded in silicon microdosimeter. 191

6.3.3 Tissue equivalent conversion for silicon mushroom microdosimeter in response to an avionic isotropic neutron field. 193

6.3.4 Comparison microdosimetric spectra for cubic and cylindrical SV. 198
6.4 Conclusion 199
Chapter 7 201
Large Area 3D-Mesa "Bridge" Microdosimeter: Charge Collection Study 201
7.1 Introduction 201
7.2 Material and Methods 203
7.2.1 Design of the 3D mesa bridge microdosimeter 203
7.2.2 Scanning Electron Microscopy Study 204
7.2.3 Ion Beam Induced Charge (IBICC) Technique 205
7.3. Results and Discussions 205
7.3.1 SEM Images of 3D mesa bridge microdosimeter 205
7.3.2 Charge Collection Studies 207
7.4. Conclusions 217
Chapter 8 218
Mixed Radiation fields components in ^{12}C Heavy Ion Therapy: Geant4 Simulation of ΔE-E Telescope Response 218
8.1 Introduction 218
8.2 Materials and Methods 221
8.2.1 ΔE-E Telescope System Description. 221
8.2.2 Geant4 Simulation Application 223
8.2.3 In-Field and Out-of-Field Response of the Detector 227

8.3 Results and Discussion 228

8.3.1 Characterisation of ^{12}C ion beam mixed radiation field 228

8.3.2 Characterisation of ΔE-E telescope response in-field 233

8.3.3 Characterisation of ΔE-E telescope response out of field 240

8.4 Conclusion 245

Chapter 9 246

Experimental Silicon Microdosimetry in ^{12}C ion therapy facility at HIMAC, Japan 246

9.1 HIMAC Facility 246

9.2 Materials and Methods 248

9.2.1 Experimental Setup 248

9.2.3 Theoretical estimation of RBE 251

9.3 Results and Discussions 252

9.3.1 Microdosimetric Spectra 252

9.3.2 Lateral Out-of-field Response 258

9.3.3 RBE Derivation with Silicon Microdosimetry 262

9.4 Conclusions 266

Chapter 10 268

Conclusions and Future Plans 268

Bibliography 274

List of Figures

Figure 1.1 Illustration of the p-n junction a) energy band diagram for p-type and n-type silicon, b) energy band diagram displaying the generation of the contact potential. 45

Figure 1.2 Characteristics of the Current-Voltage for a p-n junction [2] 47

Figure 1.3 Illustration of depletion region in reverse-biased p-n junction detector and electric field distribution and potential distribution. 50

Figure 1.4 Diffused junction detector 53

Figure 1.5 Fabrication steps of passivated planar silicon detector [6] 55

Figure 1.6 Definition of detector energy resolution, H_o is a centroid. [5] 58

Figure 1.7 Rossi proportional counter..... 74

Figure 1.8 Illustrations of four types of wall effects in low pressure proportional counter 76

Figure 1.9 First generation SOI microdosimeter 78

Figure 1.10 Second generation SOI microdosimeter a) 2D planar and b) Pseudo 3D Mesa p-i-n structure 78

Figure 1.11 Third generation microdosimeter a) a single cell topology of n-SOI microdosimeter; b) A view from top of microdosimeter (cylindrical SV) 79

Figure 1.12 Schematic cross sections of planar and 3D detector. 82

Figure 1.13 Processing of 3D active edge detector (image was adapted from [33]) 83

Figure 1.14 Comparison of initial oxide growth at 920ºC for oxidation in wet and dry-oxygen ambient [34]. 85

Figure 1.15 Pattern transferred process using positive and negative photolithography [33]. 87

Figure 1.16 Sputtering systems for metallization [34] 89

Figure 1.17 SEM image shows the protective sidewall polymers during DRIE process without damage to the wall [36]..... 90

Figure 1.18 Etching profile obtained with (a) isotropic chemical etching and (b) dry anisotropic etching in a plasma or reactive-ion etching system [33]. 92

Figure 1.19 Single-sided approach to fabricate full active edge detector.... 94

Figure 1.20 Schematic cross-sections of proposed approaches to the 3D technology. 96

Figure 1.21 Partial inventory of Geant4 hadronic physics models (Geant4 version 10) [43]. 102

Figure 2.1 Schematic of heavy ion microprobe beam line [44] 106

Figure 2.2 ANSTO heavy ion microprobe. 107

Figure 3.1. A cross sectional schematic of the large area silicon alpha particle detector..... 113

Figure 3.2 I-V characteristics of large area silicon alpha particle detectors with substrate resistivity 0.95 kΩ.cm and 4 kΩ.cm. 115

Figure 3.3(a). C-V characteristic of large area silicon alpha particle detectors with substrate resistivity 0.95 kΩ.cm and 4 kΩ.cm. 116

Figure 3.3(b). $1/C^2$ versus bias of large area silicon alpha particle detectors (0.95 kΩ.cm and 4 kΩ.cm). Linear behavior without saturation suggests that detectors are partially depleted. 117

Figure 3.4 Alpha spectra of ^{241}Am and ^{148}Gd source for large area silicon detector 119

Figure 3.5 Schematic of experimental setup 120

Figure 3.6 a) Energy resolution along the horizontal and vertical diameter of the detector with substrate resistivity 0.95 kΩ.cm. 121

Figure 3.6 b) Energy resolution along the horizontal and vertical diameter of the detector with substrate resistivity 4 kΩ.cm. 121

Figure 3.7 Simulated spectra for 3.183 MeV alpha and 5.486 MeV alpha of large area detector. 123

Figure 3.8 Charge collection study of the detector (0.95 kΩ.cm**)** for scanned 1.4 mm^2 area at different scanning positions across of active are of the detector with 5.5 MeV He^{2+} ions microbeam (a) MCA spectra (b) An IBICC median energy map of collected charge (c) Scanning beam position on the detector active area 125

Figure 3.9 Charge collection study of the detector (4 kΩ.cm**)** for scanned 1.4 mm^2 area at different scanning positions across of active are of the detector with 5.5 MeV He^{2+} ions microbeam (a) MCA spectra (b) An IBICC median energy map of collected charge (c) Scanning beam position on the detector active area. 126

Figure 3.10 Plot of *E'* as a function of (1/cosθ-1) of detector (0.95kΩ.cm). 130

Figure 3.11 The alpha particle spectra of a sediment sample measured by large area silicon alpha detector 4kΩ.cm. 132

Figure 4.1 Layout of the of the test diode 137

Figure 4.2 I-V characteristic of the 3D detectors type 1E, 2E, 3E, 4E and 5E. 139

Figure 4.3 Capacitance of different types of 3D detectors at 60V. 140

Figure 4.4 Scanned area of 1E 3D detector and MCA spectra at **(a)** 0 V bias and **(b)** 100 V bias. 141

Figure 4.4 An IBICC median energy map of the response of 3D detector (1E type) to the microbeam of 5.5 MeV He^{2+} **(c)** at 0 V and **(d)** at 100 V. 141

Figure 4.5 Median energy maps in different energy ranges of charge collection of 1E detector at bias 100 V. 143

Figure 4.6 An IBICC median energy map of the response of the 3D detector1E at the top left corner to the microbeam of 5.5 MeV He^{2+} **(a)** at 0 V and **(b)** at 100 V. 144

Figure 4.7 An IBICC enlarge median energy map of 2E detector in response to 5.5 MeV He^{2+} at 0 V. 144

Figure 4.8 An IBICC median energy map of the response of detector 2E at the bottom left side to the microbeam of 5.5MeV He^{2+} **(a)** at 0 V and **(b)** at 100 V. 145

Figure 4.9 An IBICC median energy map comparison of 3D detector type 3E in response to 5.5 MeV He^{2+} at different biases **a)** 0 V, **b)** 30 V, **c)** 40 V, **d)** 50 V, **e)** 70 V and **f)** 90 V..... 147

Figure 4.10 An IBICC enlarge median energy map of 5E detector in response to 5.5 MeV He^{2+} at **a)** 0 V and **b)** 5 V. 148

Figure 4.11 An IBICC MCA spectrum and median energy map of the charge collection of 5E type detector at bias 5 V for energy window (5100-5300 keV). 149

Figure 4.12 An I-V characteristic comparison for 3D detectors type 1E, 3E, 5E before and after 10 MRad gamma ^{60}Co irradiation. 150

Figure 4.13 An I-V characteristic comparison for 3D detectors type 1E, 3E, 5E before and after neutron irradiation with fluence of 6.2 x 10^{10} n_{eq}/cm^2. 151

Figure 4.14 IBICC MCA spectra and median energy maps for gamma irradiated sample (3E type) at bias 60V **a)** before irradiation **b)** after gamma irradiation..... 152

Figure 4.15 IBICC MCA spectra and median energy maps for neutron irradiated sample (1E type) at bias 100 V; **a)** before irradiation **b)** after neutron irradiation..... 154

Figure 4.16 IBICC median energy maps at 1x scan size for gamma irradiated sample (5E) at biases a) 0 V, b) 10 V and c) 30 V. 155

Figure 5.1 Cross-section of ultra-thin 3D detector (not to scale) [54]..... 161

Figure 5.2 Illustration of the U3DTHIN detector mounting. 161

Figure 5.3 I-V characteristic of the U3DTHIN detector 163

Figure 5.4 C-V characteristic of the U3DTHIN detector 163

Figure 5.5 MCA spectra obtained with the detector for 5.5 MeV He^{2+} at -20 V with the ion beam incident a) from the front and b) from the back of the device..... 167

Figure 5.6 a) Scanned area of the ultra-thin 3D detector, b) median energy map of the response of the detector to 5.5 MeV He^{2+} at -20 V bias and c) median energy maps in different energy windows corresponding to MCA spectrum obtained at the same position..... 169

Figure 5.7 MCA spectra of the response of the detector to 20 MeV ^{12}C at -30 V bias with ion beam incident from: a) the front and b) the back of the device..... 170

Fig. 5.9 illustrates a full presentation of the charge collection in the U3DTHIN detector at different biases when the ion beam was scanning across the edge of the detector (the same position as shown in Fig. 5.9). At 0 V, no charge was observed under the Al leads at the edge of the detector, however with increasing bias the charge collection efficiency was increasing. 170

Figure 5.8 IBICC median energy maps of a U3DTHIN detector in response to a beam of 20 MeV ^{12}C ions a) at 0 V; b) at -30 V..... 171

Figure 5.9 IBICC median energy maps illustrating the response of the edge of the U3DTHIN detector to 20 MeV ^{12}C ions at a) 0 V; b) -5 V; c) -10 V; d) -30 V. 172

Figure 5.10 Median energy map of the response of the detector to 5.5 MeV He^{2+} at a) -1 V bias and b) -10 V bias. 174

Figure 5.11 Comparison of the pre-irradiation and post-irradiation MCA spectra for the U3DTHIN detector with 20 MeV ^{12}C ions. The detector was biased at 0 V. 174

Figure 5.12 Median energy map of the charge collection from the detector in response to: 20 MeV ^{12}C at a) 0 V bias and b) -30V bias (scanning size of 85 μm x 85 μm), c) 0 V bias and d) -30 V bias (scan size of 350 μm x 350 μm). 175

Figure 6.1 Geometry of 3D SV array microdosimeter modeled in Geant4 simulations. (a) SOI 3D SVs array embedded in Si on thick Si substrate. (b) SOI 3D SV array embedded in PMMA ("mushroom") with back etched thin Si substrate and PMMA layer attached (SiO_2 layer between device layer and substrate has not been shown)..... 186

Figure 6.2 Energy deposition event spectrum for 3D mushroom microdosimeter with/without 0.5mm PMMA converter in response to ^{252}Cf; 5.10^8 events were executed in the simulation. 189

Figure 6.3 Energy deposition event spectrum for 3D mushroom microdosimeter with/without 0.5 mm PMMA converter in response to Pu-Be; 5.10^8 events were executed in the simulation. 190

Figure 6.4 Microdosimetric spectra obtained with 3D SV microdosimeters as presented in a Fig. 5.1b mushroom (dashed line) and Fig. 5.1a (solid line) in response to avionic isotropic neutron field. 192

Figure 6.5 Geometry of 3D mushroom microdosimeter as in Fig. 6.1b with and tissue equivalent spherical SV used in the Geant4 simulation. 193

Figure 6.6 Comparison of microdosimetric spectra of the 3D mushroom microdosimeter and tissue equivalent spherical SV. 195

Figure 6.7 The Geant4 simulation of different components that contributed to total lineal energy deposition events in SV of the 3D mushroom microdosimeter. The spectra have been converted to muscle using mean chord length MCL of muscle sphere. 197

Figure 6.8 The Geant4 simulation of different components contributed to total lineal energy deposition events in SV of the tissue equivalent sphere. 198

Figure 6.9 Comparison microdosimetric spectra of the cubic SV and the cylindrical SV of 3D "mushroom" microdosimeter. 199

Figure 7.1 A schematic of the design of SOI bridge microdosimeter. a) 3D view; b) A cross-section of the microdosimeter behind the silicon bridge... 204

Figure 7.2 SEM images of arrays of SVs 206

Figure 7.3 Cross-section image of single SV obtained in one plane. 207

Figure 7.4 Energy spectrum obtained from 10 μm thick n-SOI bridge microdosimeter irradiated with 2 MeV H ions. The detector was biased at -10V. 208

Figure 7.5 Median energy map illustrating the spatial distribution of energy deposited by 2 MeV H ions in the SVs of the even array. The detector was biased at -10 V..... 208

Figure 7.6 Median energy map illustrating a single SV when biased at a) 0 V and b) -10V. 210

Figure 7.7 Response of 3D mesa bridge microdosimeter to 5.5 MeV He^{2+} at different biases. Top image: MCA spectrum; Bottom image: Median energy map. The data were obtained using 3 x scan size corresponding to scanning area of 0.9 mm x 0.9 mm. 212

Figure 7.8 Response of 3D mesa bridge microdosimeter to 5.5 MeV He^{2+} at 0 V bias. Top image: MCA spectrum with indicating of median energy window; Bottom image: Median energy map. The data were obtained using 1 x scan size corresponding to scanning area of 0.3 mm x 0.3 mm. 213

Figure 7.9 Response of the microdosimeter at -10 V (odd and even arrays are connected in parallel). Scanning area is 0.9 x 0.9 mm^2. 214

Figure 7.10 Response of the microdosimeter at -10 V (odd and even arrays were connected in parallel). Scanning area is 150 x 150 μm^2. 215

Figure 7.11 Charge collection characteristic of the device near the pad... 216

Figure 8.1 Schematic of ΔE-E telescope. Figure adapted from [71]. 223

Figure 8.2 Schematic representation of the simulated geometry of ΔE-E telescope in the Geant4 simulation. 226

Figure 8.3 Schematic representation of out of field positions of the ΔE-E telescope in the Geant4 simulations and experiments. Positions F4 and E4 corresponding to 47 mm lateral distance from the edge of the radiation field were not shown in Fig. 3 due to space limitation..... 227

Figure 8.4a Dose per incident ^{12}C ion. The contribution deriving from incident ^{12}C ions and secondary fragments are represented in blue and red, respectively. The sum of the two contributions is represented with the black curve. The energy deposition at the BP was normalised to 1..... 229

Figure 8.4b Energy deposition deriving from the most significant secondary nuclear fragments and recoil secondary carbon ions. The total secondary fragments component was normalised to 1. 230

Figure 8.5 2D energy distribution of primary and secondary particles in the PMMA phantom for HIMAC experiment set up. The results are shown per incident particle. 232

Figure 8.6 Geant4 simulation of the Bragg peak for 290MeV/u ^{12}C with associated ΔE-E telescope measurement positions. 234

Figure 8.7 Response of ΔE-E telescope to 290 MeV/u ^{12}C ion at depths 0, 58, 128.5, 129.5, 130, 131.5 mm in the PMMA phantom (two-dimensional ΔE-E plot). The results are shown per incident particle. 237

Figure 8.8 Microdosimetric spectra derived from the ΔE stage at positions D, I, J, K, L and M. Separated dose weighted components have been shown in each microdosimetric spectrum. 239

Figure 8.9 Response of the telescope detector when positioned out-of-field at 0mm, 20×10^6 primaries were used for both face on (F1) and edge on (E1). The results are shown per incident particle..... 241

Figure 8.10 Microdosimetric spectra derived from the ΔE stage in out of field study at 0 mm, 2 mm, 7 mm and 47 mm from the edge of the beam at the Bragg peak. Separated components have been shown in each microdosimetric spectrum. 244

Figure 9.1 Model of the HIMAC facilities, top left: Radio frequency quadrupole linac; bottom left: HIMAC synchrotron; top right: biological radiation room; bottom right: treatment room..... 247

Figure 9.2 Experimental setup for microdosimeters. a) microdosimetric probe with dual 2nd generation SOI microdosimeters for increasing the sensitive area; b) microdosimetric probe with the 1st generation single SOI microdosimeter; c) two probes placed side by side in PMMA phantom. 249

Figure 9.3 a) Schematic representation of the experimental setup for measurements in out-of-field study using 1st generation of microdosimeter at the end of the SOBP (at 128 mm depth)..... 250

Figure 9.3 b) Schematic representation of the experimental setup for measurements in out-of-field study using ultra-thin 3D detector (membrane) in the middle of the SOBP (at 117 mm depth). 250

Figure 9.4 Microdosimetric spectra obtained by 1st generation of microdosimeter in response to 290 MeV/u ^{12}C ions at HIMAC. 253

Figure 9.5 Microdosimetric spectra obtained by 2nd generation of microdosimeter in response to 290 MeV/u ^{12}C ions at HIMAC. 254

Figure 9.6 Microdosimetric spectra obtained by ultra-thin 3D membrane detector in response to 290 MeV/u ^{12}C ions at HIMAC. 256

Figure 9.7 Microdosimetric spectra obtained by 3D mesa bridge microdosimeter in response to 290 MeV/u ^{12}C ions at HIMAC. 257

Figure 9.8 Lateral out of field measurement obtained by 1st generation of SOI microdosimeter. 259

Figure 9.9 Lateral out of field measurement obtained by the ultra-thin 3D detector at various positions. Top left image shows the experimental setup of the measurement. 261

Figure 9.10 RBE_{10} distribution obtained by 1st generation of microdosimeter in response to 290 MeV/u SOBP ^{12}C ions. 262

Figure 9.11 RBE_{10} distribution obtained by 2nd generation of microdosimeter in response to 290 MeV/u SOBP ^{12}C ions. 263

Figure 9.12 RBE_{10} distribution obtained by ultra-thin 3D detector in response to 290 MeV/u SOBP ^{12}C ions. 263

Figure 9.13 RBE_{10} distribution obtained by 3D mesa bridge microdosimeter in response to 290 MeV/u SOBP ^{12}C ions 264

Figure 9.14 RBE_{10} distribution obtained by the TEPC (circles) and Treatment Planning System (solid line) at NIRS, HIMAC in response to 290 MeV/u SOBP ^{12}C ions. The graph was adapted from [82]. 265

List of Tables

Table 5.1 Ions specifications used in IBICC study 162

Table 6.1 Fabrication steps for proposed 3D microdosimeter. 181

Table 7.1 Ions specifications used in IBICC study 205

Table 8.1 Number of secondary particles produced per single incident ^{12}C ion..... 231

Glossary of Abbreviations

ANSTO……	Australian Nuclear Science and Technology Organisation
BNL……	Brookhaven National Laboratory
BP……..	Bragg Peak
CCE……	Charge Collection Efficiency
CNM……..	National Centre for Microelectronic
CMRP……	Centre for Medical Radiation Physics
C-V…….	Capacitance-Voltage
ΔE-E……..	Delta E-E
DNA……..	DeoxyriboNucleic Acid
DRIE……..	Deep Reactive Ion Etching
DSB……	Double Strand Break
FBK……	Fondazione Bruno Kessler
FWHM…….	Full Width at Half Maximum
GEANT…….	Geometry And Tracking
HIMAC…….	Heavy Ion Medical Accelerator in Chiba
HIT…….	Heavy Ion Therapy
IBICC……	Ion Beam Induced Charge Collection
IC…….	Ionisation Chamber
ICRP……..	International Commission on Radiological Protection
ICRU……..	International Commission on Radiation Units

I-V……..	Current-Voltage
LEM……..	Local Effect Model
LET……	Lineal Energy Transfer
LQ……..	Linear Quadratic
MC……..	Monte Carlo
MEMS……..	MicroElectroMechanical Systems
MKM……..	Microdosimetric Kinetic Model
NIRS……..	National Institute for Radiological Science
PT……..	Proton Therapy
QA……..	Quality Assurance
RBE……	Relative Biological Effectiveness
SEM……..	Scanning Electron Microscope
SOBP……	Spread Out Bragg Peak
SOI……	Silicon On Insulator
SSB……	Single Strand Break
SV……..	Sensitive Volume
TDRA……	Theory of Dual Radiation Action
TEPC……	Tissue Equivalent Proportional Counter
U3DTHIN……	Ultra-thin 3D Detector
UOW……..	University of Wollongong
VLSI……..	Very-Large-Scale Integration

Thesis Outline

This thesis covers the development of detectors and simulations of their response, their application in identifying isotopes of contaminated soil from accidents at nuclear power plants, as well as microdosimetry to derive the quality of radiation and RBE predictions in a mixed radiation field for heavy ion therapy Quality Assurance (QA) and space radiation environment.

The thesis outline is as follows:

Chapter 1: Presents a literature review that introduces semiconductor detectors, microdosimetry concepts, and the GEANT4 simulation toolkit.

Chapter 2: Presents the Ion Beam Induced Charge (IBICC) technique for charge collection studies using the heavy ion microbeam at ANSTO.

Chapter 3: Describes the development of a large area silicon alpha particle detector to measure the radioactivity of soil and plant samples contaminated by accidents at nuclear power plants.

Chapter 4: Presents a charge collection study of the ATLAS 3D detectors fabricated at SINTEF in response to a 5.5 MeV He^{2+} ion that was investigated using the Ion Beam Induced Charge (IBICC)

technique. It also explains the effect on the detector's charge collection efficiency induced by fast neutron and gamma irradiation.

Chapter 5: Presents a study of the charge collection of an ultra-thin 10 µm 3D detector fabricated at CNM, Barcelona, Spain, including the effect it has on the charge collection of the detector in response to 5.5 MeV He^{2+} and 20 MeV ^{12}C ions.

Chapter 6: Describes the design and fabrication processes of a newly proposed 3D microdosimeter and its response to neutron fields from ^{252}Cf, Pu-Be sources and avionic radiation environment was investigated using the Geant4 Monte Carlo toolkit. This study aimed at optimising the design of the 3D microdosimeter.

Chapter 7: Describes an intermediate stage in fabricating of a full 3D SVs microdosimeter by applying a mesa structure using plasma etching technology at a microelectronic foundry SPA-BIT, Kiev, Ukraine. It also presents the charge collection characterisation of the new device in response to different kinds of heavy ions.

Chapter 8: Presents a study of the components from mixed radiation

fields and the response of the ΔE-E telescope in ^{12}C heavy ion therapy that was carried out using the Geant4 simulation toolkit.

Chapter 9: Presents the applications of silicon microdosimetry in heavy ion therapy and the RBE estimation.

Chapter 10: Presents the conclusions and future plans

Chapter 1

Introduction

Humans are exposed to radiation from a variety of natural and artificial sources; natural sources include terrestrial radioactive minerals found in certain rocks and agricultural commodities such as meat, fruit, vegetables, and milk, and cosmic radiation from outer space is in another substantial source. The compositions of background radiation from galactic cosmic rays are complex and involve a mixed radiation field and much higher dose rates than terrestrial radiation, which is why the exposure that astronauts and aircrew experience must be strictly monitored. Artificial sources include medical radiation for the diagnosis of diseases and treatment of cancer, and radiation released from industrial processes such as mining and accidents at nuclear power plant.

The purpose of this thesis is to develop novel silicon detectors for radiation protection and QA in hadron therapy applications.

Literature Review

1.1 Introduction to Semiconductor Charged Particle Detectors

Semiconductor detectors are widely used in radiation detection because they are small, have a high resolution in particle detection, a low bias voltage, and a fast time response. They are commonly used for charge particles spectroscopy as well as environment monitoring [1]. Three standard types of silicon radiation detectors are commonly used, including diffused p-n junction, surface barrier detectors, and ion implanted detectors.

1.1.1 P-N Junction

The p-n junction is a key concept in semiconductor detector physics and the p-n junction formation is obtained by joining p-type and n-type materials together. The silicon crystal typically has two dopants types: donors and acceptors. Phosphorous and boron are commonly used donor and acceptor dopants for n- and p-type materials.

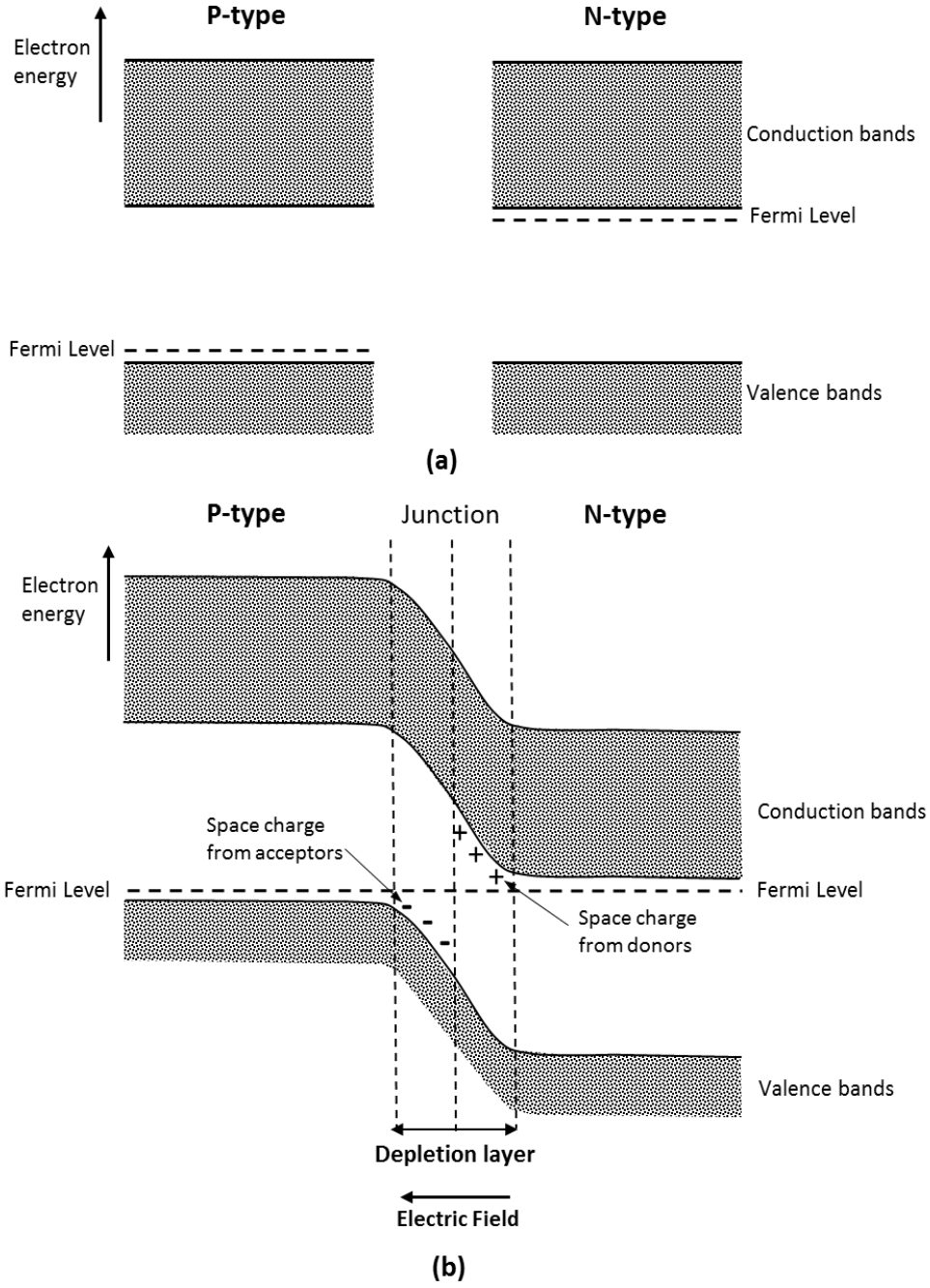

Figure 1.1 Illustration of the p-n junction a) energy band diagram for p-type and n-type silicon, b) energy band diagram showing the generation of the contact potential.

In the intrinsic material, the Fermi level lies between the conduction and valence bands and it corresponds to an equal number of electrons and holes. In p-type silicon, the Fermi level is located toward the valence band, but in n-type silicon the Fermi level is close to the conduction band (Fig. 1.1a). The holes are the majority carriers and electrons are the minority carriers on the p-side, whereas on the n-side the electrons are the majority carriers and the holes are the minority carriers. When the p and n regions are put together, the charge starts moving across the interface between the two regions, where part of the p-region attracts the electrons and becomes negatively charged while part of the n-region attracts the holes and becomes positively charged. An electric field is thus generated and an area of motionless space charge is formed, the so-called *depletion region*. The electric field generates the potential difference through the junction, which is the contact potential (Fig. 1.1b).

The p-n junction works like a diode and has the typical characteristic of rectification which allows the electrons to flow in one direction only. When a forward bias is applied, a large current will flow due to the motion of the majority carriers across the junction, but when a reverse bias is applied, a minute current produced by the impurities, and a recombination and generation mechanism will flow in the opposite direction. The forward bias applied for a large current flow in silicon diodes is approximately 0.7 V, whereas the reversed bias can be up to thousands of volts depending on the

doping concentration of the p-n junction. By increasing the reverse bias, the reverse current grows slightly until it reaches critical state that is called *breakdown voltage* (Fig. 1.2).

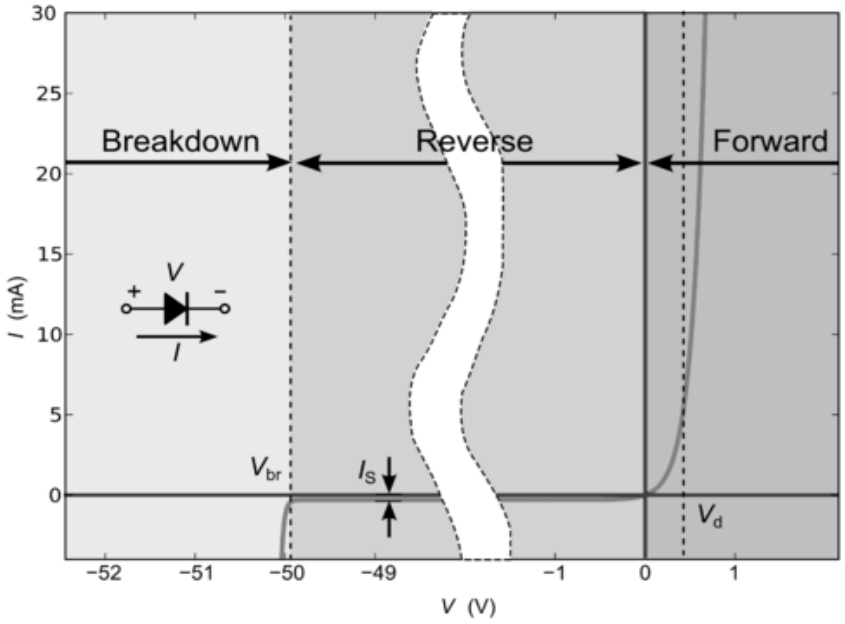

Figure 1.2 Characteristics of the Current-Voltage for a p-n junction [2]

A p-n junction diode is commonly operated as a radiation detector, so when a charged particle passes through the p-n junction resulting in electron-hole pairs along the track in reverse bias, the particle loses its energy; this is also called ionization energy via the creation of electron-hole pairs. When a positive bias is applied to the n^+, electrons and holes are pulled out from the depleted region, no current can flow through the junction except the reverse current. The energy required for an electron-hole pair to be created in silicon is much less than in a gas ionization chamber (3.65 eV

for silicon and 30 eV for a gas filled chamber), which makes the energy resolution of the silicon detectors superior to ionization chambers [3].

Depletion Region

The depletion region is created by the diffusion of electrons from the n-type side to the p-type side, due to their attraction to the holes. Diffusion establishes immobile negative ions on the p side and immobile positive ions on the n-type side with no free charge carriers in depletion region, and the width of this depletion region depends on the impurity of the n and p dopants. Poisson's equation can be applied if the charge density distribution is in the depletion region:

$$\frac{d^2V}{dx^2} = -\frac{\rho(x)}{\varepsilon_o} \tag{1.1}$$

where $\rho(x)$ is the space charge (C/m^3), and

ε_o is the dielectric constant.

An abrupt junction detector is one where the concentration of impurities on one side of the junction is higher than on the other side ($N_A << N_D$) (Fig 1.3 a), and where the width of the depletion region can be determined if the charge distribution is uniform in the depletion region:

$$\rho(x) = eN_D \text{ when } 0 < x < d \tag{1.2}$$

The electric field distribution of an abrupt junction is shown in Fig. 1.3b and it can be obtained using the first integration of equation (1.1):

$$-\varepsilon(x) = \frac{d\varphi}{dx} = -\frac{eN_D x}{\varepsilon\varepsilon_o} + \frac{eN_D d}{\varepsilon\varepsilon_o} = \frac{eN_D}{\varepsilon\varepsilon_o}(d - x) \tag{1.3}$$

Where $\mathcal{E}(x)$ is the electric field,

φ is the build-in potential,

e is the charge of the electron,

N_D is the donor impurities,

d is the distance from the surface of the detector,

ε_{Si} is the permittivity of silicon.

When $0 < x < d$, and the second integration of equation (1.1) is used we can obtain:

$$\varphi(x) = V(x) = \frac{eN_d x}{\varepsilon\varepsilon_o}\left(d - \frac{x}{2}\right) \tag{1.4}$$

$$\varepsilon(x) = \frac{eN_d}{\varepsilon\varepsilon_o}(d - x) = \frac{2V}{d}(d - x) \tag{1.5}$$

When the detector is irradiated, electron-hole pairs are created along the track and the electrons are attracted by the p^+ side and the holes are attracted by the n^+ side.

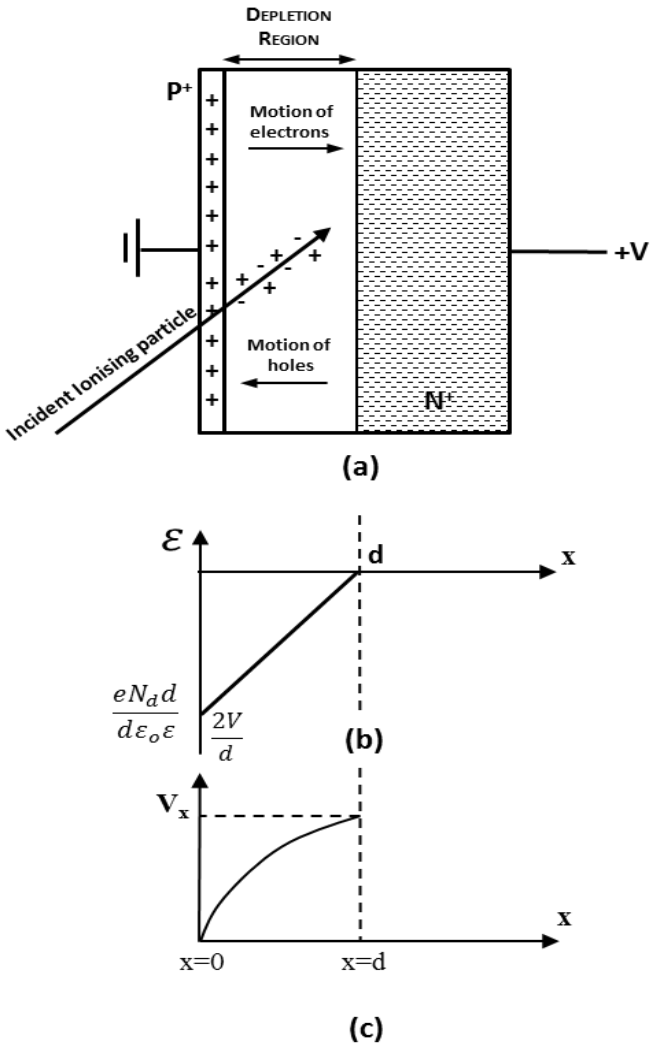

Figure 1.3 Illustration of depletion region in reverse-biased p-n junction detector and electric field distribution and potential distribution.

Finally, the width of the depletion region can be determined by:

$$W = \sqrt{\frac{2\varepsilon_o \varepsilon V_x}{eN_D}} \tag{1.6}$$

Resistivity ρ_n is given by:

$$\rho_n = \frac{1}{e\, n\, \mu_n} \tag{1.7}$$

The width of depletion can be represented as:

$$W = \sqrt{2\, \varepsilon\, \varepsilon_o\, \mu_n\, \rho_n\, V} \tag{1.8}$$

Where $\mu_n = 0.14\ m^2V^{-1}s^{-1}$

$\mu_p = 0.05\ m^2V^{-1}s^{-1}$

Capacitance

When a depletion region is formed at the junction of a semiconductor detector, charges are built up on the p-side or n-side of the junction that can act like a charged capacitor and also contribute to the noise of the detector. The capacitance for a reversed bias junction can be estimated using the formula for a general parallel plate capacitor where the distance between the two plates is the depletion width of the junction.

$$C = \varepsilon\, \frac{A}{W} \tag{1.9}$$

where **A** is the area of active region,

ε_o is the dielectric constant,

W is the depletion width,

C is capacitance.

The capacitance per unit area for a one sided abrupt junction is given by the equation:

$$C_A = \frac{\varepsilon\ \varepsilon_o}{W} = \sqrt{\frac{\varepsilon\ \varepsilon_o e N_D}{2V}}\ or\ \ \frac{1}{{C_A}^2} = \frac{2V}{e\ \varepsilon\ N_D} \tag{1.10}$$

1.1.2 Classification of Semiconductor Detector

1.1.2.1 Diffused Junction Detector

Diffused junction detectors are usually fabricated on a homogenous p-type crystal with a thin n-type layer formed on one side of the detector by a diffusion of n-type impurities (usually phosphorus); Figure 1.4 show a diffused junction detector. When an ionizing particle passes through the n-type surface layer it loses a portion of its energy before it reaches the depletion region. The n-type layer represents an entrance window for the diffused junction detector because this layer is highly doped compared to the p-type silicon bulk.

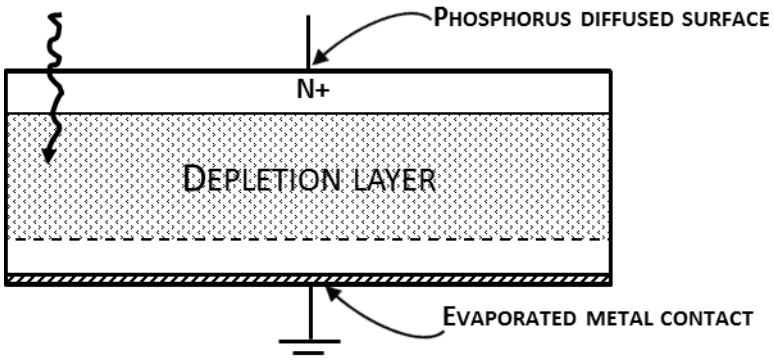

Figure 1.4 Diffused junction detector

1.1.2.2 Surface Barrier Detector

A surface barrier detector is formed at the p-n junction in the same way as the diffused junction detector, and then the detector surface is etched and an electrical contact such as gold is evaporated onto the n-type layer to form a barrier [4]. This edge protection is applied to enable the detector to handle a very high voltage and minimise the reverse leakage current. While a surface barrier detector has an extremely thin entrance window, it is also very sensitive to light, and as such, high noise can be produced due to photon interactions from ambient light [5].

1.1.2.3 Ion Implanted Detector

An alternative method for creating doping impurities at the surface of a silicon detector is ion implantation. Mono-energetic ions corresponding to added impurities are produced using an accelerator. The temperature

required for annealing after forming the n^+ and p^+ layers in the ion implantation process is much lower than that required to manufacture a diffused junction detector. Annealing is needed to maintain the lifetime of the charge carriers, otherwise they would have high reverse leakage current.

1.1.2.4 Passivated Planar Detector

A passivated planar process for manufacturing silicon detectors was developed to overcome the limitations of the diffused junction and surface barrier detectors. This detector achieves a much lower leakage current by using an oxide-passivated surface. Moreover, its entrance window is thinner and more uniform because a p^+ layer is formed through the ion implantation method which provides better energy resolution for the detector. The gold surface contact in the surface barrier detector has been replaced by an aluminised front surface that is sturdier in the passivated planar detector. The process of manufacturing a passivated planar detector is shown in Fig. 1.5 [6].

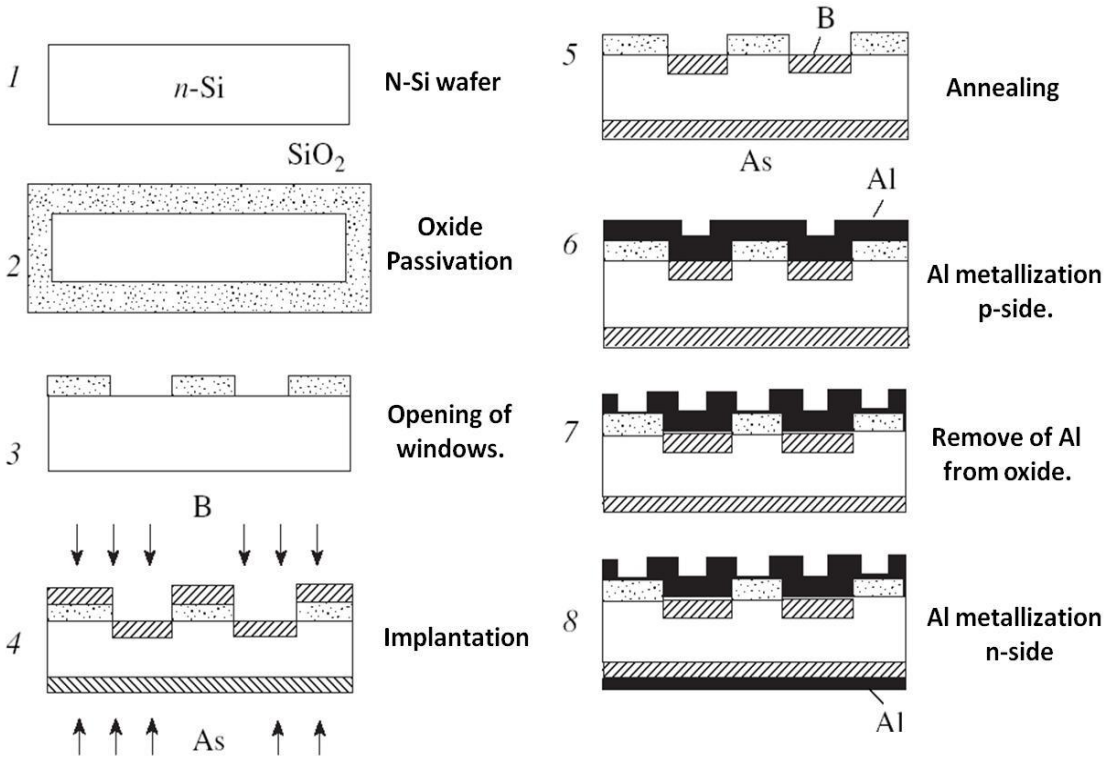

Figure 1.5 Steps used to fabricate a passivated planar silicon detector [6]

1.1.3 Operational Characteristics

1.1.3.1 Leakage Current

The leakage current is normally seen when a bias is applied to the detector. The leakage current emanates from two sources, the bulk and surface leakage of the detector. Bulk leakage is related to the direction of the electric field across the depletion region when the majority carriers are diffused from the p and n regions to the edge of the depletion region. The minority carriers are diffused freely on both sides of the junction and cause a leakage current. Moreover the thermal generation of electron hole pairs

within the depletion region is considered to be the bulk leakage that arises within the depletion volume. Silicon detectors can generally be operated at room temperature because they have a large energy gap. Surface leakage occurs at the edge of the detector depending on its surface condition, and whether the surface has been damaged or is contaminated.

The current-voltage characteristic for an ideal p-n junction diode is given by the equation:

$$I = I_{sat}\left(e^{\frac{qV}{k_B T}} - 1\right) \tag{1.11}$$

$$I_{sat} = q\left(\frac{D_p p_{n0}}{L_p} + \frac{D_n n_{p0}}{L_n}\right) \tag{1.12}$$

where I_{sat} is the saturation reverse current,

k_B is the Boltzmann constant,

$D_{n,p}$ is the diffusion coefficient for carriers,

n_{p0}, p_{n0} are the minority carriers density,

L_p, L_n are the diffusion length.

The reverse saturation current depends on the diffusion coefficient of electrons and holes, and since minority carriers are thermally generated, the reverse saturation current depends on the temperature, where an increase temperature causes an increase in the density of minority charge carriers. The reverse current is least dependent on the reverse applied bias until it

reaches breakdown voltage, but before it reaches this stage it depends only on the reverse bias when the temperature increases as a result of increasing bias.

1.1.3.2 Electronic Noise

Electronic noise is one of the most important factors that must be considered in silicon detectors because noise can destroy its real response to ionizing radiation and thus cause inaccurate results. Electronic noise has two sources, parallel noise and series noise. Bulk and surface leakage [1.1.3.1] are considered to be parallel noise and noise that includes bad contact or series resistance is considered to be series noise. Electronic noise can be measured using a pulse generator, where the width of the pulse peak represents its contribution.

1.1.3.3 Energy Resolution

A radiation detector must have good energy resolution because this characterizes of how well a detector can distinguish energy peaks produced by different radioisotopes. The energy peak measured by MCA has an ideal Gaussian distribution (Fig. 1.6), such that its energy resolution is defined by the Full Width Half Maximum (FWHM) divided by centroid H_o (Fig. 1.6). σis a width parameter which corresponds to the FWHM of any Gaussian distribution and FWHM = 2.35σ

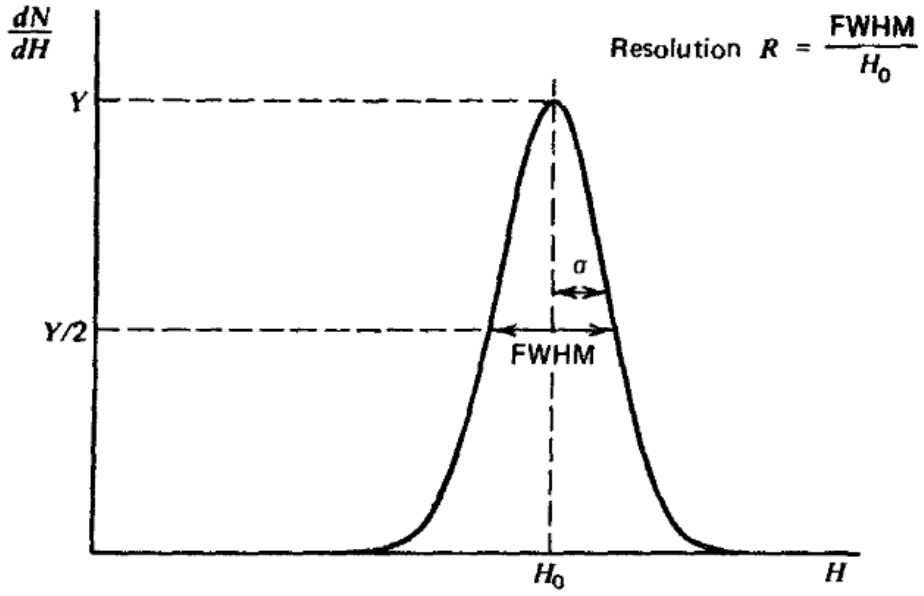

Figure 1.6 Definition of detector energy resolution, H_o is a centroid. [5]

1.1.3.4 Entrance Window or Dead layer

Semiconductor detectors generally have an entrance window (or dead layer) at the surface that can be created during fabrication by either a passivation process, contact formation, or doping. When heavy charged particles such as alpha particles or protons pass through a dead layer, some energy will be lost before they reach the sensitive region of the detector. The charge collection in the dead layer is normally inefficient and can depend on the applied voltage.

The effective thickness of the dead layer can be determined by measuring the energy loss at different angles of incidence of the charged particle. The energy loss in the dead layer at 0^o of incidence is given by:

$$\Delta E_o = \frac{dE_o}{dx} t_{dl} \tag{1.11}$$

where t_{dl} is the thickness of the dead layer, and the energy loss in the dead layer at an angle of incidence θ is given by:

$$\Delta E(\theta) = \frac{\Delta E_o}{cos\theta} \tag{1.12}$$

1.1.4 Applications of Charged Particle Detector

Charged particle silicon detectors have been used since the 1960s. They were typically applied in heavy charged particles spectroscopy [5] which measures the energy loss of charged particles in transmission detectors. A semiconductor detector has: good energy resolution, good stability, exceptional timing characteristics, as well as small size and extremely thin entrance windows which allow it to be used in many applications. However, semiconductor detectors are not an ideal choice for large surface area detector fabrication because the large capacitance reduces its energy resolution. A common area for a silicon charged particle detector ranges from 1 to 5 cm^2 with depletion depths of up to 1 mm [7], however special configurations are available where the surface area can be produced up to 20 cm^2 and depletion depths up to 5 mm.

For particles with a range in a detector material less than the depletion depth, such as alpha particles, silicon detectors are ideal to operate at room

temperature. A charged particle silicon detector for alpha spectroscopy is calibrated by measuring the pulse height spectrum from an alpha emitting source. The most common alpha source used in the laboratory for calibration is ^{241}Am having an energy range of 5.486 MeV.

A silicon detector can also be used for particle identification using monolithic combinations of ΔE and E detectors produced by ion implantation. A ΔE detector is extremely thin and used to measure the specific energy loss dE/dx of an incident particle, whereas an E detector measures the total energy. When ΔE and E detectors are operated in coincidence, the dE/dx and E can be obtained for each incident particle, which allows the types of particles to be identified.

1.2 Microdosimetry

1.2.1 Microdosimetry Approach

The biological effect of radiation depends not only on an absorbed dose, defined as the energy deposition per unit mass, but also on the types of ionizing radiation. Sparsely ionizing radiation such as X-rays, gamma, or electrons produces approximately the same biological effect for the same absorbed dose, but with heavy ions, different biological effects can occur for the same dose depending on the energy and atomic number of the ions, due

to their dense track of delta electrons along the trajectories and local deposition of ionizing energy. In order to describe this effect, the relative biological effectiveness (RBE) of a radiation field was introduced. Microdosimetry was introduced to study the statistical fluctuations of energy absorption in small volumes that are similar to cells or a cell nucleus. Regional microdosimetry involves measuring the deposition of stochastic energy on an event-by-event basis. Energy depositions are, on a micron scale sensitive target volume (SV), comparable in size to a human cell, and they arise from charged particles traversing the SV from either the primary radiation field or from secondary particles originating via nuclear interactions within the surrounding tissue. Using microdosimetry, it is possible to deduce the dose equivalent in any arbitrary mixed radiation field [8]. This is a major advantage over other dosimetry methods that can only measure the absorbed dose, or require prior knowledge of the field composition.

1.2.1.1 Microdosimetric Quantities

The microdosimetric quantities were given in ICRU report 36, 1983 [9]. Experimental microdosimetry is based on the measurement of stochastic quantities such as energy imparted ε, specific energy z, and lineal energy y. Energy imparted is defined as the difference of kinetic energy of ionizing radiation flowing into and out of the reference SV [10]. The specific energy z,

is given as the quotient of the energy imparted ε by ionizing radiation to matter by its mass, m:

$$z = \frac{\varepsilon}{m} \tag{1.13}$$

The units of specific energy are J/kg, or Gy.

The microdosimetric quantity used to describe the energy imparted to the matter in a volume of interest by a single energy deposition event ε divided by $\bar{l}$ is called lineal energy (y).

$$\mathrm{y} = \frac{\varepsilon}{\bar{l}} \tag{1.14}$$

where $\bar{l}$ is the mean chord length of the volume of interest.

Lineal energy is most commonly expressed as keV/μm. The mean chord length in a volume is the average length of randomly oriented chords in that volume where the volume is exposed to a uniform isotropic field of infinite straight lines. In a convex volume, the mean chord length is given by:

$$\bar{l} = \frac{4V}{S} \tag{1.15}$$

Where V is the volume and S is the surface area of the volume.

If *F(y)* is the probability that the lineal energy is equal to or less than y, the probability density or lineal energy distribution *f(y)* can be determined by:

$$f(y) = \frac{dF(y)}{dy} \tag{1.16}$$

The frequency-weighted mean lineal energy $\overline{y_F}$ is a non-stochastic quantity given by:

$$\overline{y_F} = \int y f(y) dy \tag{1.17}$$

If *D(y)* is the fraction of an absorbed dose with a lineal energy equal to or less than y, d(y) is the dose probability density and can be determined by:

$$\mathrm{d(y)} = \frac{dD(y)}{dy} = \frac{1}{\overline{y_F}} y f(y) \tag{1.18}$$

The dose-weighted mean lineal energy $\overline{y_D}$ is given by:

$$\overline{y_D} = \int y d(y) dy \tag{1.19}$$

The dose-weighted mean lineal energy can also be expressed as:

$$\overline{y_D} = \frac{1}{y_F} \int y^2 f(y) dy \tag{1.20}$$

The microdosimetric spectra are usually presented in log scale because the lineal energy *y* and its distribution *f(y)* span through a wide range of y

values in realistic radiation fields. In order to graphically display spectra of the fraction of events having lineal energy ranges in a given range of interest, *yf(y)* versus *log(y)* can be used and presented as:

$$\int_{y_1}^{y_2} f(y)dy = \int_{y_1}^{y_2} [yf(y)]d\,log(y) \tag{1.21}$$

With knowledge of the microdosimetric spectra of a radiation field, (i.e. $y^2f(y)$ vs *log(y)*), the Dose Equivalent, *H*, used in radiation protection can be derived using:

$$H = D \int Q(y)y^2 f(y)d\big(log(y)\big), \tag{1.22}$$

where *Q(y)* is a Quality Factor obtained from radiobiological experiments and *D* is the absorbed dose [10].

1.2.2 Radiobiological Models based on Microdosimetry

The classic model describing time-dose relations in radiobiology is a Linear-Quadratic Model (LQ Model). The LQ model is a mathematical model used to predict the survival levels at different doses for different types of ionizing radiation. After the DNA structure was discovered [11], an estimated assumption of cell damage that depended on the effect of radiation to the DNA structure, and their repair, was introduced. Based on that estimation, an LQ model was derived:

$$S = exp\ (-\alpha D - \beta D^2) \quad (1.23)$$

where S is a cell survival fraction and D is a dose, and α *and* β are individual to tissue type radiosensitivity coefficients (α, in units of Gy^{-1} and β, in units of Gy^{-2}).

Two approaches can be used to derive the equation for the LQ model: the experimental and mechanistic methods.

- The experimental method involves radiobiological experimentation that studies cell survival after irradiation.
- The mechanistic method is used to derive the Linear Quadratic expression. These models are applied in Treatment Planning Systems (TPS) for heavy ion therapy in Japan and Germany, and include:

- A dual radiation action model
- A kinetic-microdosimetric model (MKM)
- A Local Effect Model (LEM)

1.2.2.1 Theory of Dual Radiation Action

The theory of Dual Radiation Action (TDRA) was first proposed by Kellerer and Rossi in 1972 [12], aimed at understanding the RBE values vs dose per fraction for high LET radiations, especially the neutrons of moderate energies (from around 100 keV to around a few MeV) relative to

low LET (X-rays or gamma) radiation. The RBE can be expressed according to a simple relationship, depending on the absorbed dose of neutrons:

$$R = kD^{-1/2} \tag{1.24}$$

Where R is RBE and k is a constant. An equivalent representation is:

$$R = k^2 {D_L}^{-1} \tag{1.25}$$

Where D_L is the absorbed dose of low-LET radiation.

The main idea with this theory is that the biological effect for instant mutation or inactivation of the cell, only occurs when sub-lethal events were produced in pairs by a single event. Based on this assumption, the biological effect can be estimated as a function of specific energy deposited in the SV, and it is based on the probability of any two lesions occurring within the same SV. The TDRA has developed through 3 stages, namely the site model, the distance model, and compound dual radiation action (CDRA). These models were based on fundamental concepts such as the geometrical distribution of sub-lesions. Kellerer and Rossi decided that an SV should be approximately 1 μm, which would be probably be enough for sub-lethal events that occur in coincidence.

The RBE of radiation H relative to another radiation L, is defined by [12]:

$$RBE = \frac{D_L}{D_H} \tag{1.26}$$

Where D_L and D_H are the absorbed doses of the two radiations causing an equal effect.

In radiation therapy, the relative biological effectiveness (RBE) can be derived based on a Linear Quadratic Model (LQM) of the cell survival response to radiation S:

$$S = exp\,[-\alpha D - \beta D^2] \tag{1.27}$$

$$logS = -[\alpha D + \beta D^2] \tag{1.28}$$

Based on equation (1.26) the RBE of higher LET to lower LET radiation is given by:

$$RBE = \frac{\alpha_L}{2\beta_L D_H}\left[\sqrt{1 + \frac{4\beta_L\left(\alpha_H D_H + \beta_H {D_H}^2\right)}{{\alpha_L}^2}} - 1\right] \tag{1.29}$$

Where D is the absorbed dose and α *and* β are coefficients depending on the quality of radiation.

However the TDRA provides a biological effect without considering the probability of cell repair after irradiation, which is why combined models of microdosimetric-based and repair kinetic models were introduced to estimate the biological effect. This model is called the Microdosimetric-Kinetic model (MKM).

1.2.2.2 The Microdosimetric-Kinetic model (MKM)

The MK model was developed by Hawkins as an extension of the assumption in the TDRA [13]. It combines the repair kinetic principles and the TDRA for the final expression of survival. The biological effect in the MK model is determined by the probability of 3 types of damage occurring, including a non- repairable double strand break, a 1 track single strand break, and a 2 track double strand break.

The two kinds of parameters used in the MK model are tissue-specific parameters and the dose-mean lineal energy derived from the lineal energy distributions measured with a Tissue Equivalent Proportional Counter (TEPC).

A derivation of RBE according to the MK model was presented by [Hawkins 1994, 2001]. In the MK model, a domain has a spherical shape and the nucleus of the cell is filled with domains. These domains were introduced to set the restricted region in a cell nucleus as a pair of sub-lethal lesions created in close proximity to each other by a single event that produces a lethal lesion. The MK model proposes a mathematical expression for the mean number of lethal lesions L in a domain using an LQ model of specific energy z:

$$L(z) = Az + Bz^2 \tag{1.30}$$

From (1.30) the dose-effect relationship for this model can be described as:

$$L(D) = \alpha D + bD + cD^2 = (\alpha+b)D + cD^2 \tag{1.31}$$

Where a, b, and c are the probabilities of a non-repairable 1 track-single strand break (track-ssb), 1 track-double strand break (track-dsb), and 2 track-double strand break, actually occurring.

The microdosimetric quantity of therapeutic beams is represented by d(y), which is the distribution of an absorbed dose in lineal energy measured by the conventional TEPC with simulated volumes having a diameter of 1 µm. $\overline{y_D}$ value is an index of the biological effectiveness of the microdosimetric spectrum when RBE is proportional to $\overline{y_D}$, and this only applies at low absorbed doses. At very high doses a saturated biological effect occurs, so the empirical quantity y* was introduced to take saturation [12] into account:

$$y^* = \frac{y_o^2 \int_0^\infty \left(1 - exp(-y^2/y_o^2)\right) f(y) dy}{\int_0^\infty y f(y)\, dy} \tag{1.32}$$

Where y_0 was typically chosen to be 125 keV/µm. y* is the saturation-corrected dose-mean lineal energy used where the deposition of excessive local energy leads to an over kill effect (saturation effect).

Using the modified MK model allows the RBE for a given kind of mammalian cells irradiated by ions to be derived. The surviving fraction S of human salivary gland (HSG) tumor cells was expressed based on a linear quadratic function of the dose D in equation (1.27) where:

$$\alpha = \alpha_0 + \frac{\beta}{\rho \pi {r_d}^2} y^* \tag{1.33}$$

The model parameters $\alpha_0 = 0.13\, Gy^{-1}$ is a constant that represents the initial slope of the survival fraction curve in the limit of zero LET, $\beta = 0.05\, Gy^{-2}$ is a constant independent of LET, $\rho = 1\, g/cm^3$ is the density of tissue, and $r_d = 0.42\, \mu m$ is the radius of a sub-cellular domain in the MK model.

The RBE_{10} for HSG cells corresponding to 10% cell survival can be obtained using the following formula [14]:

$$RBE_{10} = \frac{2\beta D_{10,R}}{\sqrt{\alpha^2 - 4\beta ln(0.1)} - \alpha} \tag{1.34}$$

where $D_{10,R}$ = 5.0 Gy is the 10% survival dose of 200 kVp X-rays for HSG cells [15].

1.2.2.3 Local Effect Model

The Local Effect Model (LEM) was introduced by M. Scholz and Kraft in 1994, 1996 and 2004 [16], [17], [18]. The RBE values can be calculated in the treatment planning system at GSI using LEM which is based on the

fundamental assumption of cell inactivation. LEM assumes that the lethal events which caused cell inactivation do not depend on the type of radiation, they depended on the track structure produced in the molecule of these lethal events. When a cell population is exposed to X-rays, the dose is distributed homogenously, whereas in the case of ion beams the dose is distributed locally, so it is also called local dose distribution.

The lethal events for X-rays were randomly distributed and therefore the number of survival cells can be obtained by the equation:

$$S_x = e^{-\overline{N_{lethal,X}}} ; \overline{N_{lethal,X}} = -logS_X \tag{1.35}$$

From equation (1.35) the frequency number of lethal events within the target volume for X-rays can be obtained:

$$\nu_X(D) = \frac{\overline{-N_{lethal,X}(D)}}{V_{nucleus}} = \frac{-logS_X(D)}{V_{nucleus}} \tag{1.36}$$

With ion beams, the dose was not distributed homogenously but locally, and therefore the dose distribution should be derived at a small point in the cell nucleus. Based on LEM, the frequency of lethal events and the number of lethal events produced by heavy ions can be obtained by the equation:

$$\nu_{Ion}(D(x,y,z)) = \frac{d\overline{N^{nucleus}_{lethal,Ion}}}{dV^{Nucleus}} = \frac{d\overline{N^{nucleus}_{lethal,Ion}}}{dxdydz} \tag{1.37}$$

$$\overline{N_{lethal,Ion}^{nucleus}} = \int_x \int_y \int_z \nu_{Ion}(D(x,y,z))\, dxdydz \tag{1.38}$$

If the number of lethal events produced by ions is equal to those produced by X-rays, we will finally have:

$$\overline{N_{lethal,Ion}^{nucleus}} = \int_x \int_y \int_z \frac{-logS_x\big(D(x,y,z)\big)}{V_{nucleus}} dxdydz \tag{1.39}$$

where $\overline{N_{lethal,Ion}^{nucleus}}$ is the number of lethal events produced by heavy ion

S_x is the number of survival cells for X-ray

$V_{nucleus}$ is the nucleus volume

D(x,y,z) is the local dose distribution

The LEM model assumed that the radio-sensitivity of the cell and size of the nucleus remained unchanged in different phases of the cell cycle. This assumption may cause uncertainty for this model because the size of the nucleus and radio-sensitivity of the cell is supposed to increase during the cell cycle, and in LEM the effect of the dose rate was not considered.

Using LEM, the radiobiological effect produced by heavy ion particles can be obtained using X-ray survival curves. This is based on the assumption that an equal number of lethal events will be produced by heavy charged particles and X-rays at a point where the same dose is absorbed. Regardless of whether this dose is deposited by X-rays generating secondary electrons or electrons of the ion track structure, this assumption works better when a

nano-scale volume is considered, and where the dose was distributed mostly due to the track structure. However, in larger volumes the interactions with material are different for X-rays and ions, so this will result in different biological effectiveness. LEM is purely a theoretical model based on track structure simulations for ions and secondaries of different energies, including their parameterization which depends on the radial distance of the track. This approach in RBE verification can only be verified with radiobiological experiments, while the MKM approach is based on experimental measurements of the microdosimetric spectra followed by RBE derivation.

1.2.3 Experimental Microdosimetry

1.2.3.1 Proportional Counter Microdosimetry

A conventional microdosimeter uses a tissue equivalent proportional counter (TEPC) that incorporates a spherical SV filled with tissue equivalent gas that can model a micron sized biological cell using low pressures gas. Typical TEPCs have a 2.5 cm diameter SV filled with propane gas at 17 Torr, which is equivalent to a 1 μm diameter tissue equivalent spherical SV [19]. The metal anode contact sits across the internal diameter of the chamber and a bias is applied between the chamber wall and the collecting anode.

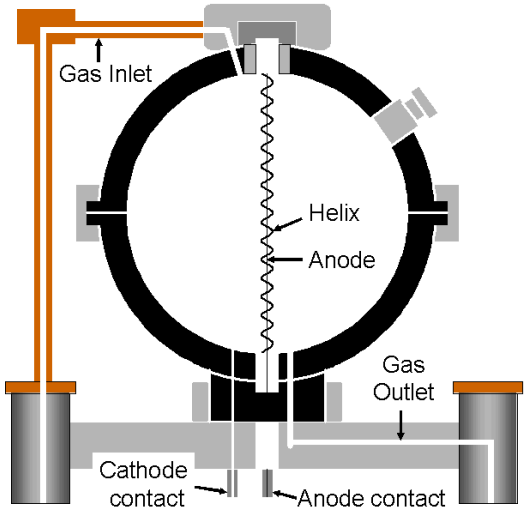

Figure 1.7 Rossi proportional counter [19]

Different approaches have been used to simulate a sensitive volume down to 0.3-0.5 μm by increasing the electronic gain by a factor of 10 (p94, [10]), or using smaller diameter electrodes [20]. However, a solution is still a challenge due to the smaller sensitive volume, which causes a lower mean lineal energy deposition that is difficult to distinguish from the noise level. Further discussion about TEPCs can be found in [21]. Several limitations have been observed in the experimental measurements carried out by TEPC, and include a high voltage operation, wall effects, large size (i.e. poor spatial resolution), and it can only mimic a single, isolated cell [22]. Wall effects may occur due the scattering effect of the primary and secondary particles caused by the difference in density between the cavity and the surrounding wall [9]; this may cause distortions in the experimental microdosimetric

spectra. Below are illustrations of four types of wall effects which were suggested and studied by Rossi [23] and Kellerer [24, 25].

Delta-ray Effect: In the case of non-uniform density of wall material and TEPC gas, the primary particle and its delta ray enter the cavity and deposit energies to the simulated sensitive volume (Fig. 1.8a left), whereas the events for a small volume of uniform density can be collected separately in different small volumes (Fig. 1.8a right). This effect happens more frequently in the TEPC when a primary particle is a heavy ion particle traversing with a dense distribution of delta rays that may lead to an increase of $\overline{y_F}$ *and* $\overline{y_D}$, even though $\overline{y_D}$ is not affected significantly because the energy deposited by the delta rays is much less than the primary particle.

Re-entry Effect: This effect typically happens when an electron re-enters a cavity after it has first traversed via a curled track (Fig. 1.8b, left). In actual microscopic volumes, there is a low probability of having a re-entry effect due to the reasonable distance between the exit point and re-entrance point of the electron escaping and re-entering the volume (Fig. 1.8b, right). The re-entry effect is substantial for electrons energies up to 1 MeV only.

V Effect: This effect is common in non-elastic nuclear interactions where several nuclear fragments originated outside the cavity. Fig. 1.8c (left) shows two charged particles entering the same large volume cavity whereas Fig.

1.8c (right) shows that the charged particles traverse two microscopic volumes separately.

Scattering Effect occurs when neutral particles such as neutrons or photons interact with the surrounding medium and produce more than one charged particle which traverses through the cavity (Fig. 1.8d, left). In actual microscopic volumes, two charged particles tracks cross two separate volumes because the volume is less than the distance between the charged particle tracks (Fig. 1.8d right).

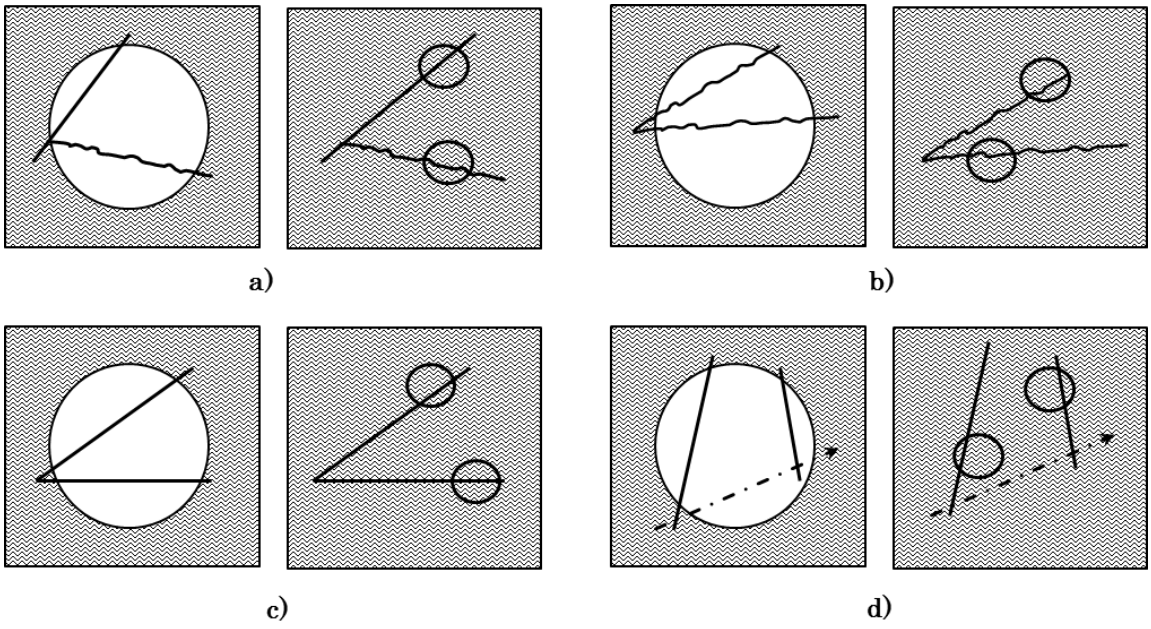

Figure 1.8 Illustrations of four types of wall effects in a low pressure proportional counter: a) Delta-ray effect, b) Re-entry effect, c) V effect, d) Scattering effect

1.2.3.2 Silicon Microdosimetry

A solid state microdosimeter was proposed by the Centre for Medical Radiation Physics (CMRP) at the University of Wollongong as a new method of measuring energy deposition in an array of micron sized SVs [10, 22]. The concept of silicon microdosimetry aims to address the above shortcomings of the TEPC [22, 26]. A silicon microdosimeter is based on an array of micron sized silicon SVs to mimic an array of biological cells, instead of gas. The array of silicon SVs was fabricated using silicon on insulator (SOI) substrates. Three generations of SOI microdosimeters have been developed and investigated; they include the 1st generation of planar SOI devices made up of a 2D 30 μm x 30 μm diode array of elongated parallelepiped shaped micron sized SVs fabricated on 2, 5, or 10 μm thick p-SOI with the SV's adjacent to each other (Fig. 1.9) [22]. Studies of the charge collection characteristics of these devices found that the charge collection efficiency (CCE) of the device varies with the position of an incident charged particle around the SV due to a lateral distribution of the electric field within the planar RPP SV and diffusion of charge into the SV's from outside [26, 27]. Additionally, capacitive crosstalk between neighbouring SVs also affected the response of the SOI microdosimeters.

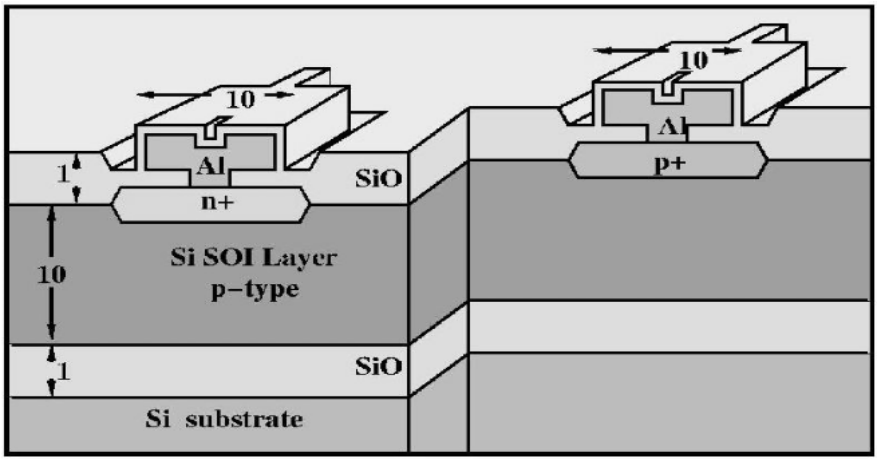

Figure 1.9 First generation SOI microdosimeter

The second generation of SOI devices was based on an array of physically isolated, cylindrical 2D planar and pseudo 3D mesa p-i-n structures, with a 15-30 μm diameter SVs (Fig. 1.10) [28-30]. The cylindrical geometry reduces the chord length variance throughout the SV and supports a radial electric field that leads to better charge collection in the SV. However, the effective yield of SVs was not 100% due to the technological challenges related to track interconnects between the SVs in case of mesa structures.

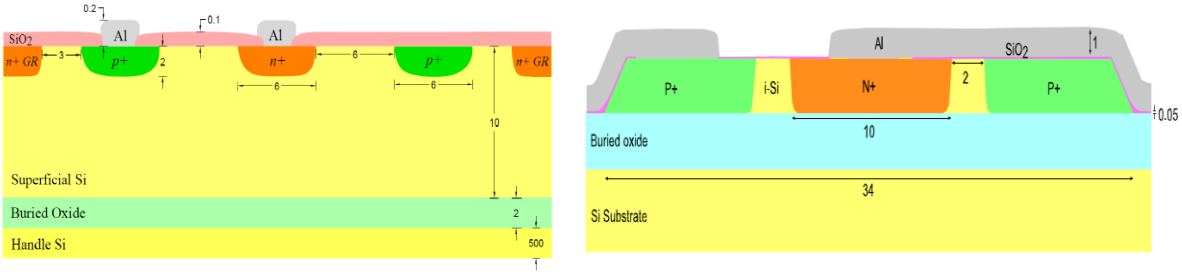

a) b)

Figure 1.10 Second generation SOI microdosimeter a) 2D planar and b) Pseudo 3D Mesa p-i-n structure

The third generation of SOI devices were large area, 4 mm x 5 mm segmented microdosimeters with separated cylindrical 2D planar SVs (10 µm in diameter) fabricated on 10 µm thick n-SOI, that demonstrated a 100% yield of working SVs (Fig. 1.11) [31].

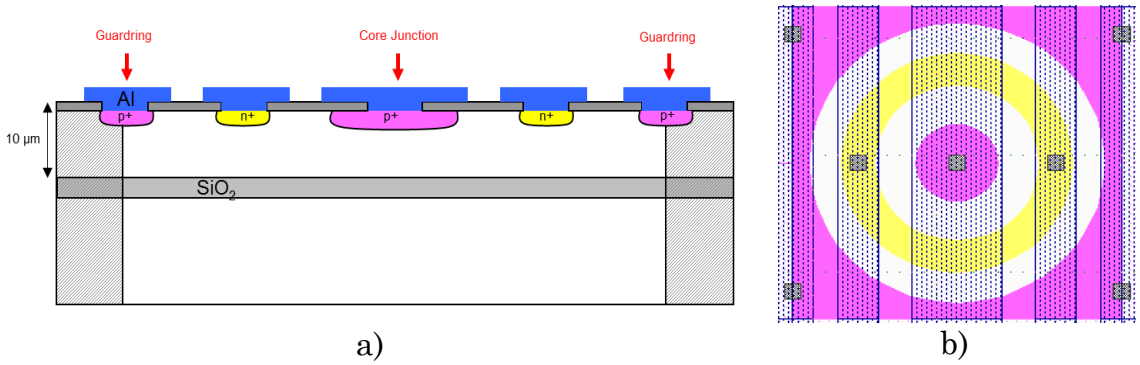

Figure 1.11 Third generation microdosimeter a) a single cell topology of n-SOI microdosimeter; b) A view from top of microdosimeter (cylindrical SV)

A detailed investigation of the newly developed SOI microdosimeters was carried out in mixed radiation fields typical of space [32, 33], avionics [34], and hadron radiation therapy [35] radiation environments. The results demonstrated the ability of the SOI microdosimeters to closely match the microdosimetric spectra of TEPCs and derive a tissue dose equivalent in a mixed radiation field.

Although previous research and development at CMRP clearly proved the feasibility of the silicon microdosimetry concept, the planar technology for SOI microdosimeters fabrication still has a number of limitations. Planar technology cannot pattern the silicon any more than 1-2 µm under the

surface, whereas the active SOI layer is 10 μm thick, which limits a 3D definition of SV due to the electric field having a lateral spread. These limitations include non-uniformity of the charge collection in the SV and diffuse charge collection outside the SV [26-31].

In order to overcome these drawbacks in the existing planar technology, the CMRP has proposed to design an optimal SOI microdosimeter with free standing and true, three dimensional (3D) "mushroom" SVs. 3D SVs embedded in PolyMethyl MethAcrylate (PMMA) are being fabricated using 3D detector technology via state-of-the-art silicon processing facilities which are already well established at the SINTEF MiNalab, Oslo, Norway.

This thesis will present 3D detector technology, including the fabrication process and its application in fabricating a new 3D SV microdosimeter. Different prototypes of the 3D detectors produced by SINTEF, Stanford, and CNM nanofabrication facilities were investigated at CMRP in order to understand the charge collection and technological capability. Geant4 simulations were also carried out to optimise the designs of the new microdosimeters.

1.3 3D Detector Architectures

A 3D detector concept was first proposed by S. I. Parker in 1995 [36], and then later in 1997, active edge detector technology was proposed by C. Kenney for high energy physics and medical imaging applications [37]. The fabrication of 3D detectors has become possible in the last two decades by the latest developments in Micro-Electro-Mechanical-Systems (MEMS) and standard VLSI (Very Large Scale Integration) technologies [38].

Unlike conventional planar detector, 3D detectors have electrodes that penetrate the entire substrate. Fig. 1.12 compares a conventional planar detector where the n^+ and p^+ electrodes are on the surface of the sensor and a 3D detector where the n^+ and p^+ columns penetrate the entire silicon substrate.

In a planar detector configuration, the distance between the n^+ and p^+ electrodes is determined by the thickness of the wafer, which is typically between 300 μm and 500 μm [39]. In 3D detectors, this distance can be much shorter depending on the inter-electrode distance that can be fabricated to 10 to 50 μm. This short inter-electrode distance provides a high electric field, a short collection distance, and a flexible geometry that has many advantages in radiation detection.

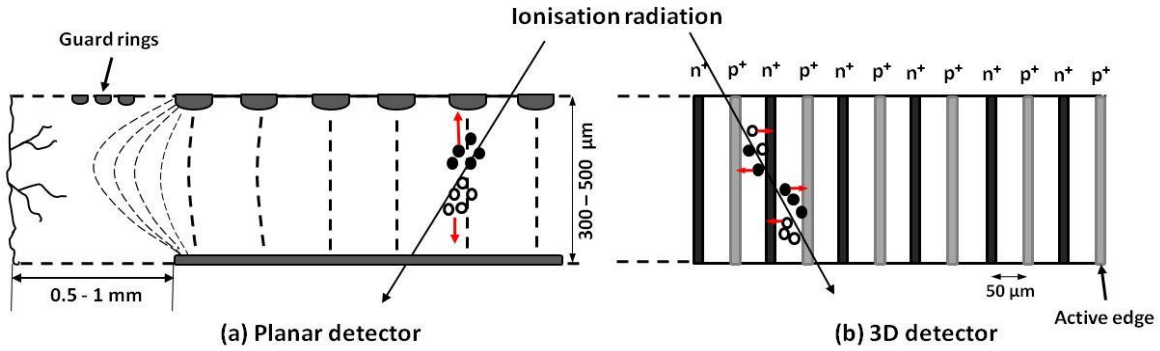

Figure 1.12 Schematic cross sections of planar and 3D detector.

The radiation hardness, rapid charge collection, and low depletion voltage provided by the high electric field and short collecting distance in 3D detectors are extremely interesting for radiation detection compared to conventional planar detectors [40].

The flexible geometry provided by 3D technology also gives rise to another feature, active edges; that is, sensors without conventional guard-rings and hence a zero dead area. A thin diamond saw was the conventional tool used to separate the devices from the wafer, but it causes cracks and chipped regions at the edge of the device which then act as generation-recombination centres that create an uneven electric field near the edge of the detector, and cause an increase in leakage current. In a planar detector the edge is normally made wide enough (0.5 to 1 mm) to gradually decrease the electrostatic potential before reaching the cracks [Fig. 1.12a]. Guard rings are therefore required to reduce leakage current and maintain a

uniform electric field, but the guard rings create a dead region of several hundred μm and sometimes up to 1 mm wide.

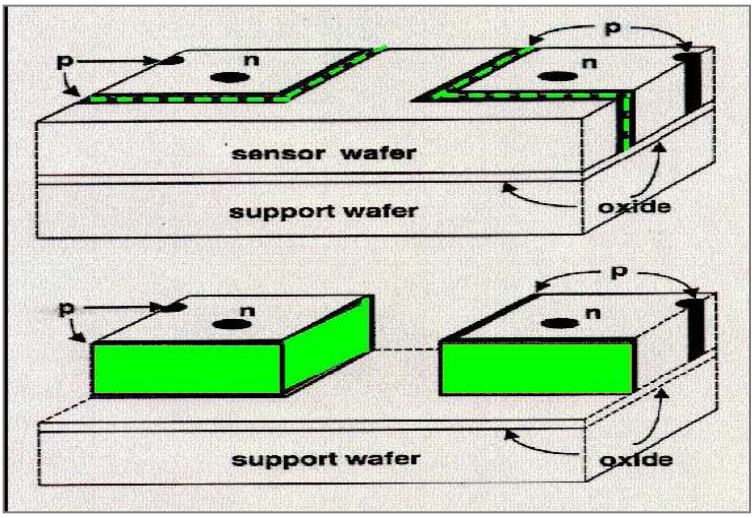

Figure 1.13 Processing a 3D active edge detector (image was adapted from [41])

A through substrate electrode that surrounds the entire periphery of a silicon sensor, as in a 3D detector, means that a traditional guard ring is not needed and therefore insensitive area for incident radiation no longer exists. An active edge detector is fabricated in the same way as cylindrical 3D electrodes, by using micro-machining and deep reactive ion etching, followed by gas phase doping and polycrystalline silicon deposition (Fig. 1.13). The active edge then acts like an ohmic contact that allows the electric field to extend right up to the physical edge of the sensor without any dead regions.

1.3.1 Conventional planar detector fabrication

Conventional planar technology has commonly been applied in the fabrication of semiconductor detectors. A number of steps are required for almost all the fabrication processes, i.e.,

- Oxidation
- Photolithography
- Wet etching
- Aluminum deposition

1.3.1.1 Oxidation

Oxidation is required before the main fabrication of a silicon detector can begin because a layer of silicon dioxide provides a good quality insulator for any electronic devices, and during fabrication it also acts like a doping barrier to prevent diffusion of the dopants and impurities. Furthermore, it also protects the surface of a detector from damage by any chemicals during the fabrication process, and also allows for easy patterning and etching as well as providing a good quality electrical insulator.

Silicon dioxide is formed on the silicon wafer as the silicon oxidises at temperatures ranging from 900 º C to 1200 º C [41]; oxidation can be either wet or dry. Wet oxidation occurs when a layer of oxide is grown in a water

vapor environment whereas dry oxidation occurs in pure oxygen. These processes are illustrated by the following chemical reactions:

Wet oxidation: $Si + 2H_2O \rightarrow SiO_2 + 2H_2$ (1)

Dry oxidation: $Si + O_2 \rightarrow SiO_2$ (2)

Wet oxidation needs much less time than dry oxidation [42], and Fig. 1.14 shows the time differences between these processes. With dry oxygen the oxide is 250 Aº thick at a time = 0.

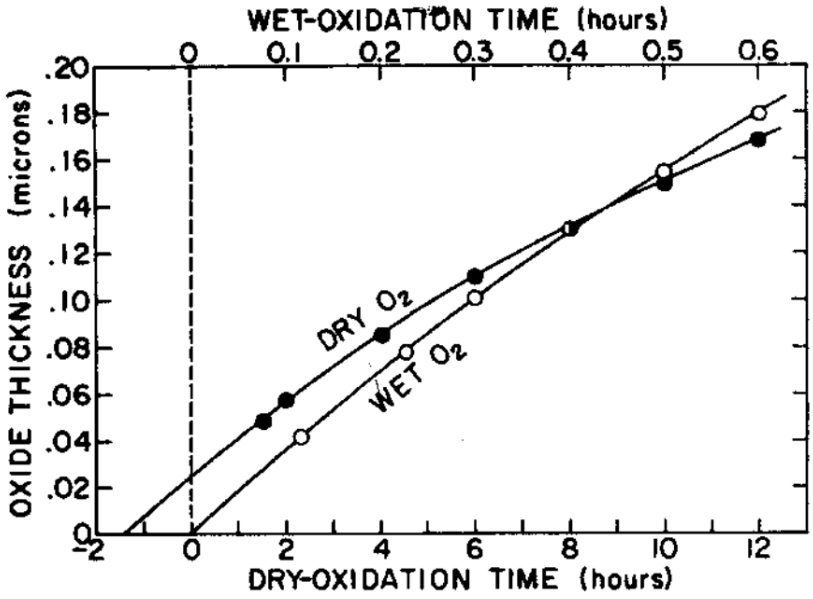

Figure 1.14 A comparison of initial oxide growth at 920ºC for oxidation in a wet and dry-oxygen ambient [42].

1.3.1.2 Photolithography

Photolithography is used to transfer the patterning on a photo-mask to the surface of a silicon wafer to form the micro-structures needed for the

specific electronic devices. Photolithography is used to pattern various layers such as silicon, silicon dioxide, aluminum, or other forms of dielectric and conductive layer, and it is an essential technique in conventional planar and 3D technology. The designated patterns determined by the electronic designers are generated on high quality photo masks usually made of quartz. The pattern is then transferred onto a light sensitive material known as photoresist that has been spun over the entire surface of the wafer to be patterned. When exposed to light, the patterns on the photo masks are engraved onto the photo resist which will then be used to pattern silicon dioxide, silicon, or another conductive layer.

There are two types of photoresist available, positive and negative (Fig. 1.15c).

- Positive photoresist allows the light to break the polymer bonds and then the exposed resist is removed.

- Negative photoresist cross-links the polymer bonds when exposed to the light, while the exposed area of resist becomes harder. Finally, the unexposed resist will be removed.

Positive resists are normally used for small geometric structures while negative resists were widely used in early integrated circuit processing.

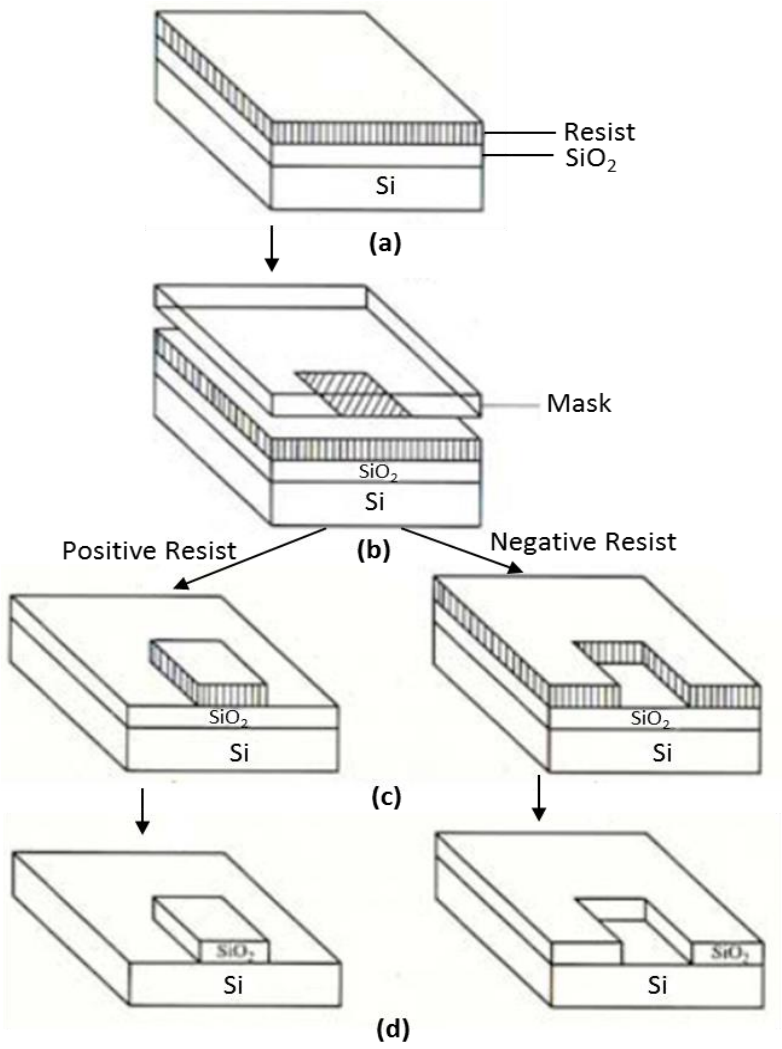

Figure 1.15 Pattern transferred process using positive and negative photolithography [41].

1.3.1.3 Wet Etching of Oxide

Etching is used to obtain a desired pattern by removing the unwanted part of the masking layer on the surface of the wafer, such as silicon dioxide and aluminum, and it is still widely used in the fabrication of sensors and integrated circuits.

Wet etching is carried out using fluid chemical etchants such as hydrofluoric acid (HF). At room temperature, buffered HF (BHF) has a high selectivity and etches silicon dioxide much faster than photoresist or silicon. The etching rate of silicon dioxide varies depending on the process parameters that took place as the oxide grew, and whether it took place in a wet or dry environment [refer to 1.3.1.1]. Oxide grown by wet oxidation tends to be etched faster than oxide grown by dry oxidation and oxide with a high concentration of phosphorus (phosphor silicate glass) is etched faster than oxide with a high concentration of boron (boron silicate glass). The principle of wet etching silicon dioxide is that only silicon dioxide is hydrophilic so it attracts HF and water molecules that remove the silicon dioxide by water sheeting. Wet chemical etching is an isotropic process that etches in all directions. Thus the final size of an opening defined by a photoresist mask depends on the defined actual opening and the thickness of film needed to be etched (Fig. 1.16a), and it is impossible to obtain an opening with wet etching that is smaller than the thickness of the film.

1.3.1.4 Aluminum Deposition

A conductive layer is needed to connect the circuit elements or electrodes, with aluminum being one of the most widely used materials. After oxidation, the window is etched through the layer of oxide to make contact with an n^+ or p^+ electrode. The sputtering method is used to deposit a

thin film of conductive material over the surface of the device. Aluminum deposition is done by bombarding a target with Ar^+ ions which knock the Al atoms from the target surface and are then deposited onto the silicon substrate [Fig. 1.18].

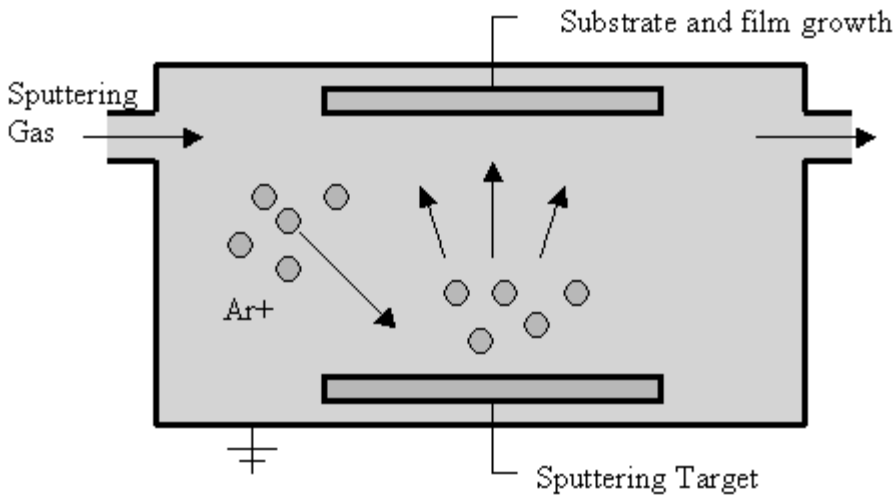

Figure 1.16 Sputtering systems for metallisation [42]

1.3.2 3D detector Fabrication

Fabricating 3D detectors utilises all the conventional technology used in planar silicon technology, such as oxidation, photolithography, wet etching, and ion implantation. The additional key technologies that enable 3D detectors to be fabricated are:

- Deep reactive ion etching
- Polysilicon deposition
- Plasma etching

- Gas phase doping

1.3.2.1 Deep Reactive Ion Etching (DRIE)

One of the key techniques in 3D detector fabrication is the fabrication of high aspect ratio hollow cylinders in the silicon substrate. This is most commonly carried out using an inductively coupled plasma system with a modified Bosch Process [43]. This process is a sequence of alternate etching and passivation that avoids any isotropic etching and etching of the side walls of the cylinders to create cylindrical shapes with high aspect ratios. [Fig. 1.17].

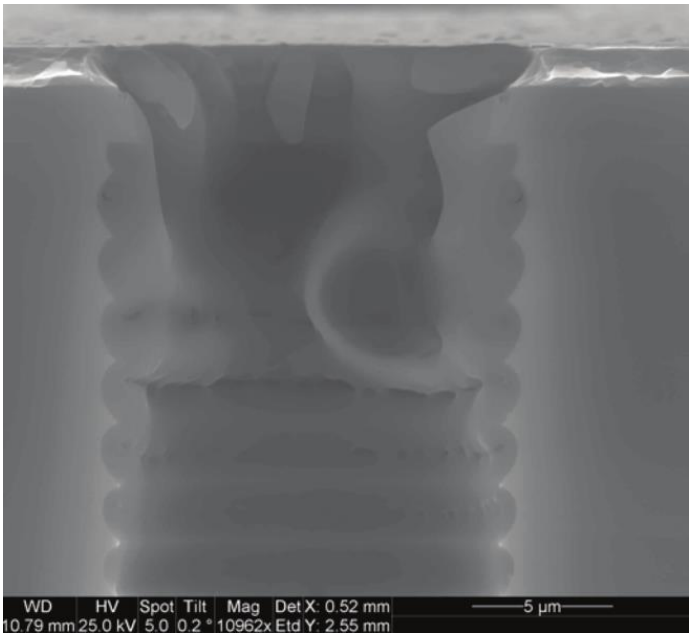

Figure 1.17 SEM image shows the protective sidewall polymers during DRIE process without damages to the wall [44].

1.3.2.2 Polycrystalline Silicon Deposition

The n-type and p-type electrodes in 3D detectors are filled with highly doped polysilicon. Polycrystalline silicon (poly-silicon) can be doped using gas phase diffusion with boron and phosphorus, the most common p and n-type dopants, respectively [45, 46]. Poly-Si is usually deposited using low pressure chemical vapour deposition (LPCVD) at about 600 ^{o}C by thermolysis of silane, SiH_4. The temperature and pressure greatly influence the parameters relating to the growth rate and quality of film; with most facilities being limited to depositing film in thicknesses of about 1 to 2 μm at a time.

1.3.2.3 Dry Etching

To overcome the disadvantages existing in wet etching, dry etching process was introduced to achieve anisotropic etching (Fig. 1.18b). The dry etching technique is commonly used in VLSI (Very Large Scale Integration) fabrication, where different types of Dry Etching Technology such as Physical Sputtering, Plasma Etching, and Reactive Ion Etching (RIE) are available.

- Physical sputtering etching uses energetic noble gas ions to bombard the wafer to knock the atoms off the surface.

- Plasma etching is done with a plasma-assisted chemical reaction where the plasma consists of fluorine or chlorine ions which etch the silicon dioxide, and then the wafer is immersed in gaseous plasma produced by radio frequency excitation in a vacuum system.

- Reactive Ion Etching (RIE) is an etching technique that uses chemically reactive plasma of high energy ions.

- Deep Reactive Ion Etching (DRIE) is a highly anisotropic process used to create deep, steep sided hollow cylinders and trenches with high aspect ratios. In recent years, trenches with an aspect ratio as high as 60:1 can be achieved. The most common process is the 'Bosch process' that alternates between two modes to create a high aspect ratio, an isotropic plasma etch, and deposit a passivation layer. While energetic plasma ions such as sulfur hexafluoride etch the wafer in a near vertical direction, a commonly used passivation layer C_4F_8 is deposited to protect the vertical sidewalls.

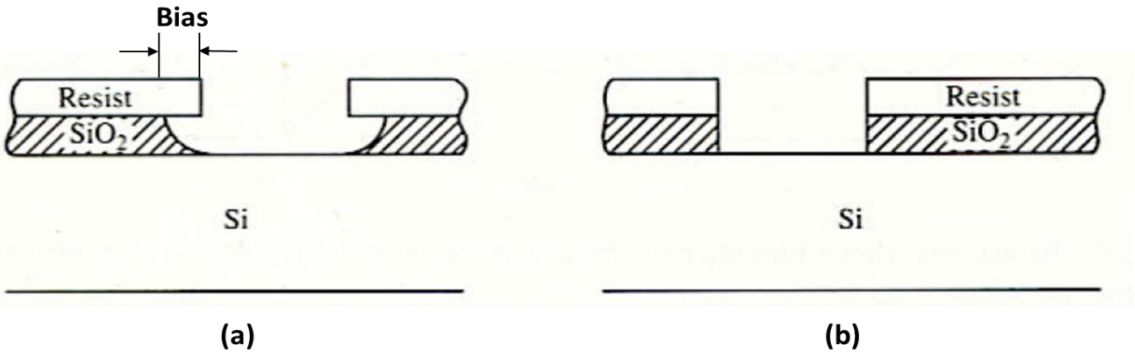

Figure 1.18 Etching profile obtained with (a) isotropic chemical etching and (b) dry anisotropic etching in a plasma or reactive-ion etching system [41].

1.3.2.3 Gas Phase Doping

The DRIE etched cylinders of 3D detectors are doped with boron and phosphorous to form p- and n-type electrodes respectively, by gas phase doping. The wafers with DRIE etched cylinders are placed in diffusion ovens at high temperatures in a boron bromide (or diborane) environment for p-type doping and Phosphoryl chloride (or phosphine) for n-type doping, which allows the dopants to diffuse into either silicon substrates or deposited polycrystalline silicon to form the required electrodes.

1.3.2 Overview of 3D Detector Manufactures

3D detector technology is currently well established in four fabrication facilities that utilize traditional radiation sensor fabrication and micro-machining, and they are:

- The Stanford Nanofabrication Facility, Stanford University, CA, USA
- The SINTEF (Stiftelsen for Industriell og TEknisk Forskning), Oslo, Norway.
- The CNM (Centro Nacional de Microelectronica), Barcelona, Spain
- The FBK (Fondazione Bruno Kessler), Trento, Italy

The 3D ATLAS R&D Collaboration was established in 2009 by those four facilities and the CERN ATLAS group. Since the development of 3D

detectors, there have been two key approaches towards this technology; the single-sided approach investigated by Stanford and SINTEF, and the double-sided approach developed by FBK and CNM.

Single-sided 3D technology involves the fabrication of n- and p-type electrodes on one side of the wafer; this was the original 3D detector proposed by C. Kenny and S. I. Parker, and which was also called a full 3D detector. In this approach the sensor wafer is bonded to a handle wafer by fusion bonding which allows the substrate electrodes and active edge electrodes that surround the entire periphery of the sensor (Fig. 1.19) to be fabricated. However, this is a more complex approach because access is only possible on one side of the sensor substrate which obviously limits the space needed for various design features, and because all the lithographic must be carried out on one side of the wafer. Moreover, in some cases the support wafer must be removed to access the side bonded to the support wafer, and that is often a difficult process. Nevertheless, the single side approach is the only technique that provides the geometric flexibility required in microdosimetry and enables the full active edges (Fig.1.19) to be fabricated.

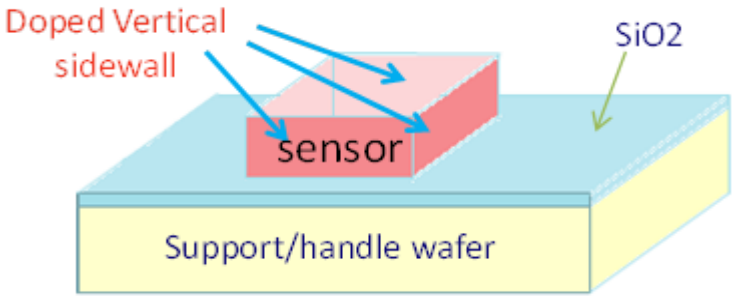

Figure 1.19 Single-sided approach to fabricate full active edges detector

A single Type Column (STC) was first proposed by FBK in 2005 where one type of electrode (n^+/p^+) was formed as a 3D column and another type was ion-implanted onto the back side as a planar device [Fig. 1.20b]. This design simplifies the manufacturing process when only one type of columns are produced, but controlling the electric field using applied bias is difficult because the columnar electrode is for one doping type only, e.g. n^+ column in p-type substrate [31], and the strength of the electric field can only be controlled using a suitable concentration of substrate doping.

A similar approach was adopted by the Brookhaven National Laboratories (BNL), Upton, New York, USA in 2007 to produce a single-type column single-sided 3D detector. The BNL single-sided 3D detector differed from the FBK one in that the back side of the BNL detector was not processed, and the planar electrode was formed on the front side [Fig. 1.20c]. This detector is also called "stripixel". Moreover, BNL also introduced a single sided double type column 3D detector that consisted of n^+ and p^+ columns formed on one side of the substrate [Fig. 1.20d].

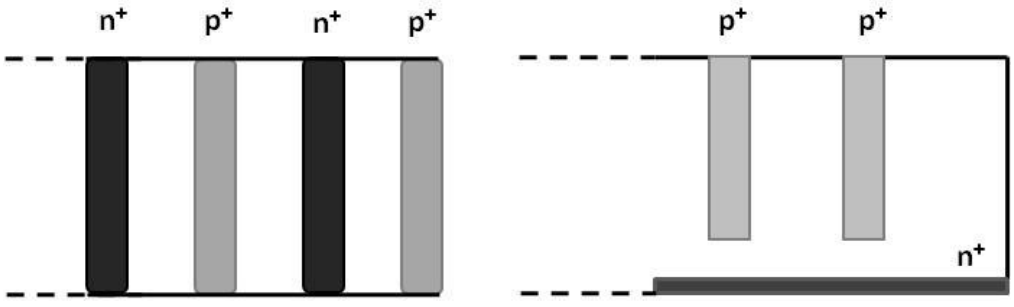

(a) Full 3D detector (b) Single Type Column (STC)

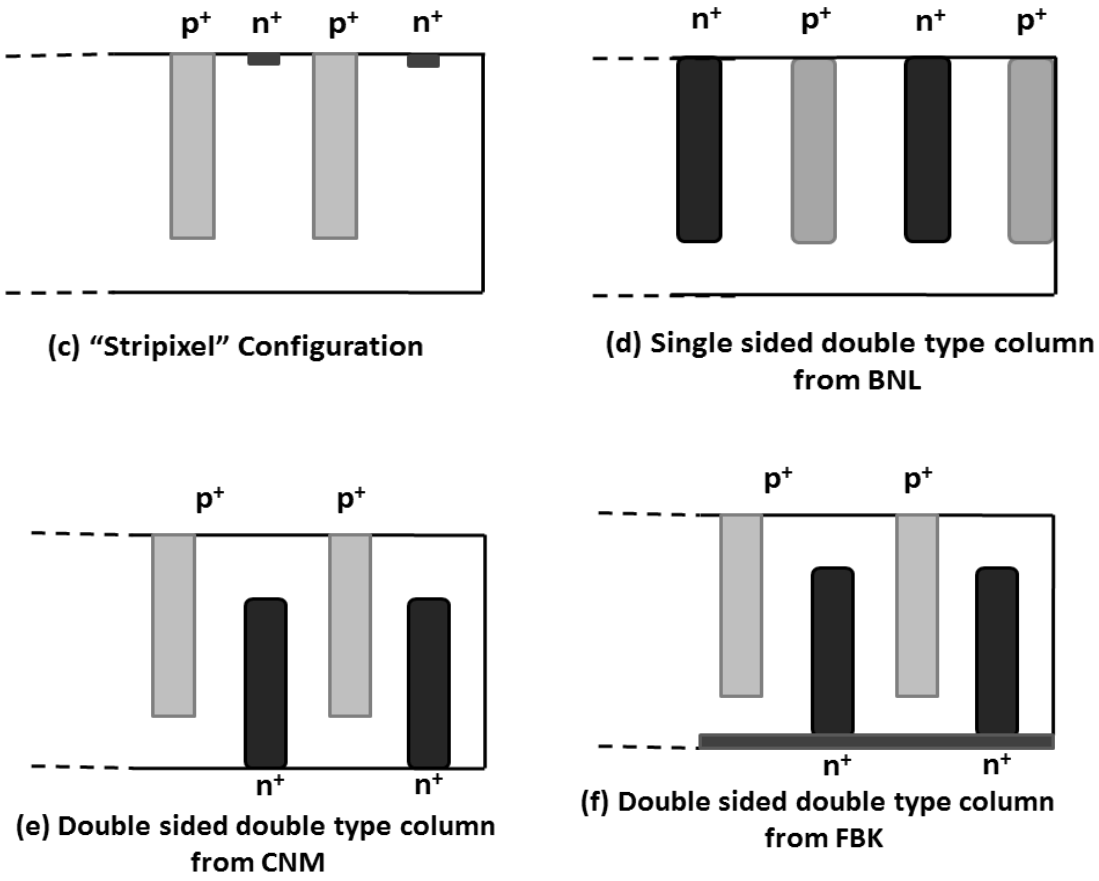

Figure 1.20 Schematic cross-sections of proposed approaches to 3D technology.

Double-sided 3D technology

The "Double-Side Double-Type Column (DDTC)" was introduced and fabricated independently at FBK and CNM where the columnar electrodes were etched from both sides of the wafer to simplify the original single-sided approach. The columns were not etched all through the substrate and a support wafer was not required [47]. The differences between the FBK and CNM designs are the column depth and backside processing, in that the

backside doping of the FBK detector represents an ohmic contact around the columns as well as on the surface [Fig. 1.19e, f].

1.4 Monte Carlo and Geant4 Simulation Toolkit

A GEANT4 (Geometry And Tracking) Monte Carlo toolkit [48, 49] is a Monte Carlo code using Object-Oriented Technology and C^{++} programming to describe how particles interact with matter, it was originally developed for high energy physics experiments and then extended to space science and medical physics .

Geant4 is an open-source, freely downloadable software developed and maintained by a large international collaboration based at CERN. Geant4 describes both electromagnetic and hadronic interactions with complementary and alternative physics models that cover the energy range between (100 eV) up to TeV scale. A Geant4-DNA package allows one to describe particle interactions down to ~eV scale. This extensive physics capability is coupled with a powerful geometrical component that allows modelling of large scale experiments such as CERN ATLAS, CMS detectors, and even down to the DNA helix.

Geant4 is a Toolkit where the user must choose the tools to use in their own Geant4 application. The user must develop a Geant4-based application

that describes the radiation field, the geometrical configuration, and the physics processes of the experimental set-up. The user can retrieve the required information from the simulation, i.e. the energy deposition and particle fluence in a detector.

Geant4 was adopted in this project to model the response of novel microdosimeters in those radiation fields of interest. Two versions of Geant4 were used in this thesis, Geant4 9.4 and Geant4 9.6.

1.4.1 Geant4 geometry component

Alternative models can be adopted in Geant4 to describe the geometries, for example: Constructive Solid Geometry (CSG) solids describe simple shapes such as boxes, cylinders, and spheres, etc., Boolean solids can be created by intersection, union, and subtraction of other solids, Boundary REPresented solids (BREP) are defined by specifying the surfaces and can be built through CAD systems, and voxelised geometries can be modelled using the Geant4 parameterised volumes.

In Geant4 it is possible to define homogeneous and heterogeneous materials, provided the chemical formula of the substance and its density is known. The materials (handled by *G4Material* class) are defined as composition of different elements. Elements are defined with their atomic number, mass, and density. It is possible to define isotopes, and it is also

possible to model a material based on its temperature, pressure, and state (solid, liquid or gaseous), where one material is associated with one geometrical component.

The composition of the materials used in the simulation project of this thesis was derived from the NIST Atomic Weights and Isotopic Compositions database [50].

1.4.2 Geant4 General Particle Source

The General Particle Source (GPS) is a component provided within Geant4 which allows complex radiation fields to be modelled with simple pre-defined user interface commands. A source with different shapes can be defined, including 2D and 3D surfaces such as discs, spheres, or boxes. The angular distribution of particles such as unidirectional, isotropic, cosine-law, and beam or arbitrary can also be defined, as can the energy of a radiation field that is defined as monochromatic or with an energy spectrum. The GPS was used in this thesis to model the radiation field.

1.4.3 Physics Processes

There are seven categories of physics processes contained in Geant4, and they include electromagnetic, hadronic, decay, photolepton-hadron, optical, parameterisation and transportation.

The electromagnetic processes for photons and charged particles are also described, particularly the Rayleigh scattering, photoelectric effect, Compton scattering, pair production, ionization, bremsstrahlung and multiple scattering, and the optical photon interactions are modelled in an energy range between ~100 eV to ~TeV scale.

The Geant4 Standard Electromagnetic Package, which is valid down to 1 keV, is more commonly used for High Energy Physics experiments, while the alternative Geant4 Electromagnetic Low Energy Package is specifically addressed to low energy studies, i.e. medical physics. The G4 Low Energy Package includes two alternative approaches: the first one is based on the Livermore Evaluated Data Libraries (which is valid down to ~250 eV) and the second one is based on the physics models of the Penelope Monte Carlo code (which is valid down ~100 eV).

Fluorescence and Auger electrons can also be modelled in the simulation.

With electromagnetic physics, a threshold of production of secondary particles (cut) must be defined. The cut is expressed in a range of secondary particles that originated in a given material, but if the range is bigger than the cut, further secondary particles are generated and tracked, otherwise their energy is considered to be deposited locally. In the simulation project of this thesis, the cut was defined to achieve fast simulation execution speed without sacrificing the accuracy of the results.

The hadronic processes include complementary and alternative physics models to describe the hadronic interactions between neutron thermal energies and the order of the TeV scale. Fig. 1.21 shows a partial inventory of the Geant4 hadronic physics models where elastic and inelastic scattering are described as well as neutron fission and neutron capture.

At high energies the Binary or the alternative Bertini model can be used to describe the intra-nuclear cascade of hadrons. Evaporation models are available to describe the nuclear de-excitation and the High Precision (HP) neutron models can be adopted to describe the neutron interactions between thermal energies and 20 MeV in detail.

Ion hadronic interactions can be described with the alternative physics models Binary Cascade, Wilson Abrasion, or the Quantum Molecular Dynamic (QMD) model.

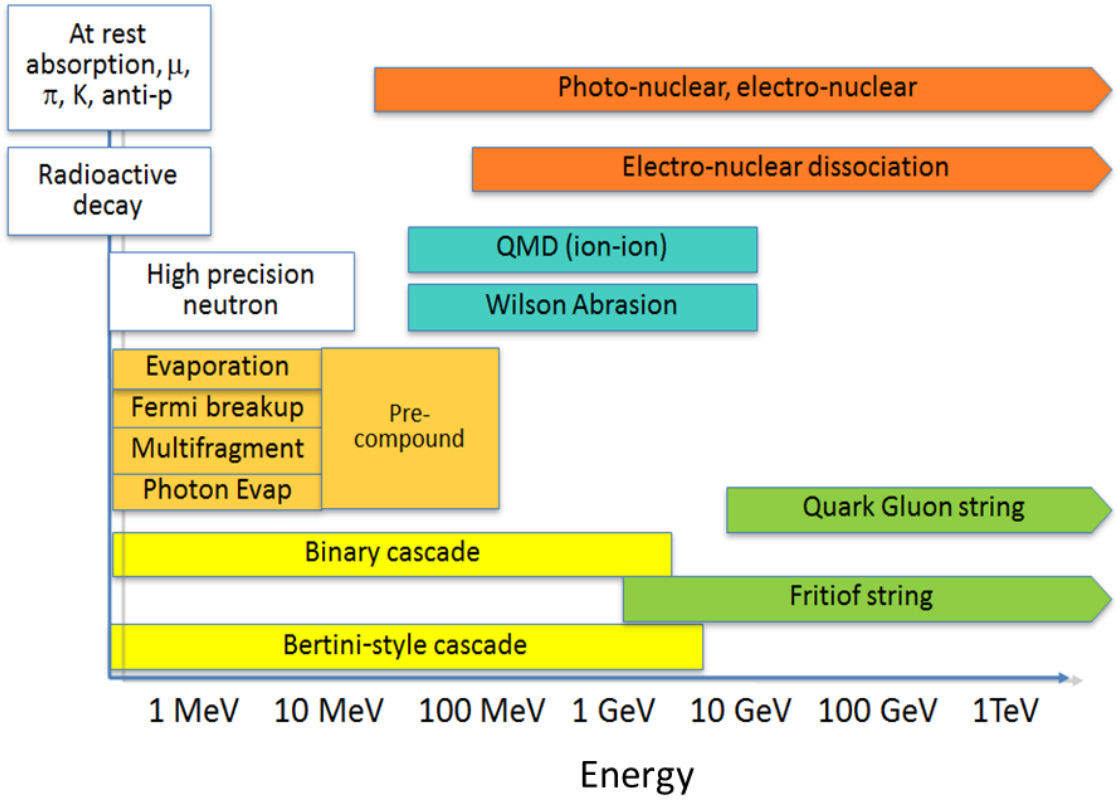

Figure 1.21 Partial inventory of Geant4 hadronic physics models (Geant4 version 10) [51].

Chapter 2

The ANSTO Heavy Ion Microprobe

The charge collection studies presented in the latter chapters of this thesis were carried out using the Ion Beam Induced Charge Collection (IBICC) technique at the Australian Nuclear Science and Technology Organisation (ANSTO). The ANSTO heavy ion microprobe is located on the 10 MV ANTARES tandem accelerator and can focus the beam down to μm size with a maximum mass energy product ME/q^2 = 100 MeV/amu [52] .

2.1 Introduction

In 1989 the US FN tandem accelerator was relocated to ANSTO and began operations in 1991. The heavy ion microprobe installation commenced at the same time [52]. The ANSTO heavy ion microprobe was aimed at analysing very small structures in man-made materials, and geological, and biological samples, etc. The ion beam is accelerated up to MeV energies using the 10 MV Van de Graff accelerator and it is then focused to a small beam size using objective and collimating slits followed by further magnetic focusing using quadrupole triplet magnets. The final micrometer diameter

focused spot is magnetically raster scanned across the sample under investigation at the focal point of the beam. The energy deposited in the sample is collected as a function of the beam position, and based on these data, a 2D image of the sample characteristics can be obtained.

2.2 Australian National Tandem Research (ANTARES) Accelerator Facility

2.2.1 Ion Sources

The accelerator requires a negative ion for the first stage of acceleration, and therefore all the ion sources produce negative ions as their output. The 10MV tandem accelerator has two cesium sputter ion sources and a charge exchange radio frequency (RF) ion source (NEC αlphatross ion source), which can accelerate most of elements in the periodic table from solid targets. The first sputter ion source was a Model 860 negative ion source with an annular ionizer, and the second sputter ion source was a Model 846 multi-sample ion source with a spherical ionizer that was developed for Accelerator Mass Spectrometry (AMS) measurements [53]. The Alphatross ion source produces negative helium ions by creating positive helium ions in plasma before extracting them through a chamber with low pressure rubidium vapour. As the positive ions travel through the rubidium vapor,

the positive ion will probably pick up two electrons and become temporarily negatively charged for pre-acceleration into the tandem accelerator.

2.2.2 Accelerator

The accelerator has two equi-potential Van De Graff sections, where the first section accelerates the negative ion using a positive potential difference towards the centre. Between the two stages a low-pressure argon stripper gas strips a number of electrons (creating various charge states) from the ions before the positive ion is accelerated in the second stage of the accelerator. The high energy ion beam generated from the accelerator is then switched by a single 30º deflection magnet to separate different charge states and neighboring isotopes. The beam is then focused and steered to the Faraday cup using einzel lens, and then enters the microprobe through a set of pre-slits [Fig. 2.1]. The pre-slits are used to stop the beam current from impinging on the object slits and to control the beam energy using 4-jaw apertures. The 4-jaw apertures and the object slits are made from good quality tantalum coated stainless steel plates to avoid the scattering effect. The object slits are mounted in a concrete block to ensure that it cannot move, and a Faraday cup and a beam viewer are positioned behind the object slits to align the beam.

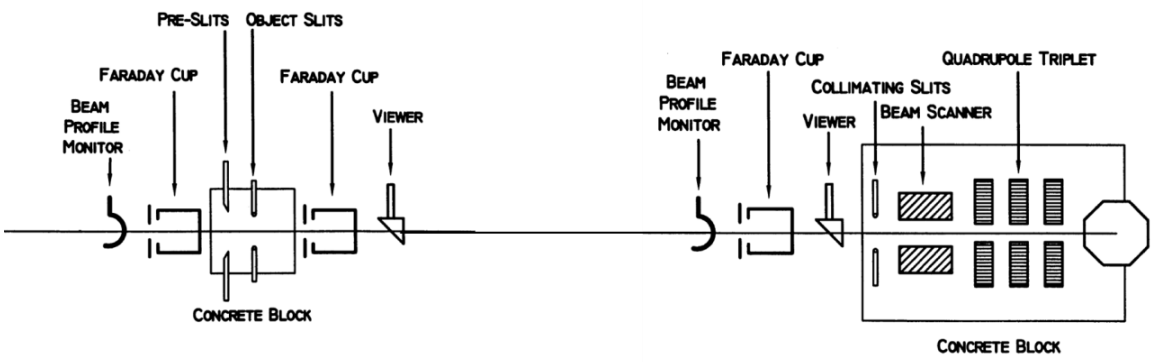

Figure 2.1 Schematic of heavy ion microprobe beam line [52]

2.2.3 Microprobe

The length from the object slits to the centre of the target chamber is 7 m, using the object and collimating slits to collimate the beam. The system located behind the collimating slits, including the beam scanning, quadruple triplet, and target chamber are attached to the concrete block to maintain the alignment of the ion beam. The target chamber is pumped down to produce a vacuum to prevent energy attenuation and scattering of the ion beam. Fig. 2.2 shows the heavy ion microprobe at ANSTO.

2.2.4 Target chamber

The target chamber is a 165 mm diameter octagonal cylinder with an x, y, and z manipulator to define the position of the sample. A surface barrier detector is connected to the target chamber for heavy ion Rutherford

Backscattering Spectrometry (RBS) and a video camera is used for ion beam focusing and sample alignment.

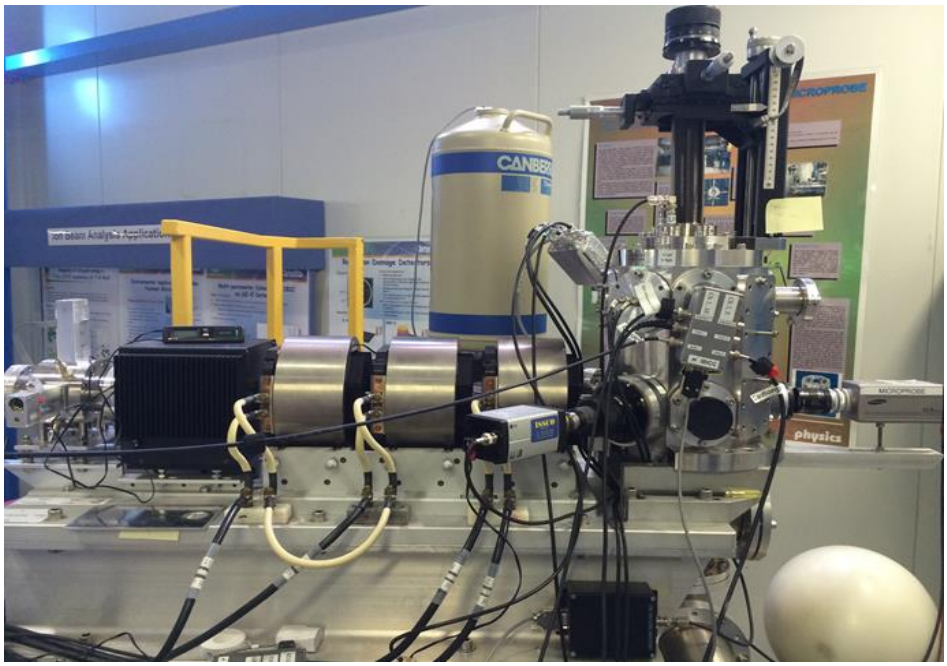

Figure 2.2 ANSTO heavy ion microprobe.

2.2.5 Data Acquisition System

The main components of the heavy ion microprobe were provided by the Oxford Microbeam, including the Data Acquisition (DAQ) system. It consists of software installed in Windows, a scanning amplifier, four 8192 channel Analogue to Digital Converters (ADCs), and a current integrator connected to the sample holder. The data acquisition system also controls the scanning ion beam.

The detector is mounted on an aluminum stick inside the vacuum chamber. The amount of energy deposited in the detector was measured using an AMPTEK A250 charge sensitive preamplifier and Canberra 2025 Shaping Amplifier with 1 μs shaping time. The signal was fed directly to a Canberra 8701 analog to the digital converter (ADC) of the data acquisition system. The IBICC signal corresponding to the beam position "X" and "Y" as well as the charge collection "E" for each event was processed into an event-by-event list mode file. The data was processed into IBICC median charge collection image maps for spatial correlation of the energy deposition of the scanned area.

A copper grid with a pitch of 25.4 μm was used to calibrate the dimensions and monitor the size of the spot. The beam was raster scanned across a 100 x 100 μm^2 area and the energy of each transmitted ion was measured using a surface barrier detector behind the grid. A median energy map of the copper grid can be produced by the list mode file. The energy deposition to the detector corresponded to those events traversing through the copper grid contributed to lower energy events due to energy loss of the incident particles. The sizes of all the images obtained in IBICC can be determined using the grid calibration and gain setting on the scan amplifier. By using the IBICC technique, the charge collection properties of the device can be studied under different biases and the angular dependence can also be investigated.

The energy was calibrated using a calibrated pulse generator previously calibrated to a 300 µm thick planar silicon PIN diode with 100% Charge Collection Efficiency (CCE), in response to an ion beam in the IBICC experiment.

Chapter 3

[1]Large Area Silicon Alpha Particle Detector

This chapter describes a new development of a large area silicon alpha particle spectroscopy detector with a surface that can be cleaned repeatedly for use in field conditions. The detector provides a good energy resolution for measuring contaminated soil and plant samples in a nuclear power plant accident or nuclear weapon testing zones. A detailed characterisation of the detector will be presented below.

3.1 Introduction

Accidents at nuclear power plants, such as those in Chernobyl and Fukushima, contaminated the surrounding areas with a wide variety of γ- and ß-emitting radioisotopes (e.g., ^{137}Cs or ^{131}I) as well as the nuclear fission products that emit α-particles. More than two decades after the Chernobyl

[1] This chapter has been published in Applied Radiation and Isotopes:
Linh T. Tran, Dale A. Prokopovich, Michael L.F. Lerch, Marco Petasecca, Rainer Siegele, Mark I. Reinhard, Vladimir Perevertaylo, Anatoly B. Rosenfeld (2014). Development of a large-area silicon α-particle detector. Applied Radiation and Isotopes. DOI: 10.1016/j.apradiso.2014.06.009. (Accepted, 14 May 2014)

accident, considerable amounts of plutonium, thorium, and uranium have been found in mushrooms grown in Poland, Spain, and the Ukraine [54]. After the Fukushima accident, α-emitting radioisotopes ^{238}U, ^{235}U, ^{239}Pu, ^{240}Pu, ^{241}Pu, ^{241}Am, ^{244}Cm were found in the surface soil [55].

Many kinds of silicon charged-particle detectors for alpha spectroscopy have been widely investigated, including diffused-junction, surface-barrier, and ion-implanted detectors [56]. The advantages that ion-implanted detectors have over conventional surface-barrier ones are higher stability and weaker dependence to their responses to the surrounding conditions [5]. To be useful in assessing the radioactivity of contaminated soils in the field, the detector must have a surface that can be cleaned repeatedly without the thin entrance window of the ion-implanted detector deteriorating. Aluminum sputtered onto the active area of the detector allows for some minimal cleaning of the detector surface without the energy resolution deteriorating, but it is recommended that the surface of such a detector be kept 3 mm above the soil sample to minimise the chance of any potential contact with the soil and, avoid damaging the surface of the detector [1]. But even when these detectors are used in the field under normal conditions, their surfaces can still be accidentally scoured by fine particles of soil.

The development of a large area ion implanted silicon radiation alpha particle spectroscopy mode detector for field and laboratory measurements of

contaminated soil and plant samples is presented in this chapter. The characterisation of a detector with a surface that can be cleaned repeatedly under field conditions was carried out.

The unique feature of these detectors is a protective layer of phosphorus silicate glass (PSG) which allows the active surface of the detector to be cleaned repeatedly with isopropyl alcohol. The PSG over layer is rugged enough to prevent damages to the detector from particles in soil samples that were investigated.

The uniformity of energy resolution over the active area of large-area detectors is extremely important [1, 7], so CMRP has developed large-area silicon detectors with different resistivity substrates, and where the electrical and spectral parameters were characterised to evaluate the fabrication process and demonstrate the performance of the detectors in terms of leakage current and uniform resolution. The charge collection characteristics were investigated using the ion beam induced charge (IBICC) collection technique.

3.2 Design and Technology of the Detector

Two large-area silicon α-particle detectors, each with the active area of 5 cm^2 and resistivity of either 0.95 or 4 kΩ.cm, were fabricated on a 400-µm-thick n-Si FZ, <100> silicon wafers. The subsequent implantation of 30-keV

boron ions created a p^+ region, while the implantation of 60-keV phosphorus ion produced an n^+ region. In addition to the traditional n^+ region on the rear side of the detector, another n^+ region was created around the perimeter to reduce its surface leakage current. The passivation silicon oxide layer (0.7 μm thick) was formed to separate the p^+ and n^+ regions. Aluminum contacts (1.1 μm thick) were deposited above the p^+ region on a 0.2-μm-thick layer of silicon oxide that had 20-μm-wide concentric octagonal windows etched in it to electrically connect the aluminum to the p^+ ion-implanted region. The aluminum layer then acts as an electrical contact and an optical light shield. A final over layer of phosphorus silicate glass (0.9-μm thick) was deposited for final passivation and robust physical protection. Fig. 3.1 shows a schematic cross section of the detector.

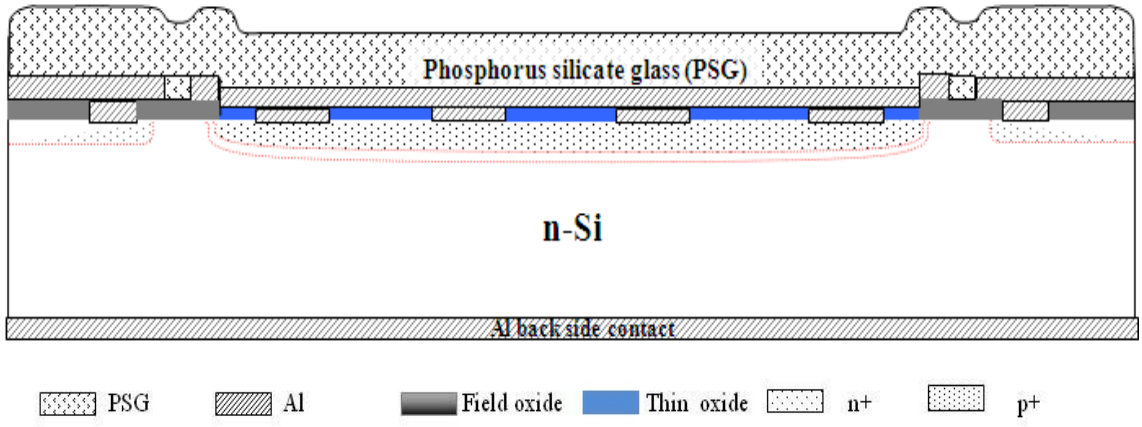

Figure 3.1. A cross sectional schematic of the large area silicon alpha particle detector.

3.3 Electrical Characterisation of the Detector

3.3.1 Methods

The electrical properties of the detectors were performed at the Australian Nuclear Science and Technology Organization (ANSTO) using *I-V* and *C-V* testing with Keithley 237 Source Measure Unit (SMU) and a Boonton 7200 Capacitance Bridge.

3.3.2 Results and Discussion

3.3.2.1 I-V characteristic

The leakage of the two large area silicon alpha particle detectors were recorded by ramping the bias from 0 to 60 V, and the results are shown in Fig. 3.2. The detectors had a low leakage current per unit area (< 4 nA/cm^2), and the detector with the higher resistivity (4 kΩ.cm) had a slightly higher leakage current than the 0.95-kΩ.cm detector. This was due to a combination of differences in the volume of the depletion region and the lifetime of the minority charge carriers.

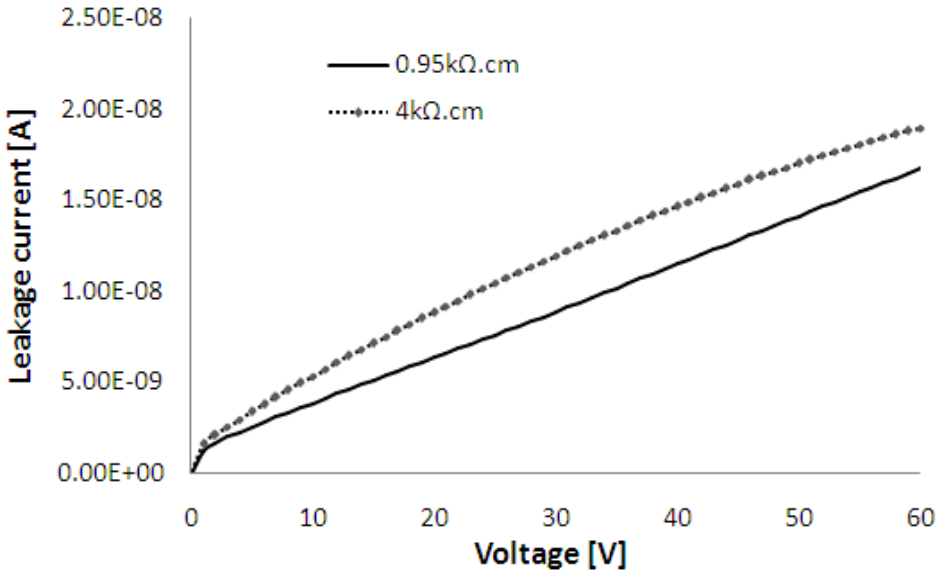

Figure 3.2 I-V characteristics of large area silicon alpha particle detectors with substrate resistivity 0.95 kΩ.cm and 4 kΩ.cm.

3.3.2.2 C-V characteristic

The C-V characteristic provides the width of the depletion layer at a given applied bias as well as the effective concentration of the carriers. For α-emitting isotopes, a 150- to 200-μm depletion region is needed to record the full energy deposited in the sensitive volume of the detector. A shorter depletion region would reduce the ß and γ contributions to the α spectra, which would increase the accuracy of measurements. By using lower-resistivity silicon it is possible to achieve a thinner depletion layer with a higher electric field. That would improve the charge collection and reduce the recombination of the charge carriers, but it would also increase the capacitance of the detector and, hence, the noise.

Fig. 3.3a and Fig 3.3b show that the capacitances were not saturated by the bias applied, which suggests that the detectors were not fully depleted before breakdown. The capacitance at 60-V bias was 400 pF for the lower-resistivity substrate and 180 pF for the higher-resistivity one. A lower-capacitance detector is usually more preferable because it has lower electronic noise in the charge sensitive preamplifier and, consequently, higher energy resolution.

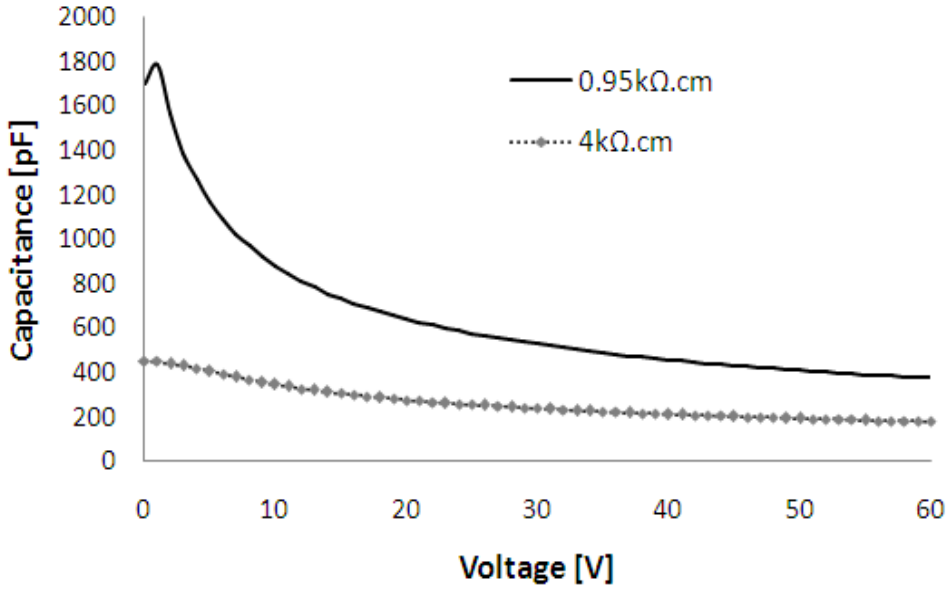

Figure 3.3(a). C-V characteristic of large area silicon alpha particle detectors with substrate resistivity 0.95 kΩ.cm and 4 kΩ.cm.

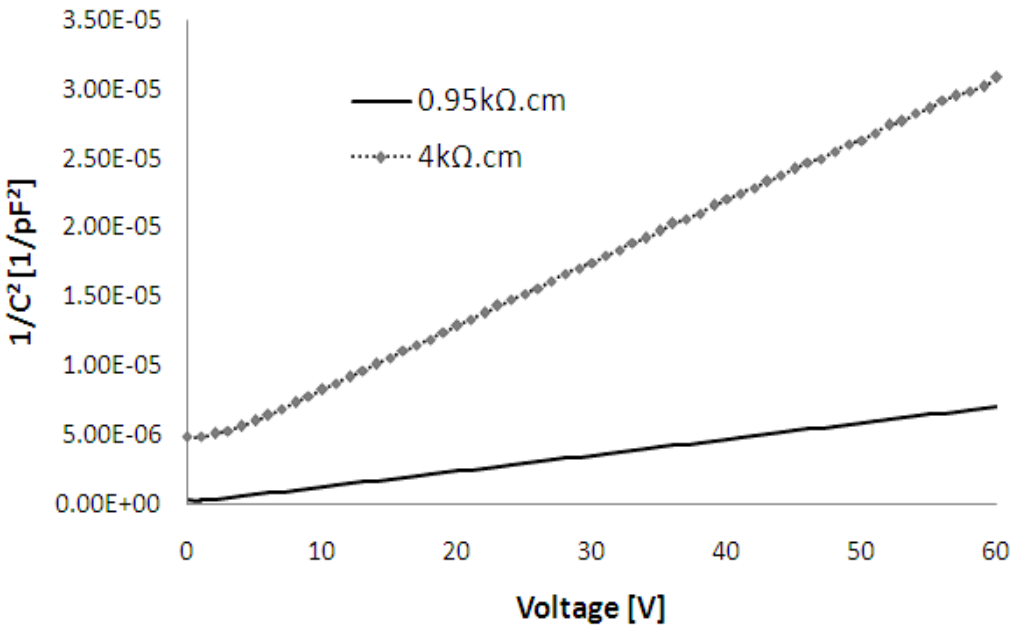

Figure 3.3(b). $1/C^2$ versus bias of large area silicon alpha particle detectors (0.95 kΩ.cm and 4 kΩ.cm). Linear behaviour without saturation suggests that the detectors were partially depleted.

3.4 Spectral Characterisation

3.4.1 Methods

Spectral characterisation was performed using an ^{241}Am α-emitting source. Alpha spectroscopy can provide detailed information about the energy loss in the over layers to determine their effective thickness and energy resolution of the silicon detectors [5].

The detector and an Amptek A250 charge sensitive preamplifier were located in a vacuum chamber to eliminate the absorption of incident α-

particles by air. The amplifier output was connected to an Ortec 571 shaping amplifier with a shaping time of 1 μs. The spectral response was recorded with an Amptek MCA 800A Multi Channel Analyzer (MCA). The energy calibration of the measurement system was performed with an Ortec 419 precision pulse generator. The pulse generator was energy-calibrated with a fully depleted Hamamatsu S3590-09 300-μm-thick windowless planar silicon PIN diode with 100% charge collection efficiency (CCE).

The calibration was performed using two α-sources, namely, ^{148}Gd (3.183 MeV) and ^{241}Am (5.486 MeV).

3.4.2 Results and Discussion

Figure 3.4 shows the energies of the ^{241}Am and ^{148}Gd α-particles deposited in the sensitive region of the detector. The absolute energy deposited in the active volume of the detector by the 3.183-MeV α-particles was 2.532 MeV, and the energy from the 5.48-MeV α-particles was 5.019 MeV. This loss of energy can be attributed to the thicknesses of the phosphorus silicate glass, and the SiO_2 and aluminum contact layers of the detector. Fig. 3.1 illustrates these over layers.

The intrinsic energy resolution of the detector was determined with a pulse generator that measured the electronic noise without the mounted detector. This noise was then subtracted from the noise of the system with

the detector mounted. The noise was calculated from the results of these experiments using the well-known formula:

$$FWHM_{\text{detector}} = \sqrt{(FWHM)^2_{overall} - (FWHM)^2_{electronics}} \tag{3.1}$$

The full width at half maximum (FWHM) of the electronics was 9 keV, the overall FWHM of the detector was 58 keV and 54 keV for substrate resistivities 0.95 and 4 kΩ.cm, respectively.

The low electronic noise did not affect the energy resolution of the detector very much, and accordingly, the energy resolution was 1.15% and 1.03% for the 0.95 kΩ.cm detector and the 4 kΩ.cm one, respectively.

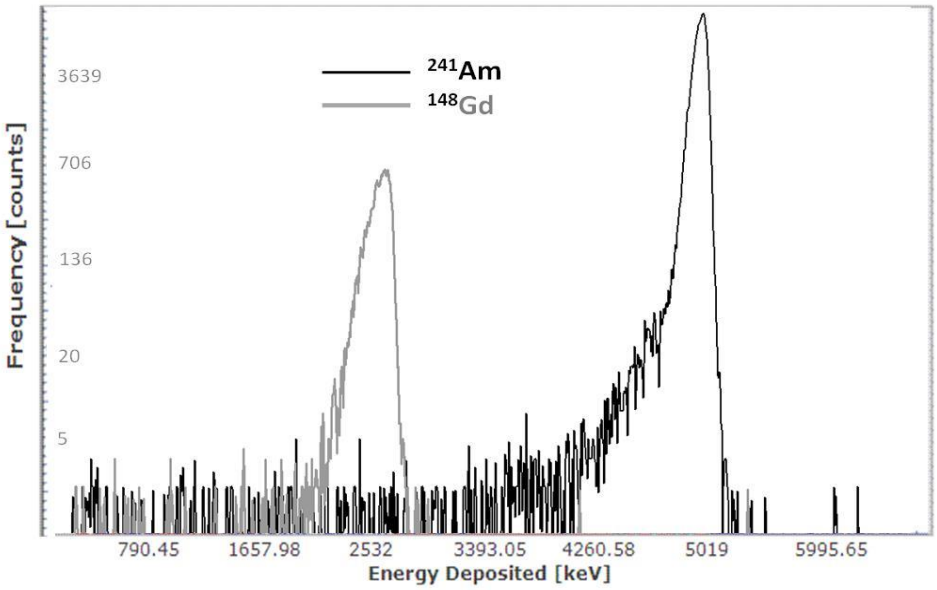

Figure 3.4 Alpha spectra of ^{241}Am and ^{148}Gd source for large area silicon detector

3.5 Radial Energy Resolution of Detectors

3.5.1 Methods

It is essential that the energy resolution for the large area detectors should be uniform over their entire 5-cm^2 active area. The uniformity of energy resolution was tested with a collimated α-particle beam from an ^{241}Am source with diameters of 1 mm, and which were arranged as shown in Fig. 3.5, with a 2mm gap between them.

3.5.2 Results and Discussion

Fig. 3.6 shows the energy resolutions along the diameters of the detector, and the varying resolutions across the sensitive area (1.2 ± 0.1)% and (1.0± 0.1)% for the 0.95-kΩ.cm and 4-kΩ.cm detectors, respectively. The energy resolution of the higher-resistivity detector was better, but both detectors were quite good in that respect.

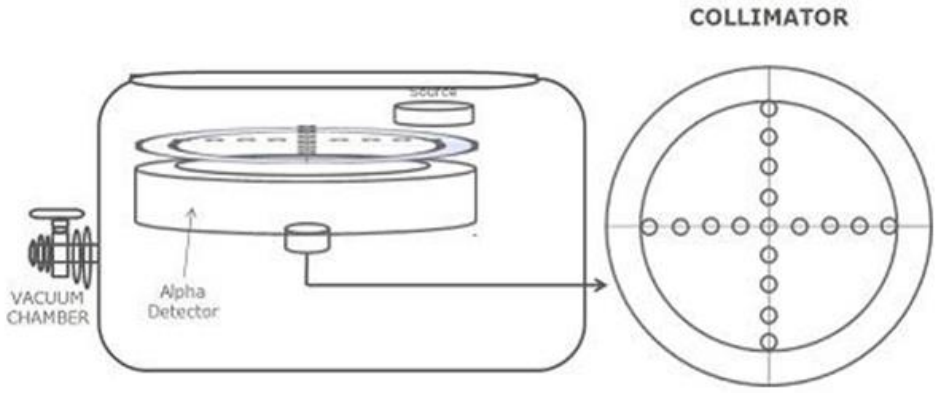

Figure 3.5 Schematic of experimental setup

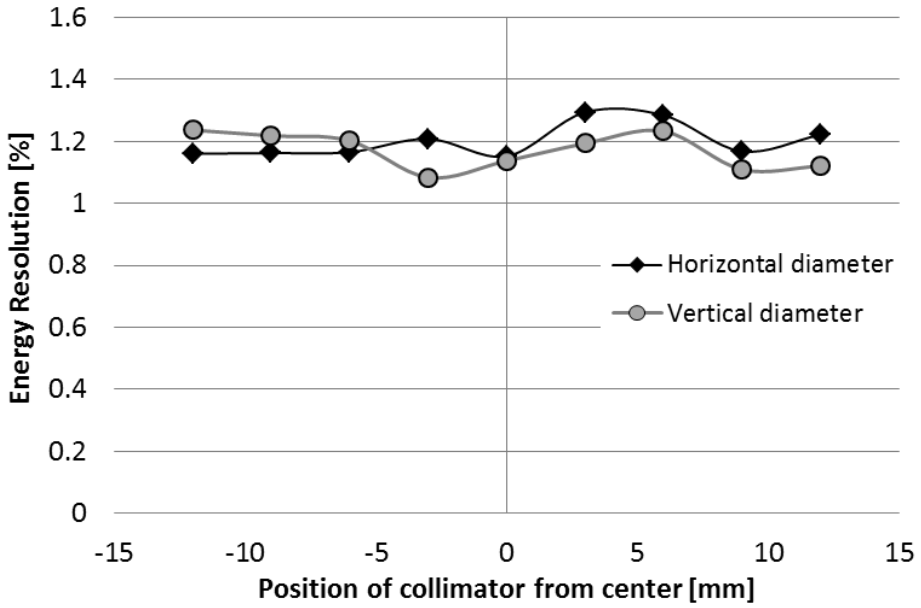

Figure 3.6 a) Energy resolution along the horizontal and vertical diameter of the detector with a substrate resistivity 0.95 kΩ.cm.

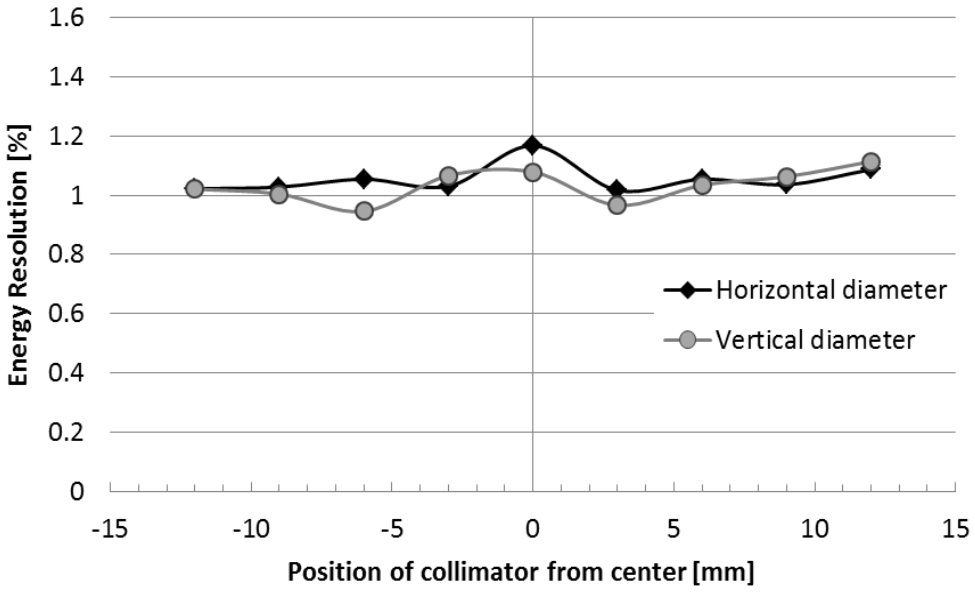

Figure 3.6 b) Energy resolution along the horizontal and vertical diameter of the detector with a substrate resistivity 4 kΩ.cm.

These results indicate that the large area detector with higher resistivity substrate (4 kΩ.cm) had better energy resolution than the lower resistivity detector (0.95 kΩ.cm), while the study revealed that the energy resolutions were uniform along the two diameters for both detectors.

3.6 Geant4 Simulations

3.6.1 Methods

The experimental MCA spectra were simulated using the Geant4 Monte Carlo Toolkit. The detector geometry was modelled with a cylindrical silicon sensitive volume having a radius of 1.25 cm and thickness of 400 μm. A 0.2-μm-thick silicon oxide over layer was located directly above the silicon detector volume. Three concentric octagonal aluminum volumes with different radii of 2.8, 6, and 9.5 mm were created in the layer of silicon oxide to contact the p^+ region above the silicon wafer (Fig. 3.1). Finally a 0.9-μm-thick phosphorus silicate glass cylindrical volume was placed over all the volumes. Each simulation was carried out for 1 x 10^6 normally incident α-particles and the energy deposition histograms were stored as Root files.

3.6.2 Results and Discussion

The results of the simulation showed that the energy deposition in the sensitive region of the detector was 5.148 MeV in response to 5.486-MeV

incident α-particles, and 2.698 MeV in response to 3.183-MeV ones. Therefore, the energy losses in all of the over layers (a trade-off for a cleanable detector design) were 338 keV at 5.486 MeV and 485 keV at 3.183 MeV. The experimental results were 461 keV at 5.486 MeV and 651 keV at 3.183 MeV which agreed with the simulation results within 2-5% uncertainty.

Moreover, the energy losses in the entrance window were simulated for an oblique incidence of α-particles with an energy of 5.5 MeV, and the results were compared with the results of experimental measurements.

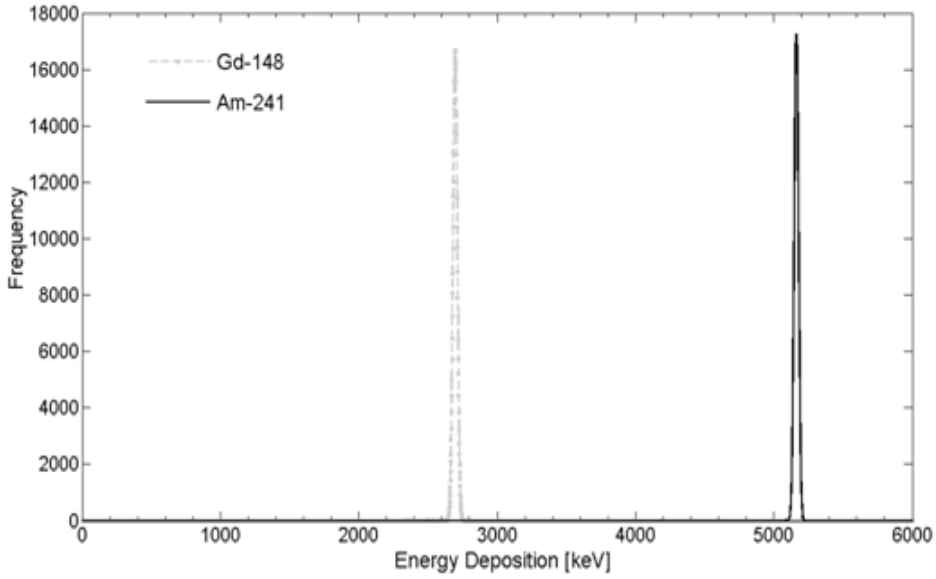

Figure 3.7 Simulated spectra for 3.183 MeV alpha and 5.486 MeV alpha of large area detector.

3.7 Charge collection studies - IBICC

3.7.1 Methods

The charge collection characteristics of the detector were measured using the ANSTO heavy ion microprobe described in chapter 2. The microprobe used 5.5 MeV He^{2+} ions focused into a narrow beam with a diameter of approximately 1 μm and detectors biased at 60 V.

3.7.2 Results and Discussion

Fig. 3.8 shows the spectral response and the IBICC median energy map of the 0.95-kΩ.cm detector for two different scanning positions on the active surface of the detector, where the energy peaked at about 5.1 MeV for all scanning positions on the detector. The median energy map (Section b in Fig. 3.8) shows the median amount of charge collected by the readout system, converted into energy in keV, as a function of the beam position. The yellow (/light grey) pixels correspond to the 5.1-MeV deposited energy in the sensitive volume of the detector. Section c of Fig. 3.8 shows six 1.4 mm^2 area scanning positions over the sensitive region of the large area detector. The median energy maps show very uniform charge collection over the whole area of the scanning beam, including the deposition of aluminum in the octagonal windows (position number 2).

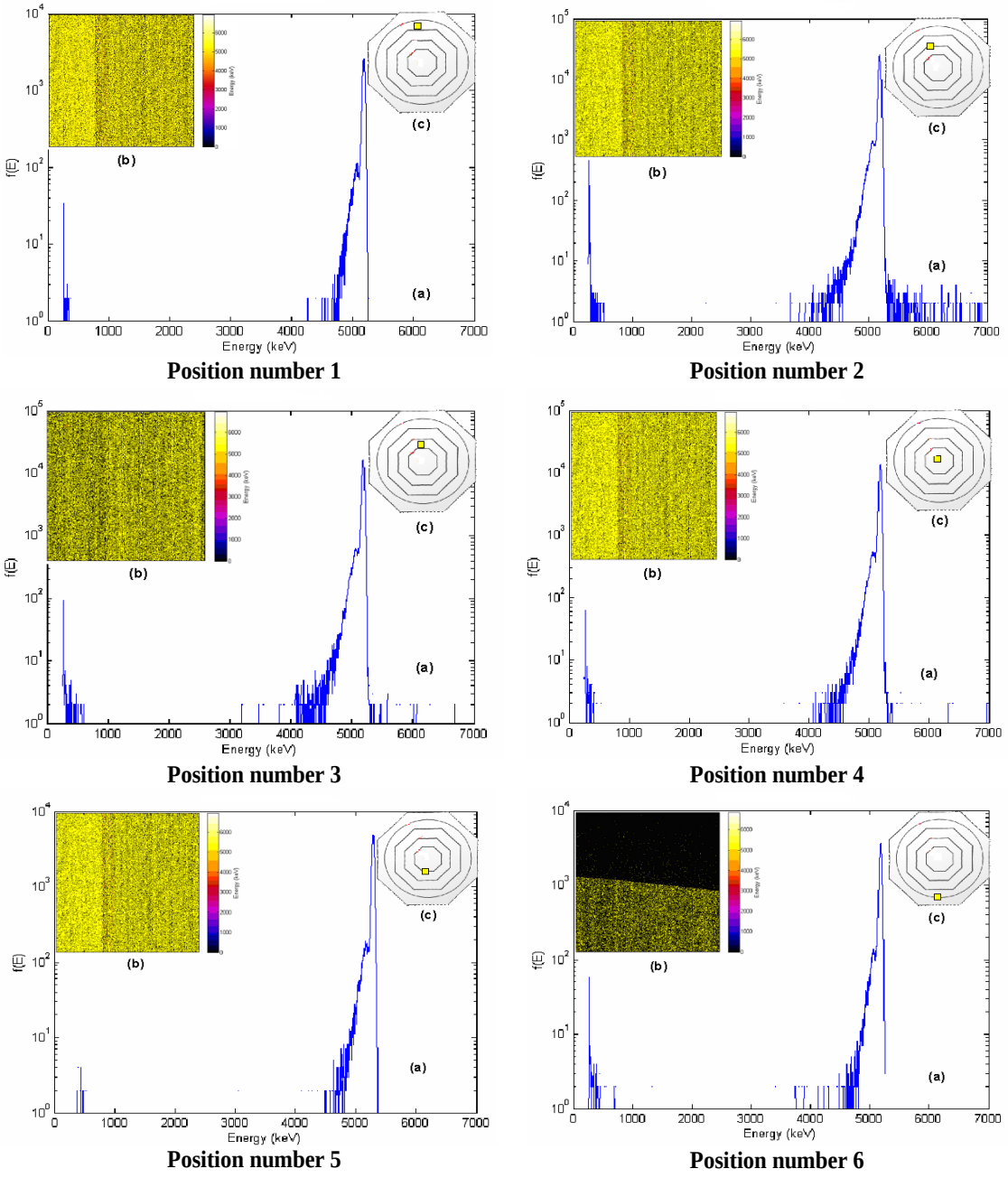

Figure 3.8 A charge collection study of the detector (0.95 kΩ.cm**)** for a 1.4 mm^2 area scanned at different positions across of active area from the detector with 5.5 MeV He^{2+} ions microbeam, (a) MCA spectrum, (b) An IBICC median energy map of the collected charge, (c) Scanning beam position of the detector active area

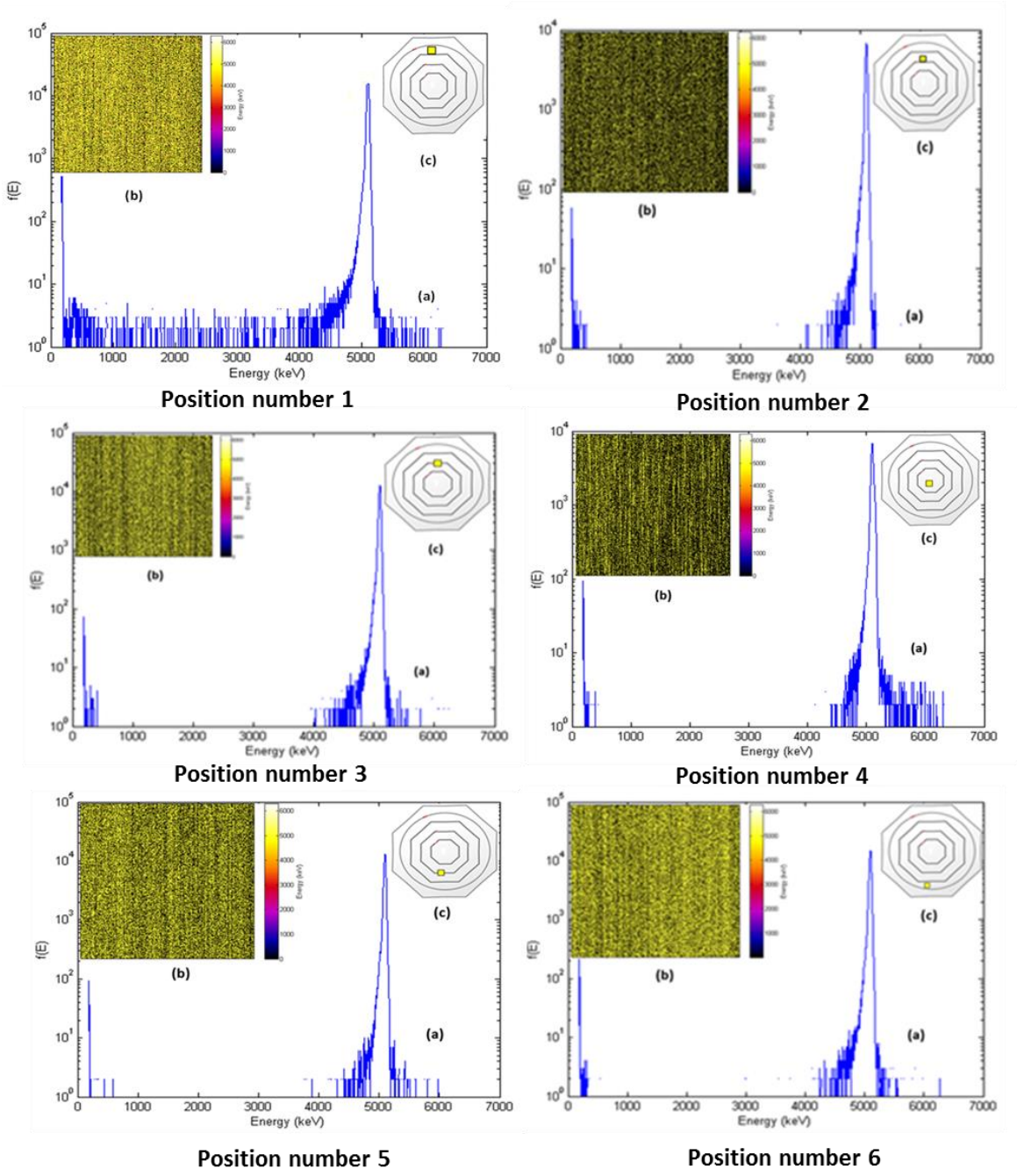

Figure 3.9 A charge collection study of the detector (4 kΩ.cm**)** for a 1.4 mm^2 area scanned at different scanning positions across an active area of the detector with 5.5 MeV He^{2+} ions microbeam, (a) MCA spectrum, (b) An IBICC median energy map of collected charge, and (c) position of the scanning beam on the detector active area.

Position number 6 was carried out on the edge of the detector to investigate the uniformity of charge collection of the detector near the edge. The results obtained show the sharp boundary of an active region of the detector without the charge collection outside the active region, and uniform charge collection inside the sensitive region (position number 6).

These results confirmed the importance of the octagonal concentric aluminum contacts to the p^+ region, which equalised the surface potential of the large active area of the detector.

Fig 3.9 shows the corresponding data for a 4 kΩ.cm detector. The median energy map shows uniform charge collection with the energy deposited in the sensitive area of the detector ranging from 5.098 MeV to 5.105 MeV.

3.8 Determining the Dead layer

3.8.1 Methods

Heavy charged particles such as α-particles, can lose a substantial amount of their energy in over layers (collectively known as a dead layer) before they reach the sensitive region of the detector.

In this study the effective thickness of the dead layer was determined by measuring the detector's response to 5.5 MeV He^{2+} ion microbeam at different angles of its incidence [5]. When the angle of incidence θ increased

the energy loss in the dead layers grew because the ion path there got longer.

3.8.2 Results and Discussion

Under normal incidence, the energy loss in the dead layer is given by the equation:

$$\Delta E_0 = \frac{dE_0}{dx} t_{dl} \tag{3.3}$$

where t_{dl} is the thickness of the dead layer. The measured energy at angle θ is described by the equation:

$$E(\theta) = E_0 - \frac{t_{PSG}}{\cos\theta}\frac{dE}{dx}\Big|_{PSG} - \frac{t_{Al}}{\cos\theta}\frac{dE}{dx}\Big|_{Al} - \frac{t_{SiO_2}}{\cos\theta}\frac{dE}{dx}\Big|_{SiO_2} \tag{3.4}$$

where E_o is the energy of the incident α-particles, while t_{PSG}, t_{Al}, and t_{SiO2} are the thickness of the phosphorus silicate glass, aluminum, and silicon oxide layers, respectively. The values $\frac{dE}{dx}\Big|_{PSG}, \frac{dE}{dx}\Big|_{Al}, and\ \frac{dE}{dx}\Big|_{SiO_2}$ are the stopping powers of the α-particles in phosphorus silicate glass, aluminum, and silicon oxide, respectively.

The difference between the measured energies of the 5.5 MeV He^{2+} ion microbeam at an arbitrary angle of incidence θ and at the normal incidence can be calculated as follows:

$$\Delta E(\theta) = \left(\frac{1}{\cos\theta} - 1\right)\left[t_{PSG}\left.\frac{dE}{dx}\right|_{PSG} + t_{Al}\left.\frac{dE}{dx}\right|_{Al} + t_{SiO_2}\left.\frac{dE}{dx}\right|_{SiO_2}\right] \quad (3.5)$$

Experimental measurements resulted in the following values of the energy differences obtained for $\Delta E(20°)$= 27 keV; $\Delta E(40°)$= 108 keV and $\Delta E(60°)$= 348 keV. These data were insufficient for determining the thicknesses t_{PSG}, t_{Al}, and t_{SiO2} separately, but the effective thicknesses of the over layers t_{PSG}, t_{Al}, and t_{SiO2} can be tested to determine when they agree with the thicknesses expected in the fabrication process. This can be done by substituting the effective thickness of the over layers in the equation (3.5) and comparing the results with the experimental data by assuming $\left.\frac{dE}{dx}\right|_{PSG}$ =149.6 keV/μm; $\left.\frac{dE}{dx}\right|_{Al}$ =153.7 keV/μm and $\left.\frac{dE}{dx}\right|_{SiO_2}$ =148.5 keV/μm (data for the 5.5 MeV Helium ions taken from SRIM [57]. Fig 3.10 shows $\Delta E(\theta)$ as a function of $(1/\cos\theta - 1)$ for the 0.95 kΩ.cm detector. As expected, the dependence is linear in the range of incidence angles from 0^0 to 60^0, and the $\Delta E(\theta)$ values for the angles 20°, 40°, and 60° agree with the experimental data.

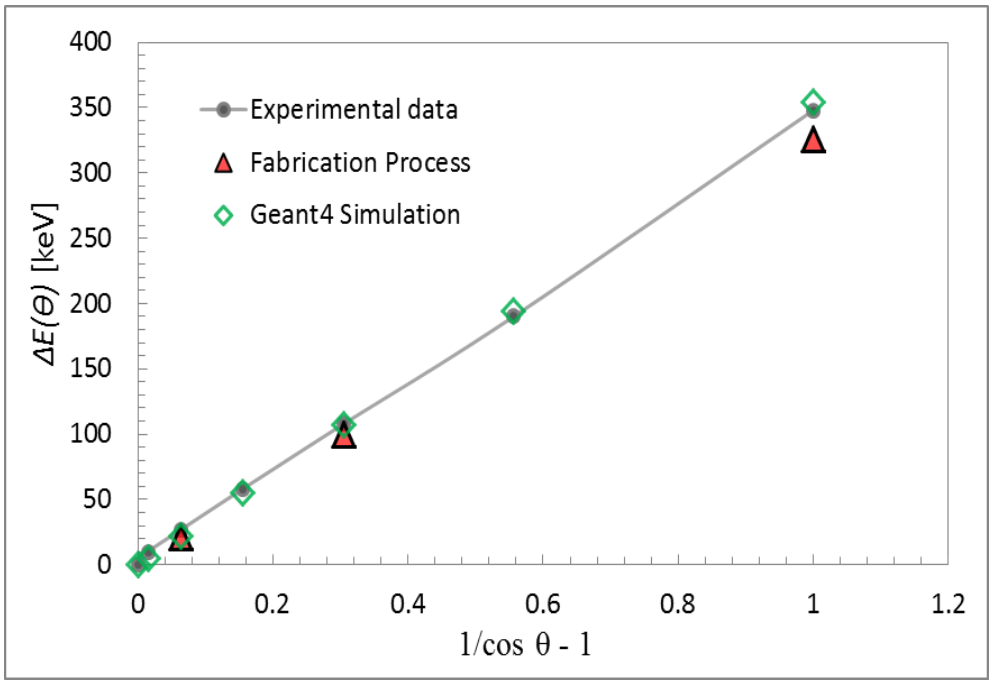

Figure 3.10 Plot of *E'* as a function of (1/cosθ-1) of detector (0.95kΩ.cm).

Similarly, a good agreement was observed for the detector with 4kΩ.cm resistivity, indeed the effective thickness of the dead layer was found to be 2.4±0.1 μm, assuming an average LET of He^{2+} ions for the three over layers.

Since the stopping power of α-particles depends on the energy, the use of a constant value of the stopping power for simulated energy loses in the over layers will result in an error which should increase with the increasing thickness of the overlayer, as seen in Fig. 3.10. That was confirmed by a Monte Carlo simulation, the results of which agreed with the experiment (Fig. 3.10). This means our knowledge of the thicknesses of the over layers and the technology of their fabrication appears to be correct.

3.9 Sediment Sample Measurement

3.9.1 Methods

The large area detector fabricated on the 4 kΩ.cm, which exhibited a better energy resolution, was used to measure the radioactivity of an sample of sediment from the Irish Sea [58]. The sample contained the following α-emitting isotopes: Ra^{226}, Th^{232}, Pb^{210}, Th^{228}, Th^{230}, U^{234}, U^{238} and Am^{241}. The measurements were carried out in a vacuum.

3.9.2 Results and Discussion

Fig. 3.11 shows the contributions from the isotopes Pb^{210}, Th^{232}, U^{238}, Th^{230}, Ra^{226}, Th^{228} and Am^{241} with the energy of α-emitting particles ranging from 3.5 MeV to 5.5 MeV. The solid line in the figure shows spectrum obtained with the large area silicon α-particle detector, while the dashed line depicts the expected peaks of various isotopes at typical energies of α-particles. The numbers on the top left of the figure are reference data from the IAEA certificate. The total specific radioactivity of the sample obtained with these measurements was approximately 380 Bq/kg, which was less than that in the certificate (497.2 bq/kg) because that data was obtained using a 4π ionisation chamber which could measure from all directions, whereas the measurement presented here was done under 2π geometry.

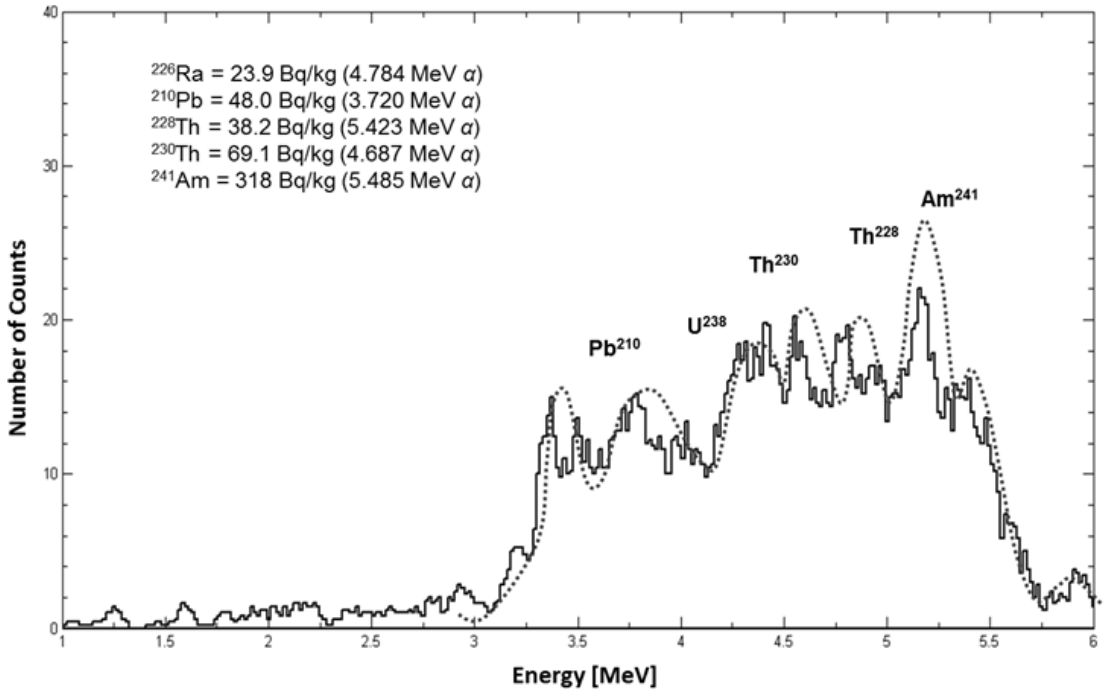

Figure 3.11 The alpha particle spectrum of a sediment sample measured by large area silicon alpha detector 4kΩ.cm.

3.10 Conclusions

In conclusion, large area silicon α-particle detectors for use in field were developed and fabricated from FZ *n*-Si with two different resistivities. The detectors have a moderate energy resolution of 1.15% (0.95kΩ.cm resistivity) and 1.03% (4kΩ.cm resistivity) for 5.48 MeV α-particle from ^{241}Am source. This lower resolution was a tradeoff for the possibility of cleaning the detector. Charge collection studies using IBICC have demonstrated very uniform charge collection across the active area of the detector, including the regions with windows in the oxide for aluminum contacts to the p^+ region.

Detectors with cleanable surfaces were developed as a part of portable spectroscopy setup for in-field environmental characterisation and radiation protection.

Chapter 4

[2]3D Radiation Detectors: Charge Collection Characterisation

This chapter presents the charge collection study of the ATLAS 3D detectors fabricated at SINTEF in response to a 5.5 MeV He^{2+} ion using the Ion Beam Induced Charge Collection (IBICC) technique. The effect of fast neutron and gamma radiation on the detector's charge collection efficiency was also investigated. 3D active edge silicon detector technology could be extremely promising technique for the fabrication of SOI microdosimeters with 3D Sensitive Volumes (SVs), and will therefore be investigated.

4.1 Introduction

3D silicon sensors were originally been designed to upgrade the pixel system in the ATLAS (A Toroidal Large hadron collider ApparatuS) experiment. SINTEF MinaLab has been representing a part of the ATLAS

[2] This chapter has been published in Nuclear Science IEEE Transactions:
Linh T. Tran, Dale A. Prokopovich, Marco Petasecca, Michael L. F. Lerch, Angela Kok, Anand Summanwar, Cinzia Da Via, Mark I. Reinhard, Kari Schjølberg-Henriksenand (2014). *3D Radiation Detectors: Charge Collection Characterisation and Applicability of Technology for Microdosimetry.* Nuclear Science, IEEE Transactions on PP (99), 1.

3D collaboration, which successfully explored and fabricated the active edge full 3D silicon sensors on a small to medium production scale [38]. CMRP proposed to apply micro-machining and the 3D technology available at SINTEF to a microdosimetry project that involves developing new 3D SVs silicon-based "mushroom" microdosimeter for radiation therapy and radiation protection applications in space, avionics, and terrestrial applications. The proposed silicon microdosimeter will be exposed to a harsh mixed radiation environment that can affect the charge collection efficiency in the 3D SVs and result in an error in measured dose equivalent. This thesis chapter presents a study of charge collection in the 3D Si detectors, which currently utilises the technology aimed at the fabrication of mushroom SVs. The effect of fast neutron and gamma radiation on the 3D detector charge collection efficiency was used to quantify the radiation sensitivity of this design.

A prior study of the radiation hardness of similar 3D detectors produced at the Stanford Nanofabrication Facility was performed using an infrared (IR) laser to inject the equivalent of approximately 2 minimum ionizing particles. These experiments demonstrated charge collection efficiencies as high as 66% after the detectors were irradiated with neutrons up to a fluence of 8.8 x 10^{15} n_{eq}/cm^2, for a 56 µm inter-electrode [59]. The proposed IBICC technique has a much higher spatial resolution than the InfraRed (IR) laser technique and will provide an accurate and fast 2D charge collection

efficiency map in the 3D SINTEF detectors with a spatial resolution approximately 1 μm. IBICC gives the advantage of being able to observe details associated with radiation damage which were not observed earlier with IR laser, and it can also tailor the depth and energy of the deposition event.

4.2 Material and Methods

4.2.1 Test structure of SINTEF 3D detectors

The SINTEF 3D detectors were fabricated on 10 kΩ.cm p-Si wafer with 1 mm x 1mm dimensions and a thickness of 285 μm, as a part of the ATLAS collaboration. Fig. 6.1 shows the layout of the metal contacts and passivation openings of the test 3D detector. Five detectors with different inter-electrode distances between the centres of n^+ and neighbouring p^+ electrodes of 3D detectors were investigated. Each pixel consisted of one 3D n^+-type electrode (1E configuration), two n^+-type electrodes (2E configuration), three n^+-type electrodes (3E), four n^+-type electrodes (4E) and five n^+-type electrodes (5E). The inter-electrode distances corresponding to each type of detectors 1E, 2E, 3E, 4E and 5E were 200 μm, 104 μm, 70 μm, 56 μm and 46 μm, respectively. Each group of n^+ electrodes had its own bond pad, while the p^+ electrodes and an active p^+ edge were connected in parallel.

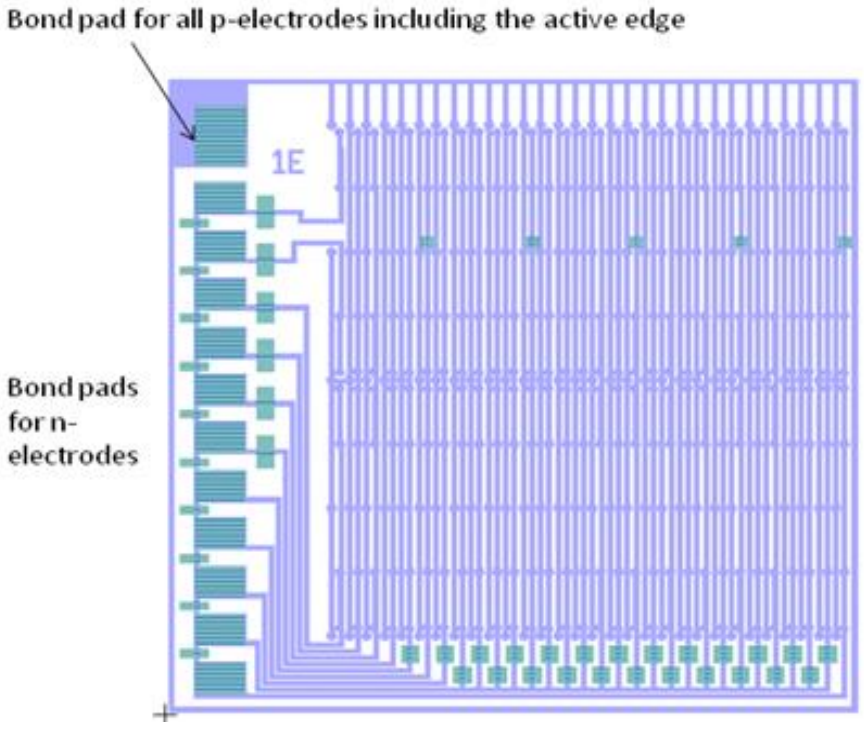

Figure 4.1 Layout of the of the test diode

4.2.2 Electrical Characterisation

The electrical properties of each detector were determined using current-voltage (I-V) and capacitance-voltage (C-V) measurements with a Keithley 237 high voltage source measure unit and a Botoon 7200 capacitance bridge. All the measurements were carried out under a controlled ambient room temperature of 20°C.

4.2.3 Charge Collection Study

The charge collection efficiency for the different types of 3D detectors was investigated using the IBICC technique on the Heavy Ion Microprobe at ANSTO. The IBICC measurements utilised a microbeam of 5.5 MeV He^{2+} ions focused to a diameter of approximately 1 µm, which was then raster scanned over the surface of the sample. The amount of energy deposited in the 3D detectors at different biases was measured using the electronic system described in chapter 2. Finally, 2D median charge collection image maps of every type of 3D detectors were produced.

The energy calibration was done using the same method presented in the previous chapter of this thesis [chapter 2]. It was performed using a calibrated pulse generator which was calibrated to a windowless planar silicon PIN diode with 100% Charge Collection Efficiency (CCE), in response to an ^{241}Am source.

4.2.4 Radiation Damage Study

The effect of 10 MRad gamma radiation and 6.2 x 10^{10} n_{eq}/cm^2 fast neutrons on the charge collection efficiency of 3D detectors was investigated using the GAmma Technology Research Irradiator (GATRI) at ANSTO and 10 Ci Am-Be source at Commonwealth Scientific and Industrial Research Organisation *(*CSIRO) research facilities.

4.3 Results and Discussion

4.3.1 Electrical Characterisation

The 3D detectors with a longer inter-electrode distance (1E, 2E and 3E type) have a reverse current of less than 80 nA at 100 V, whereas the detectors with a shorter inter-electrode distance (4E and 5E) have a higher reverse current (about 300 nA at 80 V). Fig. 4.2 illustrates the I-V characteristic of the 3D detectors type 1E, 2E, 3E, 4E and 5E. The graph of capacitance at 60 V bias versus inter-electrode distance (Fig. 4.3) shows that a shorter inter-electrode distance for the same size of the test diode raised the capacitance quite significantly.

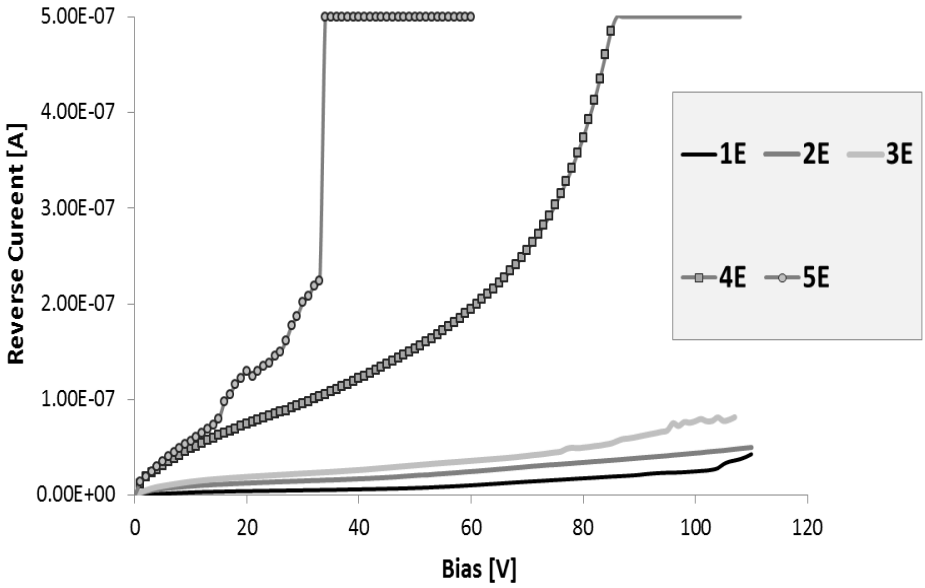

Figure 4.2 I-V characteristic of the 3D detectors type 1E, 2E, 3E, 4E and 5E.

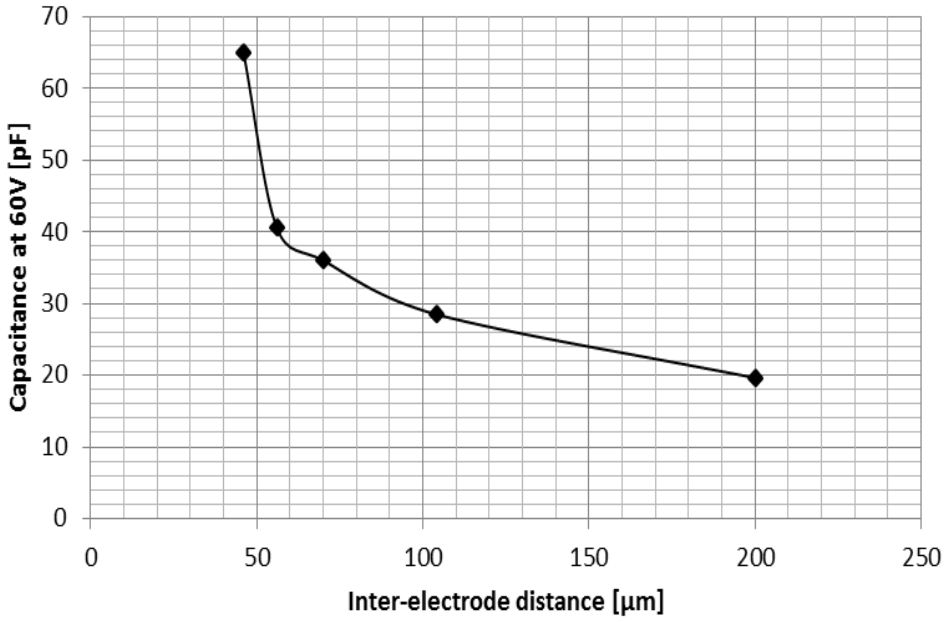

Figure 4.3 Capacitance of different types of 3D detectors at 60V.

4.3.2 Charge Collection Study

The 3D detector was scanned with 5.5 MeV He^{2+} ions microbeam at different locations. Fig. 4.4a, b shows the scanned area and Multichannel Analyzer (MCA) spectra in 3D detector type 1E with a 200 µm inter electrode distance for 0 V and 100 V bias, respectively. All the n^+ electrodes were connected in parallel.

Fig 4.4c, d shows the median energy maps of the charge collected for this scanned area under the same conditions. Even under 0 V bias, the 3D detector with the largest inter-electrode distance has reasonably diffused the charge collection with almost 100% near n^+ electrodes. For 100 V bias, a full

charge collection occurred through all the scanned area, limited by the active p^+ edge of the 3D detector.

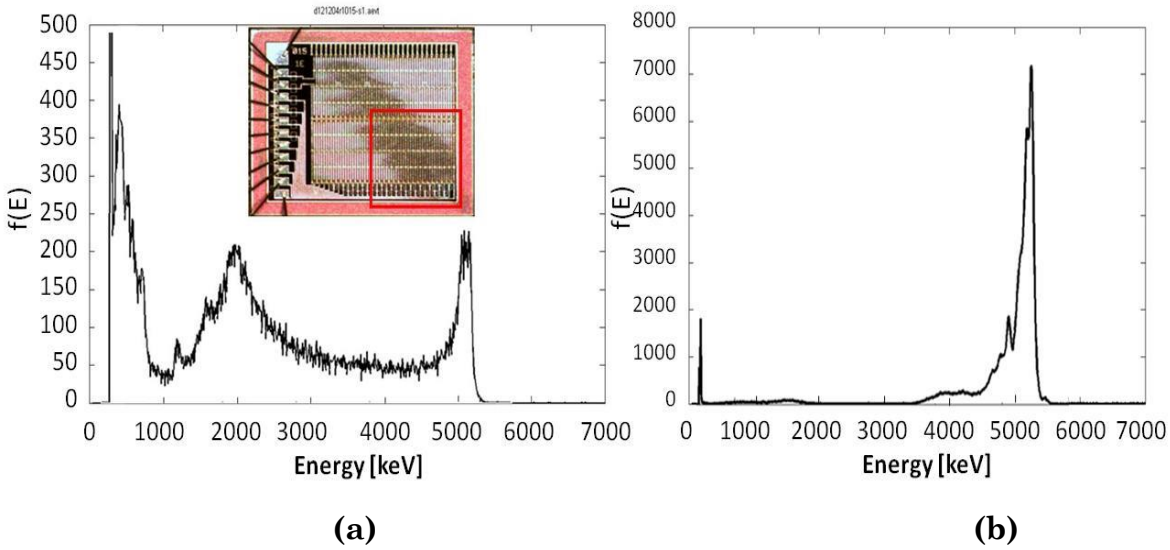

Figure 4.4 Scanned area of 1E 3D detector and MCA spectrum at (a) 0 V bias and (b) 100 V bias.

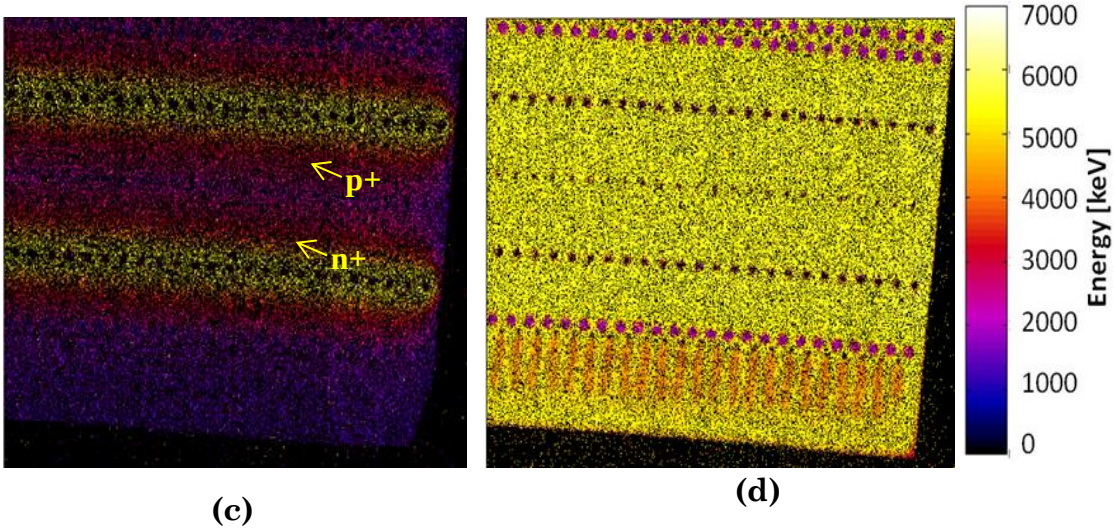

Figure 4.4 An IBICC median energy map of the response of 3D detector (1E type) to the microbeam of 5.5 MeV He^{2+} (c) at 0 V and (d) at 100 V.

This was also reflected in the MCA spectrum in Fig 4.4b. The small low energy satellite peak was due to the loss of energy by the He^{2+} ions travelling through the Al tracks connecting the n^+ and p^+ electrodes, and above the p^+ active edge on the periphery of the 3D detector.

At 100 V bias, the 3D detector has much better energy resolution than for 0 V biases, as can be seen in the fine structure of two small peaks on the left side of the main peak. This result was due to two different thicknesses of over layers, including the metallisation and oxide on p^+ columns at the bottom of the chip and outside the p^+ columns (Fig. 4.5b, c). Fig. 4.5b shows an almost fully depleted region on the edge of the detector and the performance of the edgeless detector.

A uniform full charge collection between n^+ and p^+ electrodes occurred at 100 V, as shown in Fig 4.5d, while Figs. 4.5a-d were obtained using the energy windows corresponding to the energy peaks presented on an MCA spectrum.

Fig. 4.6 shows the charge collection for the same scan size in the upper left corner of the 1E 3D detector at the same bias conditions. Bonding wires can be clearly seen on both charge collection images. A magnified view of the median energy map allows one to confirm the full depletion through the 3D detector volume and the excellent performance of the active edge. The regions with a deficit of deposited energy from He^{2+} ions were seen under the

Al contact pads, and the Al deposited above an active p^+ edge was due to the loss of energy in Al contacts (Fig. 4.6b).

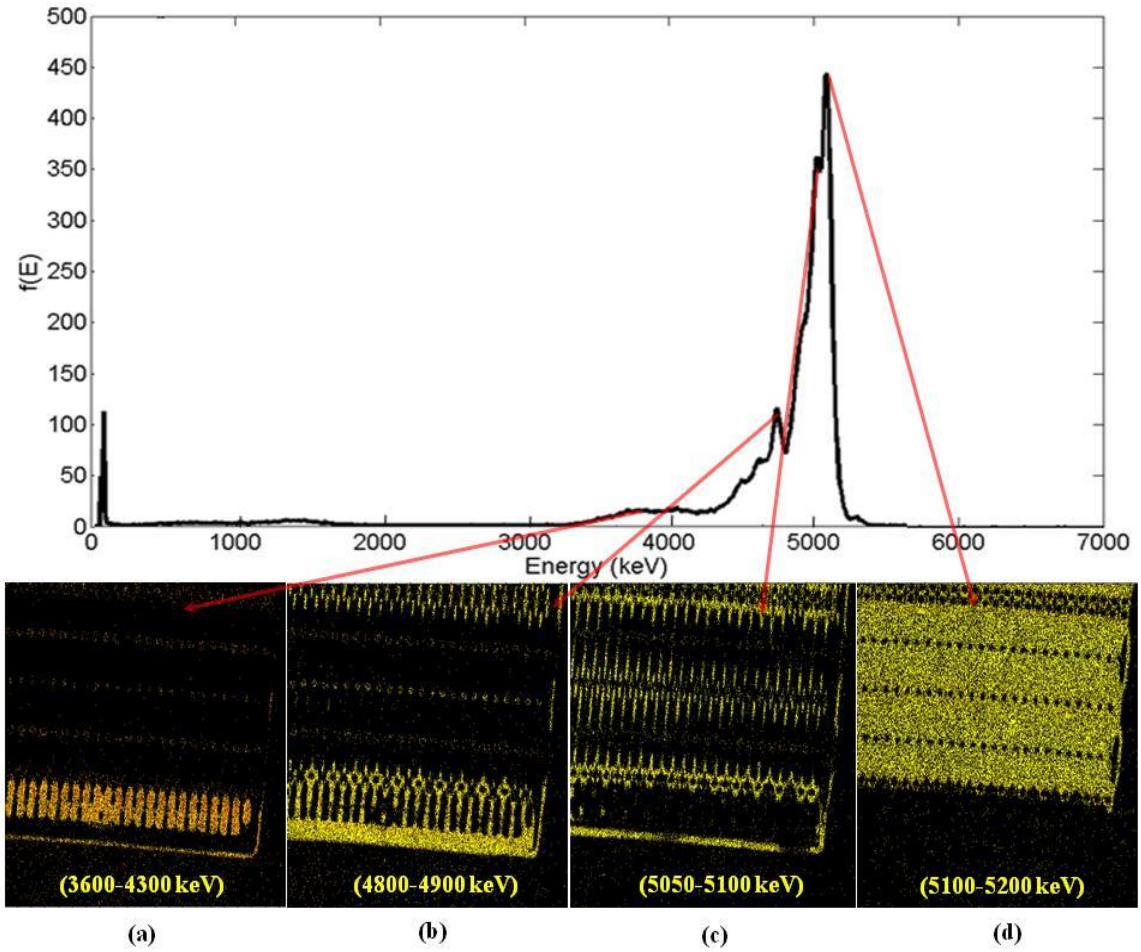

Figure 4.5 Median energy maps in different energy ranges of charge collection of 1E detector at bias 100 V.

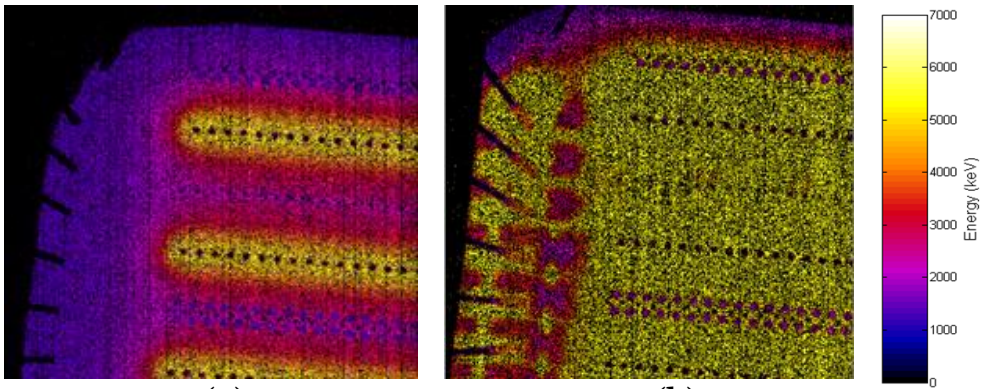

Figure 4.6 An IBICC median energy map of the response of the 3D detector1E at the top left corner to the microbeam of 5.5 MeV He^{2+} (a) at 0 V and (b) at 100 V.

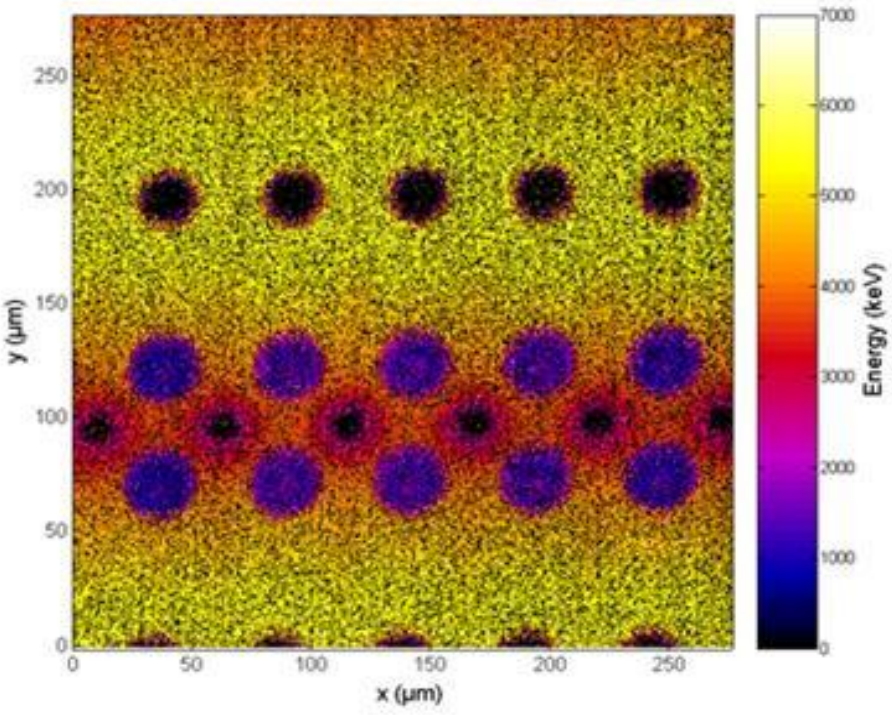

Figure 4.7 An IBICC enlarge median energy map of 2E detector in response to 5.5 MeV He^{2+} at 0 V.

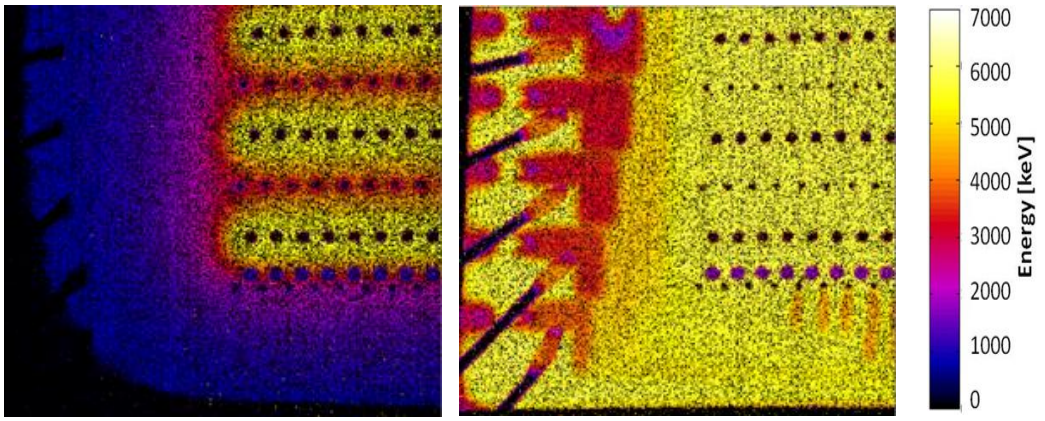

(a) **(b)**

Figure 4.8 An IBICC median energy map of the response of detector 2E at the bottom left side to the microbeam of 5.5MeV He^{2+} (a) at 0 V and (b) at 100 V.

Fig. 4.7 shows an enlarged median energy map of n^+ and p^+ electrodes in the middle of the chip for type 2E with an inter-electrode distance 104 µm. While both p^+ and n^+ 3D electrodes were produced from the same diameter, their effective diameters in terms of charge collection differed, which was also in the 1E detector. The effective diameter of the n^+ column with a zero charge collection (black color, Fig 4.7) was about 22 µm, while the p^+ column had an effective diameter of 13 µm at zero bias. Like the 3D detector type 1E, an excellent charge collection for the 2E detector occurred at 100 V bias (Fig. 4.8b). Fig. 4.8 b shows details of a wire compression that occurred during wire bonding, where part of the bonding wires became thinner due to compression so that the alpha particles lost less energy in these regions. Full

depletion between the wire contacts compression regions can be seen, and under full depletion at 100 V, the bottom edge was fully depleted.

Fig. 4.9 shows the charge collection in one part of the 3D detector type 3E in response to 5.5 MeV He^{2+} ions. Here the charge collection changed with bias, and that at 0 V, detector type 3E with an inter-electrode distance of 70 µm had lower energy events near the bottom edge of the chip (Fig. 4.9a), but as increasing bias was applied to the detector, the Al contacts connecting the n^+ columns to the bonding pads became visible with lower charge collection (red region at the edge of the chip, Fig. 4.9b, c). At 90 V, the detector was fully depleted near the edge and the slightly lower charge collection along the Al leads near the edge was due to energy loss by alpha particles in Al metallization (Fig. 4.9f). The IBICC images demonstrated a degraded charge collection on the border of p^+.

Fig. 4.10 shows a median energy charge collection image for the 3D detector type 5E which had shortest inter-electrode distance of 46 µm. Full charge collection through the 3D detector volume occurred at a bias as low as 5 V. The effective diameters of the n^+ and p^+ columns (black region) were approximately 22 µm and 13 µm respectively, with a clear diffusion charge collection from inside the p^+ 3D electrodes (Fig. 4.10a), just like the other 3D diodes. The difference in the effective diameters of p^+ and n^+ electrodes observed in all 3D diodes from this batch was possibly caused by the

difference in the radial distribution of resistivity of the filled polysilicon doped with phosphorous and boron, and also the physical size of the electrodes due to variations in the fabrication process.

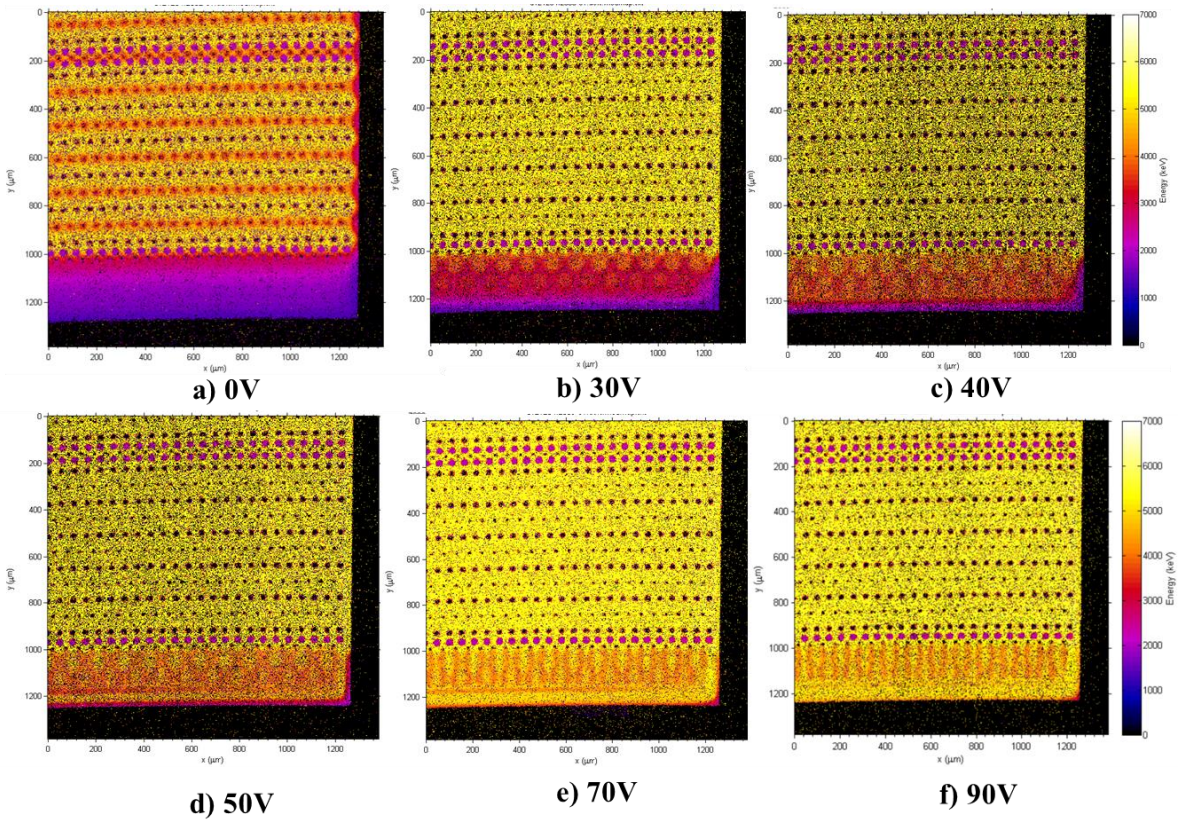

Figure 4.9 An IBICC median energy map comparison of 3D detector type 3E in response to 5.5 MeV He^{2+} at different biases a) 0 V, b) 30 V, c) 40 V, d) 50 V, e) 70 V and f) 90 V.

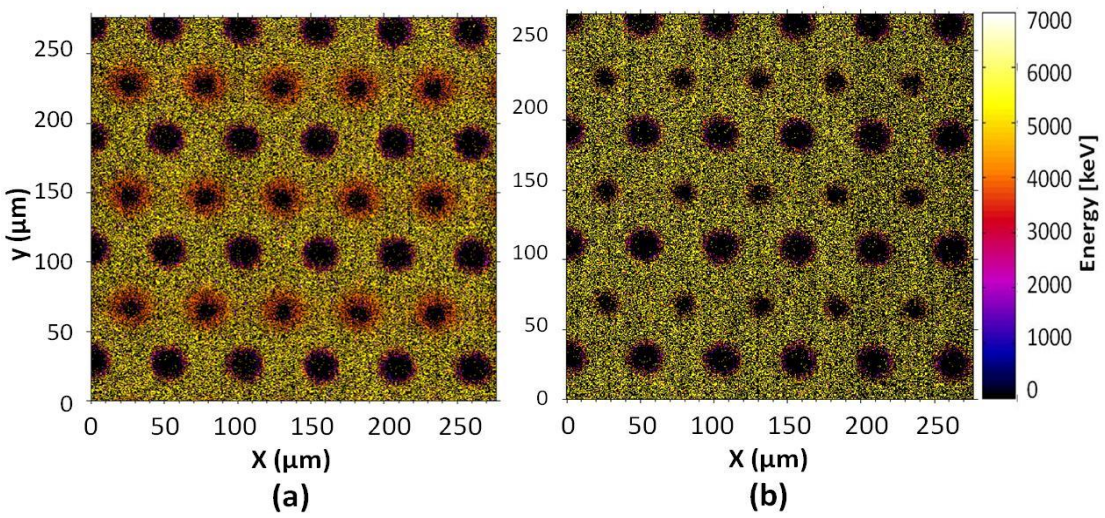

Figure 4.10 An IBICC enlarge median energy map of 5E detector in response to 5.5 MeV He^{2+} at a) 0 V and b) 5 V.

Fig. 4.11 shows an MCA spectrum and a median energy map for the energy window corresponding to the major peak 5100-5300 keV and representing 100% of the charge collection. It was demonstrating the same diameter of n^+ and p^+ electrodes and supporting explanation of diffused charge collection from inside the p^+ electrode. Based on these results, it is suggested that the resistivity of p^+ columns must not be as low as the n^+ columns.

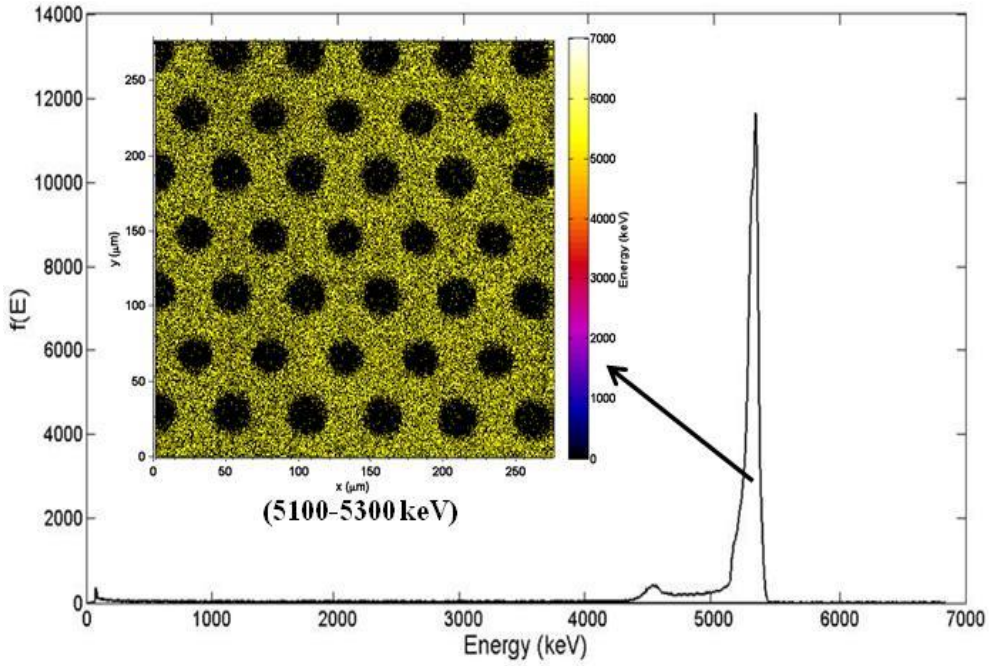

Figure 4.11 An IBICC MCA spectrum and median energy map of the charge collection of 5E type detector at bias 5 V for energy window (5100-5300 keV).

4.3.3 Radiation Damage Study

An I-V characterisation of the 3D detectors before and after irradiation was carried out. Fig. 4.11 shows the leakage current in the 3D detectors type 1E, 3E, and 5E before and after gamma irradiation. The leakage current of detector type 1E increased from 20 nA to approximately 180 nA at 80 V.

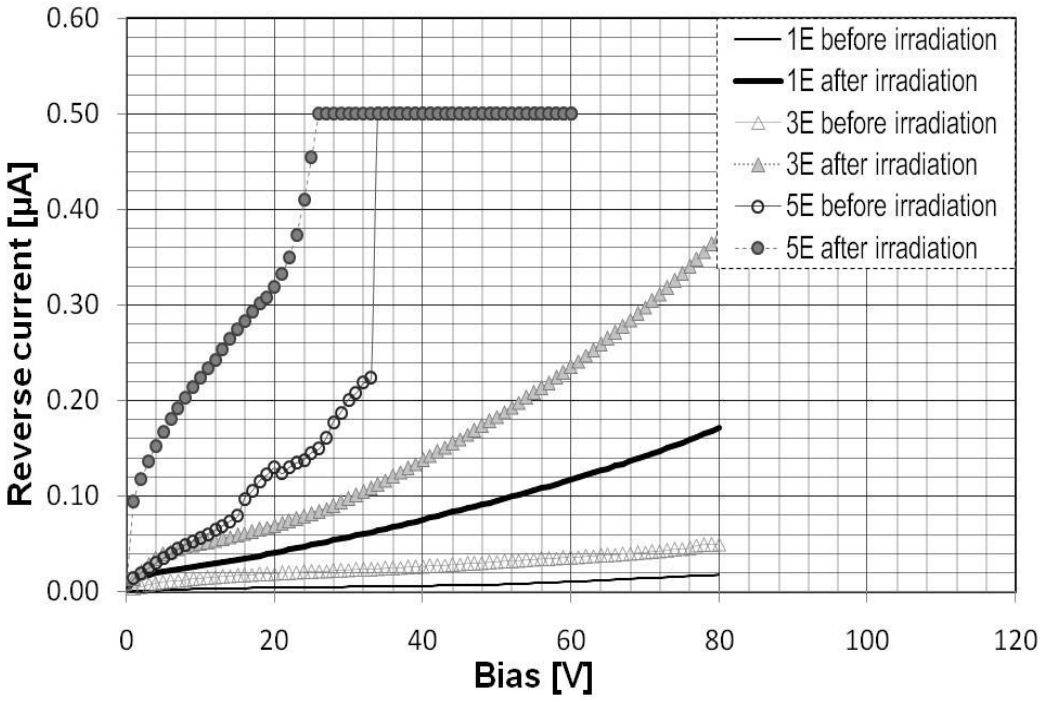

Figure 4.12 A comparison of I-V characteristics for 3D detectors type 1E, 3E, and 5E before and after 10 MRad gamma ^{60}Co irradiation.

There was a slight change in the leakage current of the neutron irradiated samples that agreed with the low neutron fluence. A previous study of the charge collection efficiency of 3D detectors showed that the samples with longer inter-electrode distances were less radiation hard than the shorter inter-electrode samples [59]. The IBICC results provided detailed effects of the charge collection after a small fluence of 6.2 x 10^{10} n_{eq}/cm^2 of fast neutrons and 10 MRad ^{60}Co gamma irradiation. Two gamma irradiated (3E, 5E) and three neutron irradiated (1E, 3E and 5E) 3D detectors were chosen for investigation by the IBICC technique.

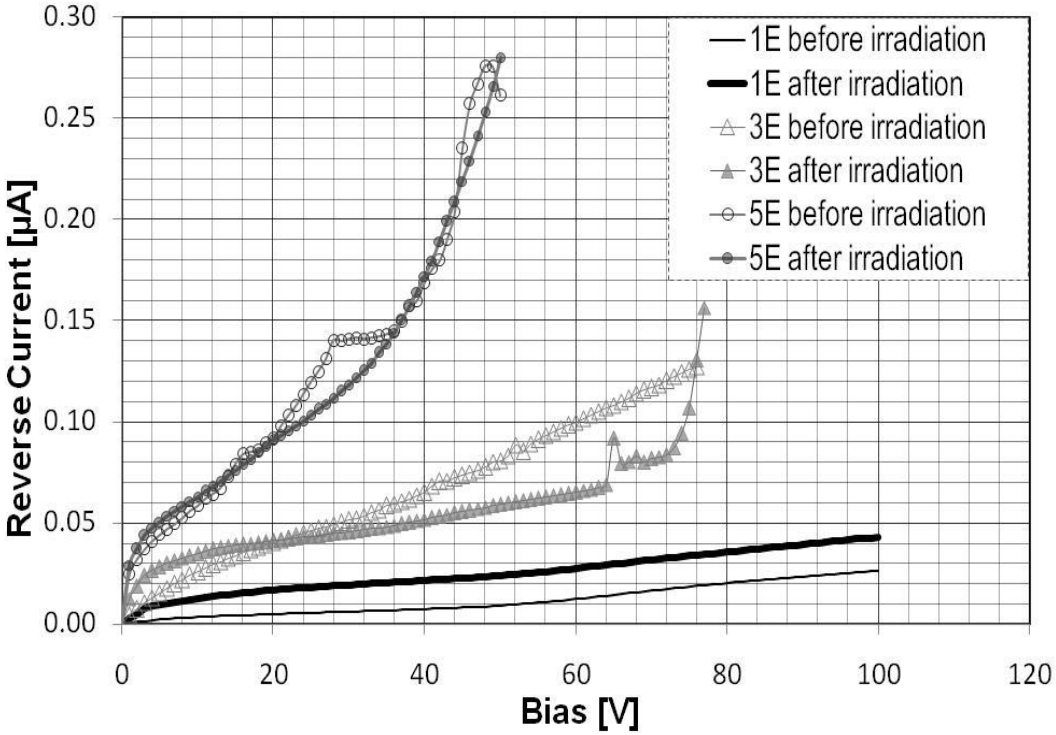

Figure 4.13 A comparison of I-V characteristics for 3D detectors type 1E, 3E, 5E before and after neutron irradiation with fluence of 6.2 x 10^{10} n_{eq}/cm^2.

Fig. 4.14 shows a comparison of the MCA spectra and the median energy maps with 1 x scan size for the 3D detectors type 3E at 60 V bias before and after gamma irradiation, and indicated that a slightly lower energy charge was collected between and along the p^+ columns due to an accumulation of positive charges in the SiO_2 layer, which is a changing electrical field distribution near the surface of the P-type silicon-SiO_2 that effected the charge collection produced by short range He^{2+} ions. This build- up charge also led to a substantial increase of the reverse current in this diode, as indicated in Fig. 4.12.

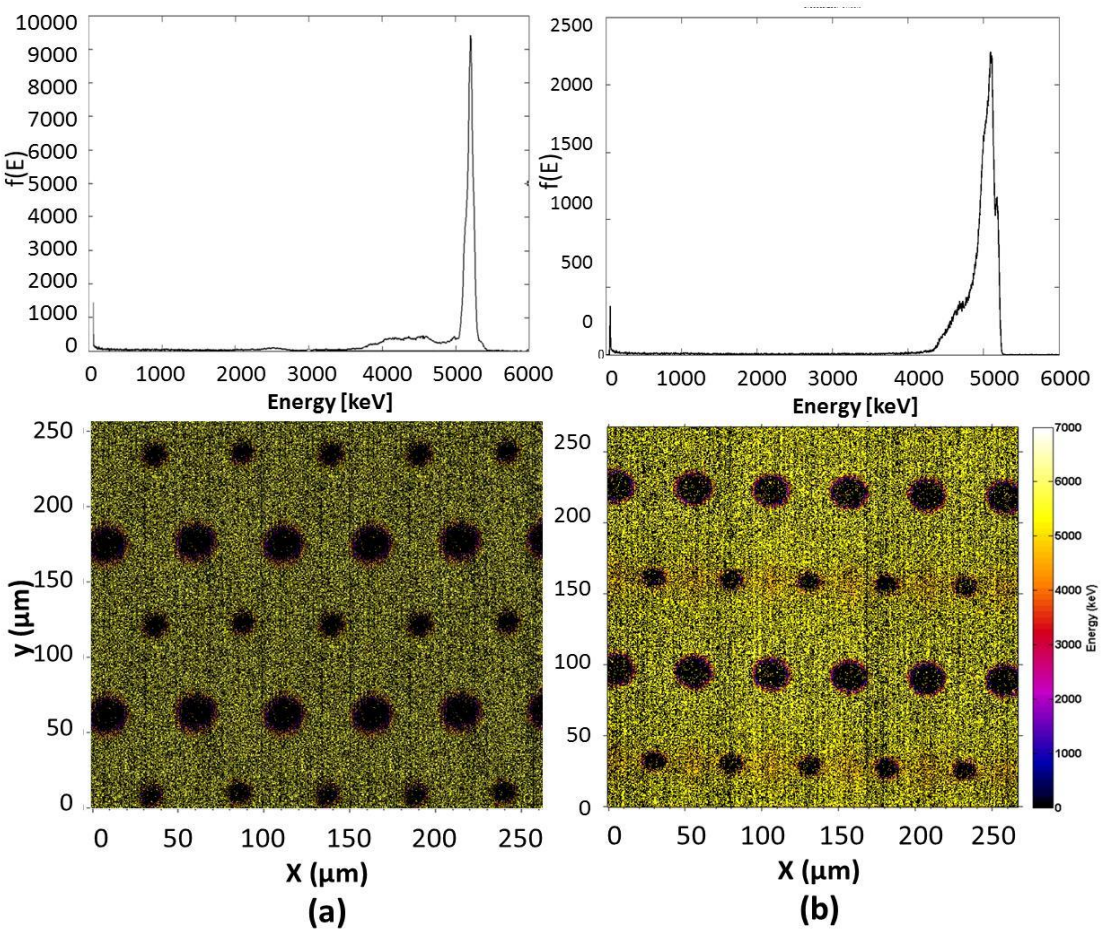

Figure 4.14 IBICC MCA spectra and median energy maps for gamma irradiated sample (3E type) at bias 60V **a)** before irradiation **b)** after gamma irradiation

Fig. 4.15 shows a comparison of the MCA spectra and the median energy maps with 5 x scan size for 3D detectors type 1E at 100 V before and after neutron irradiation. Fig. 4.15b shows that lower charge collection regions occurred near the p^+ electrodes (red region) rather than the region around the n^+ electrodes (yellow region). The statistics of these events were comparable with the statistics of higher energy events near the n^+ columns

(2 peaks with almost the same amplitude can be seen in the MCA spectrum). The regions near the p^+ electrodes were not fully depleted, even at 100 V. This deficit in the charge collection associated with a lower energy peak can be explained by the bulk damage from neutron radiation and the larger charge recombination due to induced radiation defects and related recombination centres. This agrees with [59] because the 1E diode has the largest inter-electrode distance. In this case the buildup charge in the oxide was minimal due to a much lower gamma dose during neutron irradiation compared to irradiation on a ^{60}Co source. A more detailed IBICC investigation is required with protons penetrating through the 285 μm thickness of the detector. This will ensure that the energy deposition is only due to transient radiation that has not stopped within the sensitive volume.

An abnormal effect of the positive buildup charge occurred on the 5E 3D detectors, with the shortest 46 μm inter-electrode distance, after being irradiated with 10 MRad ^{60}Co gamma. Fig 4.16a, b, and c show the median energy map for this detector for biases of 0 V, 10 V, and 30 V. While full depletion occurred at 10 V bias, there were no p^+ electrodes. This supports the hypothesis that negative inverse layers on the surface of the detector were responsible for charge collection close to the surface. This inverse layer was not affected by the absence of charge collection in the n^+ electrodes, presented as black holes on images in Fig. 4.16. There were no remarkable changes in bulk charge collection efficiency in 3E and 5E devices after

irradiation at these dose levels. This means that for small 3D SVs of SOI mushroom microdosimeter, we are not going to see the effect of radiation damage for higher doses of gamma and neutron irradiation.

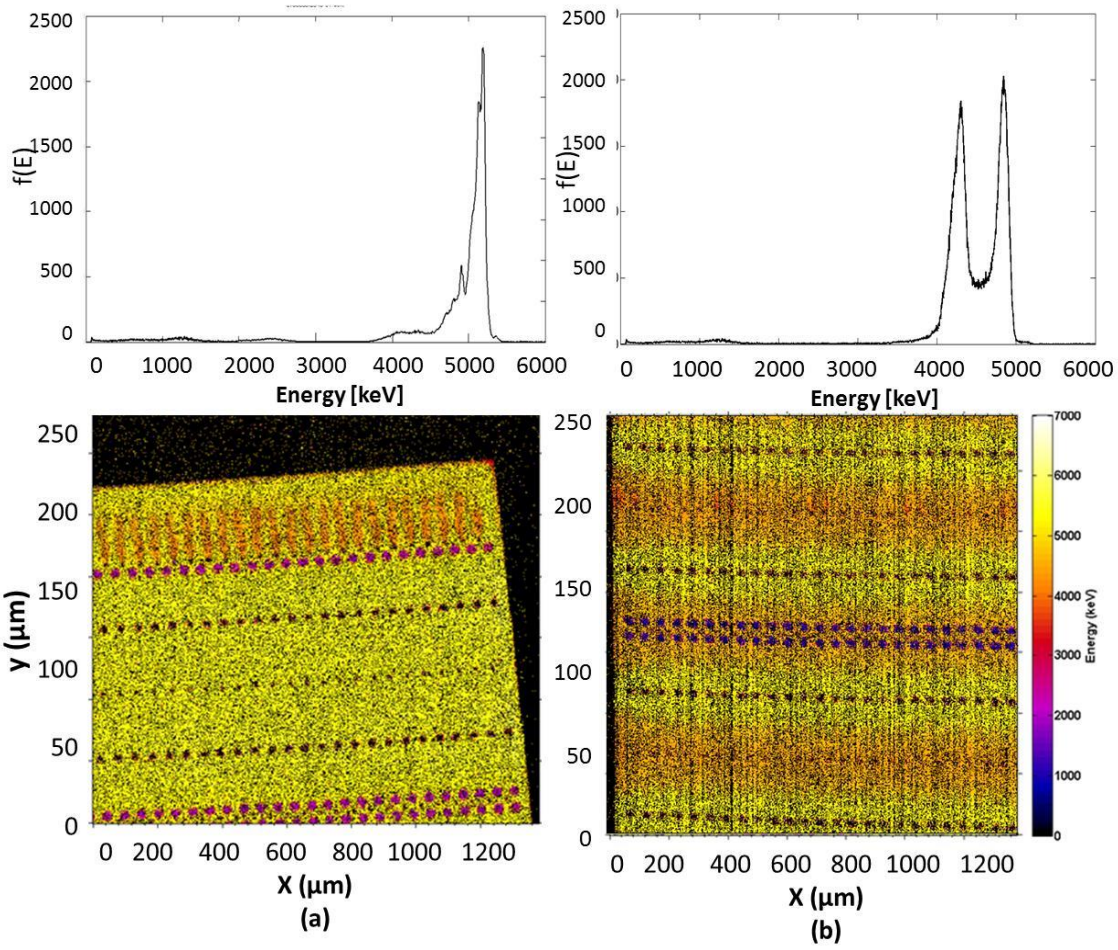

Figure 4.15 IBICC MCA spectra and median energy maps for neutron irradiated sample (1E type) at bias 100 V; **a)** before irradiation **b)** after neutron irradiation

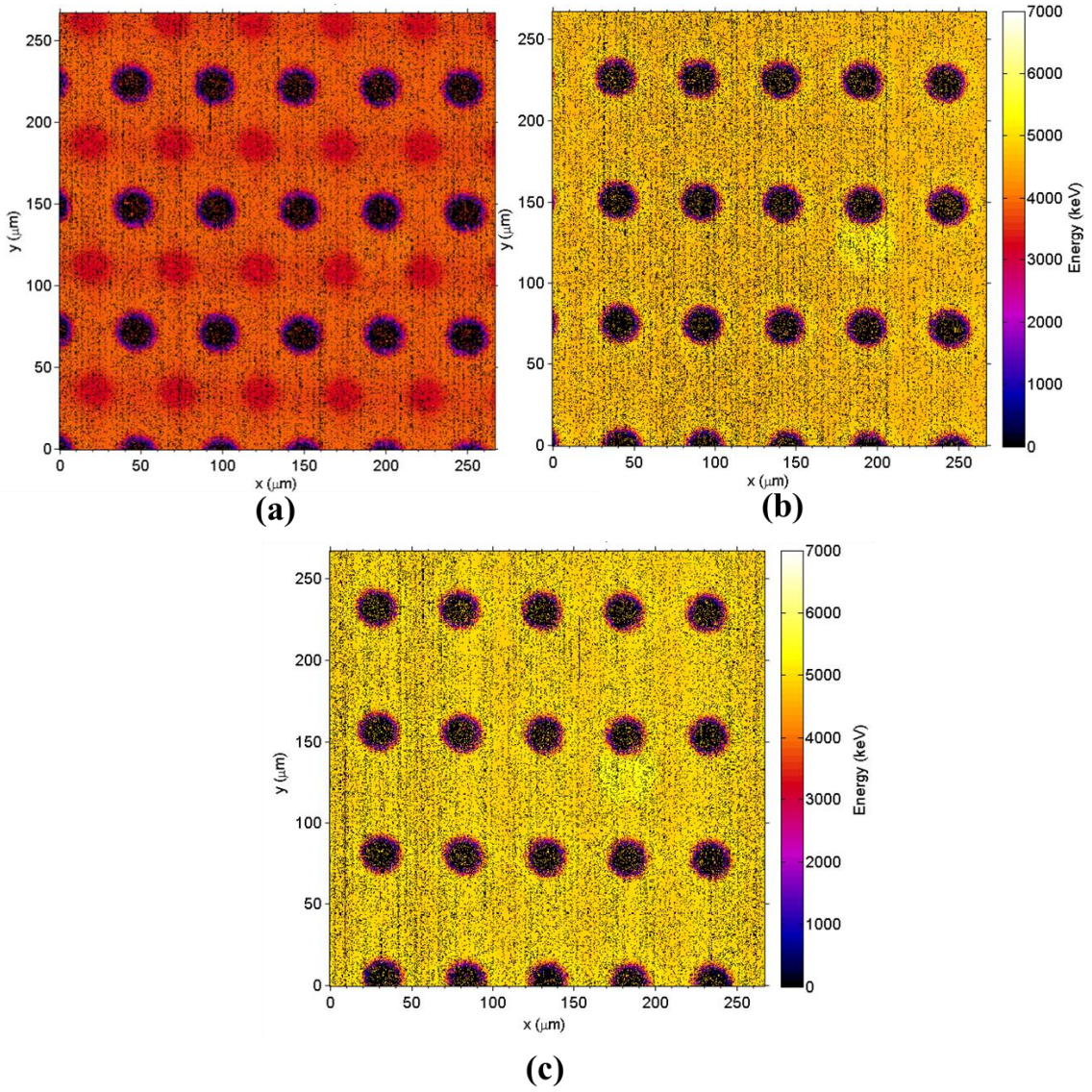

Figure 4.16 IBICC median energy maps at 1x scan size for gamma irradiated sample (5E) at biases a) 0 V, b) 10 V and c) 30 V.

4.4 Conclusions

Charge collection in the SINTEF 3D detectors was investigated. An IBICC study has shown that different types of 3D detectors have full depletion under low applied bias. 3D silicon detector technologies and active edge detectors have performed very well and show promise for use in the fabrication of mushroom microdosimeters.

IBICC technology is extremely sensitive to alternations in charge collection and has a high spatial resolution of about 2 μm. The radiation damage study of irradiated 3D detectors revealed that 3D detectors suffered no significant damage in terms of charge collection after 10 MRad gamma irradiation. Indeed, the detector with the longest inter-electrode distance exhibited slightly lower charge collections at a low fluence of neutrons. A build -up of positive charge affected the potential distribution close to the surface of the detector between the p^+ and n^+ electrodes, which also affected the lateral charge collection for short range particles.

3D technology has represented a step forward in the development of SOI microdosimeters applied in radiation protection and heavy ion therapy.

Chapter 5

[3]Ultra-thin 3D Detectors: Charge Collection Characterisation

This chapter describes a study of the charge collection of the ultra-thin 10 μm 3D silicon detector fabricated at CNM, Barcelona, Spain, and the effect that charge collection had on the detector in response to 5.5 MeV He^{2+} and 20 MeV ^{12}C ions will be investigated.

5.1 Introduction

In chapter 4 the charge collection and radiation hardness studies for the 3D detectors with 285 μm thick substrates were presented. These studies aimed at understanding the charge collection of the device. Very promising results were obtained with a full charge collection at low bias and a successful demonstration of an active edge performance. However, the required thickness of a silicon microdosimeter is normally from 5 to 10 μm.

[3] This chapter has been accepted for publication in Nuclear Science IEEE Transactions:
Linh T. Tran, Dale A. Prokopovich, Marco Petasecca, Michael L. F. Lerch, Celeste Fleta, Giulio Pellegrini, Consuelo Guardiola, Mark I. Reinhard, and Anatoly B. Rosenfeld (2014). Ultra-thin 3D Detectors: Charge Collection Characterisation and Application for Microdosimetry (accepted in August 2014).

This thickness is determined by the signal to noise (S/N) ratio required to detect the minimum lineal energy range for protons and electrons and to reduce the number of high LET stopping events (stoppers). Using SOI technology for microdosimeters with a thick supporting wafer can lead to a contribution of Si(n,α) and Si(n,p) recoils from the substrate to the charge collection of the sensitive volumes (SVs). Additional electron backscattering and dose enhancement in the SVs can occur from the silicon supporting wafer in gamma radiation fields, which would deteriorate the tissue equivalency of the microdosimeter. Moreover, a displacement current would result from an increasing deposited energy from high LET particles in an active layer. This effect is due to the parasitic MOS capacitance of the SiO_2 insulating layer, which leads to a contribution in the sensitive volume from any charge deposited beneath the insulating layer [60, 61].

To address these issues, an U3DTHIN detector was applied to microdosimetry of heavy ^{12}C ion therapy and the radiation field typical of deep space Galactic Cosmic Rays (GCR) radiation was investigated. The suitability of this type of detector for use as a dose equivalent monitor for particle therapy and space crew radiation is under investigation. In heavy ion therapy the quality of the ion beam changes dramatically with depth in water, especially within the sub-millimeter scale in the distal part of the Bragg Peak (BP). The microdosimetric Relative Biological Effectiveness (RBE) based on a Tissue Equivalent Proportional Counter (TEPC) is

currently used as a conventional method for microdosimetry in heavy ion therapy and space stations. The drawback of conventional TEPC is its poor spatial resolution due to its large physical size, which is averaging the dramatically changing RBE close to and at the distal part of the BP. Using a U3DTHIN detector, it is possible to obtain sub-millimeter high spatial resolution of RBE derivation based on the microdosimetric spectra measurements, as well as new knowledge of the RBE of low energy ions at the distal part of the BP.

5.2 Material and Methods

5.2.1 Test structure of ultra-thin 3D detectors

The large 7.52 mm x 7.52 mm area of a U3DTHIN detector was fabricated on an n-SOI wafer at the IMB-CNM (CSIC), Barcelona, Spain. The detector was originally fabricated for use in corpuscular diagnostics of High-Temperature Plasma to very low X-ray spectroscopy, which provides almost 100% detection efficiency for ions and low sensitivity to neutron and gamma backgrounds due to their extremely thin and sensitive substrate [62]. This method of back substrate thinning was used in SOI devices to study the enhancement of deposited energy for interpreting the SEU from charge ions [63]. The detector has also been tested for detecting thermal neutrons in a strong gamma field while suppressing a gamma response [64].

A schematic of the U3DTHIN detector is shown in Fig. 5.1. This detector was fabricated using 3D detector technology in 3.5 kΩ.cm n-SOI active layer followed by a thinning process to remove the 300 µm supporting wafer and leave the 1 µm SiO_2 layer unaffected. A matrix of 94 x 94 p-holes and 95 x 95 n-holes of 5 µm diameter were drilled through the 10 µm silicon active layer using Deep Reactive Ion Etching (DRIE). They were then filled with n^+ and p^+ polysilicon to act as 3D n^+ and p^+ electrodes. Aluminum contacts were deposited over the 3D n^+ and p^+ columnar electrodes, and after metallisation and passivation, Tetra-Methyl Ammonium Hydroxide (TMAH) wet etching was used to remove the support wafer underneath. All the n^+ electrodes were connected to the n^+ contact in one side of the sensor while all the p^+ electrodes were connected to the p^+ contact on the opposite side of the sensor. The U3DTHIN detector can be irradiated from the backside with a minimal energy loss of ions from the 1 µm SiO_2 supporting layer. Fig. 5.2 shows an image of the U3DTHIN detector mounted on a PC board with a hole that allows for irradiating from the backside of the detector.

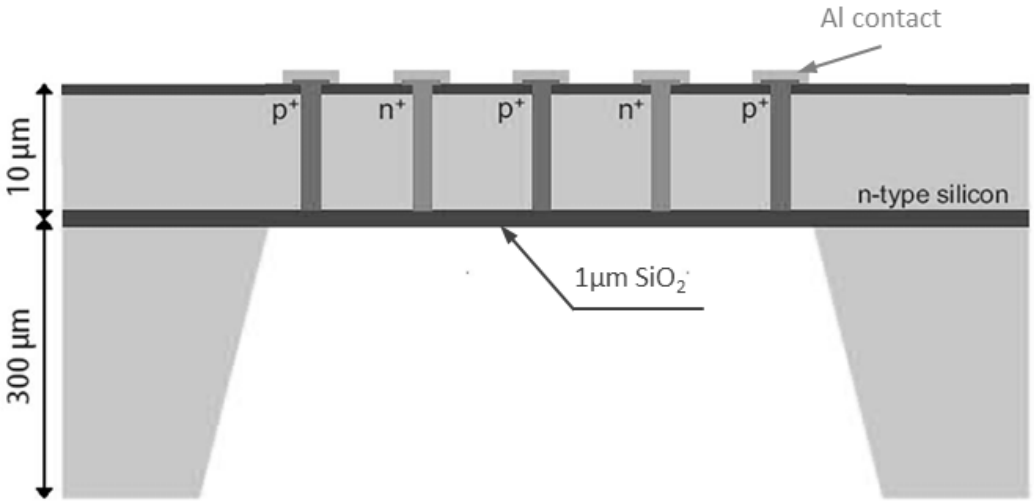

Figure 5.1 Cross-section of ultra-thin 3D detector (not to scale) [62].

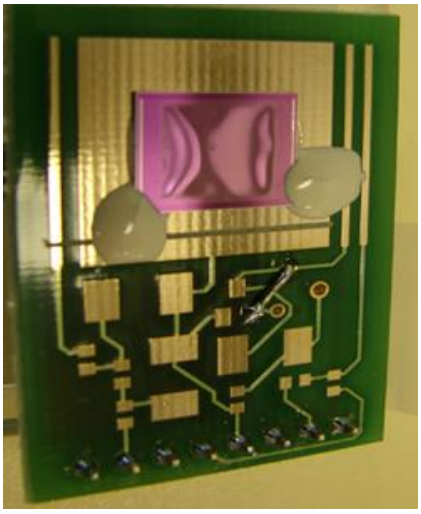

a) An U3DTHIN detector mounted on a PC board

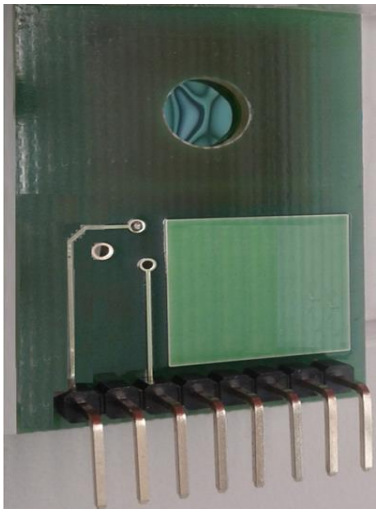

b) A hole in the PC board allowing to irradiate from the backside.

Figure 5.2 Illustration of the U3DTHIN detector mounting.

5.2.2 Ion Beam Induced Charge (IBICC) Technique

The IBICC technique utilised the heavy ion microprobe at ANSTO to characterise the properties of the detector [Chapter 2]. 5.5 MeV He^{2+} and 20 MeV ^{12}C ions were used to provide different LET particles for this study, and their specifications are shown in Table 5.1. The data were taken from SRIM [57].

Table 5.1 Ions specifications used in IBICC study

Ion	Energy (MeV)	LET in Si (keV/μm)	Range in Si (μm)
^{4}He	5.5	133.4	28.02
^{12}C	20	886.8	19.88

5.3. Results and Discussions

5.3.1 Electrical Characterisation

The reverse current and capacitance values of the U3DTHIN detector at -30 V were 38 nA and 81 pF, respectively. Figs. 5.3 and 5.4 illustrate the current-voltage (I-V) and capacitance-voltage (C-V) characteristics of the U3DTHIN detector at a bias voltage ranging from 0 V to -30 V.

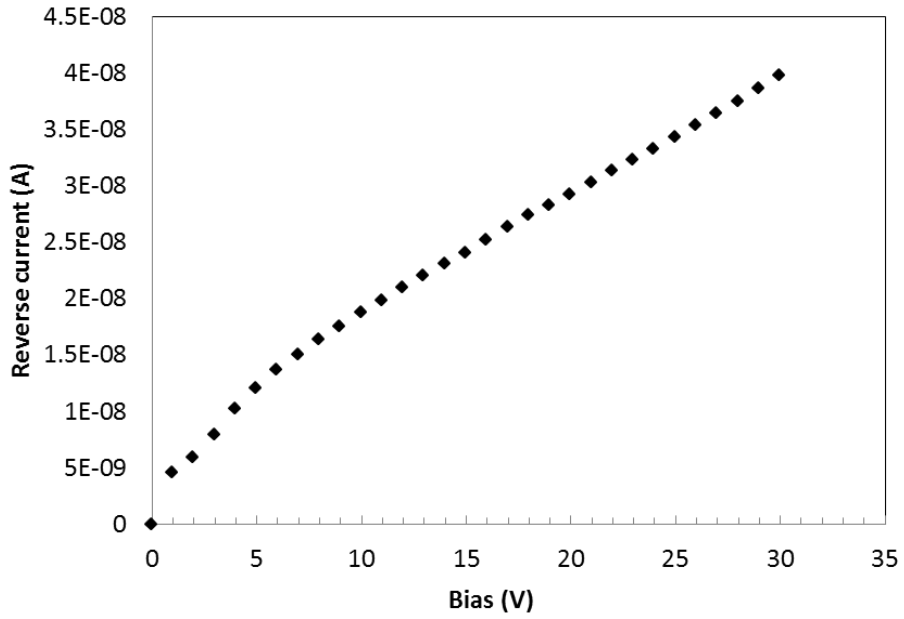

Figure 5.3 I-V characteristic of the U3DTHIN detector

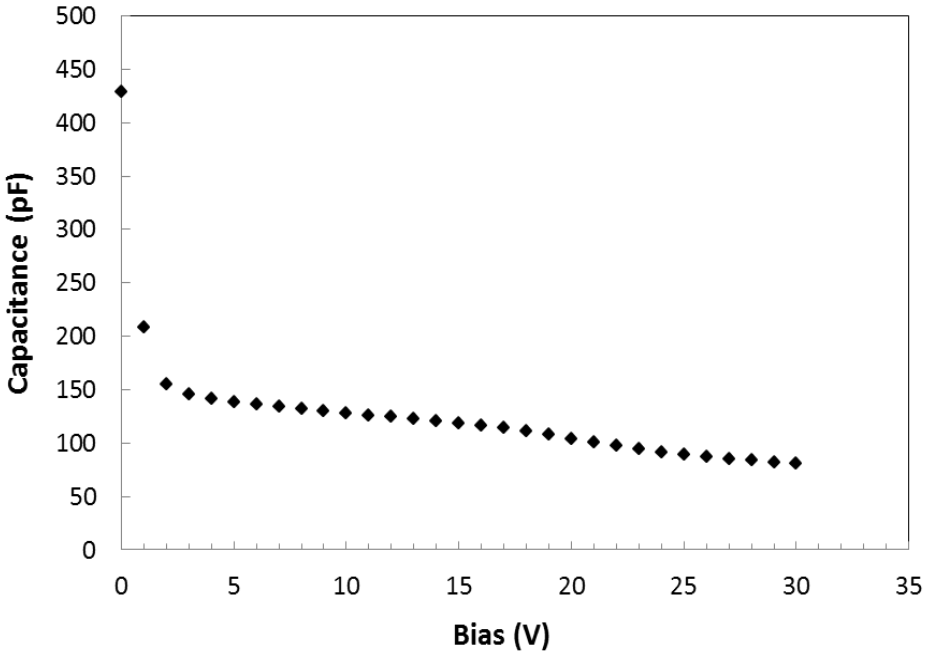

Figure 5.4 C-V characteristic of the U3DTHIN detector

5.3.2 Response of the ultra-thin 3D detector to the 5.5 MeV He^{2+} ion microbeam

The U3DTHIN detector was scanned with the 5.5 MeV He^{2+} ion microbeam at different locations. Figs. 5.5a and 5.5b show the Multichannel Analyzer (MCA) spectra obtained by the U3DTHIN detector after a 1.4 x 1.4 mm^2 area in the centre of the detector had been irradiated from the front and the back, respectively. The energy peak deposited in the 10-µm thick U3DTHIN detector was approximately 1450 keV, which was close to the expected energy deposition of 1548 keV from 5.5 MeV alpha particles in the 10 µm layer of silicon covered by the Si_3N_4 and SiO_2 over layers on the front of the detector calculated by the Geant4 simulation toolkit. Lower energy events were seen on the left of the main peak on MCA spectrum when ions were incident to the front side of the detector. Lower energy events were also seen on the left of the main peak on the MCA spectrum when the ions were incident to the front side of the detector, although this was not seen on the back irradiated detector (Fig 5.5b). A low energy tail, related to incomplete charge collected events corresponding to the events in the energy range 800 keV to 1250 keV, is shown in the median energy map in Fig. 5.5a. This phenomenon was possibly due to the p^+ and n^+ electrodes not reaching the backside completely. The fact that irradiation from the front and back of the device gives different results suggests that the electrodes do not span the

whole active region from front to back. Insufficient drilling of the electrode holes near the backside caused an effective over layer to exist, resulting in increased energy losses. For front irradiation the energy losses are less for the same sensitive depth. This effect can be also due to the channeling of the ions in silicon when the ion incident angle is parallel to the silicon atomic planes. In this case the energy deposition by the ions can be less. A small domain of events with a deposited energy of about 500 keV occurred on both MCA spectra, which was possibly related to voids in the n^+ and p^+ electrodes due to an incomplete filling of etched holes with polysilicon. This agrees with the scanning electron microscope (SEM) image of the cross section of the detector shown in Fig. 5.4 in [62].

Fig. 5.6a) and Fig. 5.6b show a scanning area of the U3DTHIN detector and the median energy map of collected charge corresponding to this scanning area respectively, when the ion beam is incident on the front surface of the detector. A full charge collection throughout the detector area between n^+ and p^+ electrodes occurred with a detector bias of -20 V, which corresponds to the main energy deposition of approximately 1450 keV in the detector (yellow region). The small peak with a mean energy of 1200 keV located on the left of the main peak in the MCA spectrum (Fig. 5.6c) corresponds to the lower charge collection outside the active area of the p^+ and n^+ electrodes, when the alpha particles were incident to the Al leads, including the remaining Al leads connecting n^+ electrodes at the edge of the

detector's active area (Fig. 5.6a). Diffused charge collection outside the active area can also be seen in a Fig. 5.6b, and it was less efficient due to a long diffusion length in high resistivity n-Si that corresponds to the low energy tail on the MCA spectrum seen in a Fig. 5.6c. The median energy map windows shown in Fig. 5.6c demonstrated the effect of high uniform charge collection in the active area of the detector where the n^+ and p^+ columnar electrodes were situated.

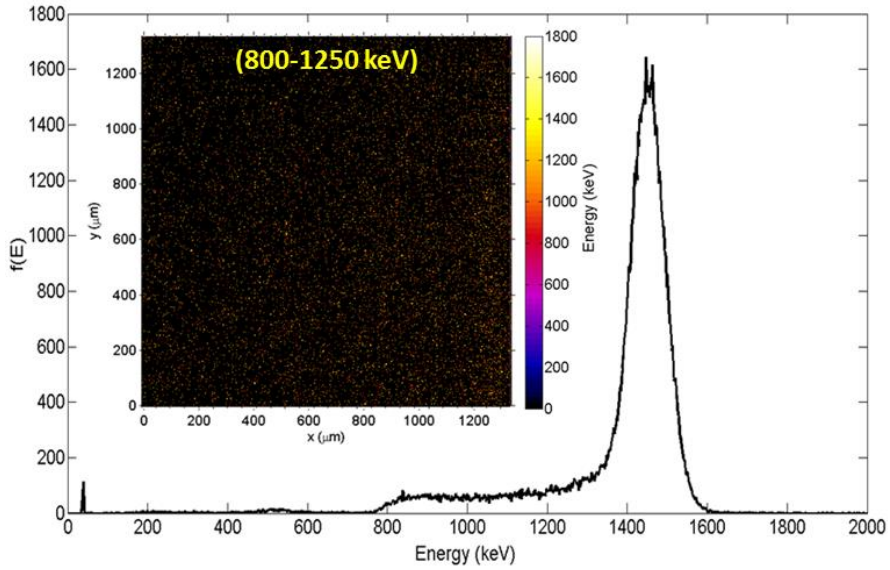

a)

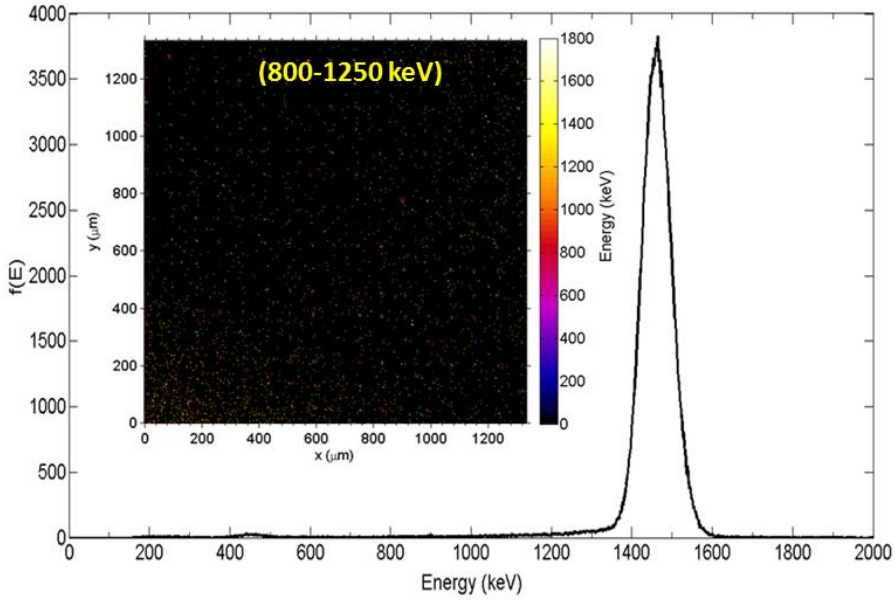

b)

Figure 5.5 MCA spectra obtained with the detector for 5.5 MeV He^{2+} at -20 V with the ion beam incident a) from the front and b) from the back of the device.

5.3.3 Response of the ultra-thin 3D detector to 20 MeV ^{12}C ion microbeam.

The charge collection was studied using a 20 MeV ^{12}C ions microbeam with a LET about 890 keV/µm scanning on both sides of the detector. Fig. 5.7 a) and b) shows the MCA spectra obtained by the U3DTHIN detector with the ^{12}C ions beam incident on the front and back side of the detector, respectively. The peak of deposited energy in the 10-µm thick 3D detector was approximately 9950 keV, which agreed with the expected maximum value of 9960 keV from 20 MeV ^{12}C in 10 µm of silicon covered by Si_3N_4 and SiO_2 over layers on the front of the detector, as calculated by the Geant4 simulation toolkit.

Like the irradiation of the detector with 5.5 MeV He^{2+} microbeam, there was a low energy tail in the front irradiated detector with ^{12}C ions. The median energy maps of the U3DTHIN detector using 20 MeV ^{12}C ions at different biases is shown in Fig. 5.8. There was a good charge collection close to the p^+ electrodes in n-Si material, even without bias (Fig. 5.8a) and at -30 V bias, there was a full charge collection in an active area where the n^+ and p^+ electrodes were situated (Fig. 5.8b). Fig. 5.8b shows that the electric field penetrated inside the p^+ column and caused a difference in the effective diameter of the n^+ and p^+ columns.

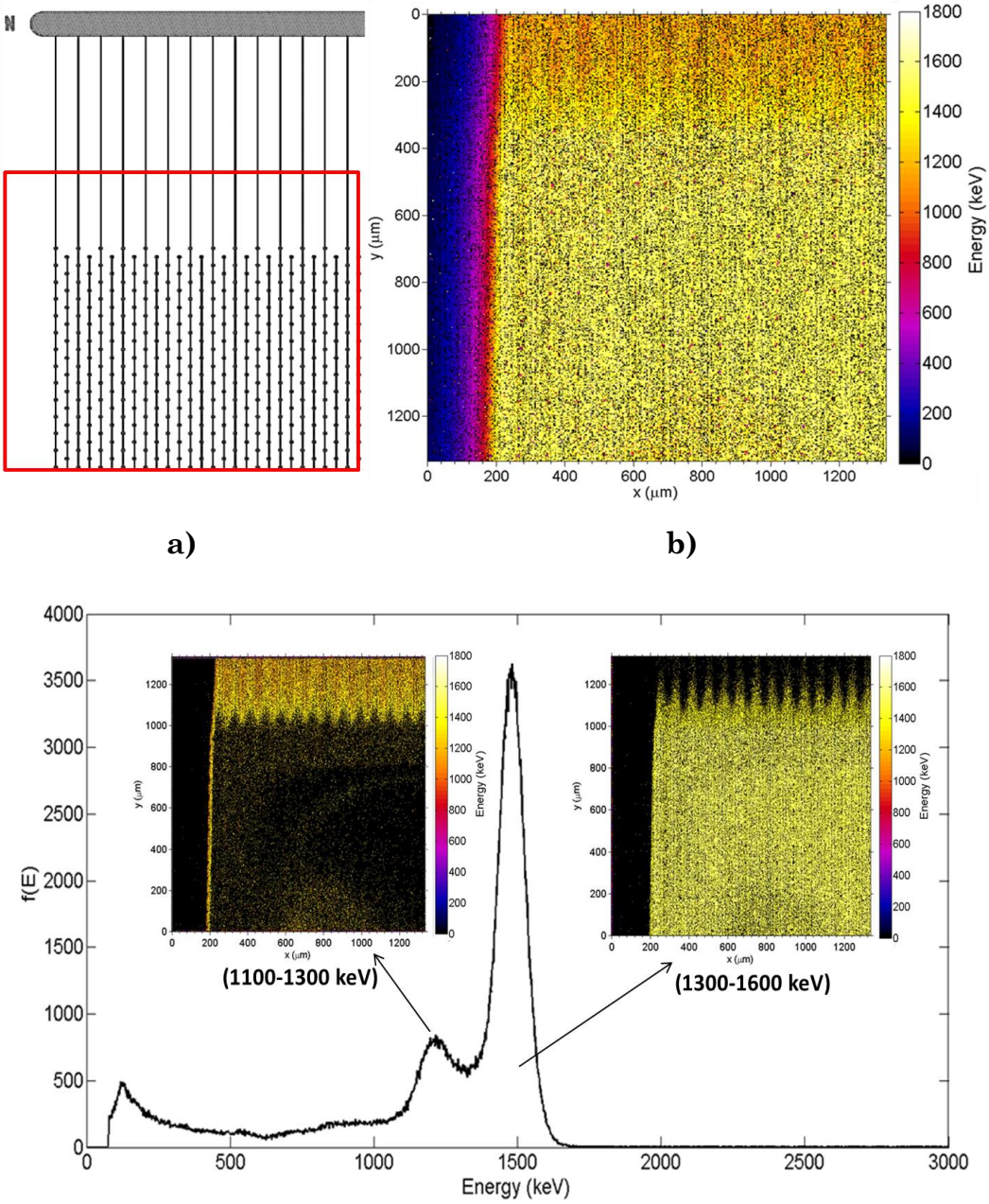

Figure 5.6 a) Scanned area of the ultra-thin 3D detector, b) median energy map of the response of the detector to 5.5 MeV He^{2+} at -20 V bias, and c) median energy maps in different energy windows corresponding to an MCA spectrum obtained at the same position.

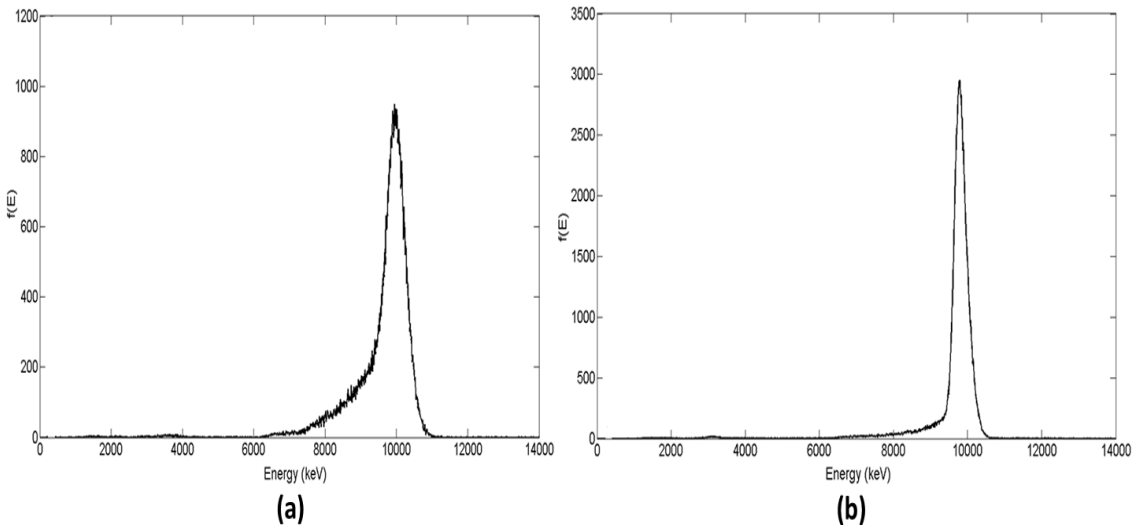

Figure 5.7 MCA spectra of the response of the detector to 20 MeV ^{12}C at -30 V bias with ion beam incident from, a) the front, and b) the back of the device.

Fig. 5.9 is a full presentation of the charge collection in the U3DTHIN detector at different biases when the ion beam was scanning across the edge of the detector (the same position is shown in Fig. 5.9). At 0 V, there was no charge under the Al leads at the edge of the detector, but with increasing bias the charge collection efficiency was increasing.

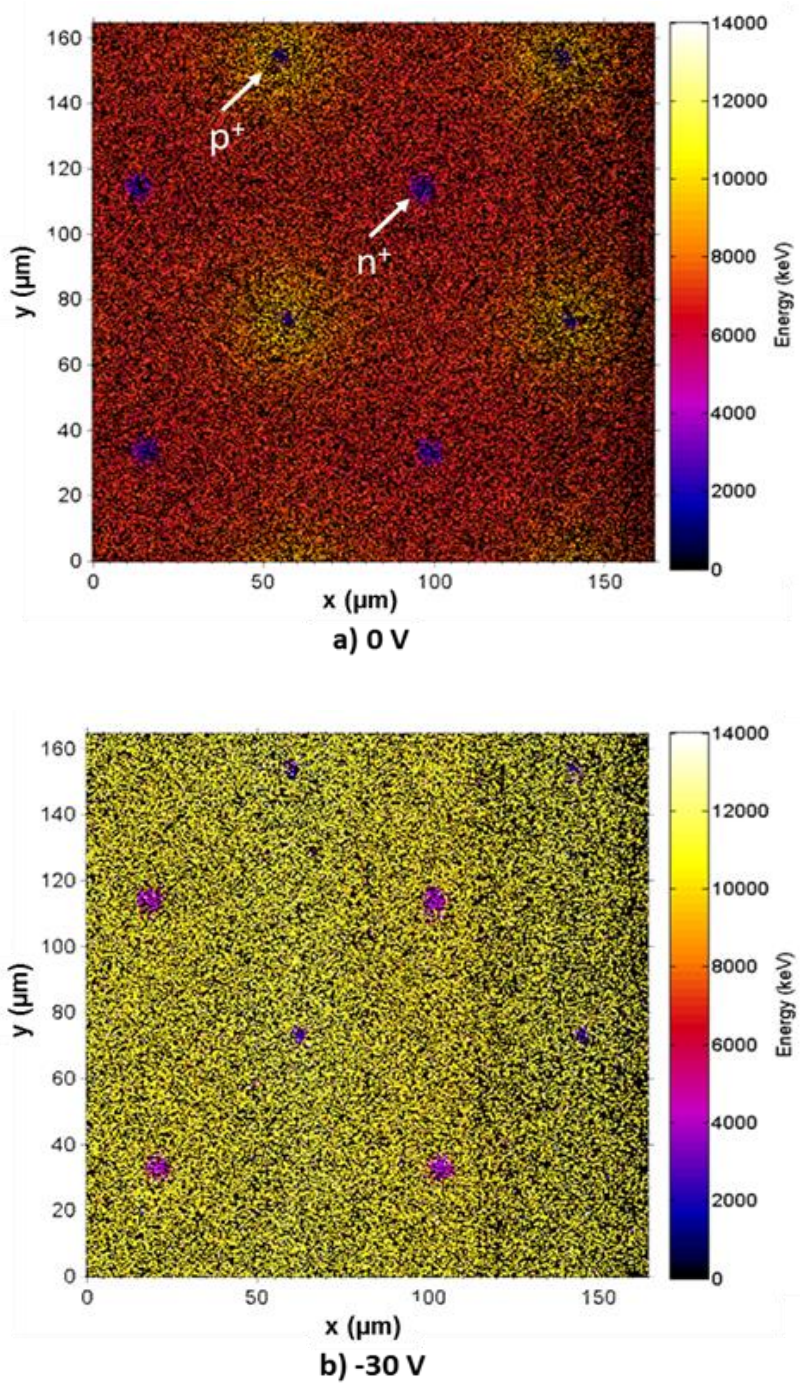

Figure 5.8 IBICC median energy maps of a U3DTHIN detector in response to a beam of 20 MeV ^{12}C ions at, a) 0 V, and b) at -30 V.

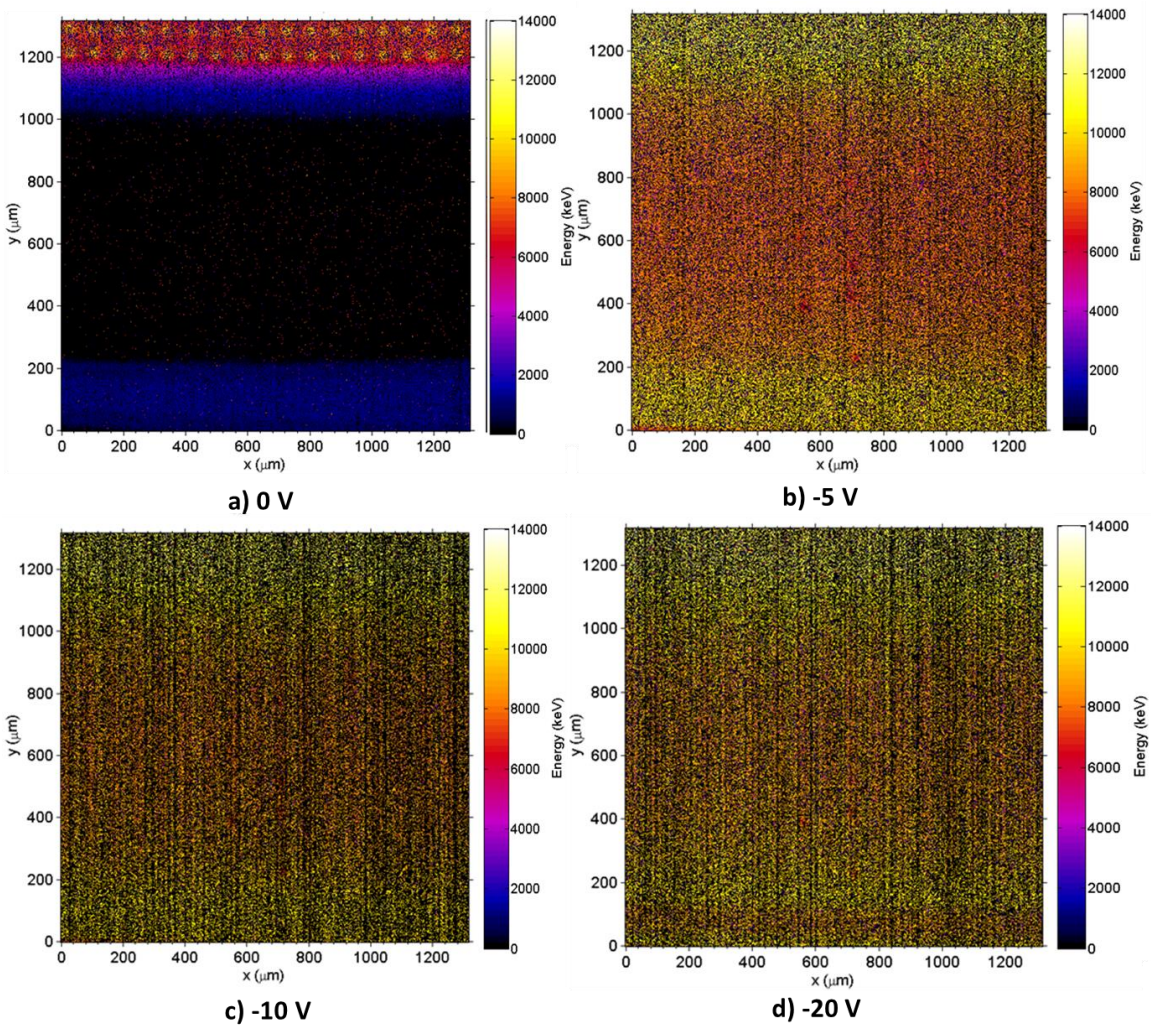

Figure 5.9 IBICC median energy maps illustrating the response of the edge of the U3DTHIN detector to 20 MeV ^{12}C ions at, a) 0 V; b) -5 V; c) -10 V; d) -30 V.

5.3.4 Effect of charge collection after scanning with heavy charged particles.

The effect of charge collection in the U3DTHIN detector when scanning with 5.5 MeV He^{2+} ions incident on the front surface of the detector using a

scanning area of 1.4 mm x 1.4 mm was studied (Fig. 5.10 a, b). A region with enhanced charge collection under a detector bias with -1V (yellow region) occurred on the median energy map, as shown in Fig. 5.10a, corresponded to the area which had been mostly irradiated with a 5.5 MeV He^{2+} ions scanning micro beam. The small 170 µm x 170 µm (green squares) region shown in Fig. 5.10a was exposed to an integral fluence of 1.52 x 10^9 He^{2+} ions/cm^2 whereas the remainder of image corresponded to much lower irradiation fluence. The improved charge collection in a previous highly exposed region was probably related to an increased resistivity of the n-Si after low-dose irradiation which led to a lateral depletion under a lower bias. For -10 V bias, there was a full uniform charge collection through the entire active area of the detector.

Fig 5.11 shows a comparison of the MCA spectra for the scanning region of 85 µm x 85 µm of the single fragment (p^+ electrode surrounded by four n^+ electrodes) of the U3DTHIN detector at an initial scan and after irradiation by carbon ions with an integral fluence of 1.05 x 10^{10} ions/cm^2. Both peaks have high and low energy tails related to not fully collecting the charge due to a 0 V bias, unlike the -30 V bias detector (Fig 5.7). Moreover, there was a deficit of charge collections after irradiation with ^{12}C ions that shifted the peak to a lower charge collection region.

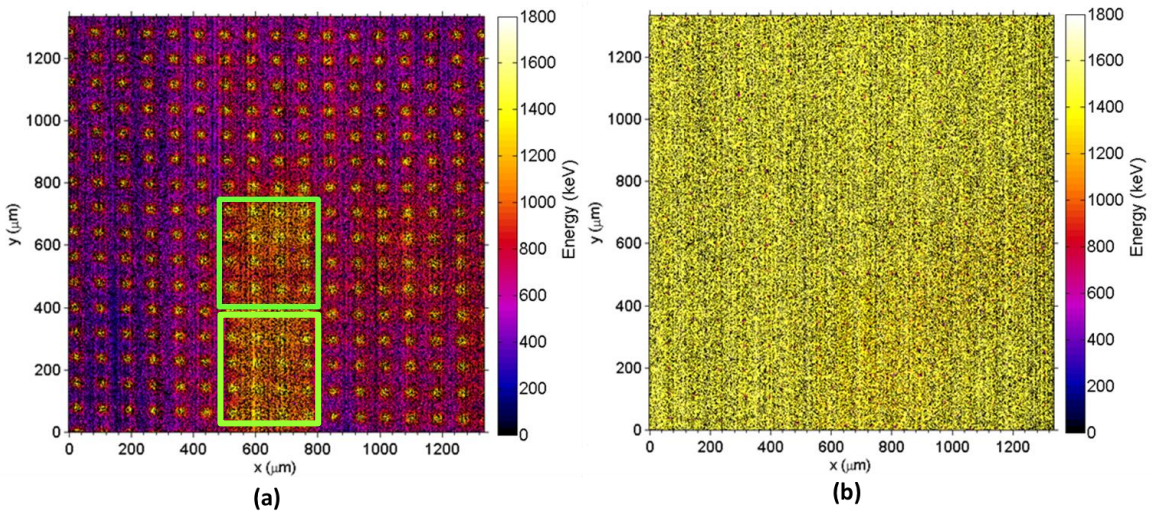

Figure 5.10 Median energy map of the response of the detector to 5.5 MeV He^{2+} at a) -1 V bias and b) -10 V bias.

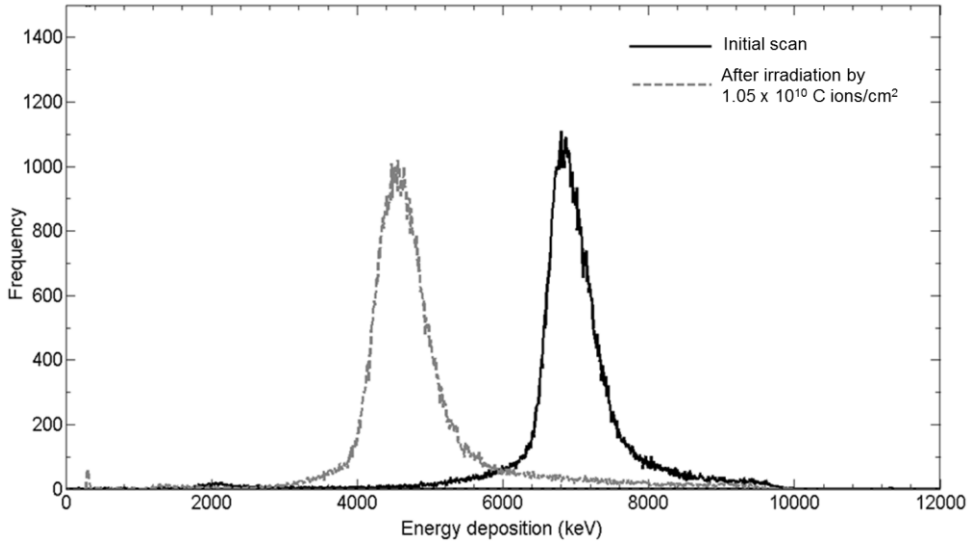

Figure 5.11 A comparison of the pre-irradiation and post-irradiation MCA spectra for the U3DTHIN detector with 20 MeV ^{12}C ions. The detector was biased at 0 V.

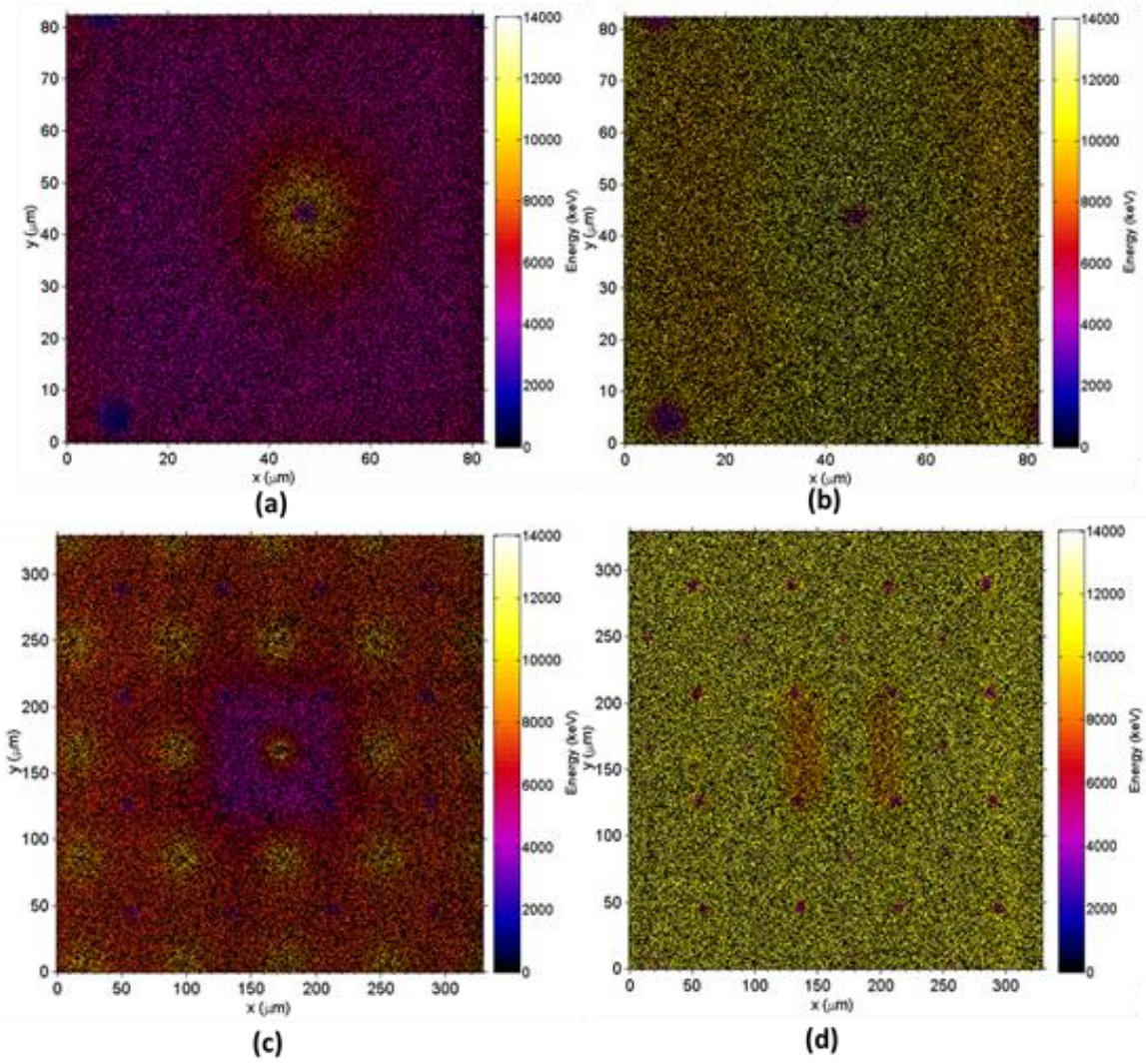

Figure 5.12 Median energy map of the charge collection from the detector in response to: 20 MeV ^{12}C at, a) 0 V bias, b) -30V bias (scanning size of 85 µm x 85 µm), c) 0 V bias, and d) -30 V bias (scan size of 350 µm x 350 µm).

The median energy maps shown in Fig. 5.12 illustrate a deficit of charge collection between the columnar electrodes of the irradiated scan for different scan sizes and different biases. The scan size was determined by an area of the scanned region which corresponded to 85 µm x 85 µm for 0.5 x

scan size and 340 µm x 340 µm for 2 x scan size. Fig 5.11a,b shows the IBICC median energy maps with 0.5 x scan size when the detector was biased at 0 V and -30 V, respectively. Fig 5.12c, d shows the IBICC median energy maps with 2 x scan size when the detector was biased at 0 V and -30V, respectively. Fig 5.12c shows there was a lower charge collection in a central part of the scanned area which corresponded to a region previously irradiated with 1.05 x 10^{10} carbon ions/cm^2. Fig. 5.12 c illustrates a median energy map of a 340 µm x 340 µm scanning area showing a deficit of charge collection in the central part of the scanned area for 0 V bias. This was in contrast to enhancement of the charge collection under -1V bias in a scanning region initially irradiated with He^{2+} ions, but with less fluence than the carbon ions (Fig. 5.12a). There was still region with a lower charge collection in this cell when the detector was biased at -30 V (Fig. 11d), which indicated there were no full charge collections between the n^+ electrodes that belonged to this cell. This strongly suggested that irradiation with higher LET carbon ions was producing more damage KERMA (Non Ion Energy Loss –NIEL) in silicon than the helium ions.

5.4 Conclusions

The charge collection characteristic of the U3DTHIN detector fabricated on n-type silicon was investigated using the IBICC technique. This

U3DTHIN detector has already demonstrated full charge collection under a low bias. The IBICC study also revealed a very uniform charge collection across the detector area containing n^+ and p^+ electrodes, while irradiating from the backside of the detector provided more uniform charge collection than from the front, as explained previously when the 3D electrodes failed to reach the backside completely.

The localised radiation damage in the U3DTHIN detector with respect to the integral fluence of 5.5 MeV He^{2+} and 20 MeV ^{12}C ions was investigated while scanning the detector with microbeams. It was observed that irradiation with 1.52 x 10^9 He^{2+} ions/cm^2 fluence was enhancing the charge collection under -1 V bias more than the detector area that was irradiated less, however there was a full uniform charge collection under -30 V bias. Irradiation with 1.05 x 10^{10} carbon ions/cm^2 fluence was leading to regions of reduced charge collection under 0 V and -30 V bias. The effect of this radiation damage should be considered in the heavy ion radiation fields. The U3DTHIN detector based on SOI structure with very good charge collection characteristics will be used to measure the RBE in heavy ion carbon therapy, and then be compared to different generations of CMRP SOI microdosimeters.

Chapter 6

[4]New 3D Silicon Microdosimeter: Designs, Fabrication Method and Simulations of the Response in Neutron Radiation Fields.

This thesis chapter explains the design and fabrication of a new proposed 3D microdosimeter for possible use in radiation protection and hadron therapy. Geant4 simulations were performed to study how the detector would respond to neutron fields of ^{252}Cf, Pu-Be sources, and an avionic radiation environment, and to optimise the design of the 3D microdosimeter.

6.1 Introduction

Cosmic radiation interacts with the upper atmosphere of the Earth and produces a secondary mixed radiation field [65] that includes protons, neutrons, electrons, gamma rays, muons, and pions. This field exposes

[4] Part of this chapter has been published in Nuclear Science IEEE Transactions:
Linh T. Tran, Susanna Guatelli, Michael L. F. Lerch, Dale A. Prokopovich, Mark I. Reinhard, James F. Ziegler, Marco Zaider and Anatoly B. Rosenfeld (2014). *A Novel Silicon Microdosimeter using 3D Sensitive Volume: Modeling the Response in Neutron Field Typical of Aviation*. IEEE Transactions on Nuclear Science, 61 (4), 1552-1557.

aircrew to radiation which could ultimately pose a severe risk to their health. It is therefore important to understand radiation protection in a mixed avionic or space radiation environment in order to minimise the cancer risk for aircrew and astronauts. Minimising their exposure to such fields by imposing annual limits to flight times can be done if the dose can be quantified accurately. Microdosimetry [10] can uniquely address radiation protection requirements in low dose rate avionics and space radiation environments by being independent of the radiation field energy or its composition [section 1.2].

This chapter explains the design, fabrication, and Geant4 radiation transport simulation modelling the response of the novel microdosimeter with array of 3D SVs in neutron fields to optimise the design of this novel device.

6.2 Materials and Methods

6.2.1 3D Microdosimeter fabrication

6.2.1.1 SINTEF MiNaLab Facilities

The SINTEF Microsystem and Nanotechnology Laboratory (MiNaLab) is located in Oslo, Norway and has 800 m^2 of cleanroom areas. The key techniques for fabricating the proposed 3D microdosimeter are micro-machining and 3D sensor technologies, which are available at SINTEF [66].

At SINTEF, a high aspect ratio of up to 60:1 through-substrate VIAs can be achieved, while deep reactive ion etching, and wet chemical etching of silicon can also be used in the fabrication of thin sensors as a tool to remove the support wafers [refer to 1.3.1]. With this technique the supporting wafer of the devices or the actual devices, can be thinned down to 5 to 10 μm.

6.2.1.2 Proposed Designs of the 3D Microdosimeter

The proposed 3D SVs microdosimeter is currently being fabricated at SINTEF MiNaLab. The designs of this 3D microdosimeter were proposed by CMRP, and it has 3D cylindrical SVs to provide a well-defined sensitive region. Fig 6.1 shows the steps taken to fabricate the proposed 3D microdosimeter. It is fabricated on silicon-on-insulator (SOI) material with a buried oxide layer that isolates the microdosimeter's SV from the support wafer (Step 1). An array of n^+ electrodes and surrounding ring p^+ electrodes are produced using DRIE, followed by polysilicon deposition and doping. Aluminum contacts are used to connect the same type of electrodes in parallel in order to increase the detection count rate statistic of the microdosimeter. In addition to the regional microdosimetry, "odd-even" arrays of the proposed 3D SVs are assigned to provide an additional prospect of analysing track structures for high energy ions by measuring them in coincidence and anti-coincidence modes.

The proposed microdosimeter can also be applied in fast neutron field dosimetry where the neutrons are incident from all directions to the SVs. To improve the tissue equivalency of the new microdosimeter, the support handle wafer can be removed and filled with a tissue equivalent material such as polymethyl methacrylate (PMMA). Details of the fabrication process are described below:

Table 6.1 Steps taken to fabricate the proposed 3D microdosimeter.

Step	Process	Schematic cross-section diagrams
1	SOI wafer with 10 µm thick active layer.	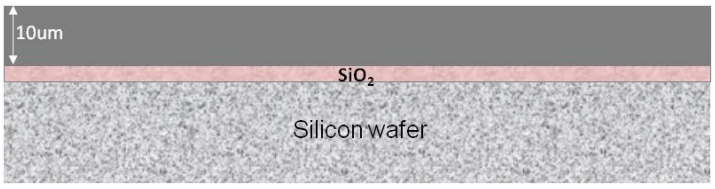
2	Dry thermal oxidation using 1.5 µm thick SiO_2 and followed by nitride deposition	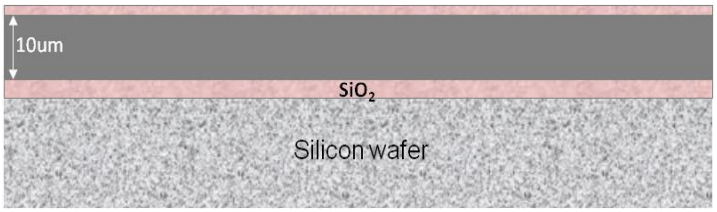
3	Oxide and nitride etch using plasma etching	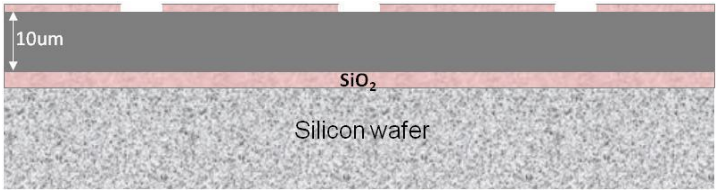

4	Etching of n^+ electrodes using DRIE technology	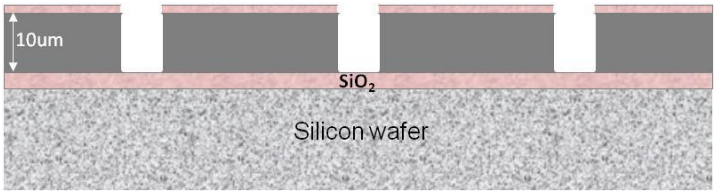
5	Filling n^+ electrodes with Polysilicon.	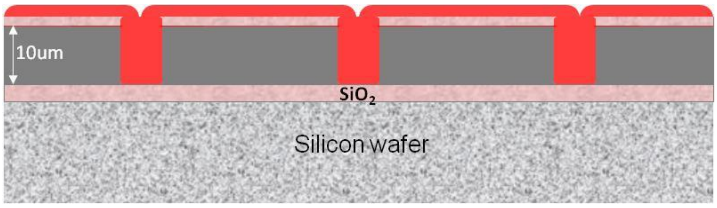
6	Removal of Polysilicon with plasma etching	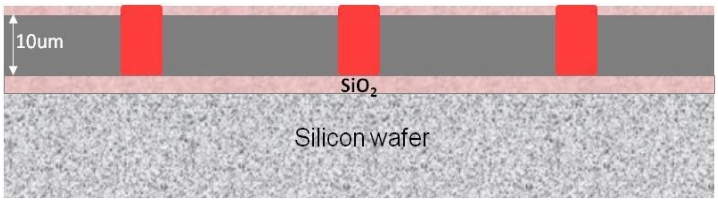
7	200 nm nitride deposition	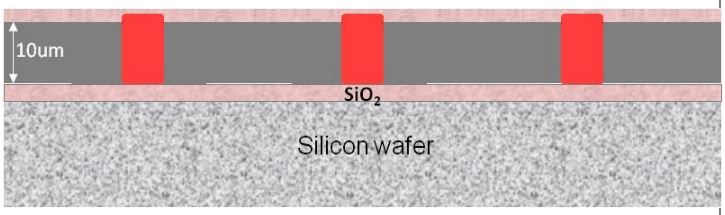
8	Oxide and nitride etch using plasma etching	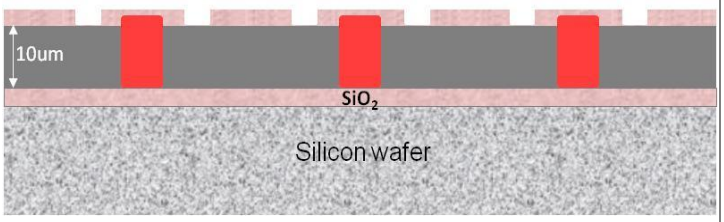
9	Etching p^+ electrodes using DRIE technology	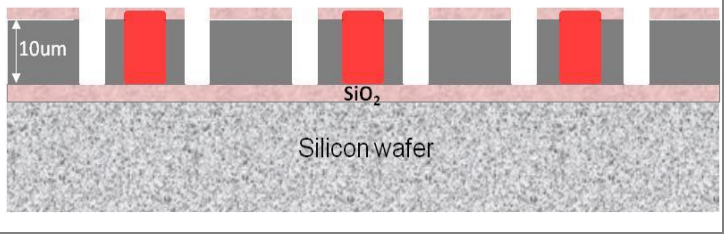

10	Filling p^+ electrodes with polysilicon	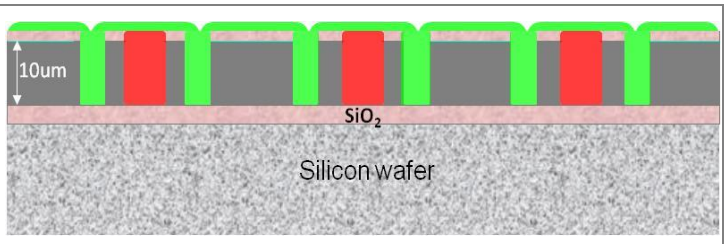
11	Removing Polysilicon with plasma etching	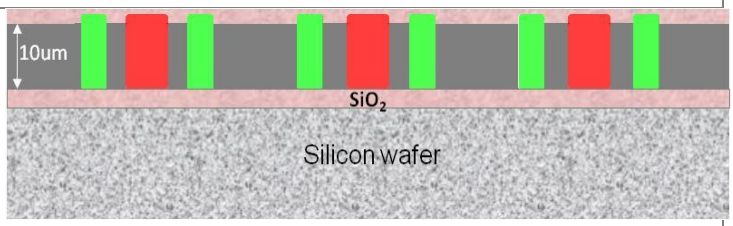
12	Oxidation and annealing	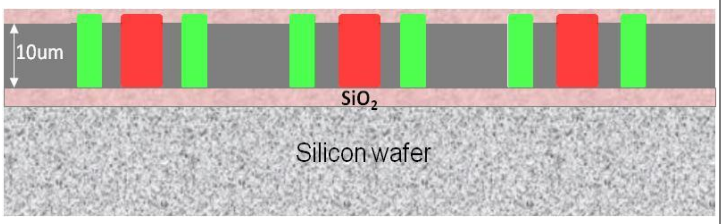
13	Oxide and Nitride etching	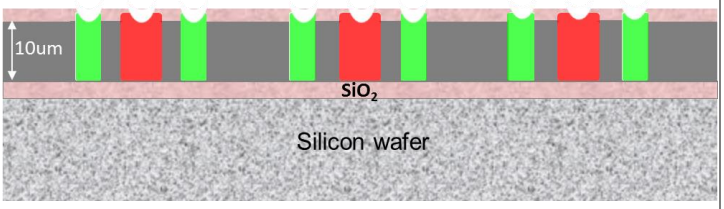
14	Aluminum deposition	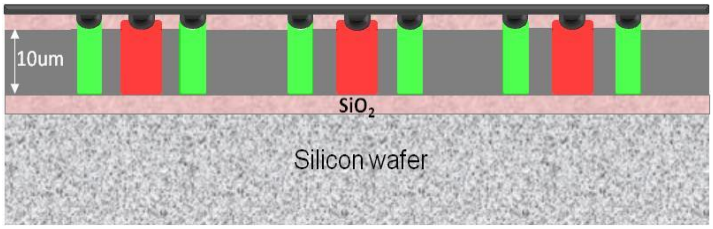

15	Aluminum etching using wet chemical etch	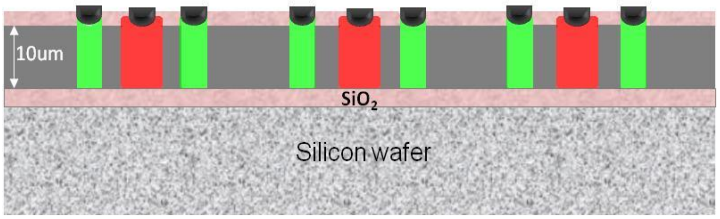

16	Etching of silicon surrounding p-i-n SVs	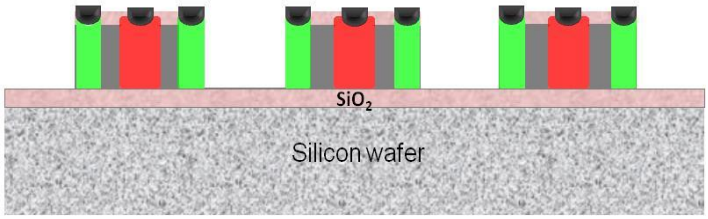
17	PMMA deposition	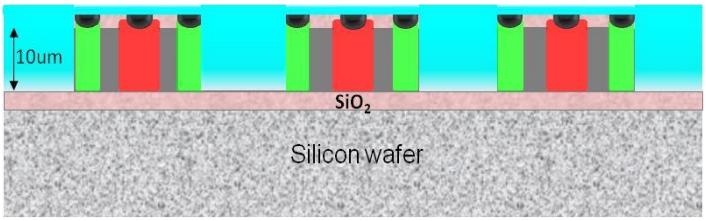
18	PMMA etching	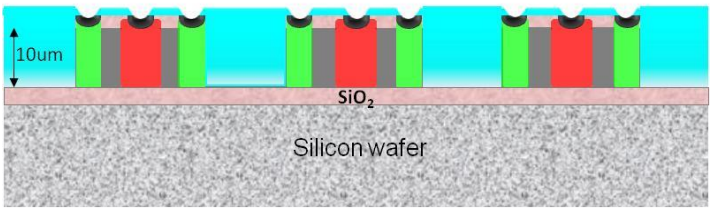
19	Aluminum deposition	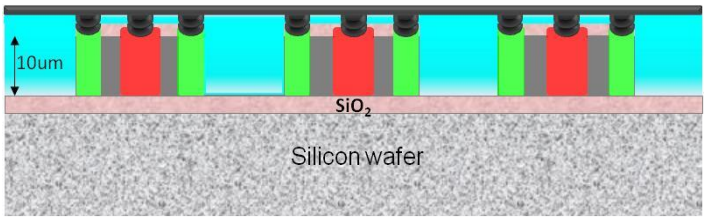
20	Aluminum etching	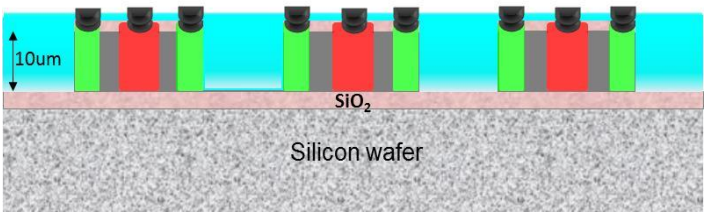

21	Finally, support silicon wafer is removed by wet chemical etching with the remaining space filled by PMMA material	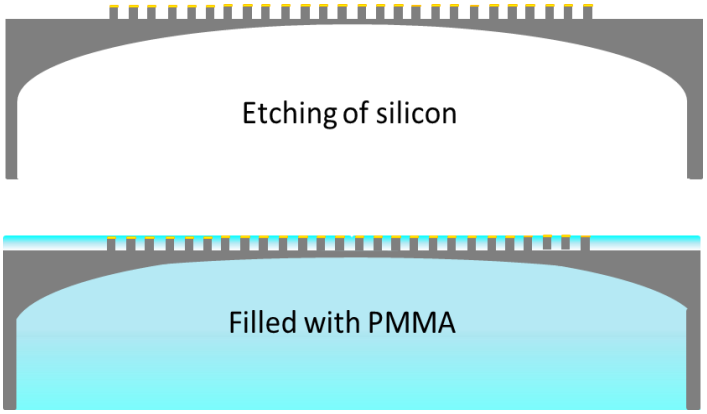

6.2.2 Geant4 Model of 3D "mushroom" microdosimeter

The Geant4 model of the p-SOI microdosimeter consists of 3D cubic or cylindrical sensitive volumes. The cubic SV is 10 µm x 10 µm x 10 µm while the cylindrical SV is 10 µm in diameter and 10 µm high. The SV array has a 40 µm pitch to avoid crosstalk with neighbouring SVs. Fig. 6.1 shows the design of the 4th generation of CMRP microdosimeters to be produced utilizing 3D detector technology. Two options of 3D SOI microdosimeters were simulated, i) cubic/ cylindrical 3D SVs with an outer P^+ electrode embedded in Si (6.1a), and ii) 3D free standing cubic/cylindrical SVs embedded in PMMA (6.1b), the so called mushroom microdosimeter. Both microdosimeters were covered with a 0.5 mm PMMA fast neutron converter. Moreover, the substrate of the 3D mushroom microdosimeter was back etched and supplemented by a PMMA layer, while the other microdosimeter has a thick Si substrate [Fig. 6.1 a, b].

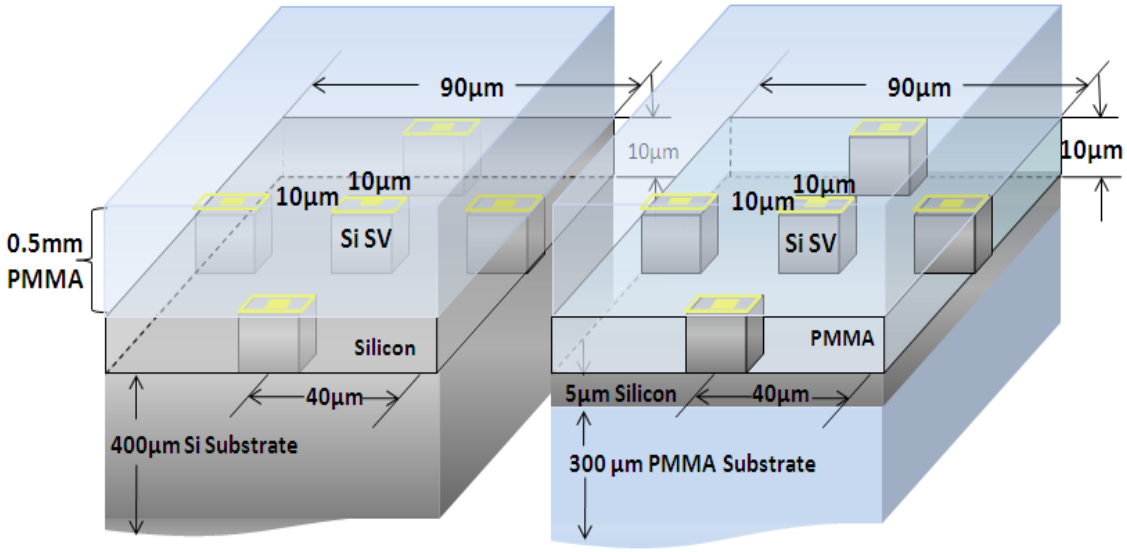

(a) (b)

Figure 6.1 The geometry of the 3D SV array microdosimeter modelled in Geant4 simulations showing, (a) SOI 3D SVs array embedded in Si on a thick Si substrate, (b) SOI 3D SV array embedded in PMMA ("mushroom") with back etched thin Si substrate and a PMMA layer attached (SiO_2 layer between device and the substrate has not been shown).

This simulation study aimed at optimising the design of the new SOI 3D SV array microdosimeter for neutron field radiation protection applications. The two designs presented in Fig. 6.1a and Fig. 6.1b were compared in terms of improving the tissue equivalency (by reducing the thickness of Si substrate and removing the silicon surrounding SVs) vs the complexity of fabrication.

6.2.3 Geant4 Simulation Application

The Geant4 [48, 49] version 4.9.4.p01 was used to calculate the energy deposition in the SV of the microdosimetric device, from the recoils generated by the neutron field in the converter and in the PMMA medium surrounding the SVs. The neutron fields under study were ^{252}Cf and Pu-Be sources, and the avionic radiation environment. The reference spectra of ^{252}Cf and Pu-Be sources were taken from IAEA Technical Report TRS 403 [67] and the recommended representation of the neutron spectrum in avionics was taken from the NASA Technical Memorandum which is related to the neutron spectra data measured at an altitude of 12.5 km [68].

The physics models used were Low Energy Livermore Package for electromagnetic physics and QGSP_BIC_HP for hadronic physics. The threshold for producing secondary particles was set to 250 eV, which was the limit of the validity of the electromagnetic models selected. The neutron sources of ^{252}Cf and Pu-Be were simulated as a parallel beam that are normally incident to the surface of the microdosimeter. An avionic neutron field was simulated as an isotropic radiation field surrounding the microdosimeter. The General Particle Source (GPS) [49] was used to model the radiation fields.

The geometry of the simulated microdosimeter is shown in Fig. 6.1. The silicon supporting wafer was modelled as a 90 μm x 90 μm x 400 μm slab.

The PMMA medium was considered to be a 90 µm x 90 µm x 10 µm slab with five Si 3D SVs embedded. The SV was a 10 µm x 10 µm x 10 µm silicon cube or a 10 µm diameter by 10 µm high cylinder. The silicon oxide layer was modelled as rectangle parallelepiped (RPP) of 0.145 µm thickness on top of each sensitive volume. Aluminum contacts (yellow regions) above the n^+ (central region of the SV) and p^+ (edge regions of the SV) were modelled as RPP with dimensions of 2 µm x 2 µm x 1 µm and a 10 µm x 1 µm x 1 µm strip along the edges of the SV, respectively. A 0.5 mm thick PMMA converter was set on top of the microdosimetric device that was placed in air. The pattern of energy deposition was calculated event by event in the central SV, as shown in a Fig. 6.1 (a, b). Each event corresponds to the generation of one particle of the primary radiation field.

6.3 Results and Discussions

6.3.1 Response of 3D SV microdosimeter to ^{252}Cf and Pu-Be neutron fields.

The responses of the 3D mushroom microdosimeter presented in Fig 6.1b) with and without 0.5 mm PMMA converter in ^{252}Cf and Pu-Be neutron fields are presented in Fig. 6.2 and Fig. 6.3, respectively. ^{252}Cf was selected as a good representation of fission spectrum typical for a reactor neutron environment. For the microdosimeter without PMMA converter, the energy

deposition in the 3D SV was mostly due to Si recoils and products from inelastic reactions caused by Si(n, particle) inside the silicon SVs. Recoil protons were generated in the PMMA surrounding the SVs, but their energy deposition in the 3D SV was limited due to the angular scatter of protons from events that occurred close to the 3D SV, and which enhanced the low energy part of Fig. 6.2 and Fig. 6.3.

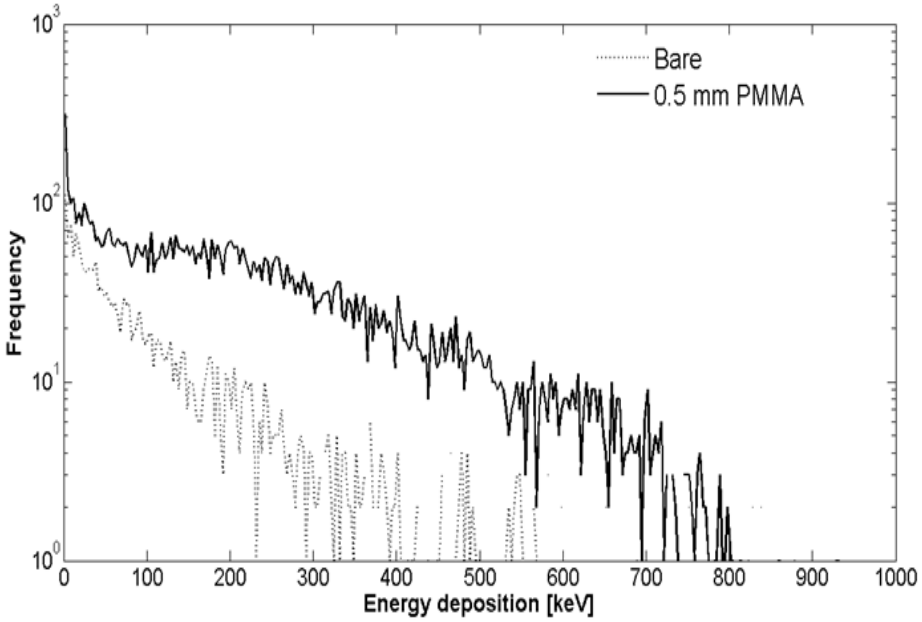

Figure 6.2 Energy deposition event spectrum for 3D mushroom microdosimeter with/without 0.5mm PMMA converter in response to ^{252}Cf; 5.10^8 events were executed in the simulation.

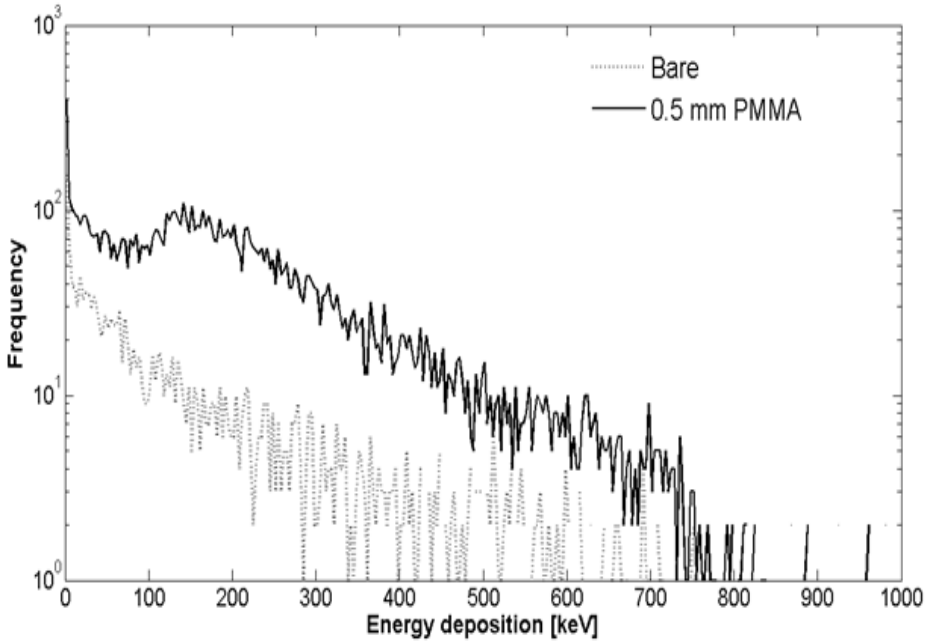

Figure 6.3 Energy deposition event spectrum for 3D mushroom microdosimeter with/without 0.5 mm PMMA converter in response to Pu-Be; 5.10^8 events were executed in the simulation.

For the 0.5 mm thick PMMA converter on top of the 3D SV, a significant contribution to the energy deposition resulted from recoil protons created in the converter that reached the SV. Their contribution actually exceeded the deposited energy from events generated in the bare Si, and therefore they will dominate the microdosimetric spectrum. The differences between the responses of 3D SV microdosimeter to ^{252}Cf and Pu-Be sources were due to the nature of the primary neutron spectra.

6.3.2 Comparison of 3D mushroom microdosimeter with 3D embedded in silicon microdosimeter.

Fig. 6.4 shows a comparison of the simulated response of the new SOI microdosimeters as shown in Fig. 6.1a and 6.1b, to an isotropic neutron field of typical avionic spectrum taken from [68]. In both cases, a 0.5 mm PMMA converter was placed on top of the microdosimeter and the microdosimetric spectra were normalised to 1.

The events within the lineal energy range between 10 and 70 keV/μm were mostly due to the proton recoils produced within the PMMA that reached the SV. It is clear that the microdosimetric spectrum for the mushroom microdosimeter (SV embedded in PMMA) has larger relative area in a range of lineal energies 10 - 70 keV/μm than the microdosimeter with 3D SVs embedded in silicon. These events corresponded to the recoil protons generated from the PMMA converter above and laterally to the SVs that led to a more efficient detection of neutrons. The high lineal energy transfer events that were part of the microdosimetric spectrum for SOI 3D SVs embedded in silicon had a much higher relative area than the SVs embedded in PMMA because much more elastic and inelastic recoils were generated from silicon. These events produced a relatively higher deposited dose to the SV compared to the SV embedded in PMMA. The difference between the two spectra became even more pronounced when we consider the convolution of

microdosimetric spectra with the quality coefficient *Q(y)* [10], which grew in a lineal energy transfer region from 70 to 200 keV/µm and also provided an enhanced error to the derived dose equivalent which was associated with the additional recoils from silicon.

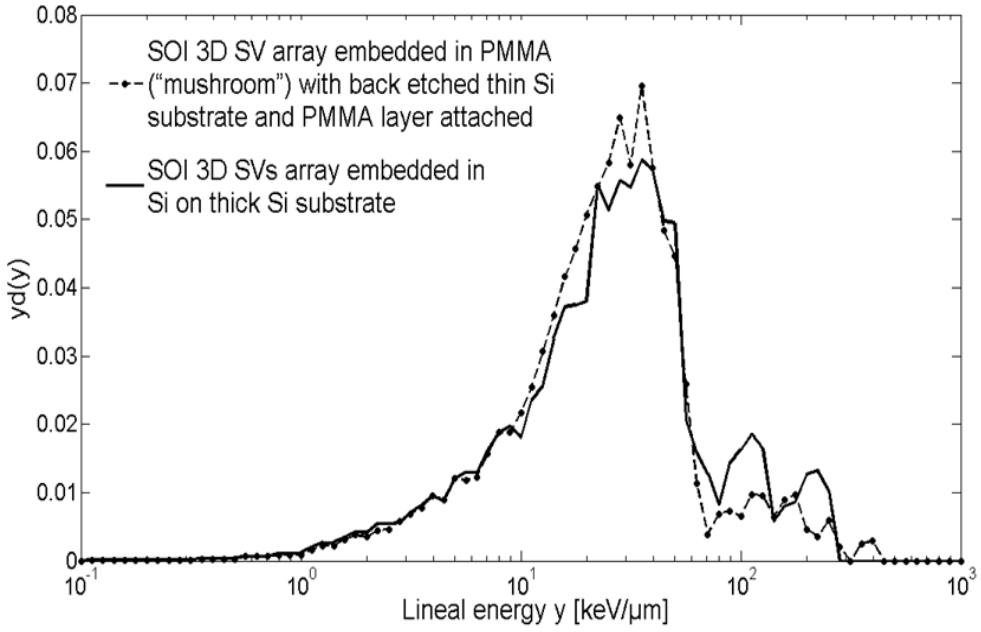

Figure 6.4 Microdosimetric spectra obtained with 3D SV microdosimeters as presented in a Fig. 5.1b mushroom (dashed line) and Fig. 5.1a (solid line) in response to avionic isotropic neutron field.

This study shows that a reduction in silicon nuclear recoils contributed to the novel mushroom microdosimeter design which will subsequently reduce uncertainty in the equivalent deduced dose.

6.3.3 Tissue equivalent conversion for silicon mushroom microdosimeter in response to an avionic isotropic neutron field.

Correcting the tissue equivalence for silicon microdosimeters by scaling the SV was proposed by us, and was used to correct the SOI microdosimeters in Boron Neutron Capture Therapy (BNCT) and the proton radiation field component of space environment [33, 69]. In this study, the tissue equivalent conversion was studied in order to convert the microdosimetric spectrum obtained in the mushroom microdosimeter to microdosimetric spectrum in a tissue equivalent spherical SV, simulated as a muscle tissue sphere with diameter of 20 µm surrounded by 1 mm diameter PMMA sphere (see Fig. 6.5). Fig. 6.6 shows the results of the Geant4 simulation.

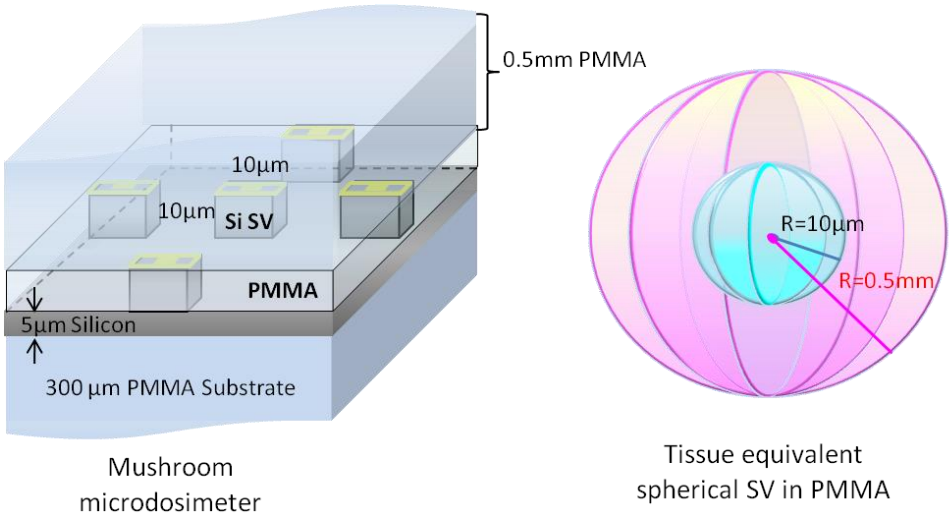

Figure 6.5 Geometry of 3D mushroom microdosimeter as in Fig. 6.1b with and tissue equivalent spherical SV used in the Geant4 simulation.

To convert the microdosimetric spectrum calculated in the mushroom microdosimeter with Si cubic SV 10 µm x 10 µm x 10 µm to tissue equivalent (TE) spectrum for a spherical tissue SV, we compared the mushroom microdosimetric spectrum with the spectrum obtained for a tissue spherical volume surrounded with PMMA. The best match for the spectrum corresponded to a tissue spherical SV with a diameter of 20 µm. In order to convert further silicon to muscle equivalent microdosimetric spectra, the average chord length <l> corresponding to the 20 µm diameter muscle sphere was used. The linear scaling factor of 0.5 between mushroom SV (10 µm side) and muscle spherical SV (20 µm diameter) can be used in the future design of 3D Si microdosimeters. The slightly reduced relative contribution from the recoil protons in the tissue microdosimetric spectrum compared to the mushroom microdosimetric spectrum (main peak) was due to the presence of high LET events, with LET > 200 keV/µm, in the tissue spectrum associated with inelastic neutron reaction on ^{12}C in a muscle tissue sphere, where the weighted concentration of ^{12}C was larger than in PMMA. The minor disagreement in the microdosimetric spectra was also due to differences between the chord length distributions for the silicon cubic SV compared to the spherical muscle SV. Fig. 6.6 shows that the contribution from heavy recoils in the tissue spherical SV surrounded by PMMA produced from neutrons interacting with muscle components such as carbon, oxygen, and nitrogen matched the high LET events in silicon microdosimetric

spectrum converted to tissue equivalence quite well. This analysis shows that apart from providing a high definition SV of the 3D SVs embedded in PMMA, they are better at detecting neutrons and match the TE microdosimetric spectrum better as well.

Fig. 6.7 and 6.8 show the dose weighted components of the microdosimetric spectra for a mushroom microdosimeter converted to tissue, and a tissue microdosimeter respectively. The main dose weighted contribution to both the simulated microdosimetric spectra was from the recoil protons originating in the PMMA converter.

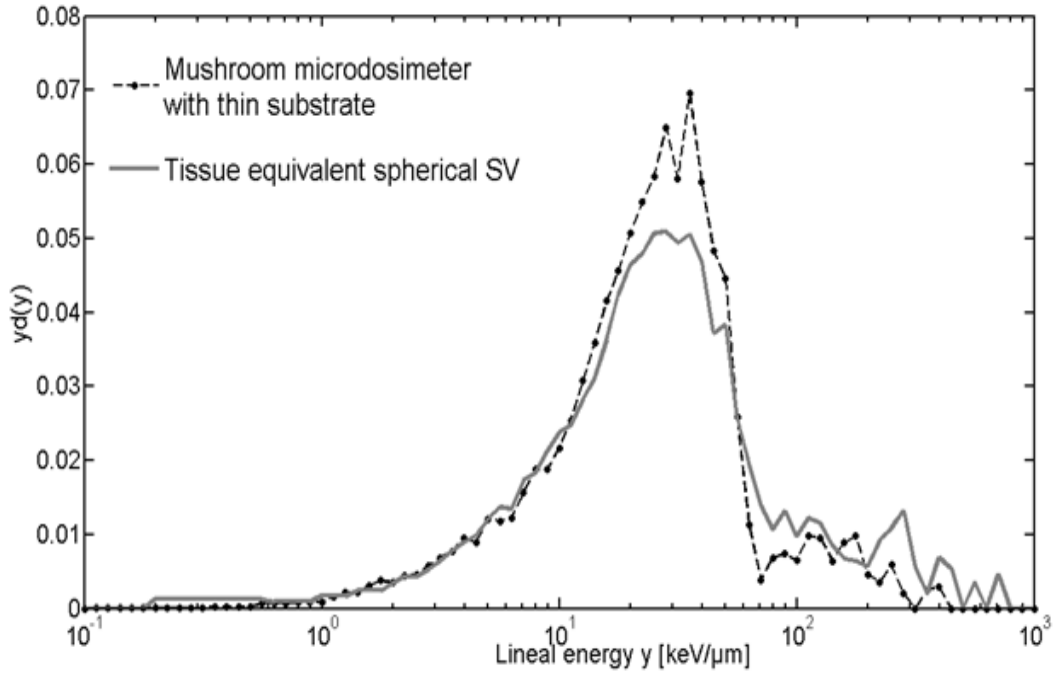

Figure 6.6 Comparison of microdosimetric spectra of the 3D mushroom microdosimeter and tissue equivalent spherical SV.

With the mushroom SOI microdosimeter, as well as the recoil protons, the second largest contribution was from the recoil Si atoms that resulted from the elastic scattering of neutrons on Si, while the smallest contribution came from the alpha particles which originated from inelastic Si (n, α) reactions in silicon SV. In the tissue sphere, SV proton recoils still predominated, and other contributions were mostly from elastically scattered oxygen and carbon and a lot less alpha particle events which originated from O (n, α) and C (n, α) reactions. While the combination of elastically scattered C and O in the tissue SV matched the Si ion contributions in silicon SV quite well, the imbalance in the high energy part of the spectra due to Si (n, α) reactions rather than the C contribution in the tissue SV was obvious, and showed the importance of minimising the Si surrounding the SVs to reduce the contribution of alpha particles to the microdosimetric spectra.

Much smaller dose weighted contribution to the microdosimetric spectrum was observed from oxygen, carbon and nitrogen nuclei in the mushroom microdosimeter, and they are not included in the list of radiation species in Fig. 6.7. These events originated from the PMMA converter and the air volume surrounding the mushroom microdosimeter and contributed to the high LET part of the microdosimetric spectra. The same may be said about the contribution from alpha particles originating from inelastic

reactions and elastically scattered C, O ions for LET spectrum of the SV of the tissue equivalent sphere (Fig. 6.8).

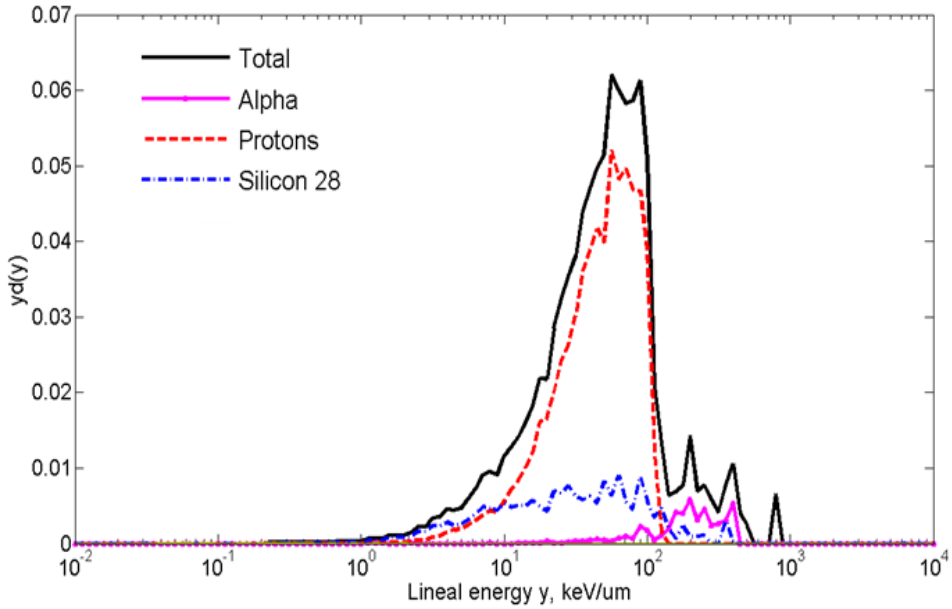

Figure 6.7 The Geant4 simulation of different components that contributed to total lineal energy deposition events in SV of the 3D mushroom microdosimeter. The spectra were converted to muscle using mean chord length MCL of the muscle sphere.

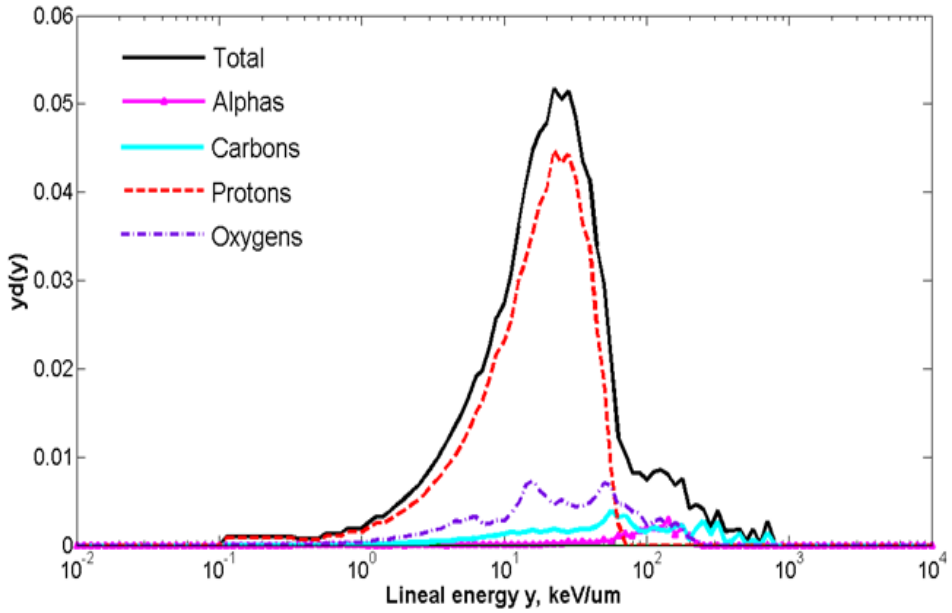

Figure 6.8 The Geant4 simulation of different components which contributed to total lineal energy deposition events in SV of the tissue equivalent sphere.

6.3.4 Comparison microdosimetric spectra for cubic and cylindrical SV.

Fig. 6.9 shows the microdosimetric spectra of the cubic SV and the cylindrical SV of the 3D mushroom microdosimeter where the cylindrical SV produced lineal energy deposition events that were similar to the cubic SV. The slightly different microdosimetric spectra of cubic and cylindrical SV occurred because of variations in the chord length distribution.

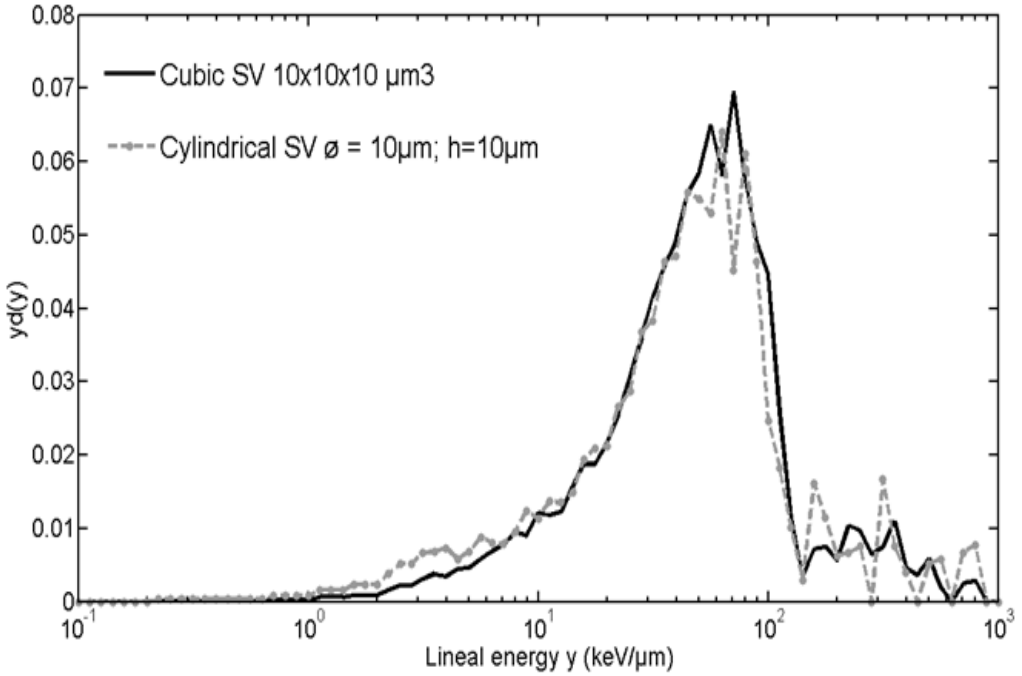

Figure 6.9 Comparison of microdosimetric spectra of the cubic SV and the cylindrical SV of 3D "mushroom" microdosimeter.

6.4 Conclusion

New SOI microdosimeters with a 3D SV array were proposed and their response was modelled with Geant4 Monte Carlo transport code in avionic, ^{252}Cf, and Pu-Be neutron fields. It was shown that the SOI 3D SV mushroom microdosimeter has two main advantages over the SOI microdosimeters with planar SV design: (i) a better defined SV, and (ii) improved tissue equivalency due to the reduced contribution from the silicon recoils and products from inelastic reactions originated from lateral to SV silicon.

The simulations showed that a linear scaling coefficient 0.5 provided a reasonably good conversion of silicon microdosimetric spectrum derived from the 3D mushroom microdosimeter to muscle tissue microdosimetric spectrum. These new improvements to the silicon microdosimeter, including free standing 3D SVs embedded in PMMA, represent a significant step forward in the development of SOI microdosimeters applied in radiation protection and radiation therapy Quality Assurance.

Chapter 7

Large Area 3D-Mesa "Bridge" Microdosimeter: Charge Collection Study

This chapter describes an intermediate step towards a fully 3D microdosimeter with free standing SVs. This microdosimeter has a mesa structure using plasma etching technology at the microelectronic fabrication facility at SPA-BIT, Kiev, Ukraine. The charge collection characteristics of the new device in response to a monoenergetic beam of ions are presented.

7.1 Introduction

Fabrication of the proposed 3D mushroom microdosimeter was presented in chapter 6 and the charge collection of different types of ATLAS 3D detectors and ultra-thin 3D detector were investigated in chapters 4 and 5, respectively. The ATLAS 3D detectors with 285 μm thick substrate fabricated at SINTEF cannot be considered as a microdosimeter due to their

thick sensitive region, but the ultra-thin 3D detector with a 10 μm-thick SOI active region fabricated at CNM, Spain can be used for microdosimetry for measurements in heavy ion therapy when the ion beam is normally incident to the surface of the detector. In this case, the mean chord length of the SV is equal to the thickness of the detector and was 10 μm. In the space environment where radiation is incident on the detector from different directions, the ultra-thin 3D detector cannot be used as a microdosimeter because radiation events travel at oblique angles and along the side of the ultra-thin 3D detector and thus create longer paths. In order to overcome these drawbacks, we have proposed further steps to optimise the SOI microdosimeters with the development of freestanding 3D SVs, a so called "mushroom" microdosimeter which was presented earlier in chapter 6. However, to fabricate real 3D SVs on a silicon substrate is complex, so as an intermediate step towards free-standing 3D SVs, an SOI microdosimeter with 3D mesa SVs was produced by etching the silicon surrounding the SVs whilst leaving thin silicon "bridges" between the SVs to support the aluminum tracks. Mesa structures have been implemented previously in a second generation CMRP microdosimeter [28], but there was a low yield of SVs because the Al tracks were damaged when lifted over the steep 10 μm mesa structure of each SV. The new microdosimeter is called a "bridge" microdosimeter because it has thin Si bridges connecting the SVs.

The purpose of this study is to investigate the charge collection characteristics and the effect of etching to avoid charge sharing between the SVs in the new microdosimeter using the IBICC technique.

7.2 Material and Methods

7.2.1 Design of the 3D mesa bridge microdosimeter

The newly developed bridge microdosimeter has a large sensitive area of 4.1 x 3.6 mm^2 designed for use in low dose rate environments such as aviation and space. This device is segmented into three sections in order to reduce the capacitance and reverse current of each segment. The microdosimeter is based on an array of planar 30 x 30 x 10 µm cubic SVs fabricated on a high resistivity of 3 kΩ.cm n-SOI active layer 10 µm thick, and a low resistivity supporting wafer. Layers of phosphorus silicate glass (PSG) and SiO_2 were deposited on top of the device, and each SV was fabricated using ion implantation to produce the square p-i-n diode structure. The 10 µm thick mesa structures of each SV were produced using an ion plasma etching process. The even and odd rows of SVs were read out independently to avoid events in adjacent sensitive volumes being read as a single event, especially in the case of oblique charged particle tracks.

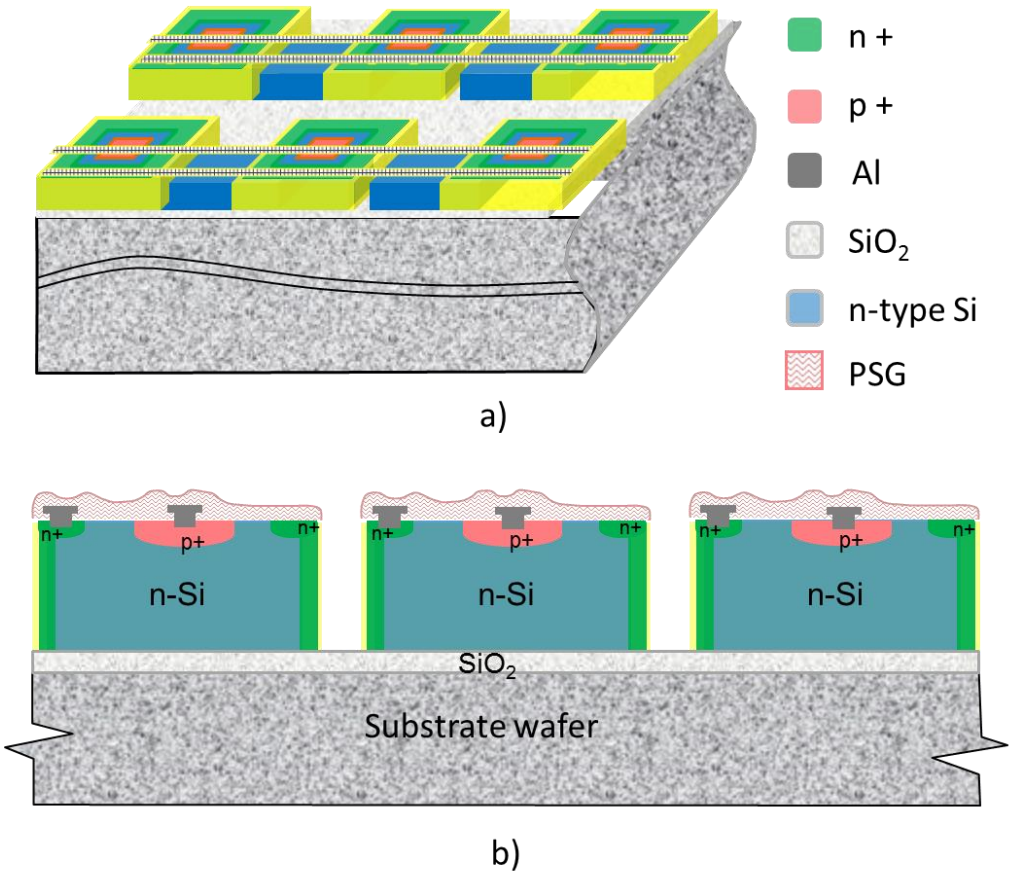

Figure 7.1 A schematic of the design of SOI bridge microdosimeter. a) 3D view; b) A cross-section of the microdosimeter from behind the silicon bridge.

Fig. 7.1 shows a simplified section of the 3D mesa bridge microdosimeter designed to provide well-defined 3D SVs as well as eliminate charge sharing between neighbouring SVs.

7.2.2 Scanning Electron Microscopy Study

The structure of the "bridge" microdosimeter was studied using a JEOL Scanning Electron Microscope (SEM) at the Australian Institute for

Innovative Materials (AIIM), University of Wollongong. This SEM can produce 3D images with a resolution of approximately 2 nm.

7.2.3 Ion Beam Induced Charge (IBICC) Technique

The charge collection efficiency for the 3D mesa bridge microdosimeter was investigated using the IBICC technique with the ANTARES heavy ion microprobe at ANSTO, which was described earlier in chapter 2. A monoenergetic beam of ions focused to a diameter of approximately 1 µm was raster scanned over the surface of the microdosimeter. The ions and their energies used in this study are shown in Table 7.1. The LET values were taken from SRIM 2008.

Table 7.1 Ions specifications used in IBICC study

Ion	Energy (MeV)	Entrance LET in Si (keV/µm)	Range in Si (µm)
^{1}H	2	26.09	47.69
^{4}He	5.5	133.4	28.02

7.3. Results and Discussions

7.3.1 SEM Images of 3D mesa bridge microdosimeter

Fig. 7.2 a, b shows SEM images of arrays of SVs where both the etched region outside the SVs and Al tracks connecting the p^+ core and n^+ lateral regions are clearly visible.

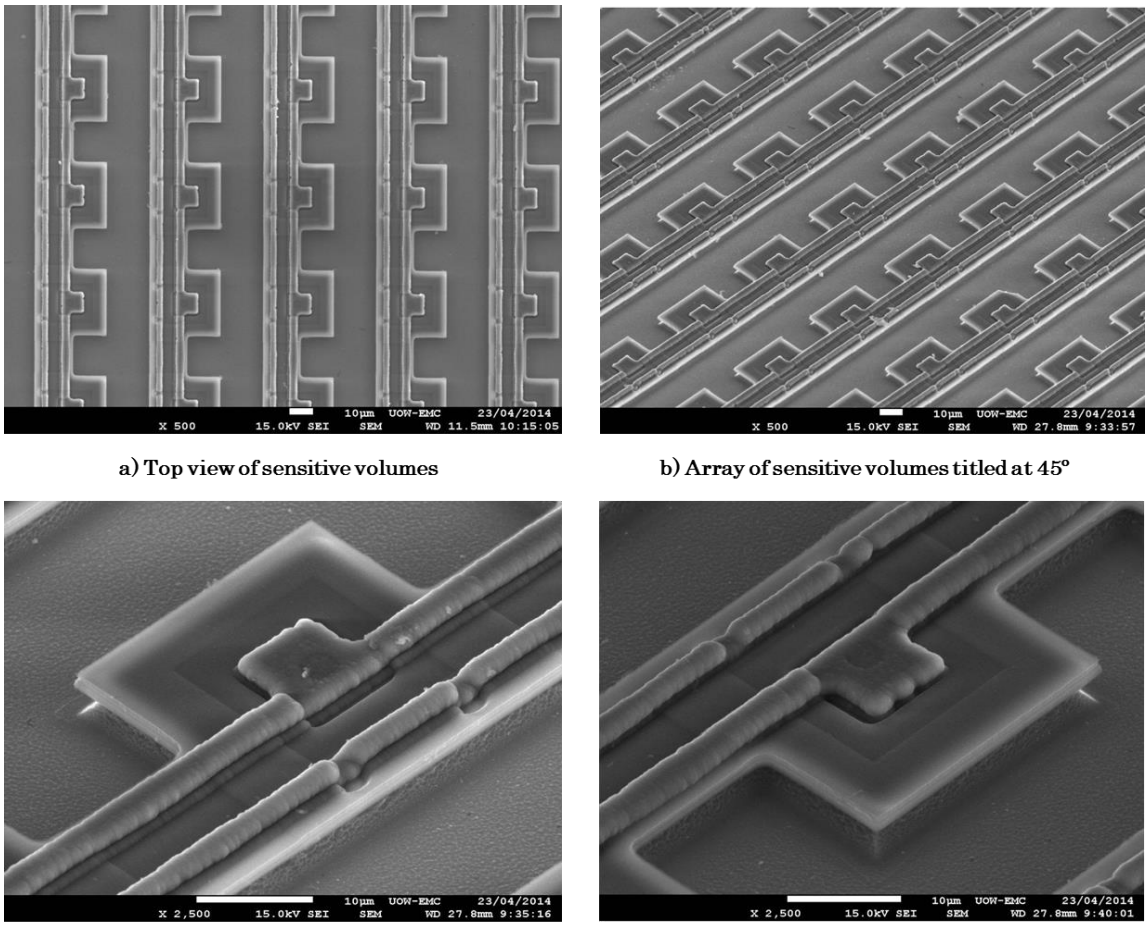

a) Top view of sensitive volumes

b) Array of sensitive volumes titled at 45°

c) Single sensitive volume

c) Rotated angle of single sensitive volume

Figure 7.2 SEM images of arrays of SVs

Fig. 7.2 c, d shows magnified images of single SVs. It is possible to see that the 3D SV has a truncated square pyramid shape due to different etching time along the SVs depth. The top layer above the SVs (Fig. 7.2 c, d) is the SiO_2 and Phosphor Silicate Glass (PSG) layers where the original size of the 30 µm x 30 µm SV was not etched due to selective etching.

Fig. 7.3 shows a SEM cross sectional image of a single SV. A 2 µm thick layer of oxide can be seen between the active region and support wafer.

Silicon surrounding the SV was etched to a depth of approximately 4.5µm, leaving a 5µm thick layer of silicon due to incomplete etching.

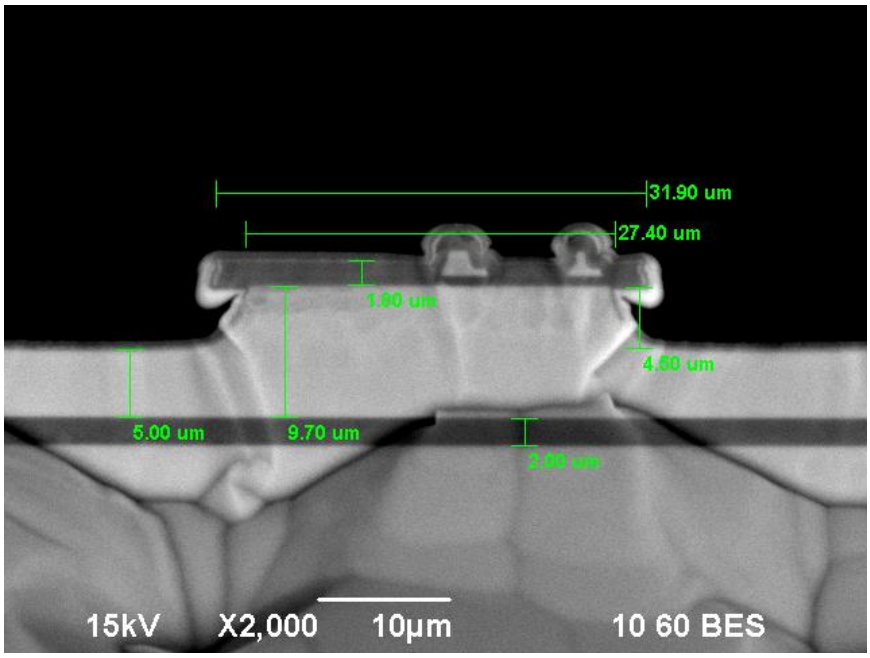

Figure 7.3 Cross-section image of single SV obtained in one plane.

7.3.2 Charge Collection Studies

7.3.2.1 Response of bridge microdosimeter to 2 MeV H

The response of the n-SOI bridge microdosimeter to 2 MeV H^+ ions is presented in Fig. 7.4. The peak of deposited energy distribution in the 10 µm bridge microdosimeter was approximately 250 keV which agreed with the expected maximum value of 260 keV from 2 MeV H^+ ions in 10 µm of silicon, as calculated by SRIM 2008 [57].

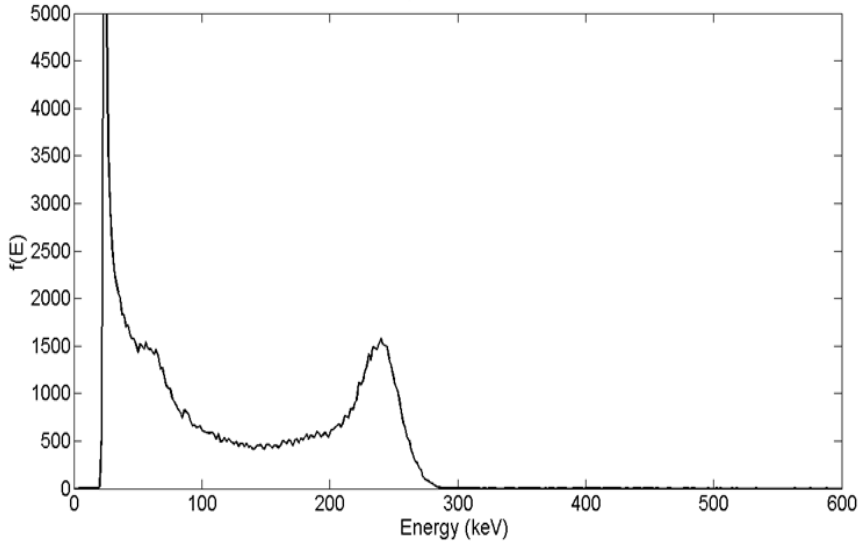

Figure 7.4 Energy spectrum obtained from 10 µm thick n-SOI bridge microdosimeter irradiated with 2 MeV H ions. The detector was biased at -10V.

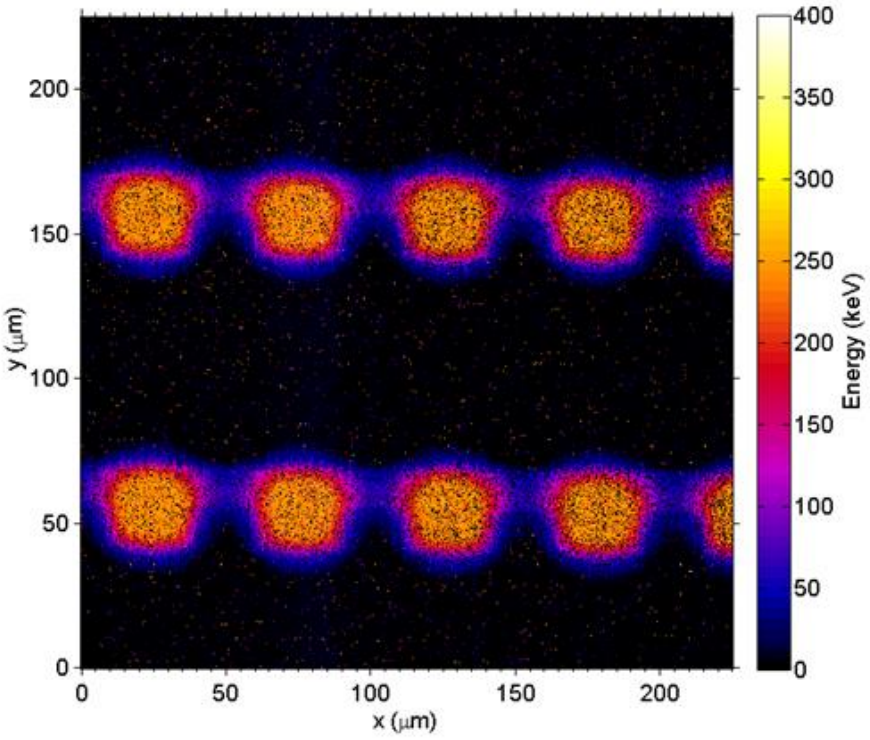

Figure 7.5 Median energy map illustrating the spatial distribution of energy deposited by 2 MeV H ions in the SVs of the even arrays. The detector was biased at -10 V.

Fig. 7.5 shows the charge collection in the SVs of 2 adjacent rows of an even array at -10 V bias while the odd array was also biased at -10V bias. Very low energy events with less than 40 keV occurred when the ions were incident outside the SVs. The energy threshold was as low as 16 keV, which corresponded to around 0.7 keV/µm of lineal energy threshold in a tissue equivalent SV. No cross talk was observed between the odd and even arrays because they were physically and electrically isolated by the etching of silicon surrounding each SV. Fig. 7.6 shows the charge collection in a single SV at different biases. Even without bias almost 100% charge collection efficiency (CCE) in a circular shape under the 10 µm x 10 µm core p^+ region of the SVs occurred, while at -10 V bias the charge collection region conformed to the physical shape of the SV. In Fig. 7.6, the white dashed square represents an area of 28 µm x 28 µm, which corresponds to the edge of the n^+ region of the SV, as seen in Fig. 7.1.

The charge collection region enclosed by the yellow dashed line (square 1) has 100% CCE which corresponds to a 20 µm x 20 µm area surrounded by the n^+ ion implanted region of 30 µm x 30 µm (Fig. 7.6 b). The region enclosed between square 1 and the white dashed line (square 2) corresponds to the region deposited by H^+ ions with energies between 170 keV and 200 keV, having slightly less than 100% CCE. This region corresponds to the n^+ implanted region of the 3D SV. A further reduction of CCE can be seen in the 3 µm wide region of the SV between square 2 and the red dashed line

(square 3). This was due to the combined effect of reduced electric field close to the boundary of the 3D SV (diffused charge collection) and partial energy deposition due to protons traversing the sides of the truncated pyramid of the 3D SV with a path that was less than 10 µm long. The charge collection image was 30 µm x 30 µm, which corresponded to the large base of the truncated square pyramid shape of the SV. The observed charge collection in the 3D SV corresponded to the etching pattern of silicon. A slight propagation of the diffused charge collection occurred outside the geometrical dimensions of the square 3D SV along the Si bridge (pink tails), and it is shown in Fig. 7.6b.

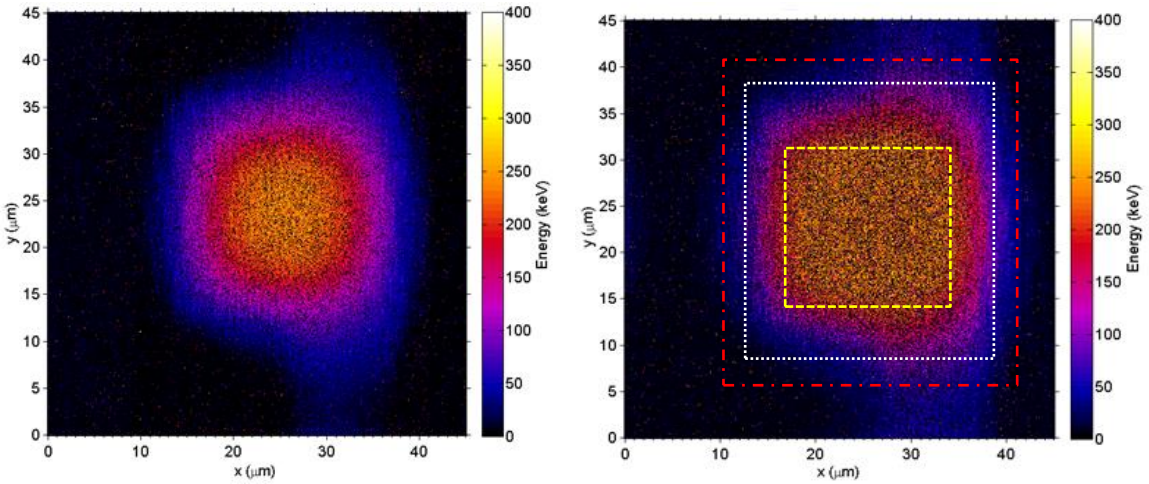

(a) (b)

Figure 7.6 Median energy map illustrating a single SV when biased at a) 0 V and b) -10V.

Although a large amount of silicon outside the SVs was etched away, charges produced by events occurring in the silicon bridge contributed

slightly to the total charge collected in the 3D SV through lateral diffusion. Despite this, the amount of charge being collected outside the SV was low compared to previous generations of SOI planar microdosimeters [28], [29], [31], which demonstrated the advantages that that semi-3D SVs have over traditional planar designs. Full etching of the surrounding silicon down to the silicon oxide layer of the SOI wafer is expected to fully remove events from outside the SVs. The truncated pyramid shape of the SV can be taken into account by calculating the average chord length through simulations used for microdosimetric spectra derivation.

7.3.2.1 Response of bridge microdosimeter to 5.5 MeV He^{2+}

The response of the bridge microdosimeter was further investigated using 5.5 MeV high LET He^{2+} ions. Fig. 7.7 shows the MCA spectra and median energy maps obtained from the even array readout only. A microbeam was scanned across the microdosimeter with a scanning area of 0.9 mm x 0.9 mm, while the microdosimeter was biased at 0 and -10 V. At 0 V the MCA energy spectrum did not show a clear peak due to a diffusion charge collection through the SVs, but at -10 V a 1400 keV peak was observed. This agreed with the expected maximum value of 1480 keV from 5.5 MeV He^{2+} in 10 µm silicon and SiO_2 over-layer calculated by SRIM [57]. The SEM images presented in section 7.3.1 showed that the silicon surrounding the SVs was not completely etched, leaving an active 5 µm layer

of silicon on the SOI device, leading to very low energy events in the energy spectrum.

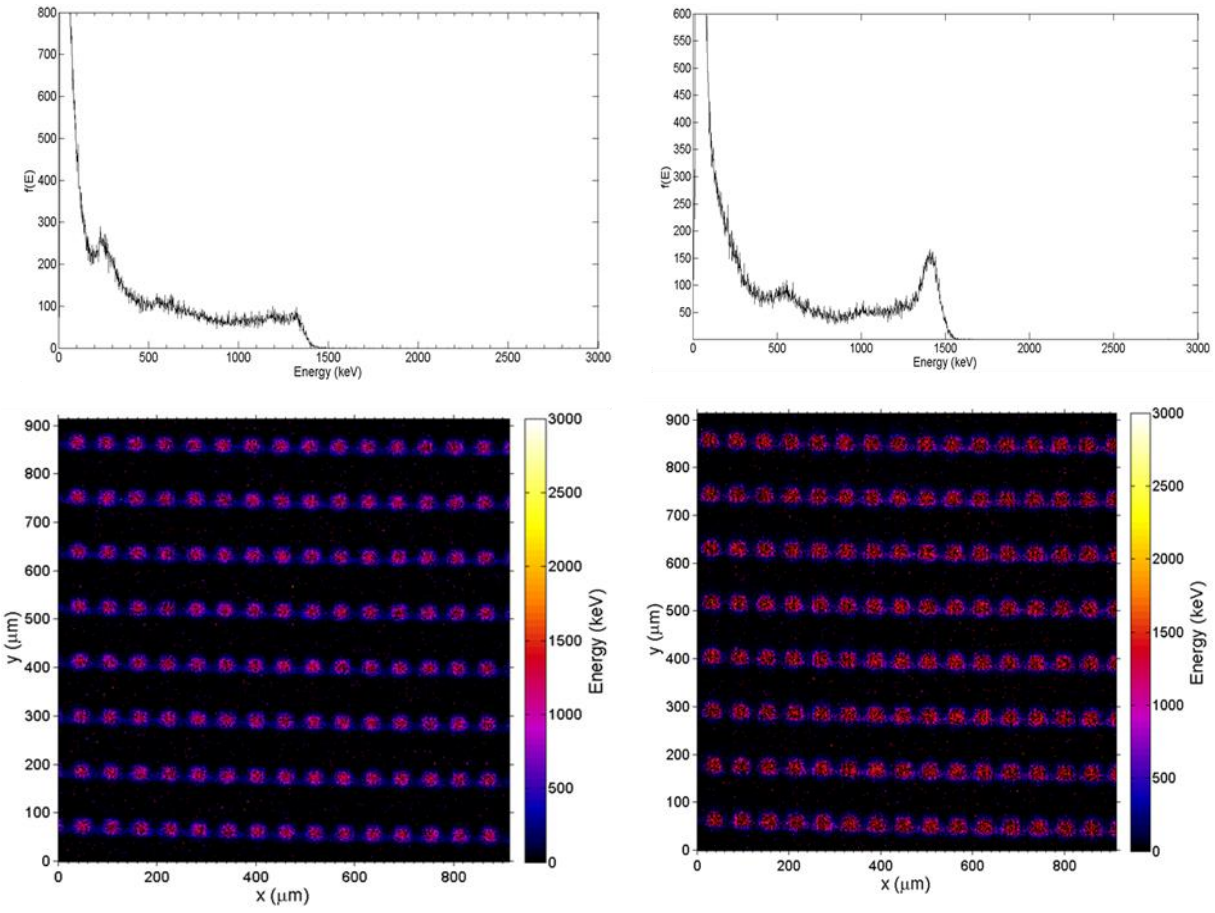

a) 0V

b) -10 V

Figure 7.7 Response of 3D even array of the mesa bridge microdosimeter to 5.5 MeV He^{2+} at different biases. (a) Energy spectrum and median energy map for 0V bias. (b) Energy spectrum and median energy map for -10 V bias. The data were obtained using 3 x scan size which corresponded to a scanning area of 0.9 mm x 0.9 mm.

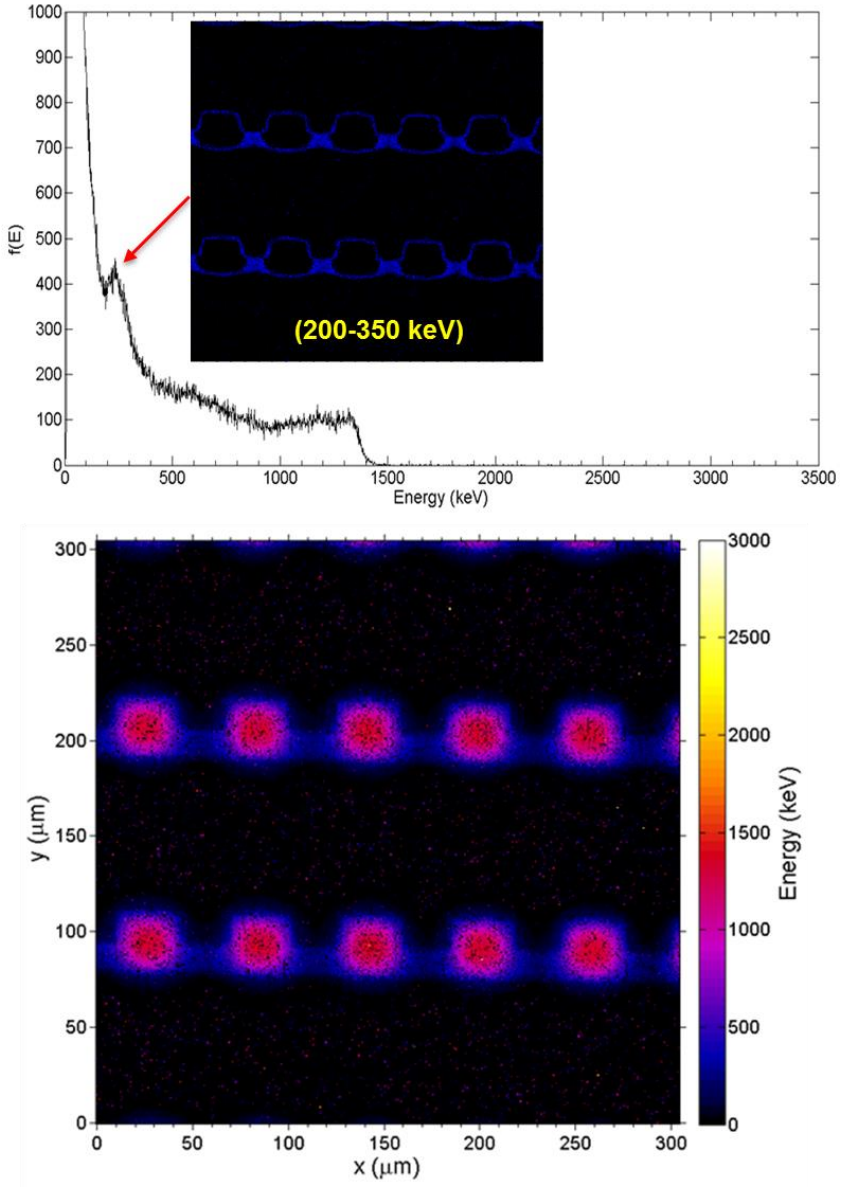

Figure 7.8 Response of 3D mesa bridge microdosimeter to 5.5 MeV He^{2+} at 0 V bias. (a) Energy spectrum with the median energy window consisting only of events in the lower energy peak, as indicated by the arrow. (b) Median energy map. The data was obtained using a scanning area of 0.3 mm x 0.3 mm.

A closer view of the charge collection in the device was obtained using a smaller scanning area of 0.3 mm x 0.3 mm (Fig. 7.8). The top image of Fig. 7.8 indicates that the peak seen at around 250 keV was mostly due to charge collection from the bridge region that connects the SVs.

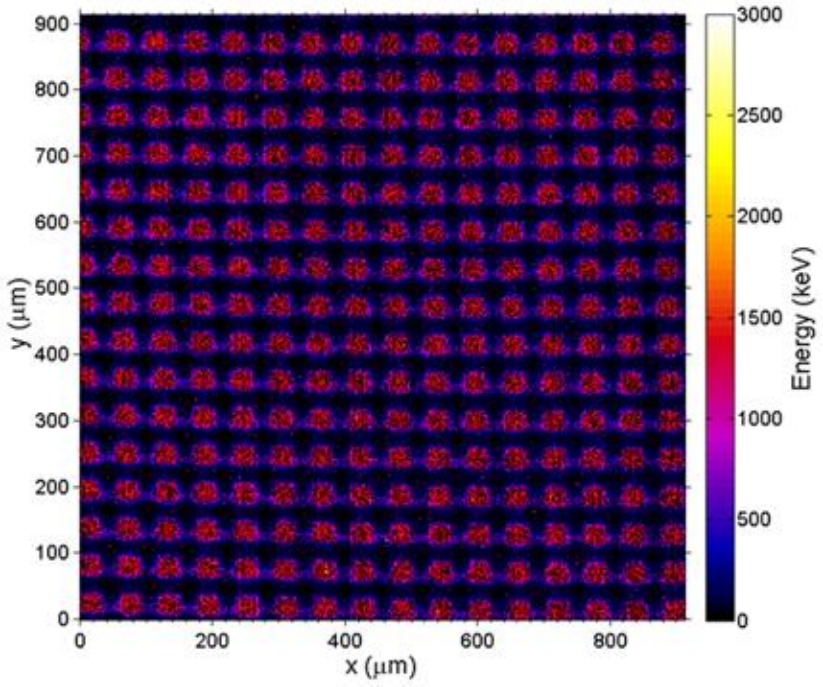

Figure 7.9 Response of the microdosimeter at -10 V (odd and even arrays are connected in parallel). The scanning area was 0.9 x 0.9 mm^2.

Fig. 7.9 shows the response of the bridge microdosimeter when odd and even arrays were read out in parallel and biased at -10 V. All the SVs were functioning and a 100% yield was demonstrated.

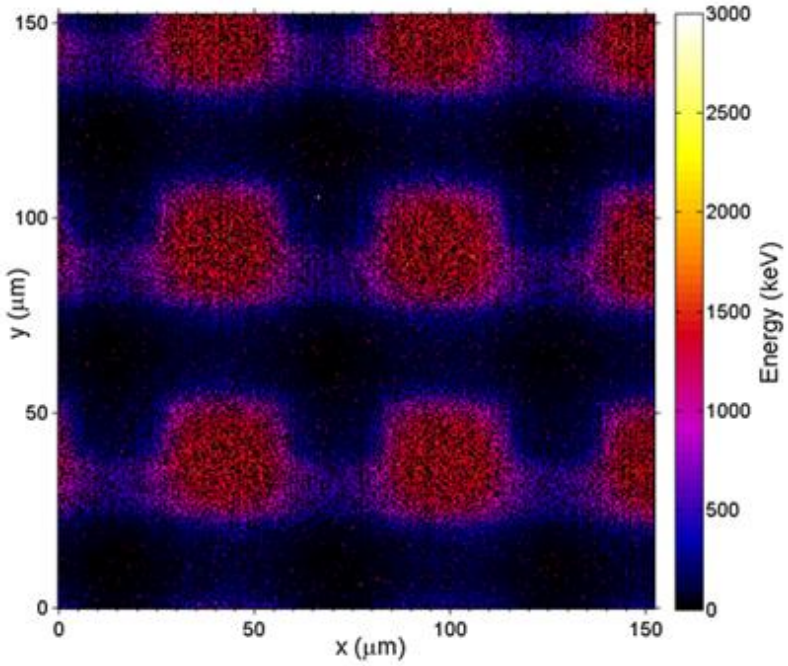

Figure 7.10 Response of the microdosimeter at -10 V (odd and even arrays were connected in parallel). The scanning area was 150 x 150 μm^2.

Fig. 7.10 provides a closer image of the charge collection characteristics seen in the SVs. An approximately square shape was seen, which agreed with the design. A lower charge collection region can be seen surrounding the SVs (purple colour shown in the median energy map), this region is related to boundaries of the truncated pyramid SVs (SEM images presented in section 7.3.1) which have shorter paths than when the particles are perpendicularly incident on the microdosimeter, as was seen with H^+ ions.

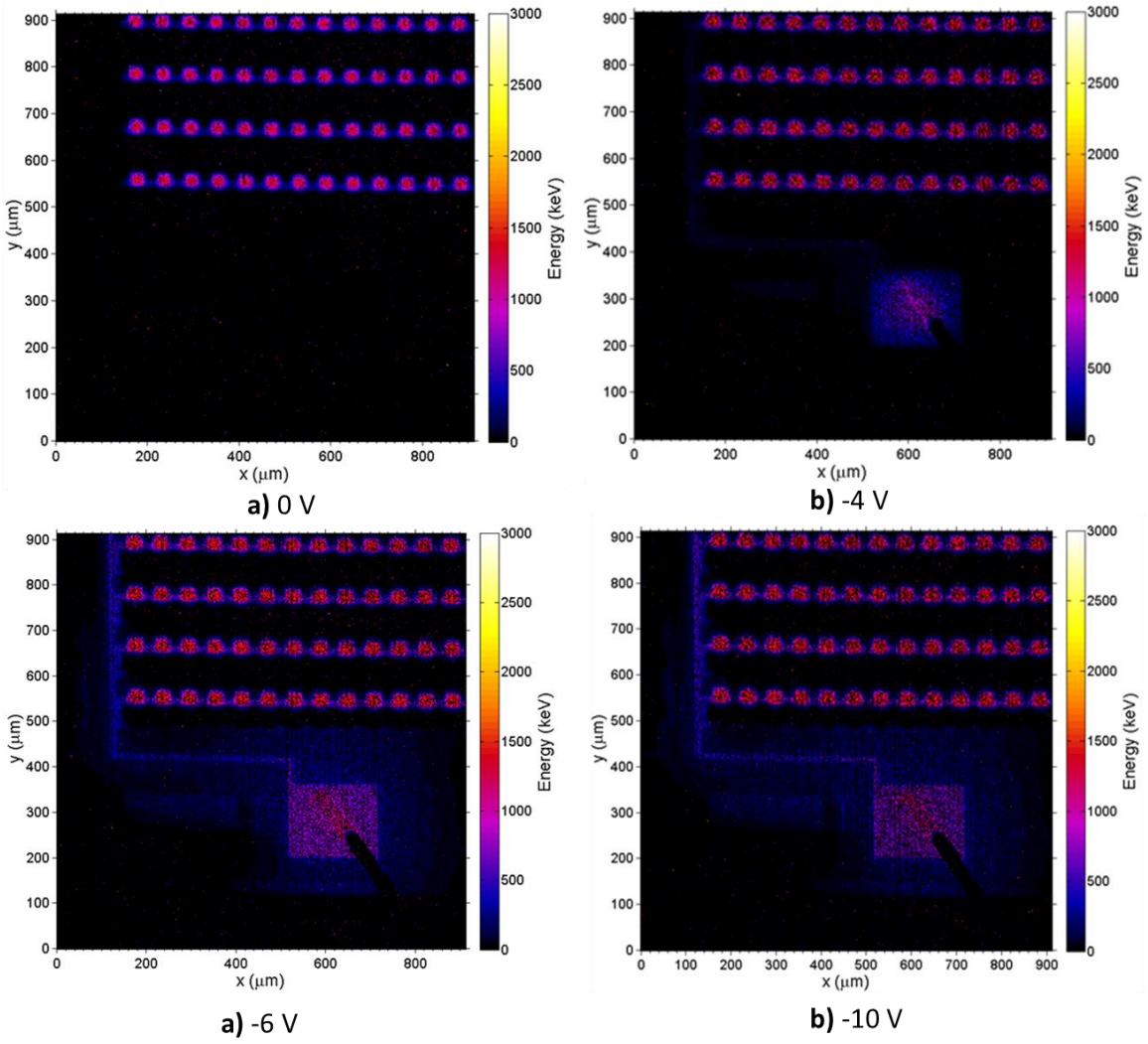

Figure 7.11 Charge collection characteristics of the device near the bonding pad at (a) 0 V, (b) -4 V, (c) -6 V and (d) -10 V.

Fig. 7.11 shows the charge collection under the Al tracks and bias pads connected to the p^+ cores of the SVs. At 0 V, there was no charge collection in these region (Fig. 7.11a), but at -4 V, the charge began to collect in the pad and extended along the aluminum track as the bias increased. This can be explained by the creation of an inversion layer under the oxide of the MOS

capacitor that produced a thin depleted region. This effect can be eliminated by implanting an n+ ion under the oxide, below the Al tracks and pad.

7.4. Conclusions

The CMRP 3D-mesa bridge microdosimeter was investigated in detail using scanning electron microscopy and 2 MeV H^+ and 5.5 MeV He^{2+} ion microbeams. When the silicon surrounding the SVs was etched, it showed low energy artifacts compared to the planar SOI microdosimeters, but the remaining un-etched silicon meant that some low energy events could still be seen. Only minimal charge diffusion to the SVs was seen, mostly from the silicon bridge close to the SVs. This bridge SOI microdosimeter was and is an intermediate step towards a fully 3D microdosimeter with free-standing 3D SVs microdosimeter. Future development of the silicon microdosimeters will include the fabrication of this 3D "mushroom" microdosimeter as well as an improved 3D mesa "bridge" microdosimeter. The improved 3D mesa bridge microdosimeter will be fully etched down to 10-µm depth and additionally, an n^+ stop layer will be ion implanted under the Al tracks and contact bias pads to eliminate charge collection below these regions at greater biases. Future work will also be focused on comparing the experimental response of the improved 3D bridge and 3D mushroom microdosimeters in a ^{12}C ion therapy beam with Geant4 simulations.

Chapter 8

[5]Mixed Radiation fields components in ^{12}C Heavy Ion Therapy: Geant4 Simulation of ΔE-E Telescope Response

This chapter describes a new method of using a monolithic ΔE-E telescope to characterise the radiation field produced by the ^{12}C ion beam in terms of the different particle components which make up the mixed radiation field, as well as the microdosimetric spectra that enable the RBE to be determined.

8.1 Introduction

Charge particle therapy with ^{12}C ions has the advantage of an enhanced physical dose distribution over X rays due to the Bragg Peak (BP) energy deposition profile. The Relative Biological Effectiveness (RBE) in the BP is higher with respect to X-ray radiotherapy and proton therapy (2.5 for ^{12}C

[5] This chapter has been submitted to Physics Medicine and Biology:
Linh T. Tran, David Bolst, Susanna Guatelli, Dale A. Prokopovich, Ying C. Keat, Marco Petasecca, Michael L. F. Lerch, Mark I. Reinhard, Alberto Fazzi, Elena Sagia, Stefano Agosteo, Naruhiro Matsufuji and Anatoly B. Rosenfeld (2014). High spatial resolution microdosimetry with ΔE-E detector on ^{12}C beam: Monte Carlo simulations.

ions, 1.0 for X-rays and 1.1 for protons) [70], [71]. The RBE of a ^{12}C therapeutic beam changes dramatically with depth, especially towards the end of the Spread Out Bragg Peak (SOBP), due to the very high Linear Energy Transfer (LET) of the ^{12}C ions in this region. Additional complexity in the determination of the RBE is associated with the nuclear fragmentation process in the SOBP. ^{12}C fragmentation produces lighter charged ions with lower LET as well as neutrons, which results in a slight reduction of the primary ^{12}C ion with increasing depth, as well as the production of a mixed radiation field which causes a low dose "tail" that extends beyond the distal edge of the SOBP [72]. The shape of the SOBP is formed through a superposition of multiple monoenergetic ^{12}C components of different energies that result in the formation of RBE ripples along the plateau of the SOBP.

It is important to derive the RBE in the SOBP and beyond because the RBE is needed as a parameter, as well as the tumour volume dose, to evaluate the risk of secondary cancer to nearby healthy Organs At Risk (OAR) outside the treatment field.

An effective approach to derive the RBE for a ^{12}C ion beam is microdosimetry which involves measuring the frequency spectra in terms of the stochastic lineal energy deposition in a micron sized tissue equivalent sensitive volume (SV) *f(y):*

$$y = \frac{E}{\langle l \rangle} \tag{8.1}$$

where y is the lineal energy deposition, E is the energy deposition with an average chord length of $\langle l \rangle$. Once the microdosimetric spectra of a radiation field is known, the microdosimetry calculated RBE_{μ} [73] can be deduced from:

$$RBE_{\mu} = \int r(y) d(y) dy \tag{8.2}$$

where $r(y)$ is a set of RBE-weighting coefficients obtained from radiobiological experiments [74] and $d(y)$ is the weighted distribution of lineal energy y.

The ΔE-E telescope is a detector used to identify products from nuclear reactions and is used for fragment particle identification [75], [76]. The latest version of the monolithic telescope has a pixelated ΔE detector with SVs similar in geometry to the CMRP SOI microdosimeter. The pixelated ΔE stage allows the device to be used as a microdosimeter while also providing particle identification [77].

The ΔE-E telescope was used to derive the RBE based on the microdosimetric approach, at defined positions along and downstream of the 100 MeV protons BP and SOBP at the proton therapy facility at Loma Linda University, USA [78]. It was demonstrated that the maximum RBE value does not coincide with the peak of physical dose but it is slightly downstream

of it. Conventional treatment planning assumes an RBE of 1 while proton treatment planning assumes a peak RBE of 1.1. An RBE estimation of the SOBP using the ΔE-E telescope shows a higher than expected RBE along the SOBP.

CMRP, in collaboration with HIMAC and Politecnico di Milano, are currently investigating the use of the ΔE-E telescope for Heavy Ion Therapy Quality Assurance in terms of measuring the microdosimetric spectra to determine the RBE both in-field and out-of-field of the ^{12}C ion beam therapeutic radiation field. The project involves experimental characterisation of the device at the HIMAC facility, Chiba city, Japan, coupled with Geant4-based simulation studies.

This chapter presented the simulation results of a characterisation of the ^{12}C beam mixed radiation field and of the ΔE-E telescope response to the in-field and out-of-field of a 290 MeV/u ^{12}C beam. Particular attention was devoted to studying the ^{12}C fragmentation and neutrons contribution to the RBE in the distal part and downstream of the Bragg peak. Experimental measurements at HIMAC and a comparison of the simulation and experimental results will be presented in following chapters.

8.2 Materials and Methods

8.2.1 ΔE-E Telescope System Description.

The monolithic ΔE-E telescope, manufactured at ST Microelectronics (Catania, Italy), consists of a 1.8 μm ΔE and a 500 μm E thick stage manufactured from a single monolithic silicon substrate. The detector provides a two-dimensional scatter plot of the ΔE vs ΔE + E energy deposition via coincidence data acquisition.

A schematic of the ΔE-E telescope is shown in Fig.1, where a thin metallised n^+ surface layer was used as the entry window for the ΔE stage with a p^+ buried anode common ground contact separating the two stages of the detector. The entire rear side of the detector was covered by an n^+ surface layer with Al metallisation. The n^+ contact ΔE was biased at +5 V and the n^+ contact of the E stage was biased at +100 V relative to the p^+ buried layer to fully deplete.

The ΔE-E particle telescope can be operated in a number of modes by utilising the ΔE and E detectors separately or in coincidence. When operated separately, an ΔE detector acts like a microdosimeter that can be used in accelerator experiments where the beam is normally incident to the surface of the detector. The mean chord length is defined by the thickness of the ΔE detector (1.8 μm) for normally incident radiation.

The ΔE-E telescope is good at distinguishing different types of particles with ranges of less than 500 μm in silicon, while also providing microdosimetric spectra with sub-millimetre spatial resolution along the

Bragg Peak. Sub-millimetre spatial resolution is impossible to achieve using existing Tissue Equivalent Proportional counters (TEPC).

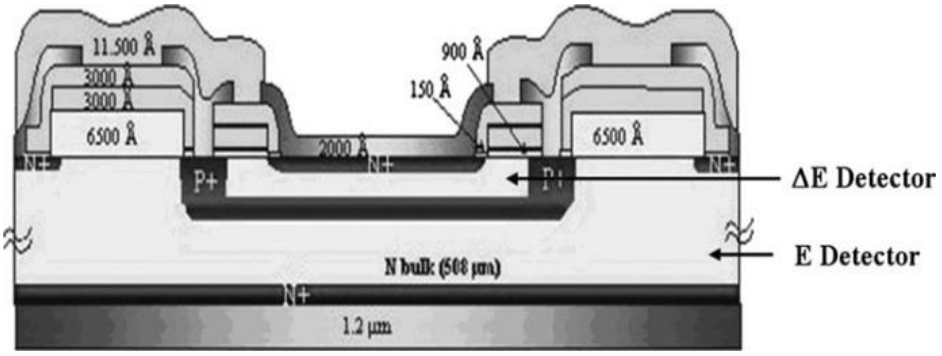

Figure 8.1 Schematic of ΔE-E telescope. Figure adapted from [79].

8.2.2 Geant4 Simulation Application

The Geant4 version 4.9.6.p01 [80] was used to model the radiation field and the response of the ΔE-E telescope to a 290 MeV/u ^{12}C beam in a PMMA phantom. The electromagnetic interactions of particles were described by means of the Geant4 Standard Physics Package (*G4EmStandardPhysics_option3*). The hadronic interactions were described by means of the *QGSP_BIC_HP* physics list. Ion nuclear interactions were modelled with the *G4IonBinaryCascadeModel*. The simulated PMMA slab phantom was simulated to be the same as the PMMA phantom used for experimental measurements, it has dimension of 30 x 30 x 30 cm^3 and the PMMA with elemental composition was taken from ICRU [81] with a density of 1.17 g/cm^3.

8.2.2.1 290 MeV/u 12C radiation field characterisation

The simulated radiation field study was carried out by considering the experimental setup used at HIMAC, Japan with 290 MeV/u ^{12}C beam. The ^{12}C ion beam was simulated with an area of 1 x 1 mm^2, and the distance from the ion beam line exit window to the surface of the phantom was 10 m, as shown in Fig. 8.2. An 0.4 mm thick lead scatterer was used for beam scattering and was placed at 5 mm from the ion beam line exit window. A 50 mm thick brass collimator with a square hole of 10 x 10 cm^2 area was placed at 30 cm from the surface of the phantom. The characteristics of the radiation field produced by incident ^{12}C ions were studied in the PMMA phantom. The output of the simulation consisted of the energy deposition in the PMMA phantom as well as the position of secondary particles generated within the phantom. The energy deposition derived from the incident beam and from the secondary nuclear fragments was tallied separately. The Bragg Peak was calculated along the direction of the incident beam with 0.1 mm spatial resolution, using the energy deposition events. The deposited energy at a given depth and lateral position was stored in the 2D histogram which had 1 mm^2 pixels.

8.2.2.2 ΔE-E telescope response characterisation.

The response of the ΔE-E telescope to a 290 MeV/u ^{12}C beam was studied to verify how well the device could identify different nuclear fragments in-field and out-of-field. The types and energies of secondary particles produced during the simulation were recorded and used to identify the particles detected by the particle telescope shown in the scatter plot.

The geometry of the ΔE and E stages were modelled as 1 mm x 1 mm x 1.8 μm and 1 mm x 1 mm x 500 μm silicon slabs staked without a gap between them. The ΔE-E telescope was placed in the PMMA phantom with direct contact between the ΔE stage and the PMMA. The Geant4 cuts per region [49] were used to reduce the simulation times without affecting the accuracy of the results. The size of the region was chosen based on a conservative consideration of the range of secondary electrons produced by the primary ^{12}C ion beam field. The maximum range of delta electrons produced by a 290 MeV/u ^{12}C was approximately 2.4 mm in PMMA (NIST database [82]). Based on these considerations the region was centred with the detector, with a lateral size of 5 mm to track all δ-electrons at the required accuracy in the surrounding ΔE-E telescope. The range cut was set low enough to track the δ-electrons down to the low energy limit of the Geant4 Standard Electromagnetic Physics of 1 keV. Outside the region, the

cut was set to 2 mm to reduce computation time because those δ-electrons with a range smaller than 2 mm cannot reach the ΔE-E telescope.

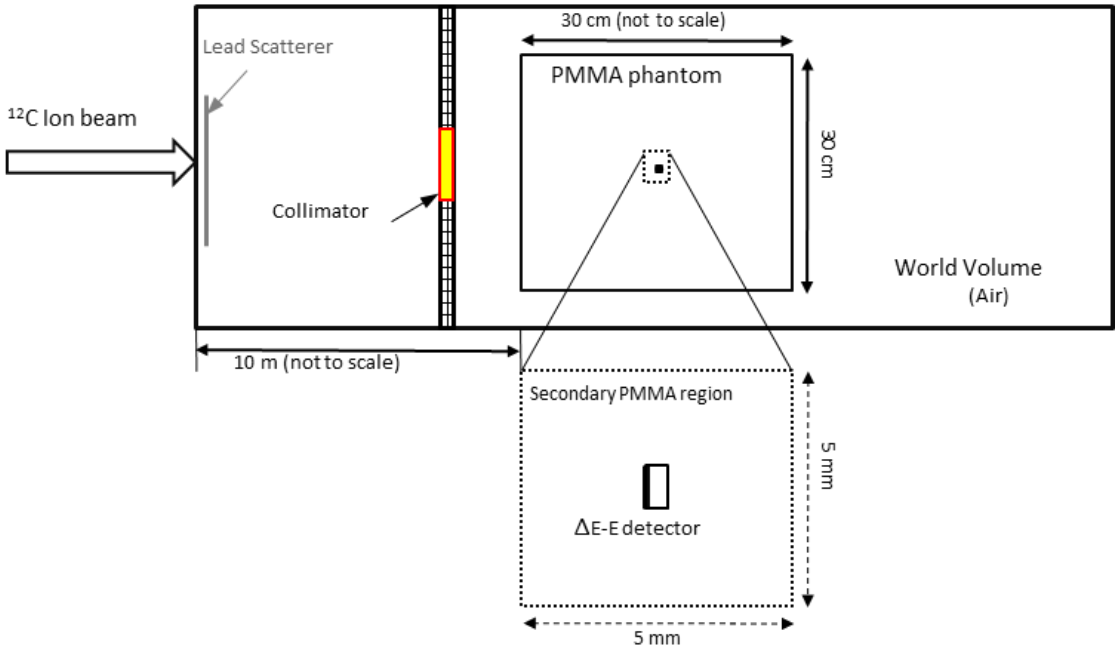

Figure 8.2 Schematic representation of the simulated geometry of ΔE-E telescope in the Geant4 simulation.

Fig. 8.2 shows the simulated experimental set-up. The energy deposition was calculated per incident particle on the device, depositing energy in both ΔE and E stages (coincidence condition). The energy deposition caused by δ-electrons and other secondary particles originating inside the two detector stages was assigned to the parent particle incident on the device. The kinetic energy, charge, and baryon number of the particle producing the energy deposition event in the device were scored.

8.2.3 In-Field and Out-of-Field Response of the Detector

The in-field and out-of-field response of the ΔE-E telescope was obtained at 15 positions along the axis of irradiation, that is: 0, 10, 58, 106, 125, 126.5, 127, 128, 128.5, 129.5, 130, 131.5, 136.5, 141, and 155 mm. These positions were selected to encompass both in-field and downstream of the BP measurements as well as to match the experimental measurement positions.

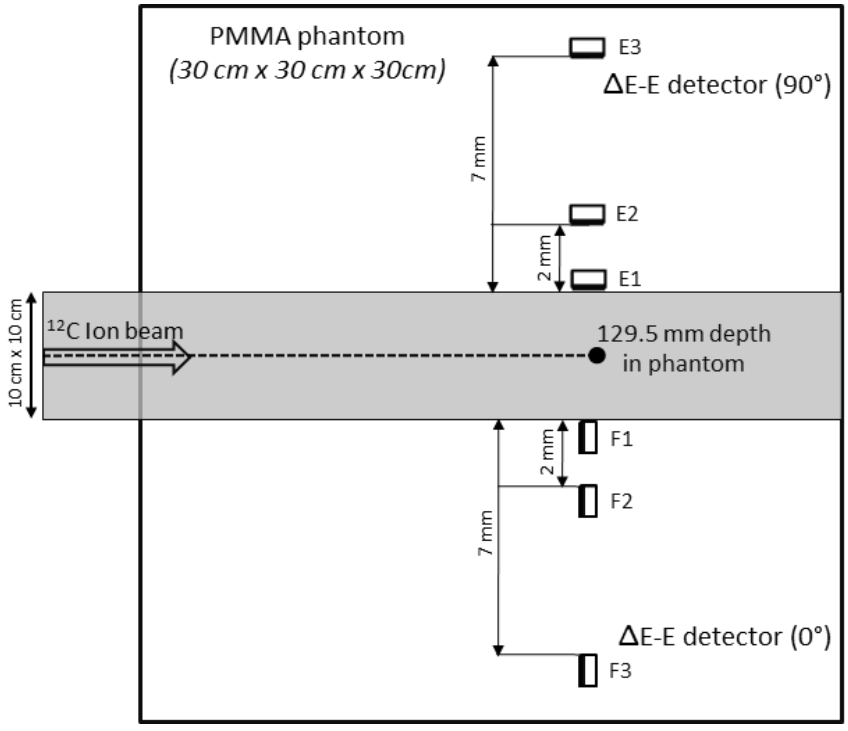

Figure 8.3 Schematic representation of out of field positions of the ΔE-E telescope in the Geant4 simulations and experiments. Positions F4 and E4 corresponding to 47 mm lateral distance from the edge of the radiation field were not shown in Fig. 8.3 due to space limitation.

The out-of-field response of the ΔE-E telescope was studied to characterise its composition, including the scattered primary ion beam, and

fragments and neutrons which are needed to estimate the stochastic probability of secondary cancer induction. The out-of-field study was done with the ΔE-E telescope facing the ^{12}C ion beam (face on 0°) and edge on (90°), as shown in Fig. 8.3 The ΔE-E telescope was placed 0 mm, 2 mm, 7 mm, and 47 mm laterally from the edge of the radiation field at the Bragg Peak region (for both cases: "face on" and "edge on").

8.3 Results and Discussion

8.3.1 Characterisation of ^{12}C ion beam mixed radiation field

Fig. 8.4a shows the energy deposited by the incident 290 MeV/u ^{12}C ions and by the secondary fragment particles. A Bragg peak was observed at 129.5 ± 0.1 mm in the PMMA phantom which agrees with expected results calculated by SRIM [57]. The main contribution of the total energy deposition was from the incident ^{12}C ion beam, fragments, neutrons, and the secondary carbon ions. Secondary carbon ions resulted mostly from neutron scattering within the PMMA, but they will be absent in a water phantom. The peak of the secondary carbon ion appeared at 120 mm in the PMMA phantom (Fig. 8.4b). Contributions to the total energy deposition were seen from secondary nuclei, due to recoils, namely H, He, Li, Be, B, N, and O. The almost negligible energy deposition contributed by N and O was not included in Fig. 8.4b.

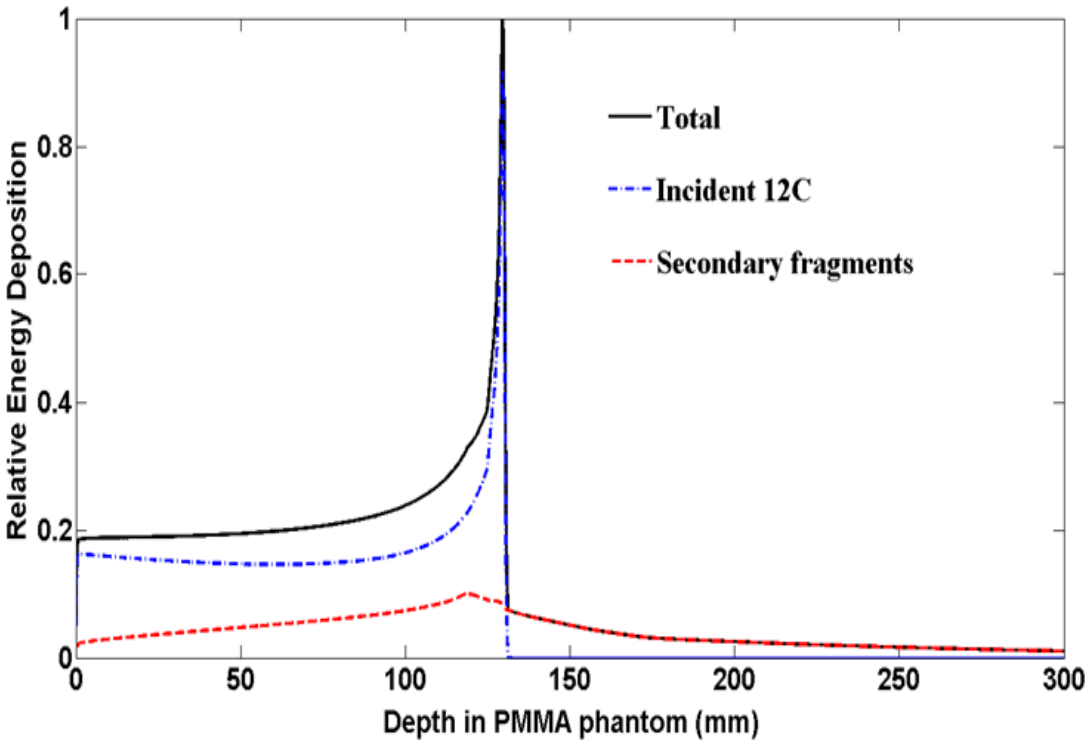

Figure 8.4a Dose per incident ^{12}C ion. The contribution deriving from incident ^{12}C ions and secondary fragments are shown in blue and red, respectively. The sum of the two contributions is shown with the black curve. The energy deposition at the BP was normalised to 1.

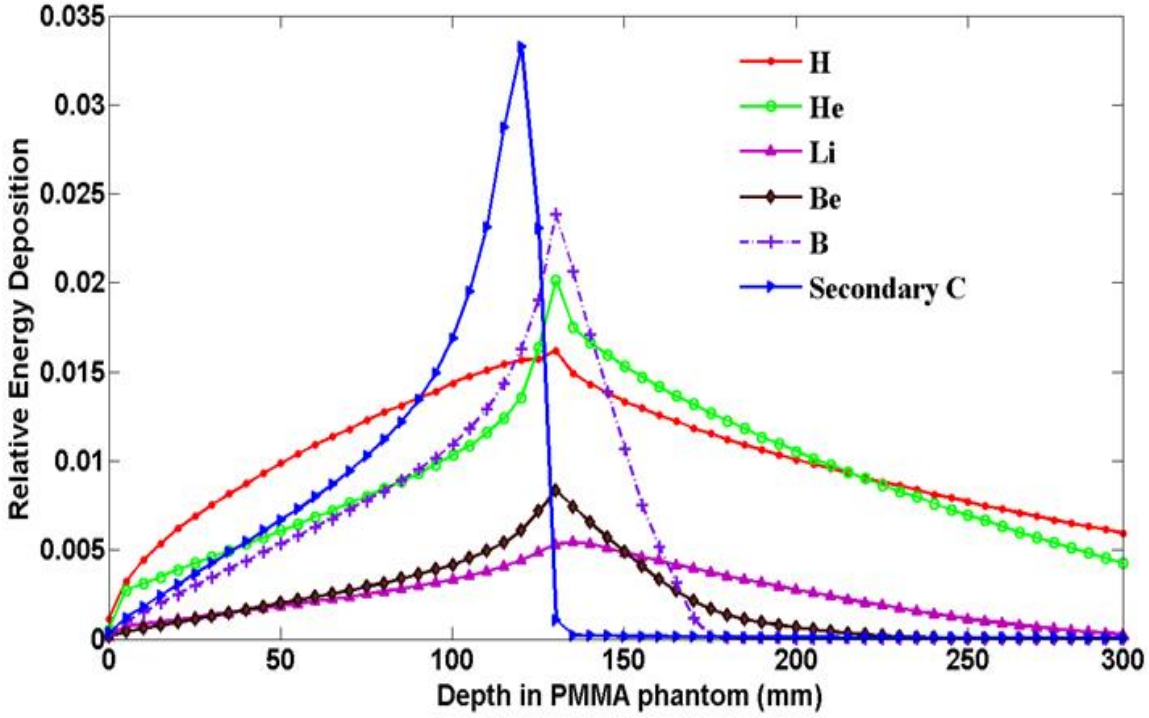

Figure 8.4b Energy deposition deriving from the most significant secondary nuclear fragments and recoil secondary carbon ions. The total secondary fragments component was normalised to 1.

Table 8.1 shows the number of secondary fragments generated per single incident ^{12}C ion and indicate that protons possess the highest yield. These protons consist of nuclear fragments as well as recoil protons generated in elastic reactions when the neutrons interacted with the hydrogen nuclei in the PMMA material. The second largest secondary particle yield was from secondary C followed by neutron O, He, B, Li, N and Be ions.

Table 8.1 Number of secondary particles produced per single incident ^{12}C ion

Particle	**Production per single ^{12}C**
H	25.3267
Secondary C	4.2563
Neutron	2.3747
O	1.4857
He	1.2932
B	0.4949
Li	0.2410
N	0.1604
Be	0.1449

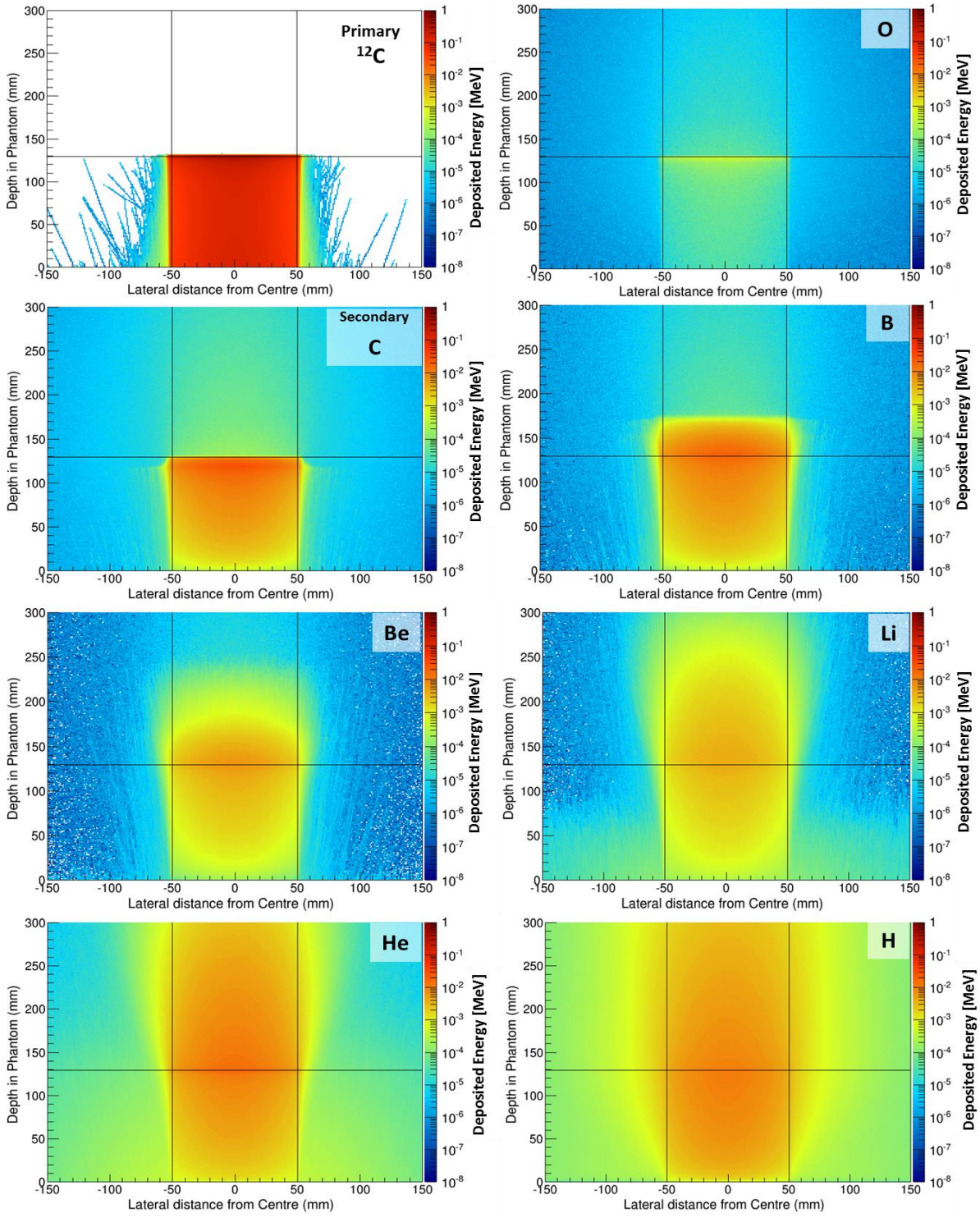

Figure 8.5 2D energy distribution of primary and secondary particles in the PMMA phantom for HIMAC experiment set up. The results are shown per incident particle.

Fig. 8.5 shows the 2D energy distribution of primary as well as secondary particles in the PMMA phantom. Two additional lines were added to mark the edge of the primary beam (10 cm x 10 cm). The 2D histogram shows the scattering of ^{12}C ions outside the radiation field and up to 70 mm from the edge of the field. These events were more pronounced at up to 20 mm laterally from the edge of the radiation field. The energy distribution of secondary carbon ion fragmentation contributed significantly to the in-field and out-of-field, especially at the Bragg Peak. Fragments of B and Be occurred significantly both within and distally to the Bragg peak, while the energy deposited by Be was higher than B. Fragments of Li and He deposited very high energy in- and out-of-field laterally and downstream of the Bragg peak, while O fragments occurred and deposited the highest energy at the Bragg peak position. In general, lighter ions undergo greater lateral scattering and therefore deposit more energy out of the primary radiation field, while the heavier nuclear fragments contribute more substantially to the energy deposition at the distal edge of the Bragg peak.

8.3.2 Characterisation of ΔE-E telescope response in-field

The simulated Bragg Peak and ΔE-E telescope measurement positions for 290 MeV/u ^{12}C ion beam are displayed in Fig. 8.6 (A-O).

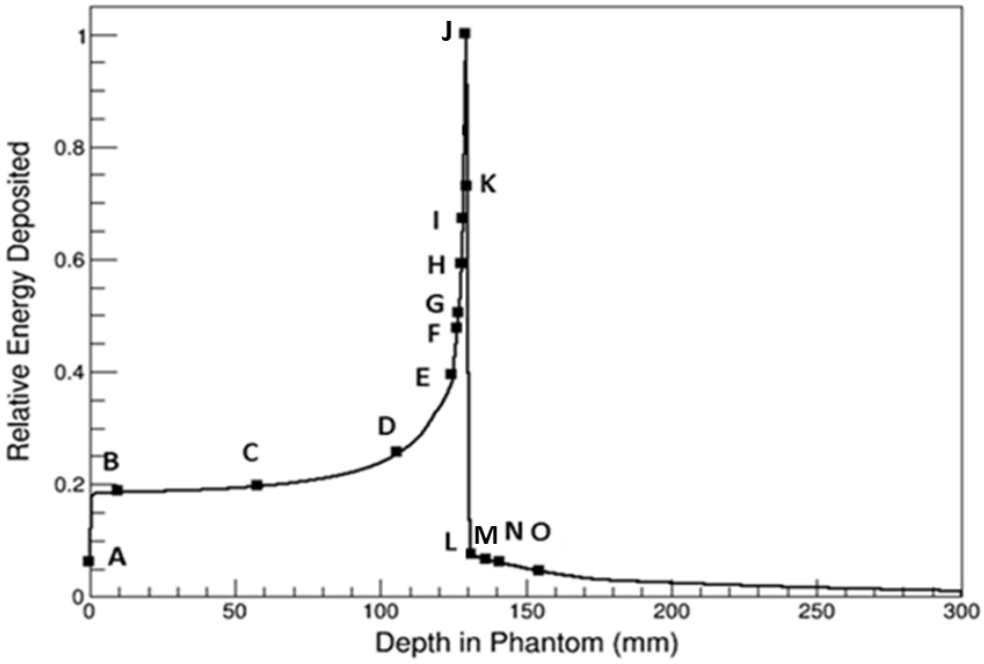

Figure 8.6 Geant4 simulation of the Bragg peak for 290MeV/u ^{12}C with associated ΔE-E telescope measurement positions.

The coincident signals from the ΔE and E detectors in response to the 290 MeV/u ^{12}C beam were mapped in a two dimensional (2D) plane as ΔE vs ΔE+E. Fig. 8.7 shows the simulated 2D ΔE-E plots at measurement positions A, C, I, J, K, L, which correspond to 0 mm, 58 mm, 128.5 mm, 129.5 mm, 130 mm, and 131.5mm depths within the PMMA phantom. The ΔE-E detector was placed along the central axis of the beam. It can be seen that at 0 mm depth in the phantom, 290 MeV/u ^{12}C ions completely traversed the E stage, rending it as a second and thicker ΔE stage. Most deposited energy, ranging from 11-13 MeV, occurred in the E detector, although several events which deposited almost the same energy into the ΔE detector but different energies

into the E detector are visible in the plot. These events stemmed from scattered carbon ions travelling with various track lengths in the E detector.

At a depth of 58 mm in the PMMA phantom, the energy deposition regions on a scatter plot corresponding to B, Be, Li, He, H fragments are clearly presented.

At 128.5 mm depth in the PMMA phantom the maximum energy deposited within the ΔE-E detector increased to 185 MeV, which corresponds to the energy of ^{12}C ion having a range of 500 μm in silicon. The lower LET region of the ^{12}C locus on the 2D scatter plot indicates events crossing the E stage and depositing part of their energy above 60 MeV in the E detector. The energy depositions by oxygen and nitrogen were observed and corresponded to particles produced by inelastic reactions when ^{12}C ions interacted with air before reaching the PMMA phantom, as well as in the PMMA phantom itself.

The 2D energy scatter plot simulated in the ΔE-E telescope placed at the pinnacle of the Bragg peak (position J at 129.5 mm) is shown in Fig. 8.7, and reveal that the maximum energy deposited in the 500 μm E stage was still 185 MeV but with much higher statistics of events with increased energy deposition up to 2.4 MeV in the 1.8 μm ΔE stage.

The main locus had a kink with the deposited energies of more than 90 MeV in the E detector due to transmitted ^{12}C ions. This revealed the high rate of energy loss of the ^{12}C ions together with an increase in statistical events concerning ^{12}C ions with a range in silicon of less than 500 μm. Both facts are confirmation of an increase of ^{12}C ions straggling at the end of their range where the lower energy part of less than 60 MeV, statistically separated from the ^{12}C locus, corresponds to most of the fragments with high energy (low LET particles) with their own loci.

The loci on the plot indicated the strong contribution of fragmentations at the distal edge. At 130 mm depth in the phantom (position K), the 2D energy deposition scatter plot for ^{12} C ions in the ΔE-E detector represents the locus without a kink due to ^{12}C ions stopping within the E detector and up to 2.4 MeV energy being deposited in the ΔE detector, which correspond to the ^{12}C ions with a range in Si 1.8 μm. Multiple loci that corresponded to the detection of different types of ions such as B, Be, Li, He, H were clearly seen. At a depth of 131.5 mm the contribution of fragmentation was still observed while at a depth of 155 mm in PMMA phantom (not presented in Fig. 8.7), there were less Be fragments. These results showed that in principle the ΔE-E detector is suitable for ^{12}C ion beam radiation field characterisation with high spatial resolution in the distal edge of the Bragg Peak, and will clearly indicate the threshold depth at which the deposited energy is due to fragments only.

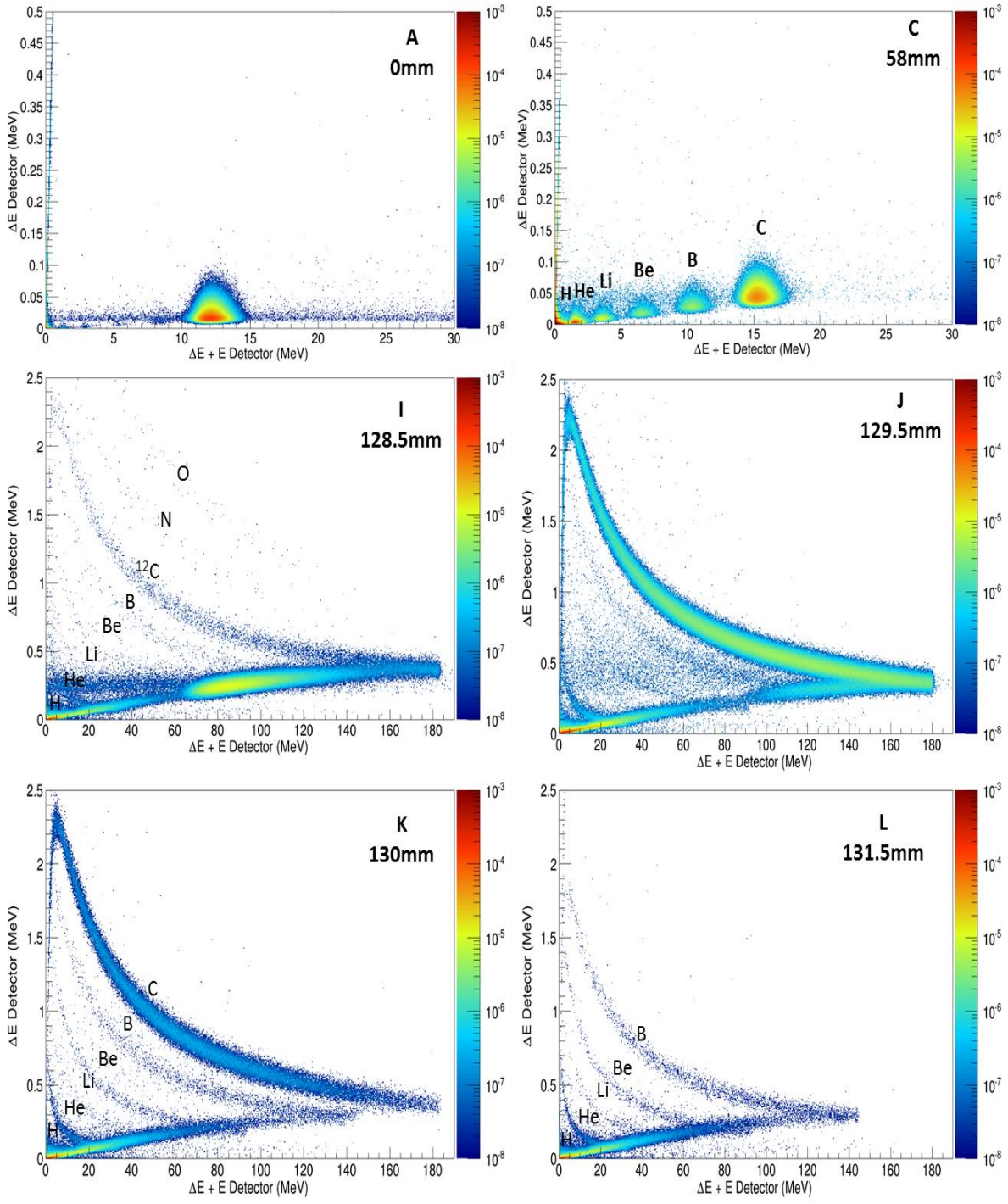

Figure 8.7 Response of ΔE-E telescope to 290 MeV/u ^{12}C ion at depths 0, 58, 128.5, 129.5, 130, 131.5 mm in the PMMA phantom (two-dimensional ΔE-E plot). The results are shown per incident particle.

The microdosimetric spectra in silicon (with area normalised to 1) in response to ^{12}C 290 MeV/u ion beam for depths 106, 128.5, 129.5, 130 and 131.5 mm in the PMMA phantom are shown in Fig. 8.8.

In the plateau region of the Bragg Peak (at a depth of 106 mm in the PMMA phantom) the main contribution of the microdosimetric spectrum was derived from ^{12}C ions, which are shown in blue. ^{11}C fragments deposited almost the same lineal energy deposition as ^{12}C ions in the detector but contributed much less to the microdosimetric spectrum compared to ^{12}C ions. The other components, which contributed with lineal energies lower than 100 keV/µm, were nuclear fragments such as B, Be, Li, ^{3}He, alpha, and protons.

At a further depth in the PMMA phantom (128.5 mm), there was higher LET ^{11}C events that deposited higher lineal energies into the detector that corresponded to ions stopping within the ΔE detector. ^{12}C events at this depth are mostly crossers going through the ΔE detector. At a depth of 129.5 mm, almost all ^{11}C were absent and ^{12}C stoppers can be seen at this depth. A second minor peak was observed that corresponded to those ^{12}C ions stopping in the detector (carbon edge). These detailed results demonstrate the theoretical capability of the silicon microdosimeter to obtain extremely high spatial resolution measurements, which were impossible with a TEPC, but which are crucial to determining the RBE accurately within the target tumor and beyond.

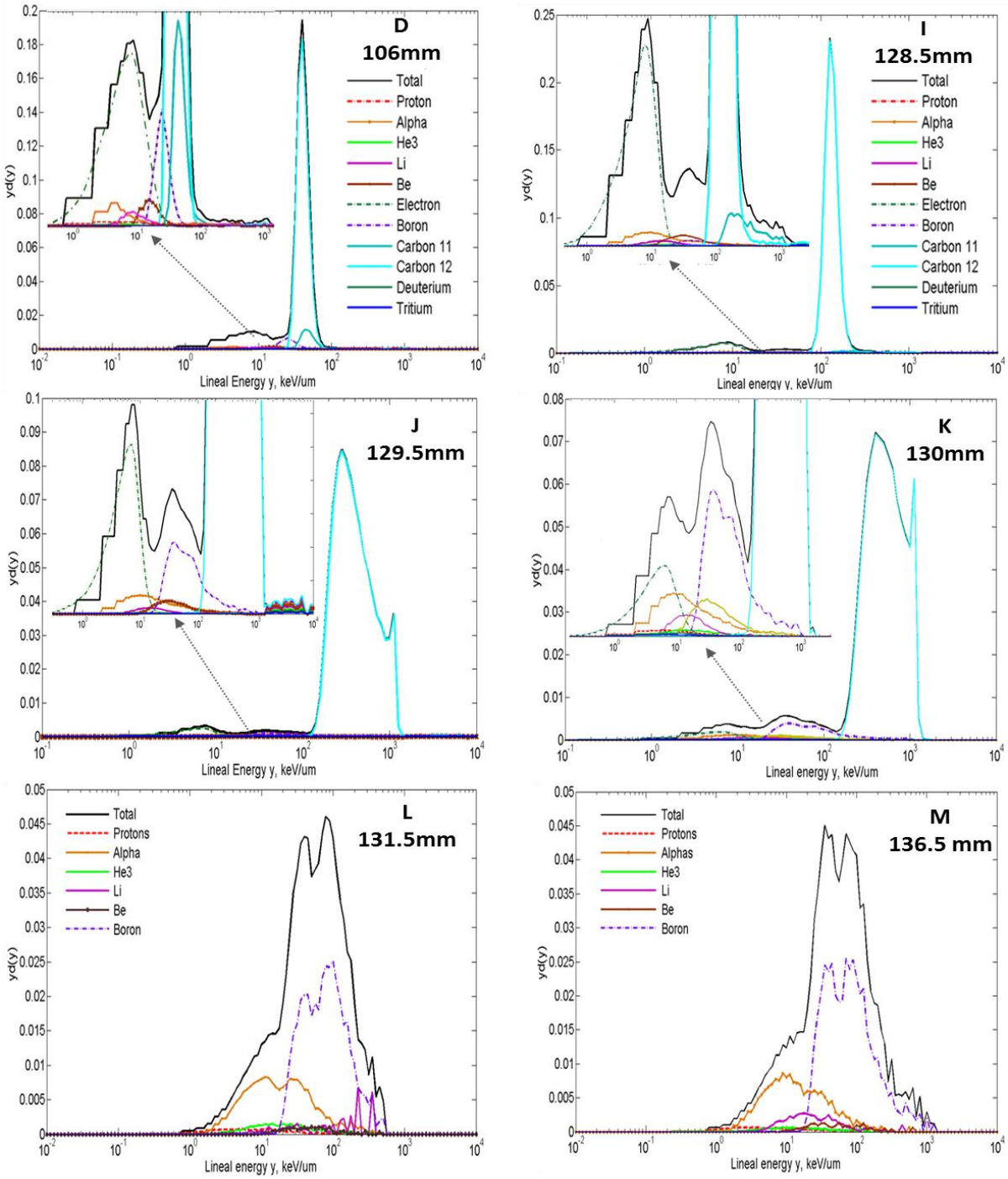

Figure 8.8 Microdosimetric spectra derived from the ΔE stage at positions D, I, J, K, L and M. Separated dose weighted components have been shown in each microdosimetric spectrum.

Measurements along the distal part of the Bragg Peak shown in Fig. 8.8 (at depths of 131.5 and 136.5 mm) indicated that ^{12}C ions were not present in this region of the radiation field, although the contribution from fragments remains significant, with the largest dose weighted contribution deriving from B ions and alpha particles.

8.3.3 Characterisation of ΔE-E telescope response out of field

The response of the ΔE-E telescope when placed out-of-field in two configurations: face on (0^o) and edge on (90^o) (Fig. 8.3) is shown in Fig. 8.9. In the face on configuration there was a clear loci that could distinguish different species of particles (Fig. 8.9 a), while the edge on configuration revealed a very different 2D energy scatter plot with an absence of clear loci (Fig. 8.9 b); this result indicated the preferable directionality of the out-of-field components. The direction of the primary and secondary particles out of field can be seen in Fig. 8.5.

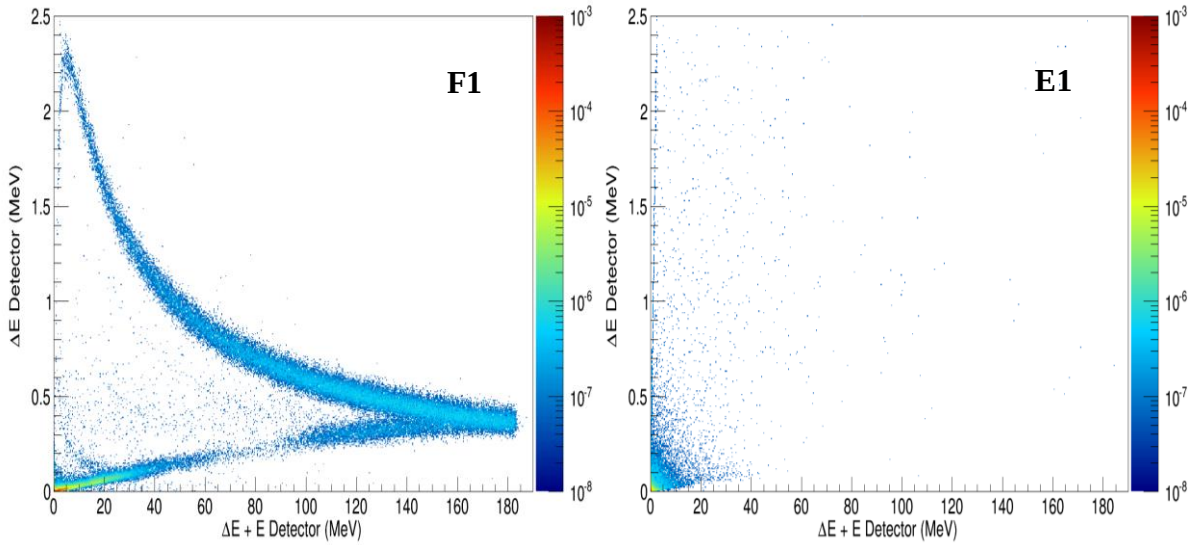

Figure 8.9 Response of the telescope detector when positioned out-of-field at 0mm, 20×10^6 primaries were used for both face on (F1) and edge on (E1). The results are shown per incident particle.

Fig. 8.10 shows the microdosimetric spectra obtained by the ΔE stage when the detector was placed face on with the beam at 0 mm, 2 mm, 7 mm, and 47 mm laterally from the edge of the beam (positions F1, F2, F3 and F4, respectively), and edge on with the beam at positions E1, E2, E3 and E4. When the ΔE-E telescope was placed at 0 mm from the edge of the beam and the surface of the detector faced the beam (F1 position), there was a significant contribution from ^{12}C ions that corresponded to the penumbra region of the beam. Fragmentation products were also observed with lineal energies between a few keV/µm and 100 keV/µm, with the largest contribution coming from B ions. At 2 mm from the edge of the beam

(position F2), the partial dose weighted contribution of the ^{12}C ions was reduced while fragments such as B, Be, Li, He, H increased. At 7 mm from the edge of the beam (position F3), almost all ^{12}C ions disappeared at this lateral depth but the fragments still remained significant, which confirmed the sharp penumbra for ^{12}C ions. At a further lateral depth of 47 mm, only protons which corresponded to the combination of fragmented and recoil protons generated from neutron interactions in PMMA were seen.

A second alignment was carried out with the detector positioned perpendicular to the beam, in edge on configuration (positions E1, E2, E3 and E4). Here more energy was deposited in the ΔE stage from ions travelling parallel to the side of the ΔE-E detector. This caused a shift to the higher lineal energies observed in E1-3 plots of Fig. 8.10, when a chord length of 1.8 μm was used. This shift was clearer at positions closer to the field because nuclear fragments have a preferential forward scattering angular trajectory from the originating ion, while the path along the ΔE detector is 1 mm long.

At 0 mm from the edge of the beam very high LET events were observed up to 100 MeV/μm, and at 2 mm from the edge of the beam ^{12}C ions with high lineal energy deposition could still be seen. This demonstrated the existence of ^{12}C ions scattering out of field and travelling almost parallel with the primary beam, and also agrees with the 2D energy distribution

histogram of ^{12}C in the radiation field study shown above (Fig. 8.5). At 7 mm from the edge of the beam almost all the ^{12}C ions disappeared and only fragmentations dominated the microdosimetric spectra, but once again with much higher lineal energies than the equivalent points in F positions. The contributions from B, Be, Li fragments, alpha particles, ^{3}He and protons were clearly seen. At 47 mm the edge and face on configurations responded the same, with contribution from the protons only due to neutron interactions in the phantom with an isotropic distribution. A much closer agreement in the microdosimetric spectra for positions F4 and E4 confirmed that the fragmented and neutron recoil proton fields were more isotropic than other heavier fragmented ions that were scattered mostly along the beam. The results showed that the microdosimetric spectra obtained by the ΔE stage of the monolithic telescope can give a detailed insight of the characteristics of the out of field beam. Certainly the microdosimetric spectra presented for positions E1-3 should not be considered as radiobiologically relevant because of the the reasons described above.

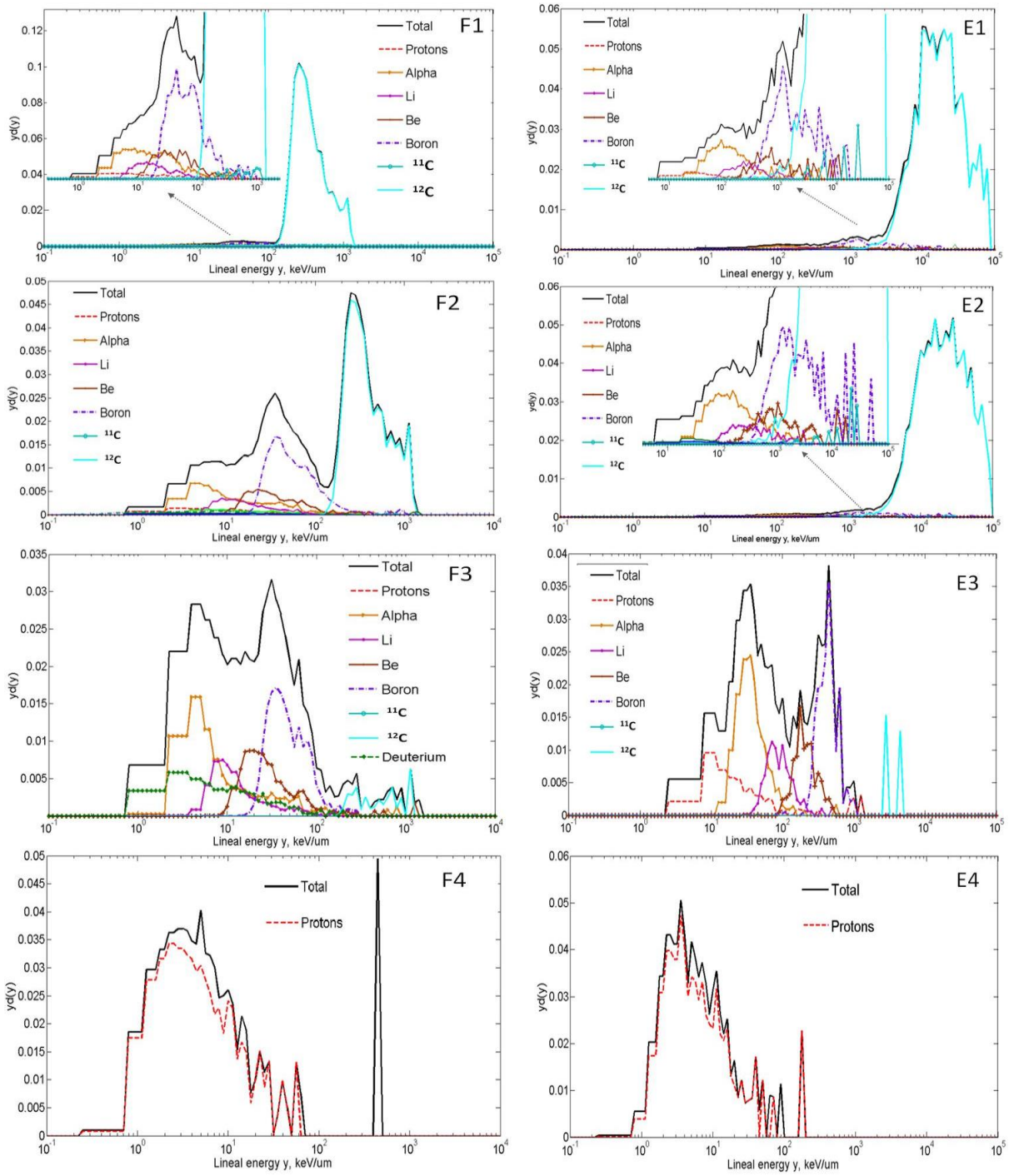

Figure 8.10 Microdosimetric spectra derived from the ΔE stage in out of field study at 0 mm, 2 mm, 7 mm and 47 mm from the edge of the beam at the Bragg peak. Separated components are shown in each microdosimetric spectrum.

8.4 Conclusion

The Geant4 9.6 Monte Carlo Toolkit was used to study the response of the ΔE-E telescope used at the HIMAC facility for Heavy Ion Therapy, in a 290MeV/u ^{12}C ion field. This study showed how the ΔE-E telescope can be used to characterise the mixed radiation field produced by the ^{12}C therapeutic beam. It is also possible to simultaneously measure the microdosimetric spectra and its dose weighted components with extremely high spatial resolution; which is not currently achievable using TEPCs. The microdosimetric spectra can also be used to determine the RBE of the radiation field.

The ΔE-E telescope can be used to improve the Quality Assurance of existing treatment planning systems in Heavy Ion Therapy.

Chapter 9

Experimental Silicon Microdosimetry in ^{12}C ion therapy facility at HIMAC, Japan

This chapter describes the experimental results obtained at the Heavy Ion Medical Accelerator in Chiba (HIMAC), Japan using the 1st and 2nd generations of CMRP microdosimeters, ultra-thin 3D detector and 3D mesa bridge microdosimeter. Derived RBE_{10} values based on the microdosimetric kinetic model and measured microdosimetric spectra for each microdosimeter are presented and compared to the obtained from the TEPC measurements at the National Institute of Radiological Science (NIRS), HIMAC, Japan.

9.1 HIMAC Facility

The experiment was carried out in a biological radiation room at the Heavy Ion Accelerator in Chiba (HIMAC), Japan. A model of the HIMAC facility is shown in Fig. 9.1. The ion sources available at HIMAC range from

He to Ar, but the facility mainly performs carbon ion radiotherapy. The HIMAC accelerator complex consists of a 7.3 m long radio frequency quadrupole linac for low speed ions, a 24 m long Alvarez type linac for medium speed ions as an injector to the two synchrotrons, with a maximum energy of 400 MeV/u. There is also an ion beam transport system with vertical and horizontal beam lines that can deliver the beam from the two synchrotrons to three treatment rooms and a biological irradiation room [83]. The bar ridge filter is used to obtain a fixed modulation depth, the wobbler system is used to laterally spread the spot beam, and the patient specific collimator is used to shape the beam.

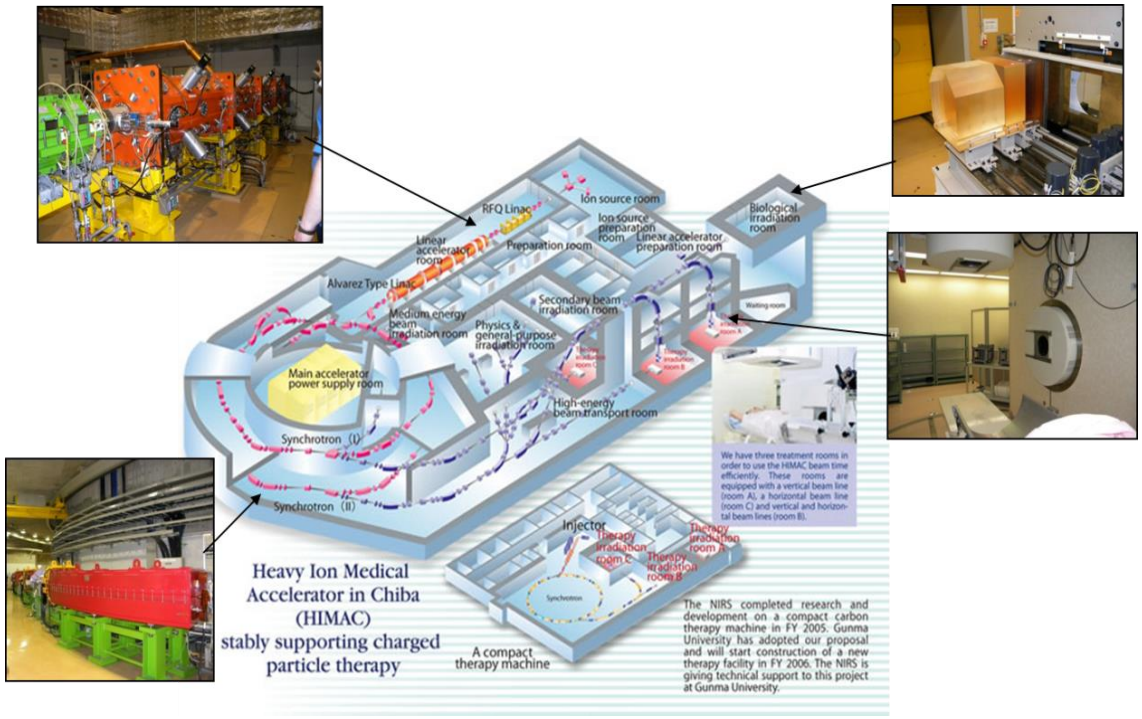

Figure 9.1 Model of the HIMAC facilities, top left: Radio frequency quadrupole linac; bottom left: HIMAC synchrotron; top right: biological radiation room; bottom right: treatment room.

9.2 Materials and Methods

9.2.1 Experimental Setup

A Spread Out Bragg Peak (SOBP) of the ^{12}C ion beam with an energy of 290 MeV/u was selected for this experiment because it is the typical energy used at HIMAC to treat prostate cancer. The measurements were acquired using the SOI Microdosimeters readout by an Amptek A250 charge sensitive preamplifier inside a thin, aluminum probe housing. A bias voltage was applied to the SOI devices in each probe using low-noise battery power supplies. The preamplifier output was connected to a Cremat CR-200 shaping amplifier with a 1 μs shaping time, while the energy output of the shaping amplifier was digitised with an Amptek Pocket MCA-8000A.

Energy calibration factors were obtained using a pulse generator that was calibrated with a 300 μm thick planar silicon PIN diode with 100% charge collection efficiency exposed to a sealed source of ^{241}Am.

The SOI Microdosimeters were placed at various positions along the central axis of the SOBP therapy beam. Slabs with different thicknesses of Polymethyl Methacrylate (PMMA) phantom were used to adjust the position of the Bragg peak relative to the devices. The experimental setup is shown in Fig. 9.2. 1st and 2nd generation SOI microdosimeters, ultra-thin 3D detector

and 3D mesa bridge microdosimeters were used to study the broad beam of 290 MeV/u ^{12}C ions.

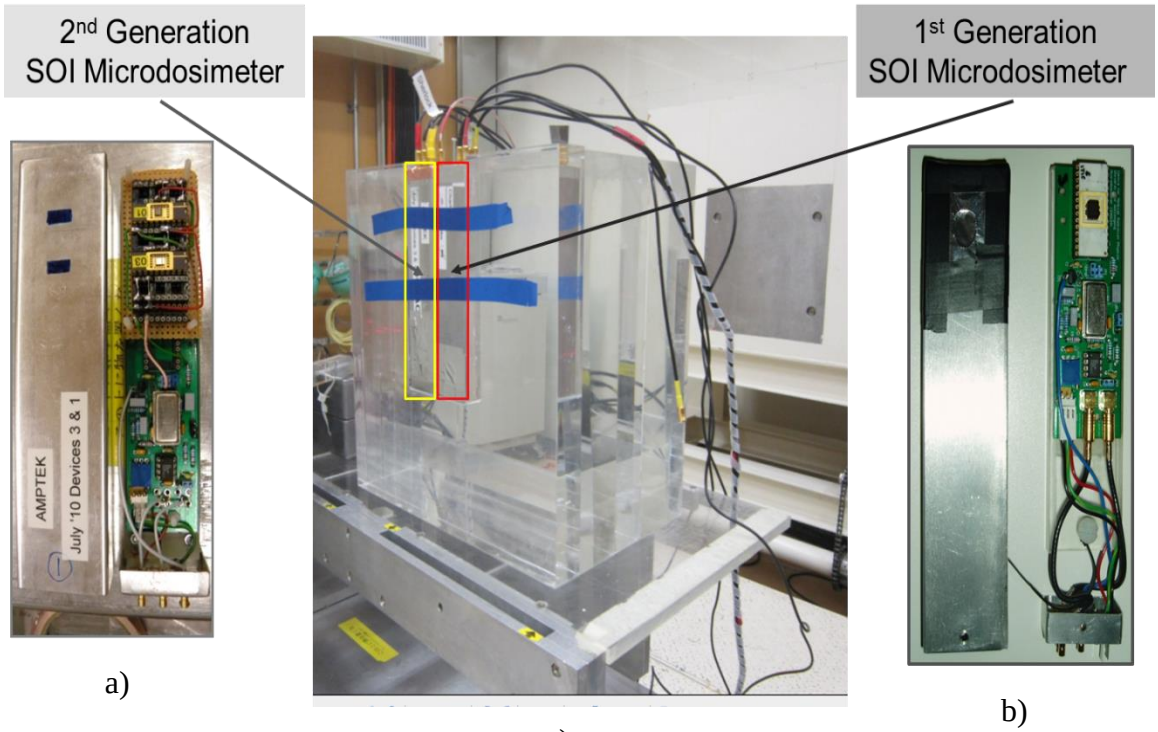

Figure 9.2 The experimental setup for microdosimeters, a) microdosimetric probe with dual 2nd generation SOI microdosimeters for increasing the sensitive area; b) microdosimetric probe with the 1st generation single SOI microdosimeter; c) two probes placed side by side in PMMA phantom.

Out-of-field study

Out-of-field measurements that were lateral to the SOBP were also taken for the 10 cm x 10 cm radiation field for both cases with the SOI microdosimeter's active area facing the beam (0^0) and along the ^{12}C beam (90^0) direction (Fig. 9.3). Microdosimetric spectra obtained with the SOI microdosimeters in face on and edge on orientations indicated on direction,

and therefore the origin of the secondary and scattered ^{12}C ions responsible for radiation dose components.

A 1st generation SOI microdosimeter was used for out-of-field measurements at positions downstream to the SOBP in order to investigate the contribution from the nuclear fragments and neutrons. The microdosimeter was placed laterally at 0 mm and 5 mm from the edge of the field at a depth close to the end of the SOBP for "edge on" configuration and 0 mm from the edge of the beam for "face on" configuration (Fig. 9.3a).

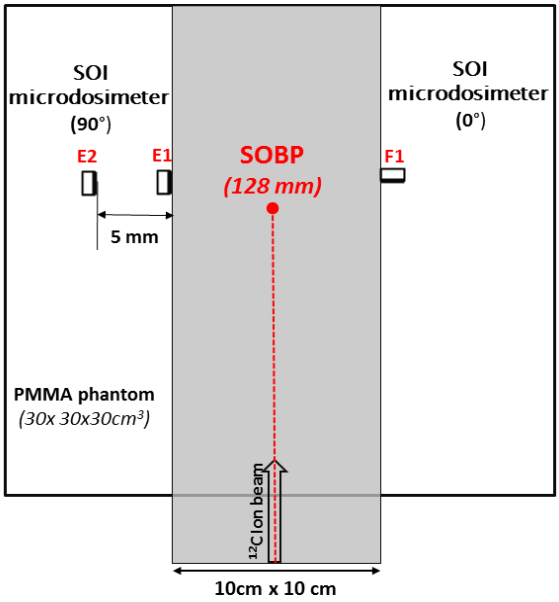

Figure 9.3 a) Schematic representation of the experimental setup for measurements in out-of-field study using 1st generation of microdosimeter at the end of the SOBP (at 128 mm depth).

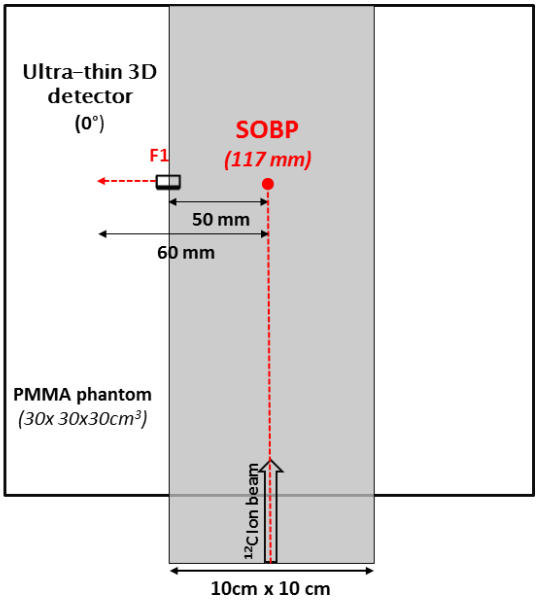

Figure 9.3 b) Schematic representation of the experimental setup for measurements in out-of-field study using ultra-thin 3D detector in the middle of the SOBP (at 117 mm depth).

The ultra-thin 3D detector previously described in chapter 5, with an area of 7.82 mm x 7.82 mm was used for measurements in the out-of-field studies. The detector was placed facing the beam, as shown in Fig. 9.3b, and the distances between the axis of the beam and the centre of the microdosimeter were 45 mm, 50 mm, 52.5 mm, 55 mm, and 60 mm (Fig. 9.3b).

9.2.3 Theoretical estimation of RBE

The RBE calculation method used in this study was based on the modified microdosimetric-kinetic model (MKM) [15], which is a combination of microdosimetric dose distribution and the repair of radiation induced lesions [13]. The RBE derivation method was previously presented in subchapter 1.2.2.

The lineal energy deposition was measured in silicon, and therefore a conversion to tissue equivalent material was needed to obtain the simulated lineal energy deposition in tissue equivalent material. A conversion factor = 0.63 was used because we derived it earlier for fast neutron therapy application [69].

9.3 Results and Discussions

9.3.1 Microdosimetric Spectra

9.3.1.1 1st and 2nd generation of SOI microdosimeter

The measurements of the dose-mean lineal energy deposition along the central axis of a 10 cm x 10 cm radiation field of the SOBP, obtained by 1st and 2nd generation microdosimeters are shown in Fig. 9.4 and Fig. 9.5, respectively. The arrows indicate the microdosimetric spectra obtained along the SOBP, and the tissue equivalent microdosimetric spectra were generated using the conversion factor to convert silicon to tissue, as mentioned above. There were significant changes in the microdosimetric spectra close to and at a distal part of the SOBP. At a depth of 128 mm in the PMMA phantom, a small peak for y > 103 keV/μm was seen on microdosimetric spectra which indicated that the "^{12}C edge" corresponding to ^{12}C stopper events had a 10 μm range that corresponded to the thickness of SOI microdosimeter. At a depth of 128.5 mm, a large fraction of the dose was still being produced by low energy ^{12}C ions, including an increased number of stoppers with a range of 10 μm in silicon. There was also a clear increase in the contribution made by fragments and neutrons that corresponded to the left part of the microdosimetric spectra below the main peak. ^{12}C stoppers were fully

stopped at this depth and at 129 mm deep, carbon ions were absent and only fragments and neutrons could be seen.

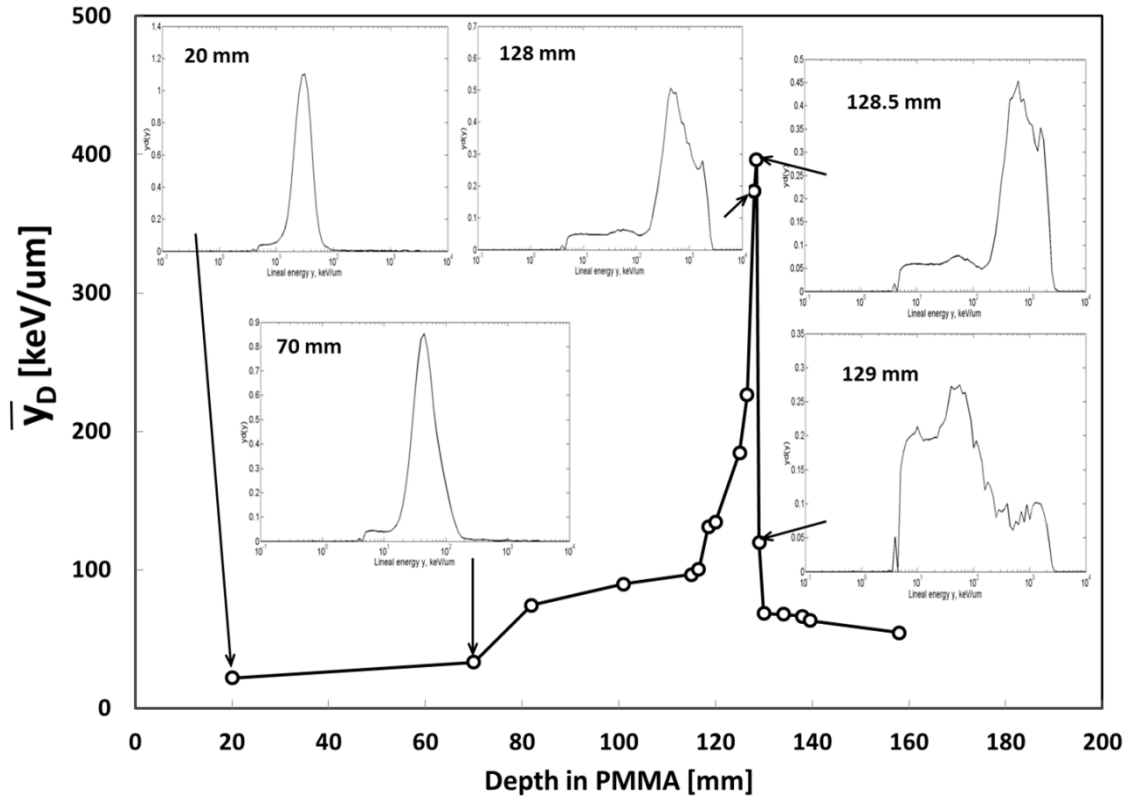

Figure 9.4 Microdosimetric spectra obtained by a 1st generation of microdosimeters in response to 290 MeV/u ^{12}C ions at HIMAC.

A similar response to the 1st generation SOI microdosimeter occurred for the 2nd generation SOI microdosimeter, except for lower lineal energy deposition events on the left side of the microdosimetric spectra (Fig. 9.5) due to the charge sharing effect between the adjacent SVs, a phenomenon previously observed in 2nd generation microdosimeters [28-30]. Unlike the design of the 1st generation microdosimeter, 2nd generation microdosimeters were based on having the SVs away from each other so that the energy

deposition from each event corresponding to a single SV rather than SVs adjacent to each other could be measured accurately. This can lead to higher lineal energy events for oblique events when the assumption is made that the average chord was for a single volume. However, both 1st and 2nd generation microdosimeters were placed at the same depth in the phantom.

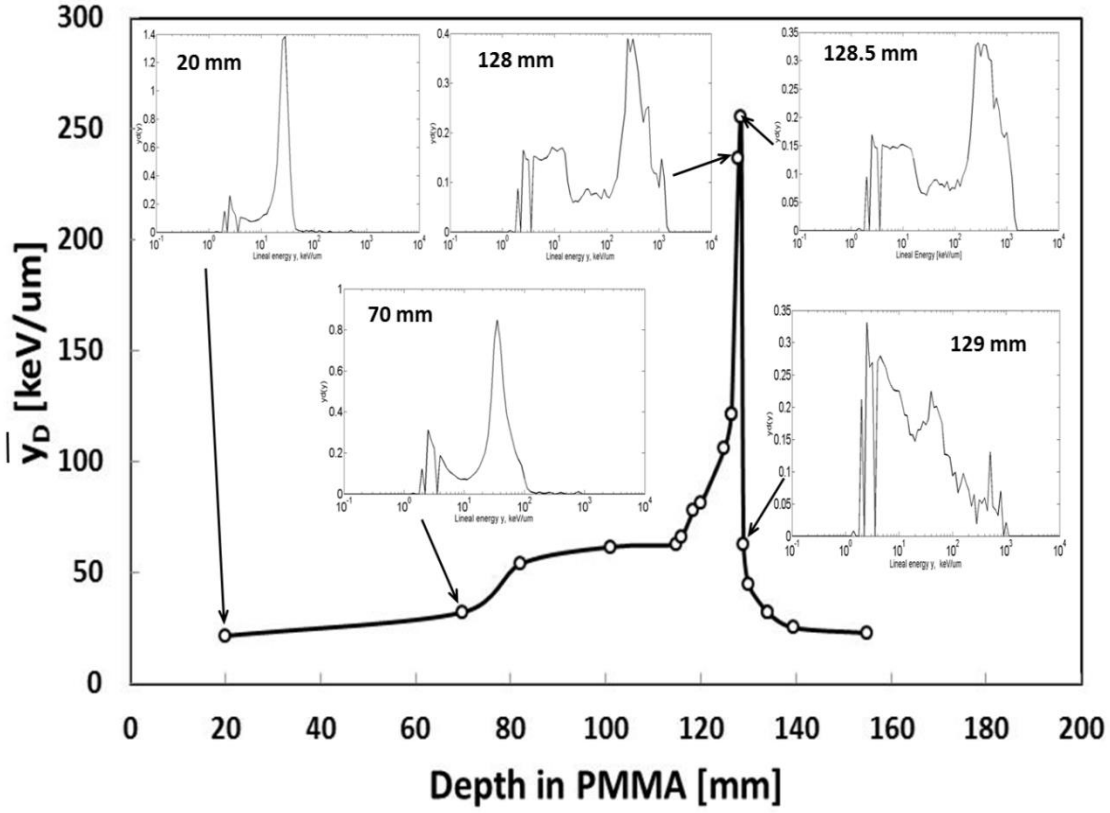

Figure 9.5 Microdosimetric spectra obtained by a 2nd generation microdosimeter in response to 290 MeV/u ^{12}C ions at HIMAC.

9.3.1.2 Ultra-thin 3D detector (membrane)

The ultra-thin 3D SOI based detector has advantages which were investigated in chapter 5, including the excellent charge collection characteristic, where there was only a 10 μm thick sensitive region and no supporting wafer that could reduce the possible contribution of silicon recoils to the active region by backscattered neutrons. Fig. 9.6 illustrates the dose-mean lineal energy along the central axis in the radiation field of the SOBP, as obtained by the ultra-thin 3D detector, and the microdosimetric spectra for corresponding points at different depths are also indicated. At a depth of 48.5 mm in the PMMA phantom, the microdosimetric spectrum was dominated by carbon ions crossing the detector and depositing a lineal energy from 7 keV/μm to approximately 30 keV/μm, and the tail below 7 keV/μm corresponded to gamma irradiation. At a depth of 67.5 mm in the PMMA phantom, there was a slight change in the shape of the microdosimetric spectrum due to a deposition of slightly higher lineal energy into the detector due to the increasing LET of ^{12}C and a visible contribution made by the fragments. At a depth of 77.5 mm, there was a clear tail due to increasing contributions of higher LET ^{12}C ions and fragments with higher lineal energy deposition produced by a single BP forming an SOBP by superposition. The microdosimetric spectra became harder with increasing

depth in the PMMA phantom and there was a clear second smaller peak at a depth of 127.5 mm due to the carbon edge, as explained above.

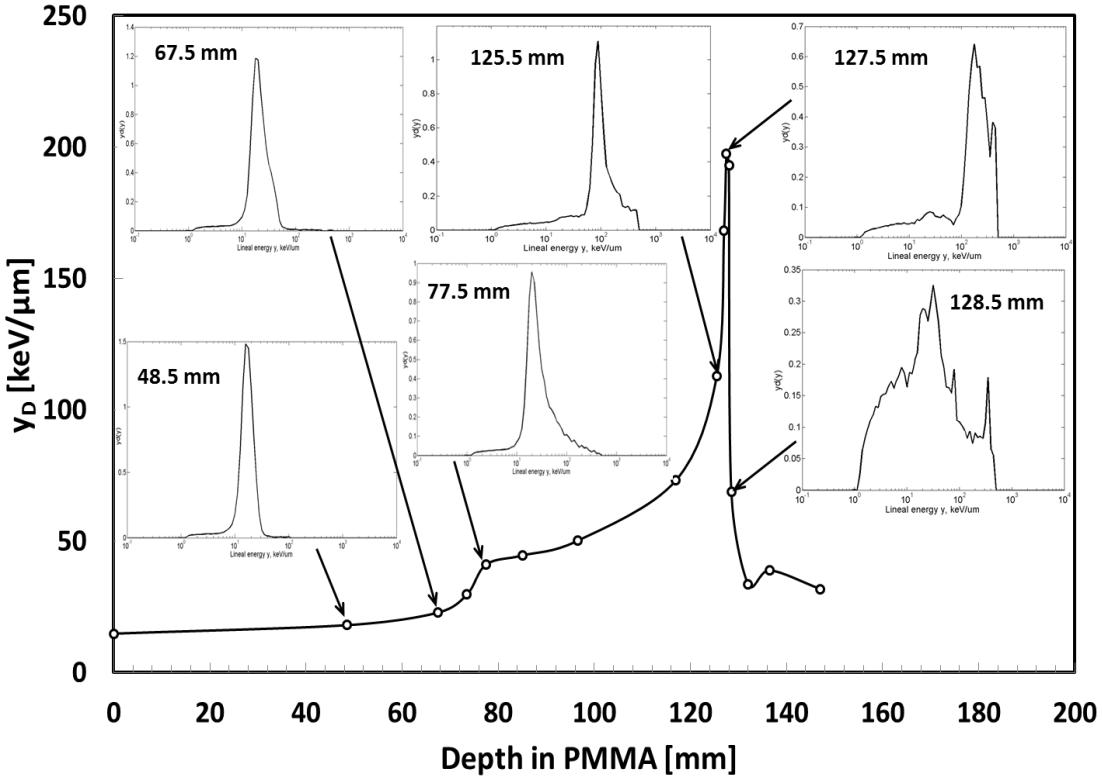

Figure 9.6 Microdosimetric spectra obtained by ultra-thin 3D membrane detector in response to 290 MeV/u ^{12}C ions at HIMAC.

At a depth of 128.5 mm the contribution of primary carbon ion events reduced significantly and the fragmentation contributed mostly to the microdosimetric spectra. Separate peaks were seen at a depth of 128.5 mm which corresponded to the stopper events of different types of fragments such as B, Be, and Li. These features were visible at the same depth on microdosimetric spectra from 1st and 2nd generation SOI microdosimeters but were less pronounced due to more noise from the devices.

9.3.1.3 3D Mesa Bridge Microdosimeter

Fig. 9.7 shows the dose lineal energy depth distribution obtained with the bridge microdosimeter for an SOBP with maximum ^{12}C ion beam energy of 290 MeV/u. In this experiment only one section of the device was used to maintain the noise level of the device, and the odd and even arrays in section N^{o} 1 were connected in parallel.

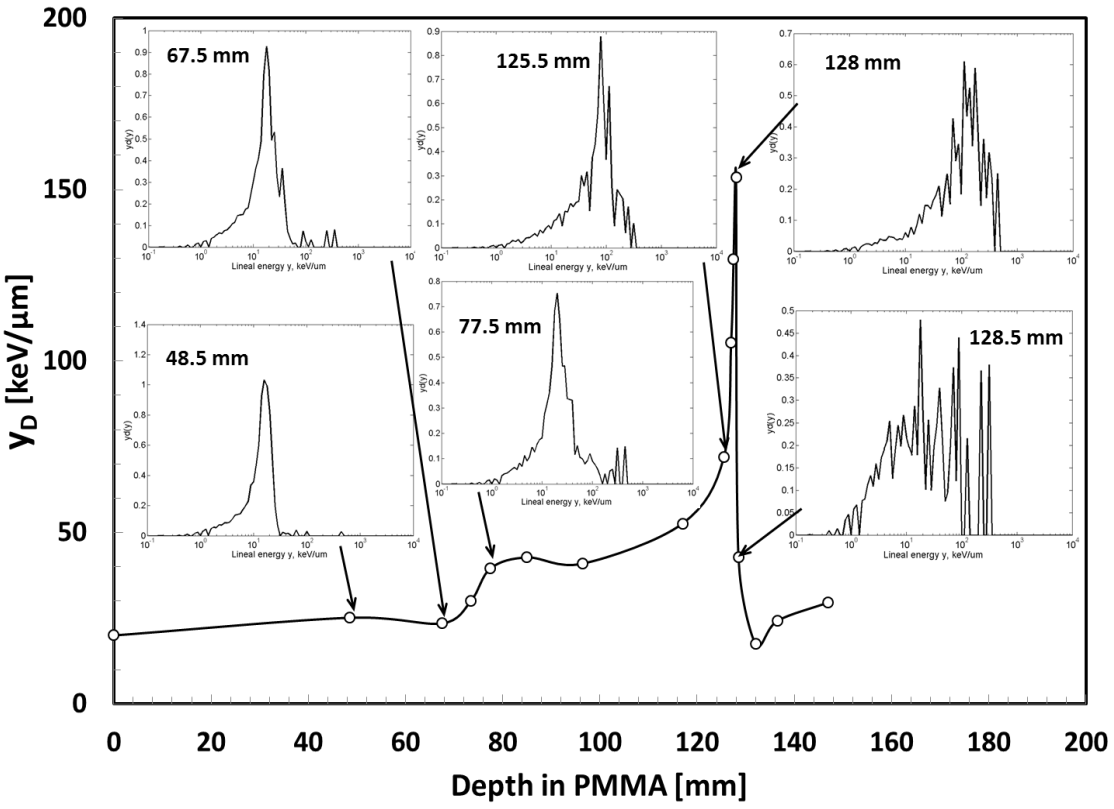

Figure 9.7 Microdosimetric spectra obtained by 3D mesa bridge microdosimeter in response to 290 MeV/u ^{12}C ions at HIMAC.

The microdosimetric spectra obtained by a single section of the 3D bridge microdosimeter that corresponded to different depths are shown in Fig. 9.7.

There was a low lineal energy tail on the left of the main peak of the microdosimetric spectra differed from those obtained by the ultra-thin 3D detector shown in Fig. 9.6 because the chord length distribution in the truncated pyramid shape of the SVs of the bridge microdosimeter (described before in chapter 7) was different. Since a single section of the bridge microdosimeter was approximately 12 times less in area than the ultra-thin 3D detector, and both devices were acquired within the same acquisition time, the bridge microdosimeter was expected to have much lower statistics than the ultra-thin 3D detector, but the bridge microdosimeter provided microdosimetric spectra that was qualitatively similar to the ultra-thin 3D detector. There was agreement in the shape of the microdosimetric spectra measured with the ultra-thin 3D detector and bridge microdosimeter, although the ultra-thin 3D detector did not have micron size SVs because most events in the ^{12}C beam (charged ions) were normally incident to the detector which provided mean path length equal to the 10 μm thickness of the ultra-thin 3D detector; this was different to proton therapy or the isotropic field.

9.3.2 Lateral Out-of-field Response

9.3.2.1 1st generation of SOI microdosimeter

Fig. 9.8 shows the lateral out of field response of the 1st generation of SOI microdosimeters to an SOBP of 290 MeV/u ^{12}C ion beam in edge on

configuration. Primary carbon had been scattered out of field but just on the edge of the field (position E1) while at 5 mm from the edge, only those fragments dominated by fragmented protons (position E2) were seen. When the microdosimeter was located 0 mm from the edge of the radiation field and faced the collimator, only neutrons and fragmented protons were seen (position F1). This showed that carbon ion has a very sharp penumbra, which is a key advantage of heavy ion therapy.

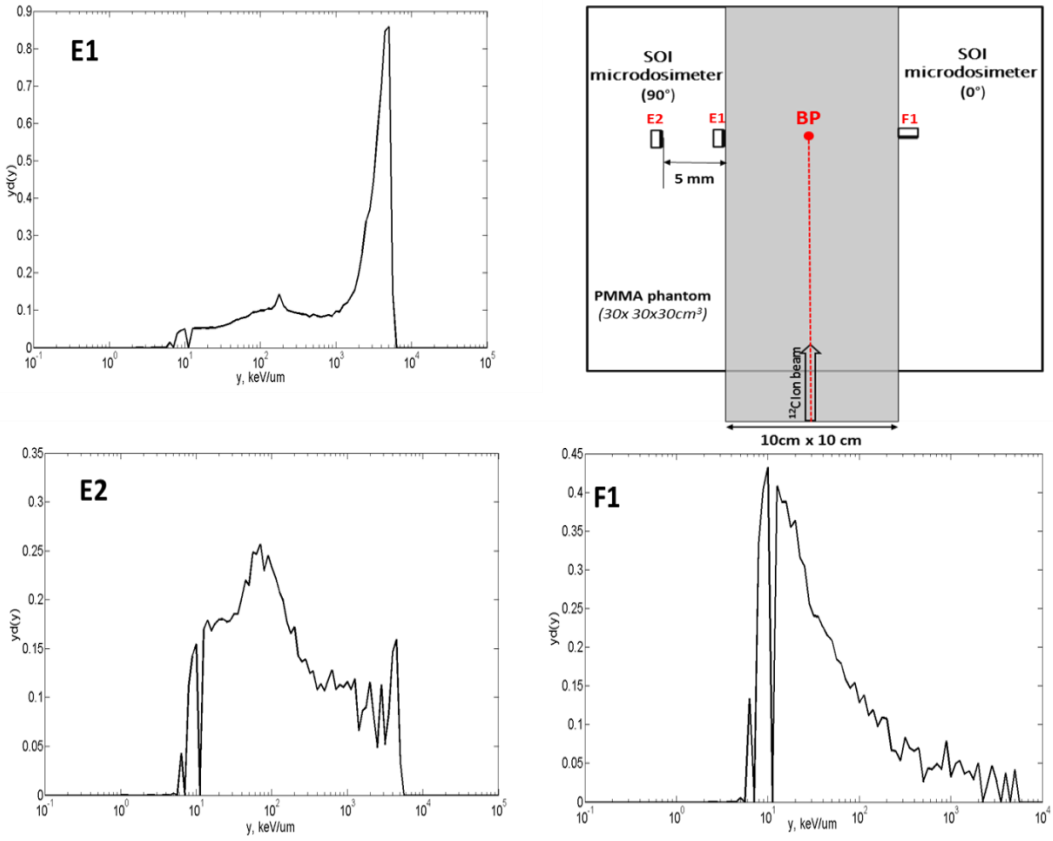

Figure 9.8 Lateral out of field measurement obtained by 1st generation of SOI microdosimeter.

9.3.2.2 Ultra-thin 3D detector (membrane)

The ultra-thin 3D detector was used to measure the lateral out-of-field of the radiation field at a depth of 128.5 mm, which corresponded with the end of the SOBP. The detector was placed facing the collimator but at varying distances from the centre of the beam. Fig. 9.9 shows the response of the ultra-thin 3D detector at 45 mm, 50 mm, 52.5 mm, 55 mm, and 60 mm from the centre of the ion beam.

At 45 mm from the centre of the beam, the detector with an area 7.2 mm x 7.2 mm was still in the 10 cm x 10 cm field. The microdosimetric spectrum indicated there were mostly carbon ions, which agrees with microdosimetric spectra shown in Fig. 9.6. At 50 mm, part of the detector remained in the field so carbons were still visible, but stopper events were also detected. These events corresponded to the peaks with higher lineal energy deposition. At 52.5 mm a few carbon ions were visible, with fragments contributing most of the microdosimetric spectra. This again confirmed the very sharp penumbra of a carbon ion beam. At 55 and 60 mm, only fragments were visible, and only a few random events from scattered carbon were detected.

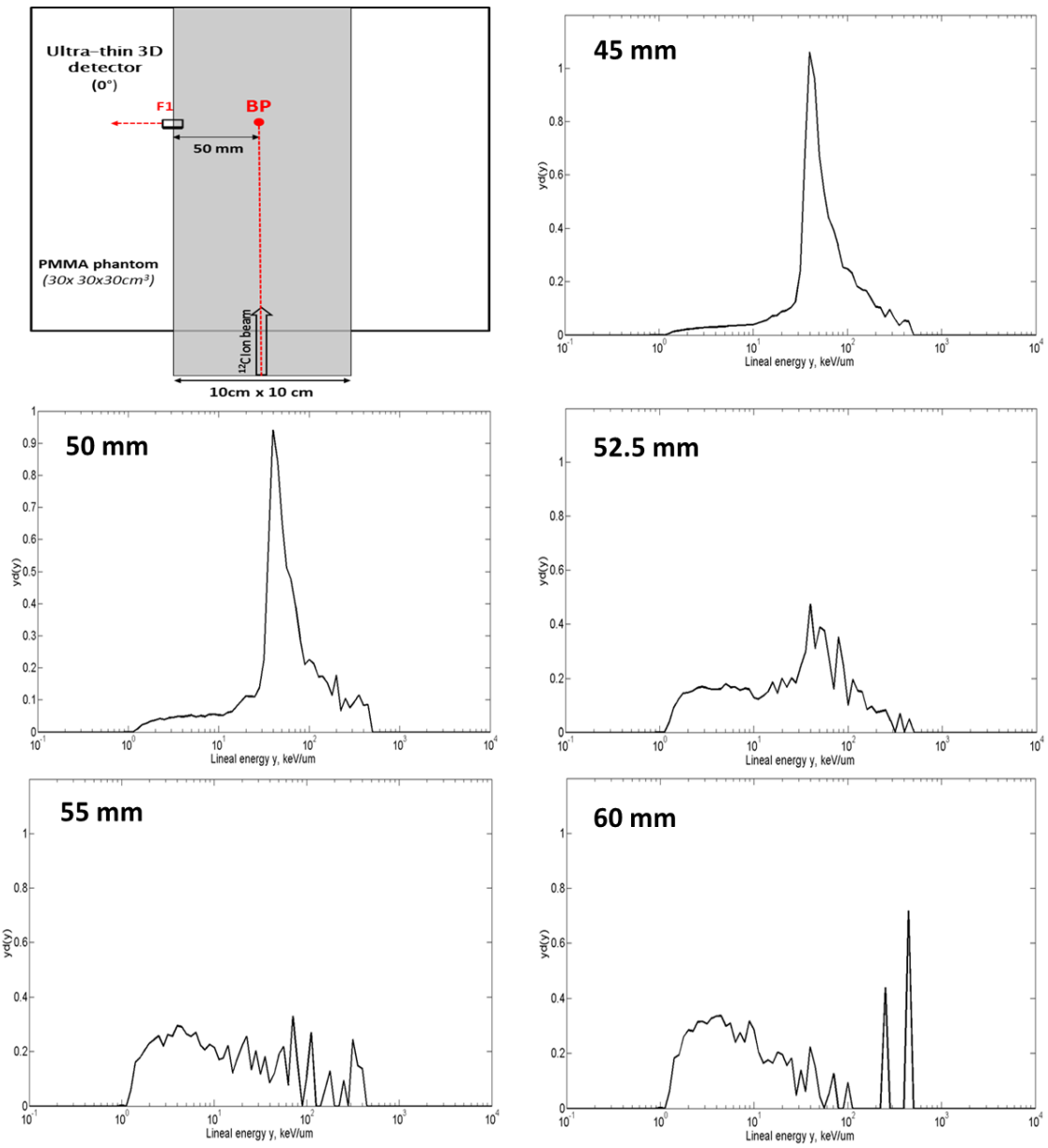

Figure 9.9 Lateral out of field measurement obtained by the ultra-thin 3D detector at various positions. The image at top left shows the experimental setup of the measurement.

By comparing the microdosimetric spectra from Fig. 9.9 (F series) with those from Fig 9.8 (E1 and E2), it is possible to see that the edge on configuration obtained by the 1st generation microdosimeter were similar in

shape to the microdosimetric spectra in a similar lateral location, but with a higher lineal energy. This is related to the design of the 1st generation of microdosimeter with adjacent SVs leading to a deposition of energy in more than one SVs for oblique events, and confirmed once again that most of the scattered primary C ions and fragments were forward peaked, which agrees with the Monte Carlo simulations (Chapter 8).

9.3.3 RBE Derivation with Silicon Microdosimetry

Figures 9.10, 9.11, 9.12, and 9.13 show the biological RBE_{10} obtained by the 1st, 2nd generation microdosimeters, and the ultra-thin 3D detector and bridge microdosimeter, respectively, in response to 290 MeV/u SOBP ^{12}C ions.

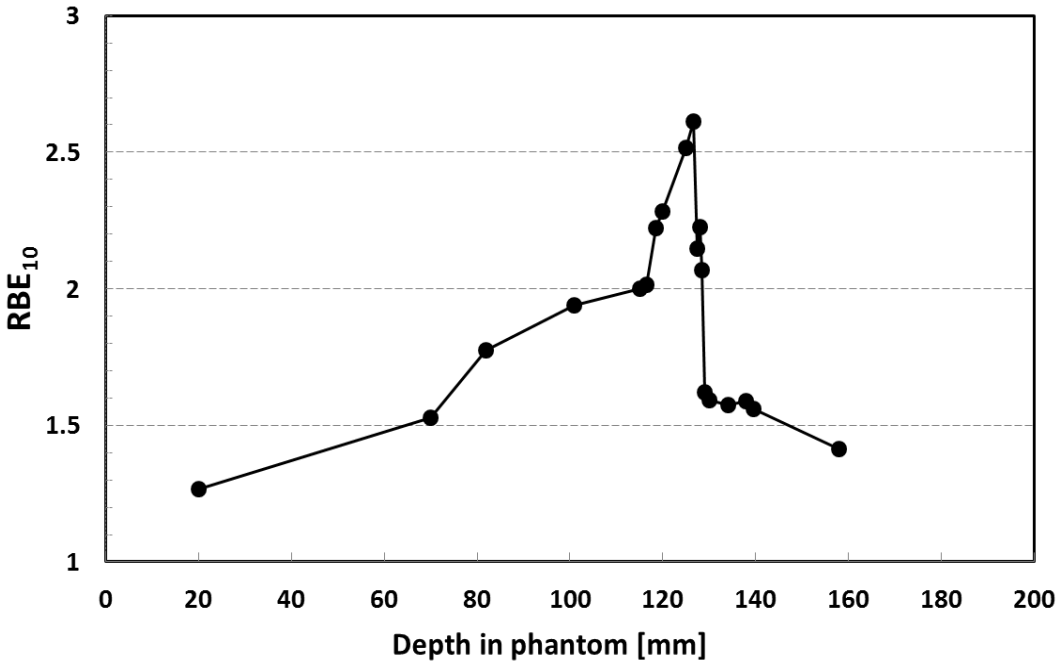

Figure 9.10 RBE_{10} distribution obtained by 1st generation of microdosimeter in response to 290 MeV/u SOBP ^{12}C ions.

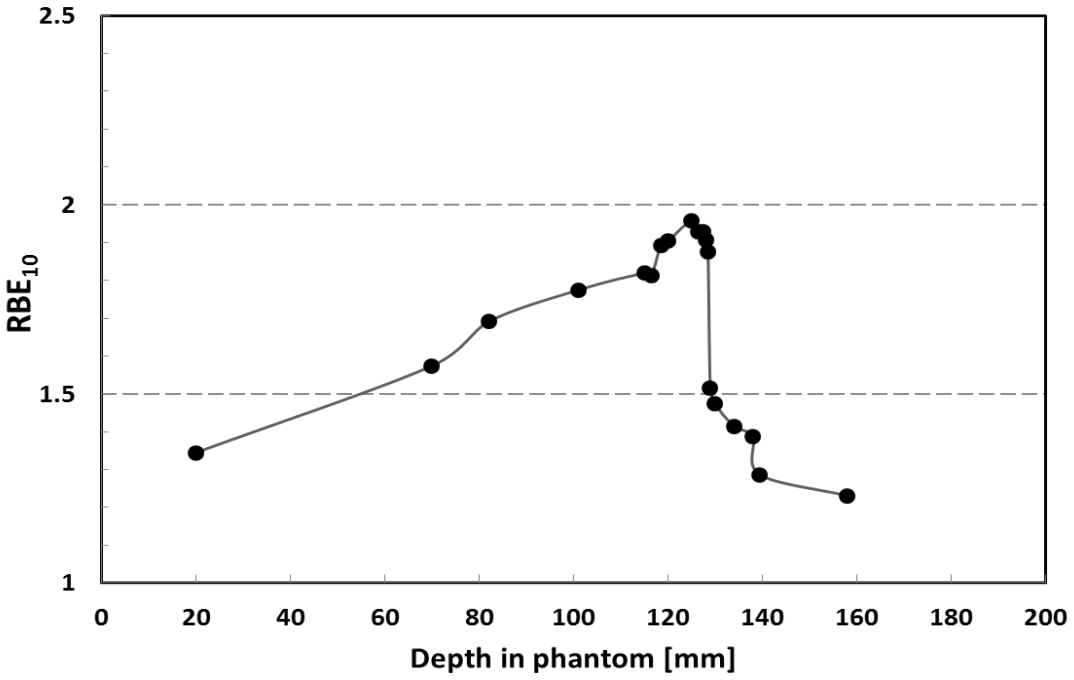

Figure 9.11 RBE_{10} distribution obtained by 2nd generation of microdosimeter in response to 290 MeV/u SOBP ^{12}C ions.

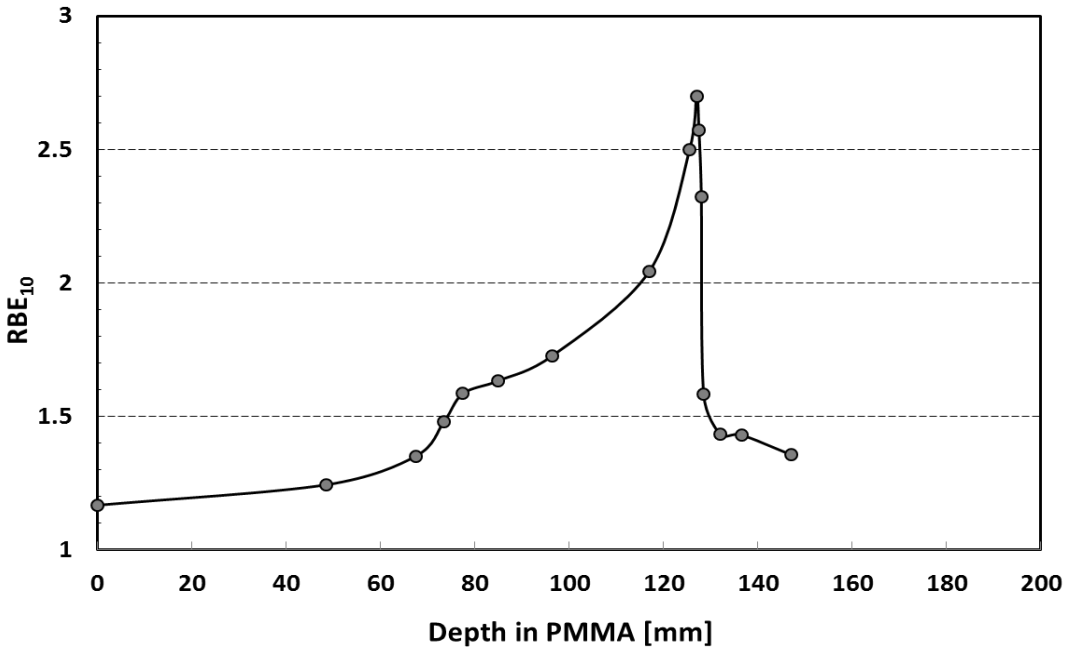

Figure 9.12 RBE_{10} distribution obtained by ultra-thin 3D detector in response to 290 MeV/u SOBP ^{12}C ions.

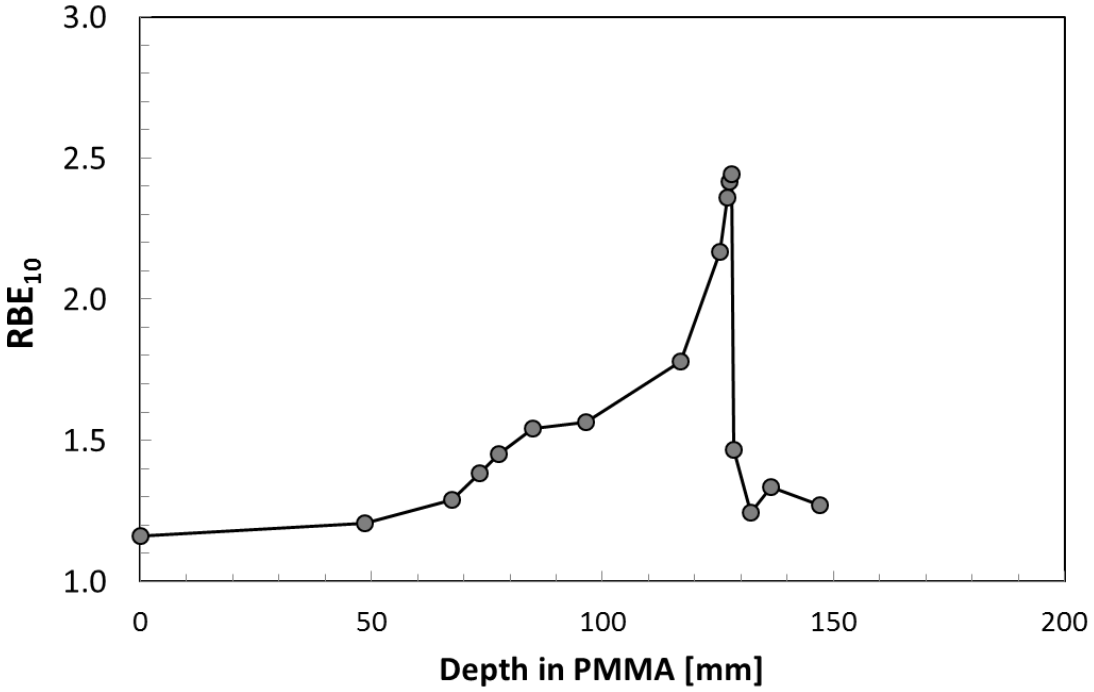

Figure 9.13 RBE_{10} distribution obtained by 3D mesa bridge microdosimeter in response to 290 MeV/u SOBP ^{12}C ions

9.3.3.1 Comparison of RBE of Silicon Microdosimetry to TEPC

Based on the RBE_{10} distribution obtained by four types of silicon microdosimeters, the ultra-thin 3D detector and the bridge microdosimeter were best matched with the TEPC presented in Fig. 9.14. The RBE_{10} distribution obtained by the 1st generation microdosimeter also agreed with the TEPC where the maximum RBE_{10} value was equal to 2.6. The RBE_{10} value at the plateau region in front of the SOBP matched the 1st generation microdosimeter, ultra-thin 3D detector and bridge microdosimeter with the TEPC quite well.

The 2nd generation microdosimeter was the only device to provide a lower RBE_{10} value. This was again related to the unwanted effect of charge sharing in this device which may lead to an underestimation of y_D, and hence RBE_{10}.

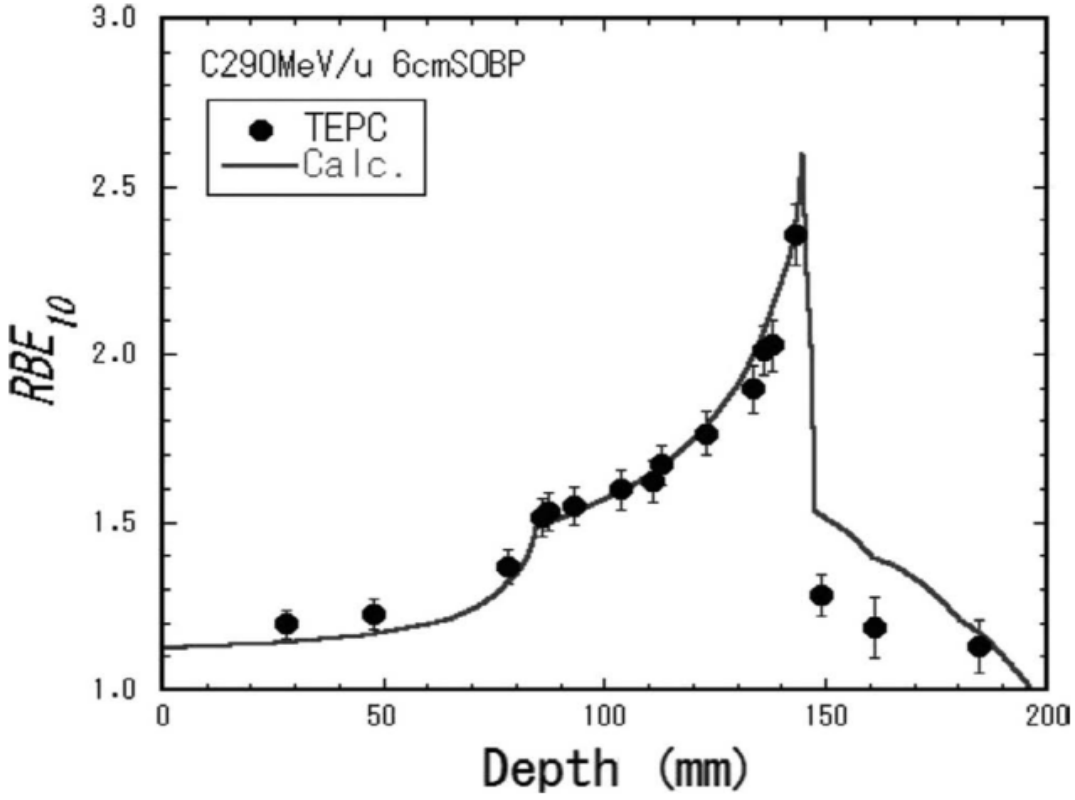

Figure 9.14 RBE_{10} distribution obtained by the TEPC (circles) and Treatment Planning System (solid line) at NIRS, HIMAC in response to 290 MeV/u SOBP ^{12}C ions. The graph was adapted from [14].

The derived RBE_{10} values based on the MK model and measured microdosimetric spectra with the SOI microdosimeter matched those obtained from the TEPC measurements in the plateau and along the SOBP

quite well, but the high spatial resolution of the SOI microdosimeters, enable more detailed RBE_{10} measurements to be obtained at the end of the SOBP than the TEPC. At the distal part of the SOBP, our experimental results showed slightly higher RBE_{10} values due to the difference in composition of the PMMA phantom used in our experiment, whereas the TEPC measurements were carried out in water, which resulted in different spectra of secondaries. This is interesting result and showed that the high quality 3D thin detector and 3D bridge microdosimeter were demonstrating small peaks in RBE_{10} downstream of the SOBP. This peak was possibly created from recoiled C ions in the PMMA and alpha particles that can be seen due to the high spatial resolution of the developed SOI microdosimeters. This result is in contrast to the low spatial resolution TEPC used in these experiments. Such unexpected and increasing RBE downstream of the SOBP in heterogeneous tissue can have an impact on critical organ damage that is not predicted by TPS. The maximum derived RBE_{10} found using the ultra-thin 3D detector and SOI bridge microdosimeter was approximately 2.6 which agrees with the TEPC measurements.

9.4 Conclusions

This work presented a novel method of RBE derivation in ^{12}C heavy ion therapy using a high spatial resolution SOI microdosimeter. It demonstrated

that the RBE_{10} value obtained by the SOI microdosimeter matched the value obtained by the TEPC at HIMAC very well, except at the distal part of SOBP, due to the difference in composition of the PMMA phantom compared to water, and an extremely high spatial resolution (absence of C atoms).

SOI microdosimeters are easy to use because they do not require gas, they have a low voltage operation (5-10 V), and only need a small preparation time. They also have an extremely high spatial resolution of 0.1 mm along the BP and SOBP, which is important for studies of RBE in a distal edge of SOBP. This work represents a comprehensive contribution to better understanding the RBE of ^{12}C ion beam in heavy ion therapy.

An SOI microdosimeter is easy to use and it does not require a lot of preparation time. It also has an extremely high spatial resolution of 0.1 mm along the BP and SOBP, which is important for studies of RBE in a distal edge of SOBP.

This study is a comprehensive work that gives a better understanding of the RBE of ^{12}C ion beam in heavy ion therapy.

Chapter 10

Conclusions and Future Plans

This thesis has presented the development of novel silicon detectors, including their electrical and charge collection characteristics and applications in radiation protection and hadron therapy.

The IBICC technique using the ANSTO heavy ion microprobe was used to study the charge collection properties of the new devices. Monte Carlo simulations using Geant4 were used to calculate the energy deposition by different types of radiation in complex detector geometries.

Highly efficient large area ion-implanted α-particle detectors with cleanable surfaces were developed to measure the radioactivity produced from samples of contaminated soil and plants found after accidents at nuclear power plants. The uniformity of the charge collection of these detectors was investigated using the IBICC technique. The detectors have a good energy resolution and can be used as part of a portable spectroscopy setup for in-field environmental characterisation and radiation protection.

The other comprehensive work presented in this thesis is the development of innovative silicon microdosimeters for radiation therapy and

radiation protection applications in space, avionics, and terrestrial applications. The designs and fabrication of the new "mushrooms" microdosimeter has been described in detail. A charge collection study for a conventional ATLAS 3D detector and an ultra-thin 3D detector was carried out to understand the ability of different microelectronic fabrication facilities. It has been proven that micro-machining and 3D electrode technology can be applied for the fabrication of high definition 3D SVs microdosimeters. Moreover, the radiation hardness characteristics of 3D detectors were also investigated. The performance of 3D SOI microdosimeters in harsh radiation environments such as space and hadron radiation therapy could be predicted.

The optimisation of the design of the 3D microdosimeter was studied using the Geant4 Monte Carlo toolkit to model the response of the new 3D "mushroom" microdosimeter to neutron fields. Remarkable improvements in design were made to the new 3D SV microdosimeter, including, silicon etching surrounding the SVs, substrate thinning, and PMMA filling surrounding the SVs to improve the tissue equivalency of the SOI microdosimeter. The response of the newly proposed 3D "mushroom" microdosimeter to neutron fields of ^{252}Cf, PuBe and avionics has shown good agreement compared to the response of the spherical tissue equivalent micron sized sensitive volume. The tissue equivalence correction for the

"mushroom" microdosimeter in a neutron field in avionics carried out and the conversion factor of 0.50 was found.

As a surrogate of the 3D mushroom SOI microdosimeter, the new microdosimeter with an array of 3D mesa SVs connected by thin silicon junctions for the deposition of thin Al leads that connect the SVs, was also designed and fabricated. This SOI microdosimeter was called a "bridge". In this thesis the charge collection characteristics of the new 3D mesa "bridge" microdosimeter were also investigated. Excellent yield and improvement in defining the SVs of the microdosimeter were also observed, but the incomplete silicon etching around the SVs caused low energy charge collection outside the SVs. This limitation will be improved by future fabrication with complete etching.

The goal of the project was to use silicon microdosimeters in ^{12}C heavy ion therapy for RBE estimation. The experimental beam line at HIMAC, Japan was modelled with a Geant4 Monte Carlo toolkit in order to understand the complex production of a mixed secondary radiation field. The results indicated a significant contribution from the fragmentation at the BP position and downstream of the BP.

The response of the ΔE-E monolithic silicon telescope placed in a PMMA phantom to 290 MeV/u ^{12}C ion beam was studied to identify the types of particles, and to study the microdosimetric response of the 1.8-μm thick ΔE

stage. This work provides extremely useful information about the secondary radiation field produced in heavy ion therapy and presents a unique method of simultaneous RBE estimation and particle identification. The next stage of this project will be to compare the results of the Geant4-based study to the experimental results obtained at HIMAC to quantify the accuracy of the results deriving from the simulations. In particular, simulation with alternative Geant4 hadronic physics models that describe ion interactions (G4IonBinaryCascade and the Quantum Molecular Dynamic model for nucleus-nucleus collisions) will be compared to the experimental data.

The 1st and 2nd generation of CMRP SOI microdosimeters, ultra-thin 3D detector and 3D bridge microdosimeter were used to investigate the in-field and out-of-field components of radiation fields within, laterally, and downstream of the SOBP of a 290 MeV/u passive ^{12}C ion beam at HIMAC in Japan. High spatial resolution SOI microdosimeters with 10 μm thick SVs can measure the sub-millimetre resolutions that cannot be measured with TEPC. It was shown that the microdosimetric spectra changed dramatically close to and in the distal part of the SOBP. There was minimal scattering ^{12}C ions out-of-field and in close proximity and laterally to the radiation field at depths corresponding to the middle of the SOBP; in fact it agreed with the low penumbra of the ^{12}C ion beam. For lateral distances of 5 mm and more, most of the microdosimetric spectra came from fragments and neutrons.

Measurements taken downstream of the SOBP revealed that dramatic changes in the microdosimetric spectra took place with depth, and they were related to different ranges of the fragments. For distances greater than 4-5 cm, the biggest contribution came from fragmented protons and secondary neutrons.

Derived RBE_{10} obtained by the 1st generation of SOI microdosimeter, ultra-thin 3D detector, and 3D bridge microdosimeter for the 290 MeV/u ^{12}C ion SOBP were compared to the existing TEPC data of $RBE_{10,}$ and showed very good agreement. The advantage of the SOI microdosimeter is its ability to measure sub-millimeter spatial resolution along and downstream of the BP/SOBP, whereas the TEPC was averaging the RBE, which changed dramatically close to and at the distal part of the BP/SOBP.

Future development of the silicon microdosimeters will be the fabrication of a modified 3D mesa "bridge" microdosimeter and a 3D "mushroom" microdosimeter. The modified 3D mesa bridge microdosimeter should have complete etching of the silicon surrounding the SVs and the silicon bridge, down to the layer of silicon oxide. Moreover, n^+ ion implanted stop layers under the connecting pads will be produced to avoid any build-up charge in a field SiO_2 on the charge collection under the pads. This would eliminate the low charge collection events surrounding the SVs. An electrical and charge collection study of the newly proposed 3D "mushroom" microdosimeter will

be carried out, including future Geant4 simulations of the new 3D "mushroom" microdosimeter response to the ^{12}C ion therapy beam.

The work presented in this thesis is a crucial step in the development of silicon microdosimetry and its application to radiation protection and Quality Assurance (QA) in heavy ion radiation therapy.

Bibliography

1. *Introduction to charge-particle detector*, 2011, Ametek Advanced Measurement Technology.
2. Kasap, S.O., *Principles of electronic materials and devices*. 2006, New York, NY: McGraw-Hill.
3. Delaney, C.F.G. and E.C. Finch, *Radiation detectors: physical principles and applications*. 1992, Oxford: Clarendon Press.
4. N. J. Hansen, R.G.S.a.D.J.H., *Surface Barrier Particle Detector.* Nuclear Inst. and Methods in Physics Research, A, 1972. **104**(333).
5. Knoll, G.F., *Radiation detection and measurement*. 2000, New York: J. Wiley.
6. Kremmer, J., Nuclear Inst. and Methods in Physics Research, A, 1984. **226**(89).
7. Technology, A.A.M., *Ion-Implanted-Silicon Charge Particle Detector*, 2010.
8. *The Quality Factor in Radiation Protection*, in *ICRU Report 40*1986.
9. *International Commission on Radiation Units and Measurements, Microdosimetry (ICRU report; 36)*, 1983: Maryland.
10. Rossi, H.H. and M. Zaider, *Microdosimetry and its applications*. 1996, New York: Springer.

11. Watson, J.D. and F.H.C. Crick, *MOLECULAR STRUCTURE OF NUCLEIC ACIDS: A Structure for Deoxyribose Nucleic Acid.* JAMA: The Journal of the American Medical Association, 1993. **269**(15): p. 1966.

12. Kellerer, A.M.a.R., H. H., *The theory of dual radiation action.* Current Topics in Radiation Research Quarterly, 1972. **8(2)**: p. 73.

13. Hawkins, R.B., *A microdosimetric-kinetic model of cell death from exposure to ionizing radiation of any LET, with experimental and clinical applications.* International journal of radiation biology, 1996. **69**(6): p. 739-739.

14. Kase, Y., et al., *Microdosimetric approach to NIRS-defined biological dose measurement for carbon-ion treatment beam.* Journal of radiation research, 2011. **52**(1): p. 59-68.

15. Kase Y, K.T., Matsumoto Y, Furusawa Y, Okamoto H, Asaba T, Sakama M, Shinoda H., *Microdosimetric measurements and estimation of human cell survival for heavy-ion beams.* Radiat. Res., 2006. **166**(4): p. 9.

16. Scholz M., K.G., *Calculation of Heavy Ion Inactivation Probabilities Based on Track Structure, X Ray Sensitivity and Target Size.* Radiation protection dosimetry, 1994. **52(1-4)**: p. 4.

17. Scholz, M. and G. Kraft, *Track structure and the calculation of biological effects of heavy charged particles.* Advances in Space Research, 1996. **18**(1): p. 5-14.

18. Scholz M., K.G., *The Physical and Radiobiological Basis of the Local Effect Model:A Response to the Commentary by R. Katz.* Radiation Research, 2004. **161(5)**: p. 17.

19. Srdoc, D., *Experimental technique of measurement of microscopic energy distribution in irradiated matter using Rossi counters.* Radiat. Res, 1970. **43**: p. 17.

20. Kliauga, P., *Microdosimetry at Middle Age: Some Old Experimental Problems and New Aspirations.* Radiat. Res, 1990. **124**: p. 10.

21. Bradley, P.D. and P. University of Wollongong. Department of Engineering, *The development of a Novel Silicon Microdosimeter for high LET radiation therapy*, 2000.

22. Bradley, P.D., A.B. Rosenfeld, and M. Zaider, *Solid state microdosimetry.* Nuclear instruments & methods in physics research. Section B, Beam interactions with materials and atoms, 2001. **184**(1-2): p. 135-157.

23. Rossi, H.H., *Energy distribution in the absorption of radiation.* Advances in Biological and Medical Physics, 1967. **11**(1st Edition New York: Academic Press): p. 58.

24. Kellerer, A.M., *Event simultaneity in cavities. Theory of the distortions of energy deposition in proportional counters.* Radiat. Res, 1971. **48**: p. 216.

25. Kellerer, A.M., *An assessment of wall effects in microdosimetric measurements.* Radiat. Res, 1971. **47**: p. 377.

26. Bradley, P.D., et al., *Charge collection and radiation hardness of a SOI microdosimeter for medical and space applications.* IEEE Transactions on Nuclear Science, 1998. **45**(6): p. 2700-2710.

27. Cornelius, I., et al., *Ion beam induced charge characterisation of a silicon microdosimeter using a heavy ion microprobe.* Nuclear Inst. and Methods in Physics Research, B, 2002. **190**(1): p. 335-338.

28. Ziebell, A.L., et al. *Cylindrical silicon-on-insulator microdosimeter: Charge collection characteristics*. IEEE.

29. Lim, W.H., et al., *Cylindrical Silicon-on-Insulator Microdosimeter: Design, Fabrication and TCAD Modeling.* IEEE Transactions on Nuclear Science, 2009. **56**(2): p. 424-428.

30. Lai, N.S., et al. *Development and fabrication of cylindrical silicon-on-insulator microdosimeter arrays*. IEEE.

31. Livingstone, J., et al., *Large Area Silicon Microdosimeter for Dosimetry in High LET Space Radiation Fields: Charge Collection Study.* IEEE Transactions on Nuclear Science, 2012. **59**(6): p. 3126-3132.

32. Wroe, A., et al., *Solid State Microdosimetry With Heavy Ions for Space Applications.* IEEE Transactions on Nuclear Science, 2007. **54**(6): p. 2264-2271.

33. Guatelli, S., et al., *Tissue Equivalence Correction in Silicon Microdosimetry for Protons Characteristic of the LEO Space Environment.* IEEE Transactions on Nuclear Science, 2008. **55**(6): p. 3407-3413.

34. Prokopovich, D.A., et al., *Comparison of SOI Microdosimeter and Tissue Equivalent Proportional Counter Measurements at the CERF Facility.* IEEE Transactions on Nuclear Science, 2012. **36**(5): p. 2501-2505.

35. Wroe, A., A. Rosenfeld, and R. Schulte, *Out-of-field dose equivalents delivered by proton therapy of prostate cancer.* Medical physics, 2007. **34**(9): p. 3449.

36. Parker, S.I., C.J. Kenney, and J. Segal, *3D — A proposed new architecture for solid-state radiation detectors.* Nuclear Inst. and Methods in Physics Research, A, 1997. **395**(3): p. 328-343.

37. Kenney, C.J., et al., *Active-edge planar radiation sensors.* Nuclear Inst. and Methods in Physics Research, A, 2006. **565**(1): p. 272-277.

38. Hansen, T.-E., et al., *First fabrication of full 3D-detectors at SINTEF.* Journal of Instrumentation, 2009. **4**(3): p. P03010-P03010.

39. DaVia, C., et al., *3D silicon detectors—status and applications.* Nuclear Inst. and Methods in Physics Research, A, 2005. **549**(1): p. 122-125.

40. Kok, A., et al., *3D detectors—state of the art.* Nuclear Inst. and Methods in Physics Research, A, 2006. **560**(1): p. 127-130.

41. Kenney, C.J., S. Parker, and E. Walckiers, *Results from 3-D silicon sensors with wall electrodes: near-cell-edge sensitivity measurements as a preview of active-edge sensors.* IEEE Transactions on Nuclear Science, 2001. **48**(6): p. 2405-2410.

42. G.W.A.D, *Introduction to microelectronic fabrication*, 1988, Elsevier Ltd. p. 823-823.

43. Deal, B.E. and A.S. Grove, *General Relationship for the Thermal Oxidation of Silicon.* Journal of Applied Physics, 1965. **18**(12): p. 3770-3778.

44. Schilp, F.L.a.A., *Method of anisotropically etching silicon*, in *Robert Bosch GmbH* US-Patent, Editor 1996.

45. Kok, A., et al. *High aspect ratio deep RIE for novel 3D radiation sensors in high energy physics applications*. IEEE.

46. Ruska, W.S., *Microelectronic Processing, An introduction to the manufacture of integrated circuits*, in *McGraw-Hill*1987.

47. Piemonte, C., et al., *Development of 3D detectors featuring columnar electrodes of the same doping type.* Nuclear Inst. and Methods in Physics Research, A, 2005. **541**(1): p. 441-448.

48. Agostinelli, S., et al., *Geant4 - A simulation toolkit.* Nuclear Instruments and Methods in Physics Research Section A: Accelerators, Spectrometers, Detectors and Associated Equipment 2003. **506**: p. 250-303.

49. Allison, J., et al., *Geant4 developments and applications.* IEEE Transactions on Nuclear Science, 2006. **53**(1): p. 270-278.

50. Livingstone, J., et al., *Charge Collection in n-SOI Planar Microdosimeters.* IEEE Transactions on Nuclear Science, 2013. **60**(6): p. 4289-4296.

51. Wight, D. *Geant4 hadronic physics*. in *Geant4 School*. 2013. Centre for Medical Radition Physics, Wollongong.

52. Siegele, R., D.D. Cohen, and N. Dytlewski, *The ANSTO high energy heavy ion microprobe.* Nuclear Inst. and Methods in Physics Research, B, 1999. **158**(1): p. 31-38.

53. Siegele, R. and D.D. Cohen, *Mapping of light elements with the ANSTO high energy heavy ion microprobe.* Nuclear Inst. and Methods in Physics Research, B, 2000. **161**: p. 354-358.

54. Mietelski, J.W., et al., *Plutonium and other alpha emitters in mushrooms from Poland, Spain and Ukraine.* Applied Radiation and Isotopes, 2002. **56**(5): p. 717-729.

55. Baumann, R.C., *Determining the Impact of Alpha-Particle-Emitting Contamination From the Fukushima-Daiichi Disaster on Japanese Semiconductor Manufacturing Sites.* IEEE Transactions on Nuclear Science, 2012. **57**(4): p. 1186-1196.

56. Franks, L.A., *Radioactivity Measurement.* CRC Press LLC, 1999.

57. Ziegler, J.F., M.D. Ziegler, and J.P. Biersack, *SRIM – The stopping and range of ions in matter (2010).* Nuclear Inst. and Methods in Physics Research, B, 2010. **268**(11): p. 1818-1823.

58. *IAEA Reference Material-Marine Sediment.* 1992.

59. Da Viá, C., et al., *3D active edge silicon sensors with different electrode configurations: Radiation hardness and noise performance.* Nuclear Inst. and Methods in Physics Research, A, 2009. **604**(3): p. 505-511.

60. Vizkelethy, G., et al., *Anomalous charge collection from silicon-on-insulator structures.* Nuclear Inst. and Methods in Physics Research, B, 2003. **210**: p. 211-215.

61. *Charge collection mechanisms in MOS/SOI transistors irradiated by energetic heavy ions*. IEEE.

62. Pellegrini, G., et al., *Fabrication and simulation of novel ultra-thin 3D silicon detectors.* Nuclear Inst. and Methods in Physics Research, A, 2009. **604**(1): p. 115-118.

63. Schwank, J.R., et al., *Direct Comparison of Charge Collection in SOI Devices From Single-Photon and Two-Photon Laser Testing Techniques.* IEEE Transactions on Nuclear Science, 2011. **58**(3): p. 820-826.

64. C Guardiola, C.F., G Pellegrini, F García, D Quirion, J Rodríguez and M Lozano, *Ultra-thin 3D silicon sensors for neutron detection.* JINST, 2012.

65. Bartlett, D.T., *Radiation protection aspects of the cosmic radiation exposure of aircraft crew.* Radiation protection dosimetry, 2004. **109**(4): p. 349-355.

66. Available from: http://www.norfab.no/lab-facilities/sintef-minalab/.

67. *Compendium of Neutron Spectra and Detector Responses for Radiation Protection Purposes Supplement to TRS 318*, in *Technical Report Series*, 403, Editor 2001, IAEA. p. 337.

68. Hewitt, J.E., et al., *Ames collaborative study of cosmic ray neutrons: mid-latitude flights.* Health physics, 1978. **34**(4): p. 375-384.

69. Bradley, P.D. and A.B. Rosenfeld, *Tissue equivalence correction for silicon microdosimetry detectors in boron neutron capture therapy.* Medical Physics, 1998. **25**(11): p. 2220.

70. *Particle accelerators in radiation therapy. Proceedings of the CROS/RTOG Part III International Workshop. Houston, Texas. February 10-11, 1982.* International journal of radiation oncology, biology, physics, 1982. **8**(12): p. 2041.

71. *Relative biological effectiveness in ion beam therapy*, in *Technical Reports Series*2008, IAEA.

72. Matsufuji, N., et al., *Specification of Carbon Ion Dose at the National Institute of Radiological Sciences (NIRS).* Journal of radiation research, 2007. **48 Suppl A**(Suppl.A): p. A81.

73. L. De Nardo, D.M., P. Colautti, V. Conte, G. Tornielli and G. Cuttone *Microdosimetric investigation at the therapeutic proton beam facility of Catania* Radiation protection dosimetry, 2004. **110**: p. 6.

74. Loncol, T., Cosgrove, V., Denis, J. M., Gueulette, J., Mazal, A., Menzel, H. G., Pihet, P. and Sabattier, R *Radiobiological effectiveness of radiation beams with broad LET spectra: microdosimetric analysis using biological weighting functions* Radiation protection dosimetry, 1994. **52**: p. 6.

75. Haruhisa Matsumoto, H.K., Tateo Goka, Masayuki Fujii, Makoto Hareyama, Nobuhiro Kajiwara, Satoshi Kodaira, Kunitomo Sakurai, Nobuyuki Hasebe, *Delta ExE silicon telescope of energetic heavy ions trapped in radiation belts.* Japanese Journal Applied Physics, 2005. **44**((9A)): p. 3.

76. Kordyasz, A.J., et al., *Response to heavy ions and fission fragments of the monolithic silicon E–Δ E telescopes produced by the Quasi-Selective Epitaxy.* Nuclear Inst. and Methods in Physics Research, A, 2004. **530**(1): p. 87-91.

77. Agosteo, S., et al., *A pixelated silicon telescope for solid state microdosimetry.* Radiation Measurements, 2008. **43**(2): p. 585-589.

78. *RBE estimation of proton radiation fields using a Δ E − E telescope.* Medical Physics, 2009. **36**(10): p. 4486-4494.

79. Agosteo, S., et al., *A feasibility study of a solid-state microdosimeter.* Applied Radiation and Isotopes, 2005. **63**(5): p. 529-535.

80. Collaboration, G., *Geant4 User's Guide for Application Developers*, 2012.

81. ICRU, *Tissue Substitutes in Radiation Dosimetry and Measurement*, 1989: Bethesda, Md., U.S.A

82. *National Institute of Standards and Technology PSTAR Database Program*. NIST.

83. Takada, E., *Carbon Ion Radiotherapy at NIRS-HIMAC.* Nuclear Physics, Section A, 2010. **834**(1): p. 730c-735c.